Fall 2016

Innovative techniques for seismic-resistant bridge columns under ground motion excitations

Ayman A. Moustafa

INNOVATIVE TECHNIQUES FOR SEISMIC-RESISTANT BRIDGE COLUMNS UNDER GROUND MOTION EXCITATIONS

by

AYMAN A. MOUSTAFA

A DISSERTATION

Presented to the Faculty of the Graduate School of the

MISSOURI UNIVERSITY OF SCIENCE AND TECHNOLOGY

In Partial Fulfillment of the Requirements for the Degree

DOCTOR OF PHILOSOPHY

in

CIVIL ENGINEERING

2016

Approved by:

Mohamed A. ElGawady, Advisor
William Schonberg
Kamal H. Khayat
Jeffery Volz
K. Chandrashekhara

PUBLICATION DISSERTATION OPTION

This dissertation consists of the following six articles which have been submitted for publication, or will be submitted for publication as follows and have been formatted in the style used by each journal:

Paper I: pages 15-35 have been published in the *Construction and Building Materials* journal.

Paper II: pages 36-70 have been accepted by the *ACI SP 555* journal.

Paper III: pages 71-105 have been published in the *ASCE Journal of Composites for Construction*.

Paper IV: Pages 106-138 have been submitted to the *ASCE Journal of Bridge Engineering*.

Paper V: Pages 139-173 have been submitted to the *ASCE Journal of Bridge Engineering*.

Paper VI: Pages 174-211 have been submitted to the *ASCE Journal of Bridge Engineering*.

Paper VII: Pages 212-245 are intended for submission to the *ASCE Journal of Bridge Engineering*.

ABSTRACT

This dissertation provides innovative alternative solutions for replacing conventional reinforced concrete columns. The proposed columns displayed enhanced seismic resistance and properties compared to their counterpart conventional columns. Two main techniques were followed and proposed to develop seismic-resistant columns. The first technique utilized rubberized concrete to internally enhance energy dissipation and damping. Materials testing of rubberized concrete with scrap tire replacement of fine aggregates were performed to evaluate its dynamic properties. Shaking table testing of a rubberized concrete column was performed and the behavior was compared to that of the conventional one. The rubberized column showed an increase of 16% in energy dissipation compared to the conventional column. This solution also had the benefit of using recycled tire rubber, which produced green concrete. The second technique utilized post-tensioned segmental columns with double-skin cross section and external energy dissipaters. Three columns with different configurations were tested on the shaking table and compared with the conventional column. These columns outperformed the conventional column; especially regarding the residual drift. The peak drift for the post-tensioned columns was 8.85% with a residual drift of 0.08% compared to 4.8% peak drift with 1.5% residual drift for the conventional column. Three-dimensional finite element models for the post-tensioned columns were developed using LS-DYNA software. The effects of ground motion characteristics including far-field motions, near-fault motions without forward-directivity, near-fault motions with forward-directivity, and near-fault motions with fling-step on full-scale column models were investigated. An analytical model for the design of post-tensioned columns was provided.

ACKNOWLEDGMENTS

First and foremost, I thank Allah the almighty for making all things possible. I would also like to express my deepest gratitude to my advisor, mentor, and friend Dr. Mohamed ElGawady, for his guidance, friendship, and unwavering support throughout this research project. He played a tremendously influential role in helping me achieve one of the greatest accomplishments of my life. This study would not have been as enjoyable as it was without his great help, advising, motivation and encouragement. Words cannot express how grateful I am to have such an amazing advisor.

I would like to thank the members of my advisory committee: Dr. William Schonberg, Dr. Kamal Khayat, Dr. Jeffery Volz, and Dr. K. Chandrashekhara. Each of them provided valuable knowledge, great technical experience, and suggestions that continuously improved my knowledge and understanding.

I could not have survived the duration of this study without my family. I would like to thank my parents for providing me with their love and prayers. I love them more than words can express. I would also like to thank my friends in the United States and back home for always being there for me when I needed them.

I would also like to acknowledge my fellow graduate students in the civil department and our research group; especially Mr. Ahmed Gheni who provided a much needed help throughout my research. Thanks are also due to the Highbay laboratory staff: Brian Swift, Gary Abbott, John Bullock, and Greg Leckrone. They offered a tremendous amount of technical assistance and support.

In closing, from all of my heart and with deep sorrow, I would like to dedicate this dissertation to my late brother Mohammed and my late sister Marwa. You are greatly missed and will always be remembered.

TABLE OF CONTENTS

SECTION

APPENDICES

LIST OF ILLUSTRATIONS

Page

PAPER II

PAPER IV

LIST OF TABLES

Page

NOMENCLATURE

Symbol	Description
A	Cross sectional area of the beam
A_0	Initial amplitude
A_n	Amplitude after n cycles
D	CFFT's internal diameter
E	Modulus of elasticity
E_{tot}	Total input energy
E_{hys}	Summation of the hysteretic energy
E_k	Kinetic energy
E_p	Potential energy
E_e	Elastic energy
E_v	Viscous damping energy
E_R	Radiation energy from rocking
E_D	Energy dissipation
E_{S0}	Strain elastic energy
E_{ct}	Transverse Young's modulus of the core
E_f	GFRP's modulus of elasticity
E_{fr}	Fracture energy
$f_c^{'}$	Concrete compressive strength
f_n	Natural frequency

$f_R^{'}$	Rubberized concrete compressive strength
F_i	Force at point i (N),
P	Applied load
P_i	Inertial load
P_t	Measured load
P_b	Bending load
Q_x	Transverse shear force
R	Replacement percentage by volume of the fine aggregate with rubber
S	Horizontal distance between the two potentiometers
t_f	GFRP's thickness
$\ddot{u}_0(t)$	Acceleration at the mid-span of the beam
Y	Specific damping capacity
δ	Mid-span deflection
ρ	Mass density of concrete
ε_i	Strain at point i,
ε_f	GFRP's ultimate strain
ζ	Viscous damping ratio
ξ_{eq}	Equivalent viscous damping
Φ	Average curvature
σ_i	Stress at point i
Δ_i	Displacement at point i.

SECTION

1. INTRODUCTION

1.1. BACKGROUND

The current seismic provisions are intended to prevent bridges collapse and loss of lives by balancing the ductility capacity of the bridge columns with the seismic demand. The conventional RC columns by design accept some damage during a design earthquake (DE), mostly in the form of rebar yielding, concrete spalling, and residual drifts. Essential bridges, post-earthquakes, need to be restored to operation as quickly as possible to avoid any service interruption especially for emergency vehicles. Moreover, repairing RC bridge columns is costly and time consuming.

Severe damage can occur in RC columns especially when subjected to near-fault pulse-like ground motions. Pictures of bridges collapse from historical earthquakes are shown in Figures 1.1-1.3. They also experience large displacements and residual drifts. Severe damage in RC columns in Japan after the 1995 Kobe earthquake was observed and more than 100 RC bridges had to be demolished. Residual drifts up to 2% were the main reason for demolishing the bridges and they were defined as non-functional as it was difficult to retrieve those residual drifts (Figure 1.4). Therefore, the Japanese seismic design specifications are limiting the residual drifts of columns to 1%.

Thus, the need for development of new systems for seismic resistance has been emerging. This dissertation contributes to these efforts by providing two innovative techniques for seismic-resistant columns.

Figure 1.1 Bridge collapse from Loma Prieta, CA earthquake

Figure 1.2 Bridge collapse from Chi-Chi, Taiwan earthquake

Figure 1.3 Bridge collapse from Kobe, Japan earthquake

Figure 1.4 Residual drift of bridge columns from Kobe, Japan earthquake

1.2. OBJECTIVE AND SCOPE OF WORK

The objective of the proposed research was to develop, test, and evaluate innovative techniques for seismic-resistant bridge columns that could outperform conventional reinforced concrete (RC) bridge columns. Two techniques were proposed for this project. The first technique was based on changing the material damping by using recycled scrap crumb tire rubber as a replacement of fine aggregate in concrete to create rubberized concrete. The second technique was based on increasing external damping combined with a self-centering system and new column cross-section. The proposed new cross-section, called a hollow-core fiber reinforced polymer-concrete-steel (HC-FRPCS) segmental cross-section, consisted of an outer fiber reinforced polymer (FRP) tube, an inner steel tube, and concrete in between the two. The following scope of work was implemented to accomplish these goals: (1) review the Literature; (2) experimentally characterize the mechanical properties of rubberized concrete (Paper I); (3) experimentally investigate the dynamic properties of rubberized concrete using three different techniques (Papers II and III); (4) conduct fidelity testing of the new shaking table; (5) experimentally investigate large-scale RC, rubberized concrete, and segmental double-skin columns under simulated earthquakes (Papers IV, V, and VI). The investigated columns are illustrated in Table 1.1; (6) develop energy dissipating mechanisms for the segmental double-skin columns (Paper V); (7) develop a three-dimensional finite element model for post-tensioned segmental columns under simulated earthquakes (Paper VII); (8) numerically investigate full-scale segmental double-skin columns under simulated earthquakes (Paper VI); and (9) develop design tools for segmental columns (Paper VI). The rubberized column was proposed as an alternative for

the conventional concrete without changing the structural system. The segmental double-skin columns were proposed to limit the residual drifts and provide functionality after major earthquakes.

Table 1.1 Test matrix for large-scale testing

Column	RC	Rubberized	SEG	SEG-ED1	SEG-ED2
Nominal outer diameter (inch)	12				
Nominal inner diameter (inch)	N.A	N.A	7		
Steel tube thickness (inch)	N.A	N.A	0.188	0.188	0.188
FRP tube thickness (inch)	N.A	N.A	0.20	0.20	0.20
Longitudinal reinforcement	8#4	8#4	N.A.	N.A.	N.A.
Transverse reinforcement	spiral #3 @ 3 inch	spiral #3 @ 3 inch	N.A.	N.A.	N.A.
Energy dissipation mechanism	reference	rubberized concrete	rocking	external #2 L = 2 in	external #3 L = 6 in

1.3. DISSERTATION OUTLINE

This thesis includes three sections and three appendices. Section 1 includes a brief introduction to the subject area and explains the need for this research. The objective and

scope of the work of the study, as well as a detailed literature review establishing the state-of-the-art on the proposed topic is also presented in this section.

Section 2 contains seven journal papers that discuss the materials testing, large scale shaking table testing, and finite element modeling for the proposed seismic-resistant columns techniques. A summary of the dissertation with reference to the papers numbers associated with each task is illustrated in Figure 1.5.

Section 3 summarizes the work that was accomplished in this dissertation. It also presents the key findings of all experiments and theoretical analyses, which were executed during this research study, as well as a proposal for future research. The appendices include detailed test data and photographs from the research study.

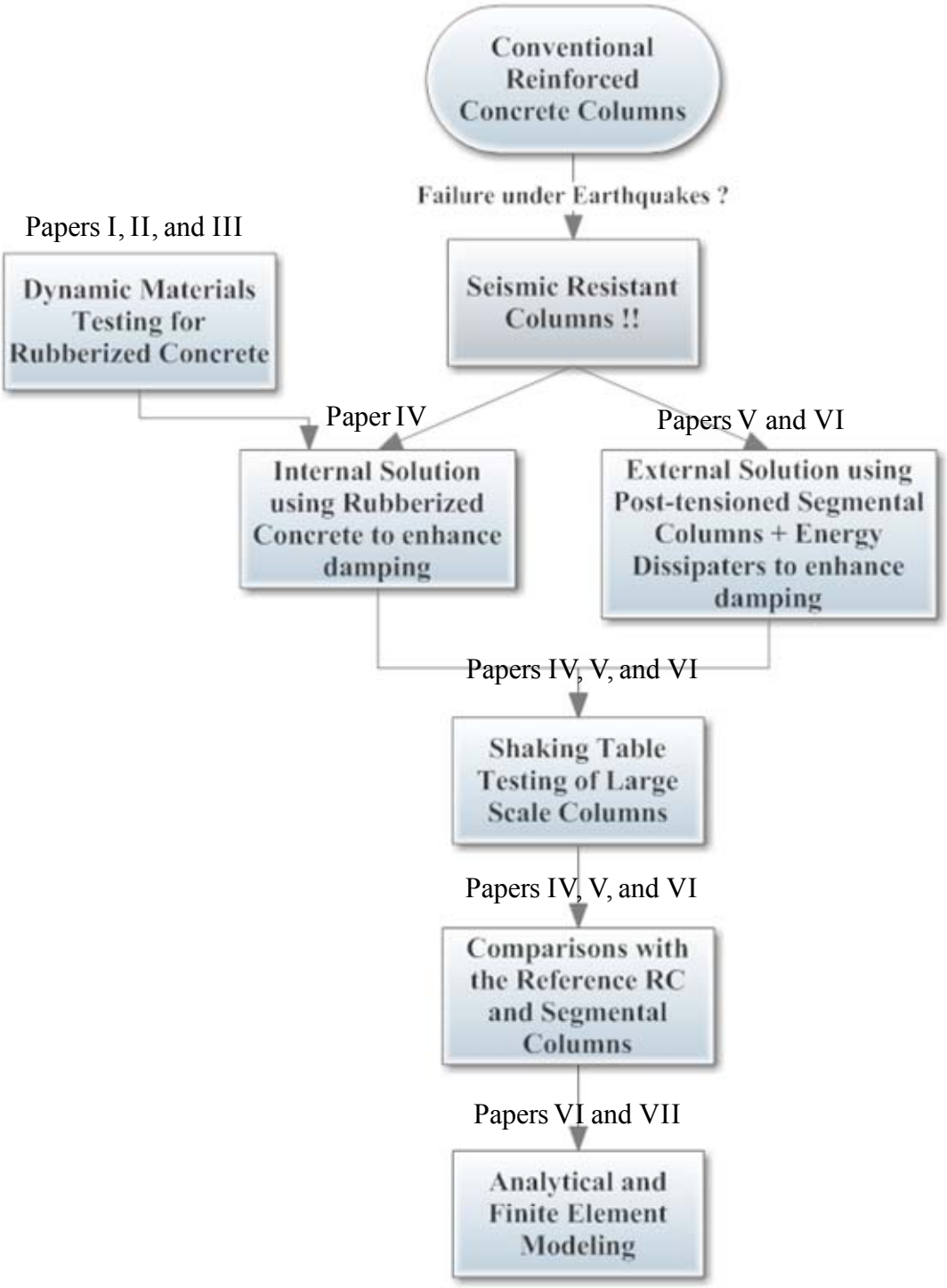

Figure 1.5 Dissertation summary

2. LITERATURE REVIEW

Over half of the nation's 607,000 bridges were built before 1940 (Kirk and Mallett 2013). Thus, these bridges have reached or are nearing the end of their useful service lives. These bridges need to be replaced and the newly constructed bridge columns need to be seismic-resistant in order to prevent damage in the future. Large residual drifts after earthquakes are the main reason for bridge demolition (Jeong et al. 2008). To reduce this excessive residual drift, the use of post-tensioning to allow controlled rocking of columns at the interface with the foundation and the superstructure can be implemented. The concept can be extended to segmental precast post-tensioned column system consisting of precast segments stacked over each other and connected by unbonded post-tensioning bars to increase the number of interfaces available for rocking (Chang et al. 2002; Chou and Chen 2006; Marriott et al. 2009; ElGawady et al. 2010; Ichikawa et al. 2016).

A very large amount of energy is emitted by an earthquake. The function of the bridge column is to dissipate this energy, preferably without damage. The addition of shredded scrap tires to concrete provides some favorable characteristics for concrete and alters some of concrete properties. The ordinary cement-based concrete is generally brittle; however, the addition of rubber to concrete, producing what is called rubberized concrete, can increase its ductility and impact resistance. It also increases the energy dissipation (Eldin and Senouci 1993; Topcu 1995; Toutanji 1996; Youssf et al. 2014).

2.1. RELATED RESEARCH ON RUBBERIZED CONCRETE

The use of scrap tires in concrete, producing what is known as rubberized concrete, represents a beneficial option for the concrete industry. Replacing virgin materials with waste materials reduces the amount of waste materials going to landfills. If improperly handled, scrap tire piles can be easily set on fire. These fires are difficult to extinguish. They also produce both heavy smoke and toxic run off. Exposed scrap tires can be a breeding space for mosquitoes that carry disease (Rubber Manufacturers Association 2014).

Recent research has shown that rubberized concrete possesses a viscous damping that is significantly higher than conventional concrete, making it a good candidate for concrete structures subjected to dynamic loads such as earthquake ground motions (Reda Taha et al. 2008, Xue and Shinozuka 2013, Moustafa and ElGawady 2015). Rubberized concrete, however, displays strength that is smaller than its counterpart conventional concrete. This drawback can be overcome by confining rubberized concrete (Youssf et al. 2014).

The mechanical properties of rubberized concrete were investigated extensively under static loading. Others have concluded that replacing a high percentage of mineral aggregates with shredded rubber reduces the concrete's compressive strength and workability. The amount of reduction depends on the percentage and type of aggregate to be replaced (either coarse or fine aggregate) as well as the size and distribution of the rubber particles (Eldin and Senouci 1993; Topcu 1995; Khatib and Bayomy 1999; Hernandez-Olivares et al. 2002; Siddique and Naik 2004; Youssf et al. 2014). Rubberized concrete, however, displays a more ductile behavior, better impact resistance, and

stronger energy dissipation than conventional concrete. Zheng et al. 2008 measured viscous damping values ranging from 0.68% to 1.67% on small rubberized concrete cubes compared to viscous damping values ranging from 0.45% to 0.74% measured on conventional concrete cubes, i.e., rubberized concrete displayed about 75% higher viscous damping than that of the corresponding conventional concrete. Xue and Shinozuka 2013 investigated the seismic behavior of reinforced rubberized concrete columns. The columns displayed an average viscous damping coefficient of 7.7% compared to 4.75% for the corresponding columns constructed out of conventional concrete, i.e., rubberized concrete displayed 62% higher viscous damping than that of the conventional concrete. Reda Taha et al. 2008 found that rubberized concrete has an impact resistance that is 33% higher than conventional concrete at replacement ratios higher than 20%.

Results of energy dissipation of rubberized concrete material showed a significant scatter and contradiction. Replacing 3.5% to 30% of mineral aggregates with scrap rubber increased the energy dissipation and viscous damping by 23% to 30% (Zheng et al. 2008). Beyond 30% replacement, the energy dissipation decreased. Moustafa and ElGawady 2015 measured rubberized concrete energy dissipation using different approach and reported an increase in energy dissipation, hysteresis damping, and viscous damping compared to conventional concrete. The increase ratio varies with the variation in the measuring approach. Xue and Shinozuka 2013 performed shaking table testing on two small-scale columns having dimensions of 40 mm x 40 mm x 500 mm with one rebar in the center. One column was constructed with conventional concrete and the other with rubberized concrete with 15% replacement of fine aggregates. However, the shaking

table test results were not used to determine the damping of the columns, but rather free vibration testing of the columns using impact hammer were used to determine the damping ratio. Using the impact free vibration results, they reported an increase of damping ratio of 62% for the rubberized concrete compared to the conventional concrete. The shaking table tests were used to report a decrease in the peak seismic response acceleration by 27% for the rubberized column compared to the conventional column. Other researchers reported no increase in energy due to rubber replacement (Resende et al. 2003). Bowland 2011 tested two full-scale footbridges; one with conventional concrete and the other with 15% replacement of fine aggregate with ground rubber. No significant change in damping between the two footbridges was reported. This may be attributed to the very low imposed excitations of only 0.05g.

Limited large scale testing of rubberized concrete columns has been carried out under pseudo static loading (Youssf et al. 2015; Youssf et al. 2016). Youssf et al. 2015 investigated the behavior of a rubberized concrete column with 20% rubber replacement of fine aggregate under reversed cyclic loading. The energy dissipation and hysteresis damping were determined from the cyclic loading and the damping ratio was determined from snap-back tests. The rubberized column had an increase of 13% in hysteretic damping while the viscous damping was decreased by 49% compared to the conventional column. Youssf et al. 2016 investigated rubberized concrete columns confined with fiber reinforced polymers (FRP). The overall behavior of the FRP confined rubberized column was very similar to that of the FRP confined conventional concrete. The rubberized concrete had an insignificant effect on the energy dissipation and damping.

While these results provide an insight about the use of rubberized concrete as a structural component, the pseudo static nature of loading can be misleading with regard to the dynamic behavior of rubberized concrete columns. In this study, the dynamic behavior of rubberized concrete bridge columns is investigated under simulated ground motions to investigate the dynamic behavior of these columns.

2.2. RELATED RESEARCH ON SEGMENTAL COLUMNS

Despite the fact that the main purpose of the post-tensioned self centering columns is to sustain dynamic loading from earthquakes, most of the research in this area is performed under static cyclic loading (Mander and Cheng 1997; Hewes and Priestley 2002; Chou and Chen 2006; Palermo et al. 2007; Shim et al. 2008; Wong et al. 2008; Marriott et al. 2009; Solberg et al. 2009; Ou et al. 2009; ElGawady et al. 2010; ElGawady and Sha'lan 2010; Kim et al. 2010; Ou et al. 2010; Ichikawa et al. 2016). In these static cyclic tests, large peak drifts and low residual drifts were achieved. The posttensioned RC columns with conventional rebar and transverse reinforcement still experienced heavy concrete spalling, rebar buckling, and in some cases loss of strand anchorage. Confinement in forms of steel or FRP tubes was adapted to overcome this issue. However, unconfined concrete above or below these tubes were often damaged. In this article, the cross-section is confined all over the column height to avoid damage.

To overcome the deficiency of the inherent low energy dissipation of the posttensioned columns, the use of energy dissipaters in forms of ductile fiber reinforced concrete (Billington and Yoon 2004; Solberg et al. 2009; Ichikawa et al. 2016), internal bonded steel (Palermo et al. 2007; Wang et al. 2008; Ou et al. 2010); and external energy

dissipaters in form of steel bars or angles (Chou and Chen 2006; Marriott et al. 2009; ElGawady et al. 2010; ElGawady and Sha'lan 2010) was researched. Marriott et al. 2009 used mild steel as an external energy dissipaters with grouted steel tube casing to prevent their buckling. This connection is promising because it provided a simple connection with ease of construction and high energy dissipation. However, rupture of the external energy dissipaters occurred due to low cyclic fatigue resulting from the bond between the bars and grout making it a bonded connection despite the design was for an unbonded connection. It should be noted that the tests were performed up to a small lateral drift of 3.5% and under static cyclic loading. In the current study, the use of external energy dissipaters in form of mild steel is implemented with unbonded steel bars detailed to act in tension only to avoid these drawbacks.

Fewer studies on the posttensioned columns were performed under dynamic loading using shaking tables. Yamashita and Sanders 2009 performed a shaking table testing on a ¼ scale rectangular column with shear keys between the segments to prevent slippage. The footing, segments, and head were joined with epoxy adhesive for segmental bridges. The prestressing strand suffered slippage and the anchorage plates popped out. The use of shear keys and epoxy would result in delaying the column construction and increasing complexity. Guerrini and Restrepo 2013 performed a shaking table testing on a posttensioned dual-steel shell column. The column achieved 8.6% drift with fracture of energy dissipating dowels at a drift of 6.6%. Motaref et al. 2013 tested five 1/3 segmental bridge columns with different materials in the plastic hinge on the shaking table. They concluded that the proposed models are suitable for accelerated bridge construction in high seismic zones because of their fast construction, high energy dissipation, minimal

damage in the plastic hinge zone, and minimal residual displacement. However, the lower segment of all columns was cast in place monolithically, violating the rocking behavior. Trono et al. 2014 investigated a posttensioned column under three dimensional shaking table test. The lower portion was armored with headed bars and built using hybrid fiber-reinforced concrete. The column achieved a peak drift of 10.8% and a residual drift of 0.4%.

Finite element models and design guidelines for segmental columns were also developed (Pampanin et al. 2001; Palermo et al. 2007; Dawood et al. 2011; ElGawady and Dawood 2012; Chou et al. 2013; Zhang and Alam 2015; Leitner and Hao 2016).

A new double-skin cross-section is proposed for the segmental post-tensioned columns in this study. The double-skin columns are columns consisting of outer FRP tube, inner steel tube, and concrete in between the two. This system combined and optimized the benefits of all three materials (FRP, concrete, and steel). Several experimental and finite element studies were conducted on the double skin columns under different static and cyclic loading conditions (Teng et al. 2007; Wong et al. 2008; Han et al. 2010; Ozbakkaloglu and Idris 2014; Abdelkarim and ElGawady 2014). However, the use of such cross-section in segmental construction, to the knowledge of the authors, has not been implied yet.

PAPER

I. MECHANICAL PROPERTIES OF HIGH STRENGTH CONCRETE WITH SCRAP TIRE RUBBER

Ayman Moustafa[1]; and Mohamed ElGawady[2]

ABSTRACT

Green construction has been a very important aspect in the concrete production field in the last decade. One of the most problematic waste materials is scrap tires. The use of scrap tires in civil engineering is increasing. This article investigates the effect of using scrap tires in high strength concrete on both the mechanical and dynamic properties. Two different rubberized concrete mixtures were designed. The first set; variable slump (VS) was intended to study the effect of rubber replacement of sand on the workability of concrete. The other set; constant slump (CS) was designed to keep the workability the same. The compressive strength of the concrete was reduced by the use of rubber with more severe loss of strength for VS compared to CS. The viscous damping ratio was investigated using free vibration tests with impact hammer on simply supported beams. The replacement of up to 30% of sand with rubber resulted in an increase in damping with the increase being more in the CS beams as well. The hysteresis damping for cylinders under cyclic loading was also investigated and the average hysteresis

[1] Graduate research assistant, Department of Civil, Architectural, and Environmental Engineering, Missouri University of Science and Technology, USA E-mail: ampyf@mst.edu
[2] Benavides Associate professor, Department of Civil, Architectural, and Environmental Engineering, Missouri University of Science and Technology, USA E-mail: elgawadym@mst.edu

damping was found to increase. The results of this article give an insight on the properties of high strength concrete with scrap tire rubber.

Key words: Damping ratio; high strength concrete; rubberized concrete; scrap tires

1. Introduction

Green construction has been an important aspect in the concrete production field in the last decade or so. The use of waste products in concrete manufacturing is beneficial both economically by replacing some of the components with waste materials and environmentally by clean disposal of waste materials. One of the most problematic waste materials is scrap tires; if improperly handled, scrap tires can be a threat to environment. Exposed scrap tires can be a breeding space for mosquitoes that carry disease. Scrap tire piles can be easily set on fire which is difficult to put out, and produces heavy smoke and toxic run off to waterways [Rubber manufacturers association 2014].

The addition of shredded scrap tires to concrete provides some favorable characteristics for concrete and alters some of concrete properties. The ordinary cement-based concrete is generally brittle; however, the addition of rubber to concrete, producing what is called rubberized concrete, can increase its ductility and impact resistance [[1]; [2]; [3]; [4]]. Rubberized concrete is used in many applications such as concrete pavements, sidewalks, and road barriers where concrete is subjected to dynamic loading from moving vehicles or people walking on sidewalks.

The mechanical properties of normal strength rubberized concrete have been extensively investigated [[5]; [6]; [7]; [8]]. An extensive literature review for the

mechanical properties of normal strength rubberized concrete can be found in [9]. Past research concluded that the addition of high percentage of shredded rubber to concrete reduces the compressive strength and workability of fresh concrete. However, these effects vary according to many factors such as the size and distribution of the rubber particles, the type of aggregate to be replaced (coarse aggregate or fine aggregate), and the percentage of rubber content in a rubberized concrete mixture. Youssef et al. [4] investigated the FRP confinement effects on rubberized concrete.

The dynamic properties of rubberized concrete have not yet received the attention it deserves. Hernandez-Olivares et al. [10] reported an increase of 23% to 30% of the dissipated energy of rubberized concrete having low rubber contents of 3.5% and 5% compared to conventional concrete. Zheng et al. [11] investigated the dynamic properties of rubberized concrete. A more recent study [12] investigated methods for increasing the damping capacity of concrete by replacing up to 20% of the fine aggregate with shredded rubber. Generally, these researchers reported an increase in damping and decrease in compressive strength was reported.

While there have been some investigations of the dynamic properties of rubberized concrete [[10]; [11]; [12]], the mechanical and dynamic properties of high strength concretes with scrap tires, to the best knowledge of the authors, have not been studied yet. In this manuscript, the mechanical and dynamic properties of high strength concrete (concrete with compressive strength of greater than 65 MPa) having scrap tire rubber as a substitution for fine gravel were studied. Furthermore, past research on dynamic properties of normal strength rubberized concrete either focused on measuring viscous damping [11] or hysteretic damping [[10]; [12]]. This study represents the first

study to carry out comprehensive evaluation of the viscous and hysteretic damping of rubberized concrete. Different percentages of replacement of sand ranging from 0 to 30% by volume were investigated. The dynamic properties of high strength rubberized concrete are also investigated using an impact hammer. The dissipated energy and hysteresis damping are also investigated.

2. Experimental investigation

2.1. Material characteristics

Two sets of rubberized concrete mixtures were designed and used during the course of this study. The first set, hereafter called variable slump (VS), was used to test the properties of concrete having 0%, 5%, 10%, 15%, 20%, and 30% volume replacement of sand with shredded rubber. The second set, hereafter called constant slump (CS), is similar to VS set but with variable amounts of superplasticizer to maintain the same workability of the fresh concrete regardless of the rubber percentages. The materials used for sets VS, and CS are shown in tables 1 and 2, respectively. The mixture nomenclature in tables 1 and 2 consists of mixture set (VS or CS) followed by the percentage of sand replacement with rubber by volume.

The cement used in all mixtures is type I Portland cement meeting ASTM C150 specifications. Limestone washed coarse aggregate with nominal maximum size of 1 in was used. The sand used was Missouri river sand. The rubber used was ground rubber with three different sizes of 8-14, 14-30, and 30- where the first number represents the sieve number of the passing particles and the second number represents the sieve number

of the retained particles. Different trial mixtures including different grading of the shredded rubber were prepared and the grading that had the best workability and consistency was selected for all mixtures. Figure 1 shows the grading of the sand, coarse aggregate and ground rubber used during the course of this research. Figure 2 shows the used ground rubber. The material characteristics of the sand, coarse aggregate and rubber are shown in table 3.

Table 1. Mixture proportions for the control concrete and for VS set.

Materials (kg/m^3)	Water	Cement	Fly Ash	Coarse aggregate	Super-Plasticizer	Sand	R(8-14)	R(14-30)	R(30-)
Normal Concrete	142.40	336.39	112.13	1057.22	1.07	576.66	-	-	-
VS 05	142.40	336.39	112.13	1057.22	1.07	544.63	10.09	3.20	0.70
VS 10	142.40	336.39	112.13	1057.22	1.07	519.00	20.18	6.41	1.41
VS 15	142.40	336.39	112.13	1057.22	1.07	490.16	30.27	9.61	2.11
VS 20	142.40	336.39	112.13	1057.22	1.07	461.33	40.37	12.81	2.82
VS 30	142.40	336.39	112.13	1057.22	1.07	403.67	60.55	19.22	4.23

Table 2. Mixture proportions for the control concrete and for CS set.

Materials (kg/m^3)	Water	Cement	Fly Ash	Coarse aggregate	Super-Plasticizer	Sand	R(8-14)	R(14-30)	R(30-)
Normal Concrete	142.40	336.39	112.13	1057.22	1.12	576.66	-	-	-
CS 05	142.40	336.39	112.13	1057.22	1.33	544.63	10.09	3.20	0.70
CS 10	144.17	336.39	112.13	1057.22	1.33	519.00	20.18	6.41	1.41
CS 15	144.17	336.39	112.13	1057.22	1.55	490.16	30.27	9.61	2.11
CS 20	144.17	336.39	112.13	1057.22	1.65	461.33	40.37	12.81	2.82
CS 30	144.17	336.39	112.13	1057.22	1.76	403.67	60.55	19.22	4.23

Table 3. Material characteristics.

Material	Specific gravity	fineness	Unit weight (kg/m^3)
Sand	2.61	2.86	1442
Coarse Aggregate	2.69	N.A*	1554
Rubber	1.16	N.A*	641

* N.A = Not available

2.2. Concrete mixing

The mixing procedure of the concrete was started by dry mixing the coarse aggregate, sand, and rubber for about 1 minute to insure distribution of the aggregates and then the cement and fly ash were added and the concrete was dry mixed for another minute. The superplasticizer was added to the water and the water was then added to the mixture and the concrete was mixed for 2 minutes and then let stand for 1 minute; then, mixed for another two to three minutes until consistency was observed. For the CS mixtures, the slump test was performed after the mixing and superplasticizer was carefully added if the slump was not satisfied.

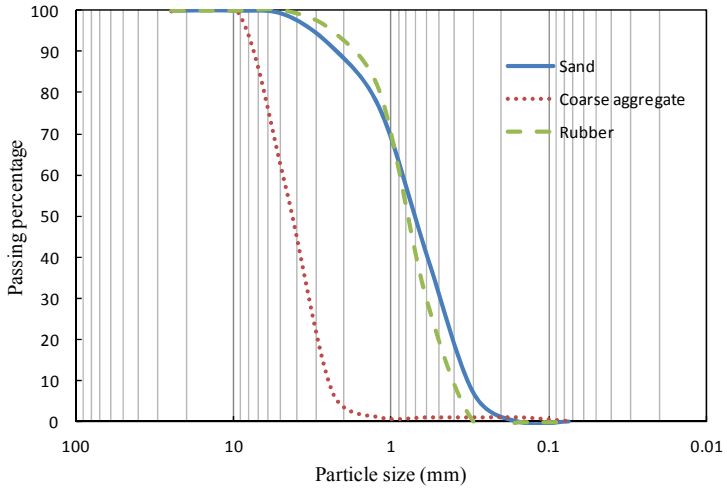

Figure 1. Grading of used materials.

Figure 2. Used ground rubber.

2.3. Test specimens

Six concrete beams of each set, VS and CS, were cast with nominal dimensions of 150 mm x 150 mm x 900 mm; one for each percentage of rubber replacement and these were used to determine the dynamic modulus of elasticity and the damping ratio of each mixture. Mechanical vibration was performed for all the beams to insure proper placement and filling of the concrete. A total of thirty-six 100 mm x 200 mm cylinders for each set were cast in the same day with the beams to determine the compressive strength of the concrete at 7 and 56 days. The cylinders were also tested under axial cyclic loading at 56 days to determine the hysteretic damping of the different concrete mixtures. The beams and cylinders were demolded after 24 hours and were moist cured in a controlled moisture room for 7 days. Then, they were removed from the curing room and left in the ambient temperature in the High-bay Lab at the Missouri University of Science and Technology.

2.4. Test setups

The compressive strengths of the concrete cylinders were determined using an MTS machine. The cylinders were grounded to assure the leveling of the surface and the two surfaces are parallel to each other. To determine the average axial strain of the concrete, two string potentiometers were placed on two opposite sides of each cylinder at a gauge length of one-third of the cylinder height. The average axial strains along a full specimen height were also measured using a Linear Variable Displacement Transducer (LVDT). The test setup for the compressive strength is shown in Figure 3.

The cylinders were monotonically tested to determine the concrete compressive strength at 7 days. At 56 days, one group of the concrete cylinder specimens was monotonically loaded in a displacement control and another group was cyclically loaded using displacement control up to failure. The loading rate for both sets was 5 mm/min. The cyclic axial compressive loading, including loading/unloading cycles, was applied based on a prescribed pattern of progressively increasing levels of axial displacements until failure occurred. Three cycles of loading/unloading were applied at each axial displacement level. Finally, the cylinders were tested for compressive strength at 56 days to represent the actual compressive strength of the beams on the test day.

Figure 3. Compression test setup.

The dynamic properties of the rubberized concrete were determined using simply supported beams excited by an instrumented impulse hammer with a capacity of 22.5 kN. Figure 4 shows the dynamic test setup. Four accelerometers were mounted on the surface of the beam. The beam was excited by hitting the beam at mid-span using the impact hammer. The accelerations were recorded using data acquisition system called Synergy box along with the instrumented hammer reading.

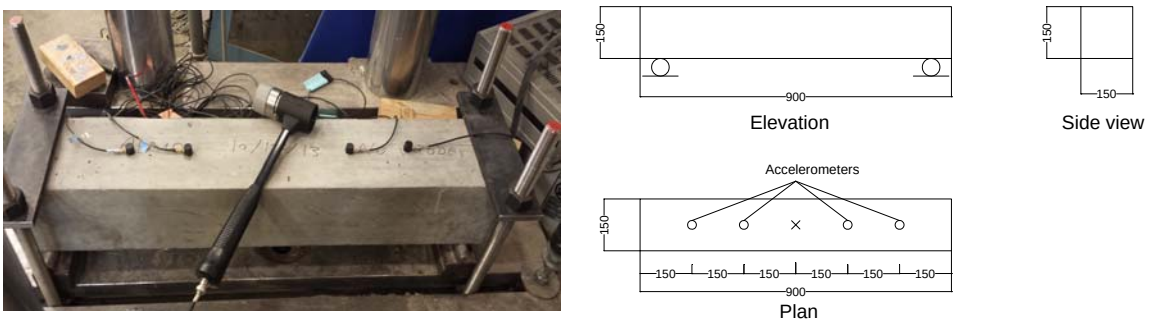

Figure 4. Dynamic test setup (dimensions are in mm).

3. Dynamic properties analysis

The hysteresis is the property of systems to follow different loading and unloading paths. The hysteresis damping for the cyclic testing is calculated from the specific damping capacity (Y), which is the ratio between the energy dissipated per unit volume of the material, E_D, and the strain energy per unit volume stored in a linear elastic system, E_{S0}, as shown in eq. 1.

$$Y = \frac{E_D}{E_{S0}} \tag{1}$$

A graphical representation of ED and ES0 is shown in Figure 5 [13].

The energy dissipated per cycle per unit volume, E_D, is measured as the area enclosed by a hysteresis loop drawn on axes of stress and strain. It can be calculated mathematically using eq. 2.

$$E_D = \sum_{i=1}^{n-1} \left(\frac{\sigma_{i+1} - \sigma_i}{2} \right) \left(\varepsilon_{i+1} - \varepsilon_i \right) \tag{2}$$

where, E_D is the dissipated energy (lb-in/in^3), n is the total number of stress or strain points, σ_i is the stress at point i (psi), and ε_i is the strain at point i.

The hysteresis damping can be expressed as the equivalent viscous damping and is calculated from the specific damping capacity using eq. 3.

$$\xi_{eq} = \frac{1}{2\pi} Y \tag{3}$$

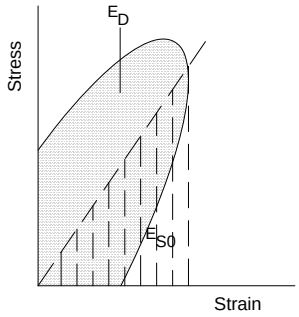

Figure 5. Dissipated energy per unit volume of the material, E_D and elastic strain energy, E_{S0}.

4. Experimental results and discussion

4.1. Fresh concrete properties

The density of each concrete mixture was measured as shown in Table 4. As shown in the table, replacing sand with rubber slightly decreased concrete density. Replacing 30% of sand with rubber decreased concrete density by approximately 6%.

Table 4. Concrete densities.

Specimen	Normal Concrete	5% Rubber	10% Rubber	15% Rubber	20% Rubber	30% Rubber
Density (kg/m^3)	2514.90	2466.84	2442.82	2419	2386.75	2386.75

As mentioned before, two sets of mixtures were investigated in this study. The first set, VS, was intended to study the effect of replacing sand with rubber on the workability of the concrete. The slump of the rubberized concrete for VS is shown in figure 6. The slump of the control mix without rubber was 150 mm and it decreased with increasing rubber content as shown in the figure. The figure shows that replacements of up to 10% rubber did not severely affect the workability of the concrete mixtures. Concrete having 5, and 10% rubber had a slump loss of 50 mm and 62.5 mm, respectively. Beyond 10% replacement, the workability degraded significantly. Using 30% rubber replacement resulted in a loss of slump of about 125 mm and the concrete was no more workable. For the 30% rubber replacement, mechanical vibration was also needed for the cylinders due to the loss of workability. The second set, CS, was tailored to achieve the same workability for all the mixes by varying the superplasticizer percentage. The slump for this set is also shown in figure 5 and it shows that the slump is almost constant.

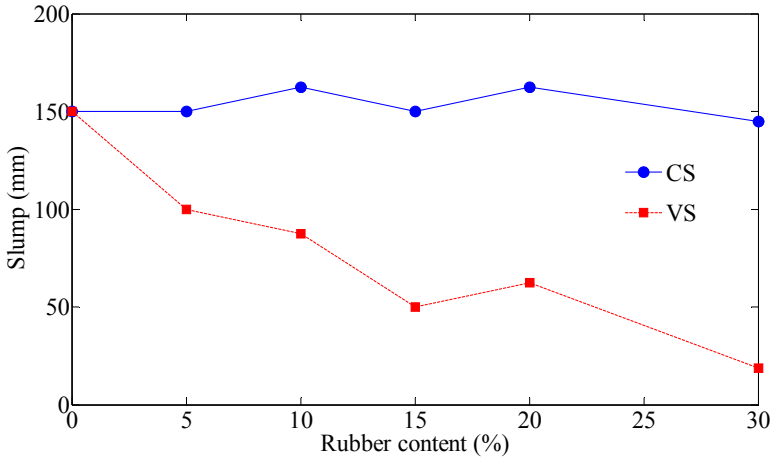

Figure 6. Slump of the rubberized concrete.

4.2. Compressive strength

The compressive behavior of VS and CS mixtures was determined at 7 and 56 days. Figure 7 shows the compressive stress after 7 days of moist curing according to ASTM C192 [14] and after 56 days. The For the CS mixture, the figure shows that for a replacement up to 15%, the 7 days compressive stress suffer very limited degradation and beyond that severe degradation was observed reaching 17.4% for 30% replacement. For the VS mix, a very large drop in the stress occurred for all replacement percentages. It can be noticed that the compressive stress for the VS mix is lower than the CS mix for all rubber percentages. This can be attributed to the effect of the superplasticizer freeing more water for the hydration and also to the loss of the workability of the concrete leading to difficulties in the preparation of the cylinders hence more voids and less strength. This was visually confirmed after demolding of the cylinders.

Figure 7 also shows the average compressive strength of concrete cylinders subjected to axial monotonic loading at 56 days. Similar to the stresses at 7 days, the figure shows higher compressive strengths for the CS mix compared to the VS mix. For CS series and unlike the 7 days stress, replacing any percentage of sand resulted in a significant reduction in strength. Replacing up to 15% of sand with rubber resulted in a strength reduction of approximately 10%. At 30% replacement, the strength reduction was approximately 32%. Three cylinders were used for determination of the compressive strength of each rubber content. The standard deviation for the VS mix was higher than that of the CS mix. This difference was caused by the non-uniform distribution of the rubber particles in the VS mix compared to the CS mix.

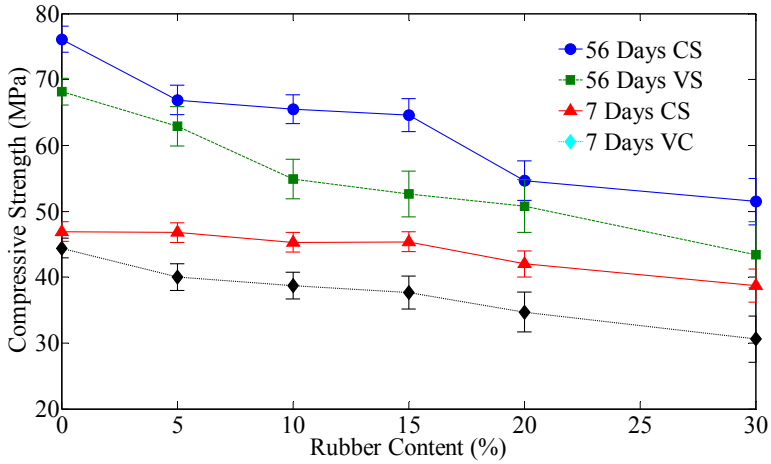

Figure 7. Average compressive stress for VS and CS cylinders.

Figure 8 shows the stress strain curves for the monotonic loading at 56 days. The figure shows a very large difference in ductility between the conventional and the rubberized concretes. The conventional concrete failed in a brittle way once it reached the peak load. The addition of 5% rubber in the VS mix did not change the brittle behavior while the addition of higher percentages of rubber increased the ductility. The addition of up to 15% rubber in the CS mix did not change the sudden failure. It should be noted that for the cyclic loading, gradual degradation of strength started at 10%. This can be attributed to the fact that the monotonic loading keeps increasing the displacement demand; preventing the rubber particles for low replacements from providing compressibility. In the cyclic loading, unloading the specimen results in expansion of the rubber particle (returning to original position); leading to an accommodation of compression in the next cycle. The difference in ductility between the two mixes is the VS mix is less uniform so the rubber particles might be concentrated in spots increasing the compressibility. This makes the VS mix a possible candidate for applications such as sidewalks and road barriers, where the impact resistance is required.

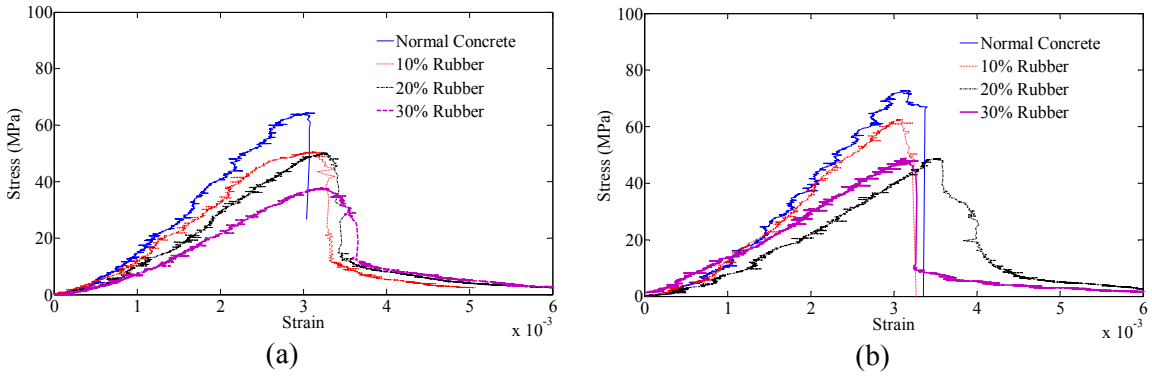

Figure 8. Stress-strain curves for a) VS and b) CS.

The mode of failure for the concrete changed with the addition of rubber. The high strength concrete with no rubber exhibited a brittle failure and shattered into small pieces when it reached the maximum load, while the rubberized concrete experienced a more ductile failure and was able to sustain loads after reaching its capacity. The stress-strain curves for these cylinders will be discussed in the next section. Figure 9 shows the failure shape of cylinders having 0, 10%, 20%, and 30% rubber replacement.

Figure 9. Failure of the concrete cylinders: a) normal concrete, b) 10% rubber, c) 20% rubber, and d) 30% rubber replacement.

4.3. Hysteresis damping results

The stress-strain curves for the normal concrete and the rubberized concretes for SV and SC are shown in Figures 10 and 11, respectively. The energy dissipated per cycle per unit volume, E_D, can be calculated for each of the stress-strain curves using eq. 2. Since the loading was displacement controlled, it is more representative to plot E_D versus the strain of the test specimen. Figure 12 shows the energy dissipated for the four different specimens. The figure shows that the energy dissipated for the normal concrete increases up to the failure strain, while the rubberized concrete dissipates energy after the peak load. Figure 13 shows the cumulative energy dissipation of the different mixtures. As shown in the figure, the cumulative energy dissipation for the rubberized concrete is much higher than the normal concrete.

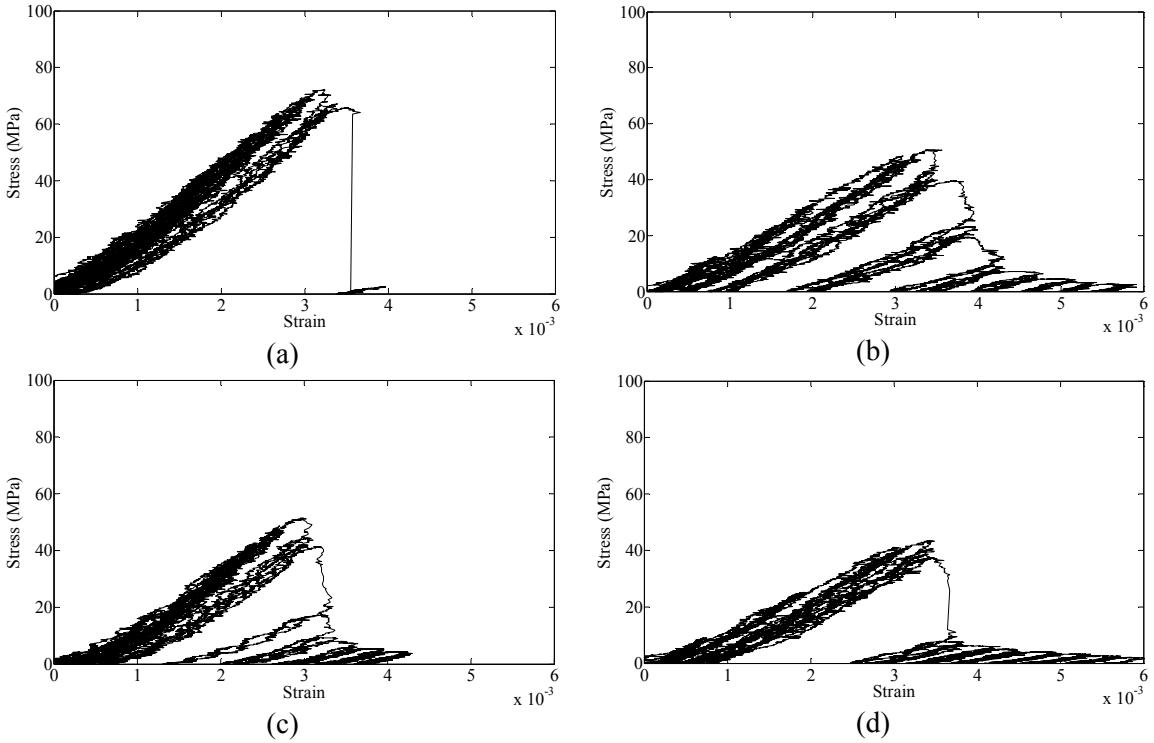

Figure 10. Stress-strain curves of VS mix for a) normal concrete, b) 10% rubber, c) 20% rubber, and d) 30% rubber replacement.

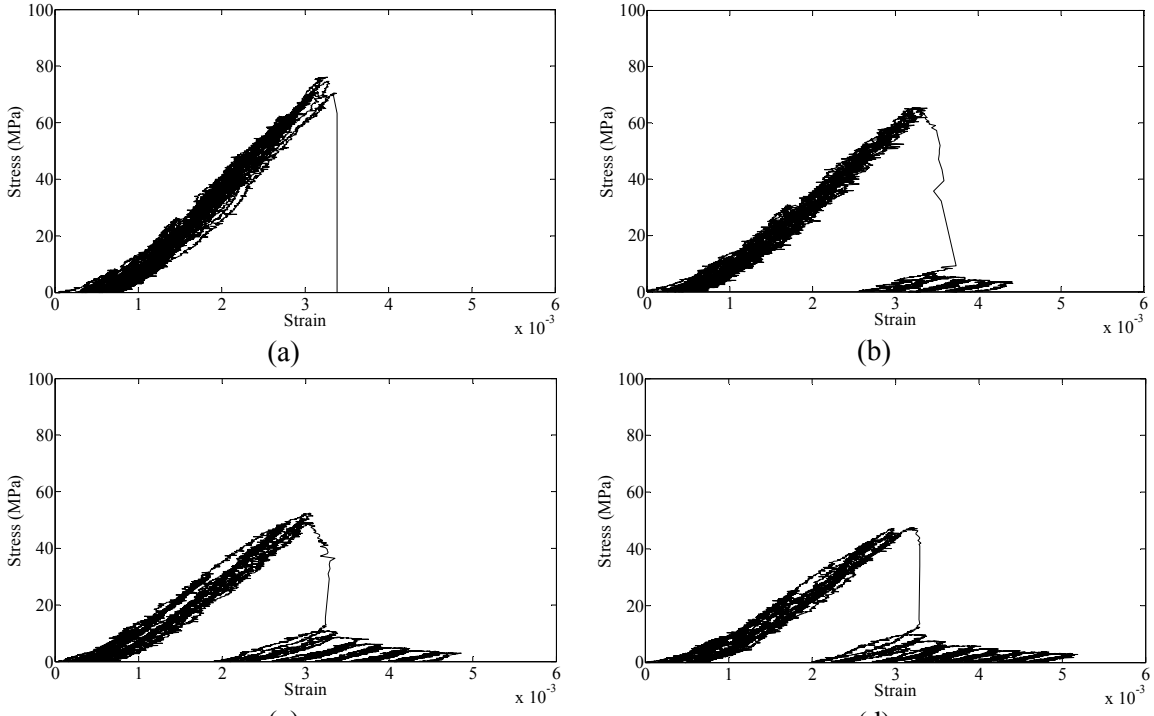

Figure 11. Stress-strain curves of CS mix for a) normal concrete, b) 10% rubber, c) 20% rubber, and d) 30% rubber replacement.

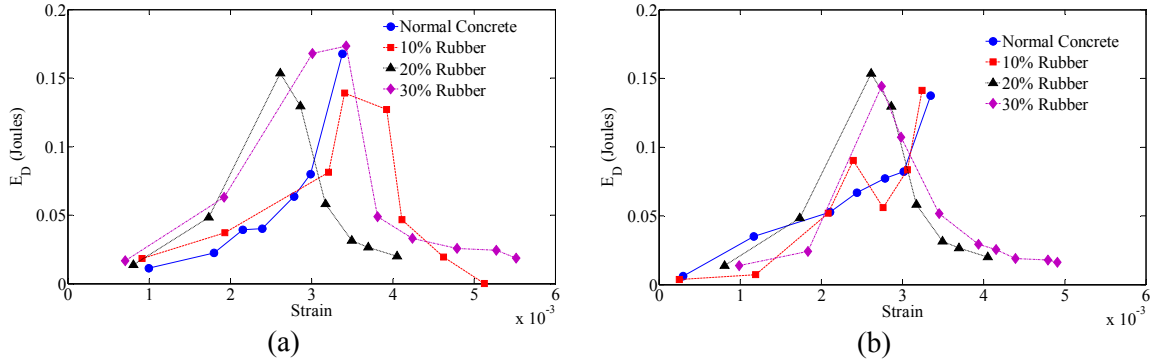

Figure 12. Energy dissipated per cycle per unit volume for a) VS and b) CS.

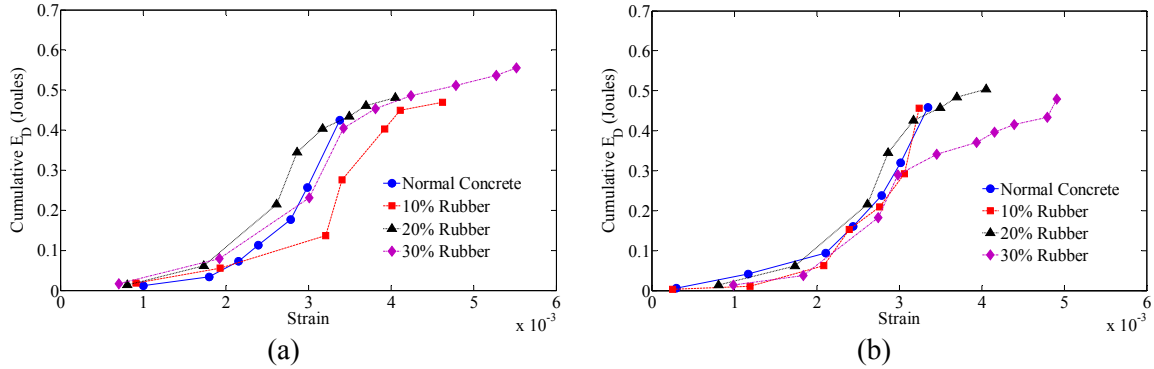

Figure 13. Cumulative dissipated energy for a) VS and b) CS.

The hysteresis damping is calculated using eq. 3 for each cycle. Figure 14 shows the hysteresis damping vs. axial compressive strain for each mixture for both sets. The figure shows that the average hysteresis damping increases with the increase of rubber content. For 20% and 30% rubber replacement the equivalent viscose damping reach approximately four times the equivalent viscous damping of normal concrete. The increase in damping is higher than that observed by [10] and [12] because of the higher replacement ratios.

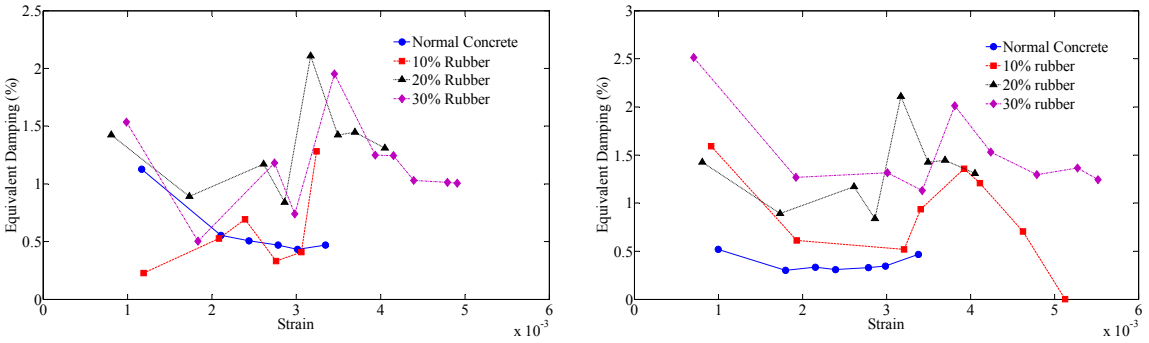

(a) (b)

Figure 14. Hysteresis damping for different rubber contents for a) VS and b) CS.

4.4. Damping ratio

The viscous damping ratio can be calculated using the logarithmic decrement method [15] for the measured accelerations. A typical damping curve is shown in Figure 15 for the measured signals. The figure shows that the actual response of the beams is not strictly exponential; hence, variation in the value of damping ratio occurs with the change in the number of cycles used to calculate the damping. In the current study, a base of 10 cycles is used to define the damping ratio and is denoted by ζ_{10}.

The change in ζ_{10} with the rubber content is shown in Figure 16. The figure shows an increasing trend of the damping ratio with the increase in rubber content for

both CS and VS mixes. The increase in the damping ratio for VS mixture was 5.3%, 19.8%, and 22.9% for 10%, 20%, and 30% replacement, respectively. For the CS mixture, the increase was 12.5%, 29.4%, and 32.5% for 10%, 20%, and 30% replacement, respectively. The larger increase in the CS mix can be attributed to the higher workability of CS leading to a uniform distribution of the rubber particles as opposed to concentration of rubber in some places like the bottom surface and the corners. The results of the viscous damping are of good agreement with the results by [11] for normal strength concrete.

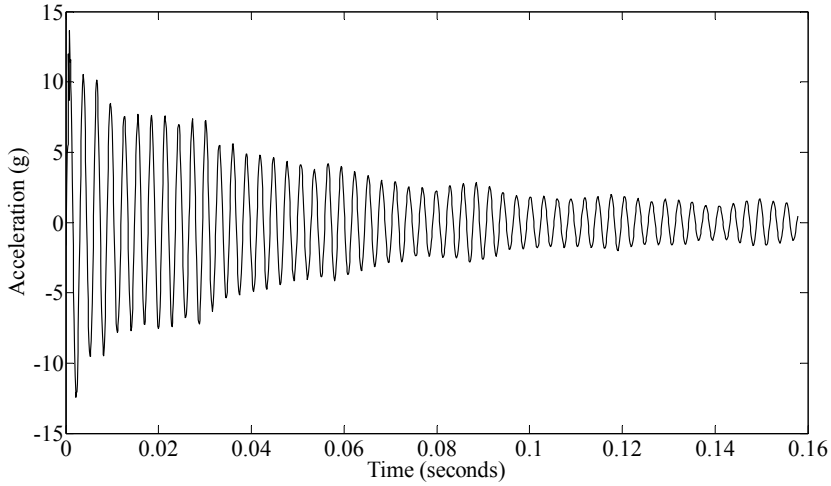

(a)

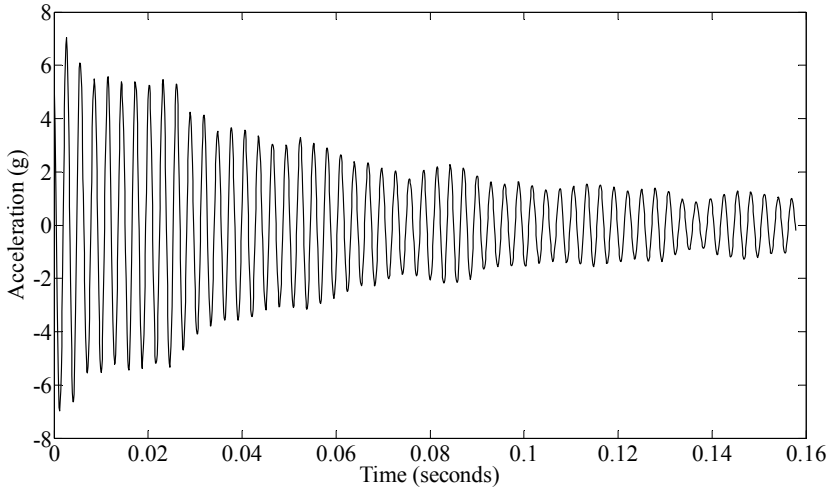

(b)

Figure 15. Typical damping curve in time domain for a) normal concrete, and b) rubberized concrete.

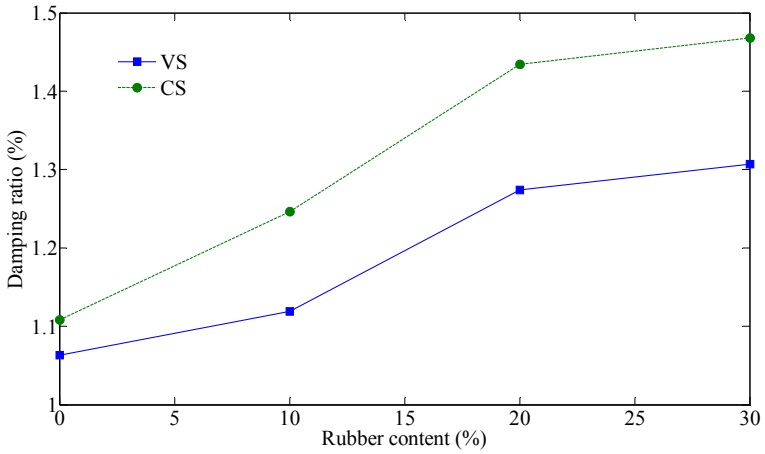

Figure 16. Damping ratio (ζ_{10}) for different rubber contents.

5. Conclusions

This study is the first to investigate the mechanical and dynamic properties for high strength concrete with scrap tires. Two different rubberized concrete mixtures, VS and CS, were designed and poured. The first set, VS was designed to investigate the effect of sand replacement by rubber on the fresh properties of concrete, especially the workability. The replacement of up to 10% did not affect the workability much; however the increase beyond 10% caused a severe reduction in workability. The other set was designed to keep the workability the same by changing the amount of the added superplasticizer. The mechanical properties of the rubberized concrete were investigated and the compressive strength was found to be reduced with the increase of rubber content. However, the replacement of up to 15% in the CS mixture was not very severe. The dynamic properties were investigated using free vibration tests with impact hammer on simply supported beams. The viscous damping was found to generally increase with increasing the rubber content. The increase in the CS set was higher due to the more uniform distribution of the rubber in the beams. The hysteresis damping for cylinders

under cyclic loading was also investigated and the average hysteresis damping was found to increase with the increase of rubber content. This research has shown that the mix design for CS has lower variation in the damping results and higher damping properties compared to either the conventional concrete or VS mixes. Hence, the CS mix can be used for structural elements subjected to dynamic loads. However, before this can be achieved, testing of structural elements constructed out of rubberized concrete needs to be carried out.

References

[1] Eldin, N.N. and Senouci, A.B., Rubber-tire particles as concrete aggregate. Journal of Materials in Civil Engineering, 1993. 5(4): p. 478-496.

[2] Topcu, I.B., The properties of rubberized concretes. Cement and Concrete Research, 1995. 25(2): p. 304-310.

[3] Toutanji, H., The use of rubber tire particles in concrete to replace mineral aggregates. Cement and Concrete Composites, 1996. 18(2): p. 135-139.

[4] Youssf, O., ElGawady, M.A., Mills, J.E., and Ma, X., An experimental investigation of crumb rubber concrete confined by fibre reinforced polymer tubes. Construction and Building Materials, 2014. 53(0): p. 522-532.

[5] Khatib, Z.K. and Bayomy, F.M., Rubberized Portland cement concrete. Journal of materials in civil engineering, 1999. 11(3): p. 206-213.

[6] Khaloo, A.R., Dehestani, M., and Rahmatabadi, P., Mechanical properties of concrete containing a high volume of tire–rubber particles. Waste Management, 2008. 28(12): p. 2472-2482.

[7] Güneyisi, E., Gesoğlu, M., and Özturan, T., Properties of rubberized concretes containing silica fume. Cement and Concrete Research, 2004. 34(12): p. 2309-2317.

[8] Segre, N. and Joekes, I., Use of tire rubber particles as addition to cement paste. Cement and Concrete Research, 2000. 30(9): p. 1421-1425.

[9] Siddique, R. and Naik, T.R., Properties of concrete containing scrap-tire rubber–an overview. Waste management, 2004. 24(6): p. 563-569.

[10] Hernandez-Olivares, F., Barluenga, G., Bollati, M., and Witoszek, B., Static and dynamic behaviour of recycled tyre rubber-filled concrete. Cement and concrete research, 2002. 32(10): p. 1587-1596.

[11] Zheng, L., Sharon Huo, X., and Yuan, Y., Experimental investigation on dynamic properties of rubberized concrete. Construction and Building Materials, 2008. 22(5): p. 939-947.

[12] Bowland, A.G., Comparison and Analysis of the Strength, Stiffness, and Damping Characteristics of Concrete with Rubber, Latex, and Carbonate Additives, 2011, Virginia Polytechnic Institute and State University.

[13] Chopra, A.K., Dynamics Of Structures, 3/E. 2007: Pearson Education India.

[14] ASTM C192, C 192M-13: Standard practice for making and curing concrete test specimens in the laboratory, 2013.

[15] Yan, L., Jenkins, C., and Pendleton, R., Polyolefin fiber-reinforced concrete composites: Part I. Damping and frequency characteristics. Cement and concrete research, 2000. 30(3): p. 391-401.

II. DYNAMIC PROPERTIES OF HIGH STRENGTH RUBBERIZED CONCRETE

Ayman Moustafa[1] and Mohamed ElGawady[2]

Abstract

Green construction has been a very important aspect in the concrete production field in the last decade. One of the most problematic waste materials is scrap tires. The use of scrap tires in civil engineering is increasing. This article investigates the dynamic properties of concrete with replacement of fine aggregate with scrap tire. Two different rubberized concrete mixtures were designed. The first set; variable slump (VS) was designed to keep the mix proportions constant with rubber replacement as the only variable. The other set; constant slump (CS) was designed to keep the workability the same using superplasticizer. The compressive strength of the concrete was reduced by the use of rubber. The viscous damping ratio was investigated using free vibration tests with impact hammer on simply supported beams and drop weight tests. The replacement of up to 20% of sand with rubber resulted in an increase in damping with the increase being more in the CS beams as well. Beyond 20%, the effect on damping was insignificant. The average hysteresis damping was found to increase with the increase of rubber content. The fracture energy was found to increase with the increase of rubber content up to 20%. Microstructure investigation was also performed on the two mixes. It is concluded that the choice of the rubber content and the mixing process can have a significant effect on

[1] Graduate research assistant, Department of Civil, Architectural, and Environmental Engineering, Missouri University of Science and Technology, USA E-mail: ampyf@mst.edu
[2] Benavides Associate professor, Department of Civil, Architectural, and Environmental Engineering, Missouri University of Science and Technology, USA E-mail: elgawadym@mst.edu

the dynamic properties of rubberized concrete. Recommendations for these two aspects were provided.

Keywords: Damping ratio; fracture energy; high strength concrete; microstructure; rubberized concrete; scrap tires

Introduction

Green construction has been an important aspect in the concrete production field in the last decade or so. The use of waste products in concrete manufacturing is beneficial both economically by replacing some of the components with waste materials and environmentally by clean disposal of waste materials. Scrap tires are mostly dumped in landfills. However, this can result in environmental hazards and contamination. Around 300 million scrap tires per year are added to the existing piles in the United States according to reports [Rubber Manufacturers Association (2014)]. Only a small amount of these tires are being recycled. Of this small amount, only 4% of the scrap tires are used in civil engineering applications [Rubber Manufacturers Association (2014)].

The addition of shredded scrap tires to concrete provides some favorable characteristics for concrete and alters some of concrete properties. The ordinary cement-based concrete is generally brittle. However, the addition of rubber to concrete, producing rubberized concrete, can increase its ductility and impact resistance [Eldin and Senouci (1993); Topcu (1995); Toutanji (1996); Youssf et al. (2014); Moustafa and ElGawady (2015); Moustafa and ElGawady (2016)]. Rubberized concrete is used in many applications such as concrete pavements, sidewalks, and road barriers where

concrete is subjected to dynamic loading from moving vehicles or people walking on sidewalks.

The mechanical properties of rubberized concrete have been investigated extensively under static loading. Past research concluded that replacing up to 5% of mineral fine aggregates with rubber has insignificant effects on concrete strength and workability. However, increasing the rubber content beyond this percentage reduces the compressive strength and workability of fresh concrete. The amount of reduction depends on the percentage and type of aggregate to be replaced (either coarse or fine aggregate) as well as the size and distribution of the rubber particles [Eldin and Senouci (1993); Topcu (1995); Khatib and Bayomy (1999); Hernandez-Olivares et al. (2002); Siddique and Naik (2004); Youssf et al. (2014); Youssf et al. (2016)]. Moustafa and ElGawady (2015) investigated the mechanical properties of high strength rubberized concrete with replacement of fine aggregate of up to 30% and found a reduction of compressive strength of up to 32%.

The dynamic properties of rubberized concrete have not yet received the attention it deserves. Hernandez-Olivares et al. (2002) reported an increase of 23% to 30% of the dissipated energy of rubberized concrete having low rubber contents of 3.5% and 5% compared to conventional concrete. Zheng et al. (2008) measured viscous damping values ranging from 0.68% to 1.67% on small rubberized concrete cubes compared to viscous damping values ranging from 0.45% to 0.74% measured on conventional concrete cubes, i.e., rubberized concrete displayed about 75% higher viscous damping than that of the corresponding conventional concrete. Bowland (2011) tested two full-scale footbridges; one with conventional concrete and the other with 15% replacement of

fine aggregate with ground rubber. No significant change in damping between the two footbridges was reported. This may be attributed to the very low imposed excitations of only 0.05g. Reda Taha et al. (2008) investigated the fracture properties of rubberized concrete under impact loading and reported significant enhancements in the impact resistance and fracture toughness of rubberized concrete. Youssf et al. (2015) investigated the behavior of a rubberized concrete column with 20% rubber replacement of fine aggregate under reversed cyclic loading. The rubberized column had an increase of 13% in hysteretic damping while the viscous damping was decreased by 49% compared to the conventional column.

Microstructure investigations of rubberized concrete have been investigated with high variation of conclusions [Hernandez-Olivares et al. (2002); Benazzouk et al. (2007); Emiroğlu and Yıldız (2008); Reda Taha et al. (2008)]. Hernandez-Olivares et al. (2002) recorded a high concentration of calcium oxides of the surface of the rubber particles. They concluded that this means that hydrated cement reacts with the rubber fiber exterior surface and a diffusion of the hydrated products happens, especially the ones with high calcium oxides content. Emiroğlu and Yıldız (2008) concluded that the interfacial transition zone in the rubberized concrete is poor compared to the conventional concrete. They reported that the bond between rubber and cement paste is very weak and resistance is resulting from the roughness of the interface instead. Reda Taha et al. (2008) concluded that the reduction of compressive strength is attributed to the behavior of the tire rubber as a soft aggregate, rather than to the reduction of bond between the tire particles and the cement paste.

Research significance

While there have been some investigations of the dynamic properties of normal strength rubberized concrete, the dynamic properties of high strength concretes with scrap tires have not been thoroughly investigated. In this manuscript, the dynamic properties of high strength concrete (concrete with compressive strength of greater than 69 MPa [10,000 psi]) having scrap tire rubber as a substitution for fine gravel were studied. Furthermore, past research on dynamic properties of normal strength rubberized concrete either focused on measuring viscous damping [Zheng et al. (2008)] or hysteretic damping [Hernandez-Olivares et al. (2002); Bowland (2011)]. The fracture behavior of rubberized concrete also lacks focus [Reda Taha et al. (2008)]. This study represents a comprehensive evaluation of the dynamic properties of high strength rubberized concrete, including viscous, hysteretic damping, and fracture energy under different loading conditions ranging from static cyclic loading to impact hammer testing to drop weight testing. Different percentages of replacement of sand ranging from 0 to 30% by volume were investigated. The microstructure features of high strength rubberized concrete were also investigated.

Experimental investigation

Material characteristics

To study the effects of mixture design on the dynamic properties of rubberized concrete, two sets of rubberized concrete mixtures were designed. The first set, hereafter called variable slump (VS), was used to test the dynamic properties of rubberized

concrete with the replacement of sand by crumb rubber as the only variable. Replacements of 0%, 5%, 10%, 15%, 20%, and 30% by volume of sand with crumb rubber were investigated. The second set, hereafter called constant slump (CS), is similar to VS set but with variable amounts of superplasticizer to maintain the same workability of the fresh concrete regardless of the rubber percentage. The materials used for sets VS, and CS are shown in Tables 1 and 2, respectively. The mixture nomenclature in Tables 1 and 2 consists of mixture set (VS or CS) followed by the percentage of sand replacement with rubber by volume.

Type I Portland cement meeting ASTM C150 specifications was used in all mixtures. Limestone washed coarse aggregate with nominal maximum size of 1 in was used. Missouri river sand was used. The rubber used was crumb rubber with three different sizes of 8-14, 14-30, and 30- where the first number represents the sieve number of the passing particles and the second number represents the sieve number of the retained particles. Figure 1 shows the grading of the sand, coarse aggregate and ground rubber used during the course of this research.

Concrete mixing

Dry mixing of the coarse aggregate, sand, and rubber was performed for about 1 minute to insure distribution of the aggregates. The cement and fly ash were then added and the concrete was dry mixed for another minute. The superplasticizer was mixed with the water and the water was then added to the mixture. The concrete was mixed for 2 minutes and then let stand for 1 minute; then, mixed for another two to three minutes until consistency was observed. For the CS mixtures, the slump test was performed after the mixing and superplasticizer was carefully added if the target slump was not achieved.

Table 1. Mixture proportions for the control concrete and for VS set

Materials (kg/m^3)	Water	Cement	Fly Ash	Coarse aggregate	Super-Plasticizer	Sand	R(8-14)	R(14-30)	R(30-)
Normal Concrete	142.40	336.39	112.13	1057.22	1.07	576.66	-	-	-
VS 05	142.40	336.39	112.13	1057.22	1.07	544.63	10.09	3.20	0.70
VS 10	142.40	336.39	112.13	1057.22	1.07	519.00	20.18	6.41	1.41
VS 15	142.40	336.39	112.13	1057.22	1.07	490.16	30.27	9.61	2.11
VS 20	142.40	336.39	112.13	1057.22	1.07	461.33	40.37	12.81	2.82
VS 30	142.40	336.39	112.13	1057.22	1.07	403.67	60.55	19.22	4.23

Table 2. Mixture proportions for the control concrete and for CS set

Materials (kg/m^3)	Water	Cement	Fly Ash	Coarse aggregate	Super-Plasticizer	Sand	R(8-14)	R(14-30)	R(30-)
Normal Concrete	142.40	336.39	112.13	1057.22	1.12	576.66	-	-	-
CS 05	142.40	336.39	112.13	1057.22	1.33	544.63	10.09	3.20	0.70
CS 10	144.17	336.39	112.13	1057.22	1.33	519.00	20.18	6.41	1.41
CS 15	144.17	336.39	112.13	1057.22	1.55	490.16	30.27	9.61	2.11
CS 20	144.17	336.39	112.13	1057.22	1.65	461.33	40.37	12.81	2.82
CS 30	144.17	336.39	112.13	1057.22	1.76	403.67	60.55	19.22	4.23

1 kg/m^3 = 16.02 lb/ft^3

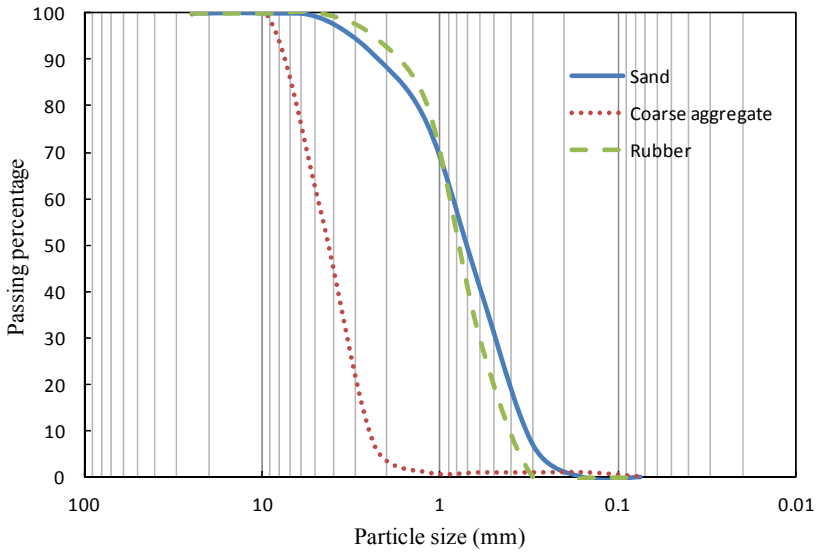

Figure 1 -- Grading of used materials

Test specimens

Six concrete beams of each set, VS and CS, were cast with nominal dimensions of 150 mm x 150 mm x 900 mm (6 in x 6 in x 36 in); one for each percentage of rubber replacement. Mechanical vibration was performed for all the beams to insure proper placement and filling of the concrete. A total of thirty-six 100 mm x 200 mm (4 in x 8 in) cylinders for each set were cast in the same day with the beams. The cylinders were used to determine the compressive strength of the concrete at 56 days. These cylinders were tested under axial cyclic loading to determine the hysteretic damping of the different concrete mixtures. The beams and cylinders were demolded after 24 hours and were moist cured in a controlled moisture room for 7 days. Then, they were removed from the curing room and left in the ambient temperature in the High-bay Lab at the Missouri University of Science and Technology.

Test Setups

Compressive strength and hysteresis damping setup

The compressive strengths of the concrete cylinders were determined using an MTS machine. The cylinders were grounded to assure the leveling of the surface and the two surfaces are parallel to each other. To determine the average axial strain of the concrete, two string potentiometers were placed on two opposite sides of each cylinder at a gauge length of one-third of the cylinder height. The average axial strains along a full specimen height were also measured using a Linear Variable Displacement Transducer (LVDT). The test setup for the compressive strength is shown in Figure 2.

The cylinders were tested to determine the concrete compressive strength at 56 days. One group of the concrete cylinder specimens was monotonically loaded in a displacement control and another group was cyclically loaded using displacement control up to failure. The loading rate for both sets was 5 mm/min (0.2 in/min). The cyclic axial compressive loading, including loading/unloading cycles, was applied based on a prescribed pattern of progressively increasing levels of axial displacements until failure occurred. Three cycles of loading/unloading were applied at each axial displacement level. Finally, the cylinders were tested for compressive strength at 56 days to represent the actual compressive strength of the beams on the test day. Three cylinders for each test were tested and the average of the three readings was used.

Figure 2 -- Compression test setup

Instrumented impact hammer setup

The dynamic properties of the rubberized concrete were determined using simply supported beams excited by an instrumented impulse hammer with a capacity of 22.5 kN (5000 lb). Figure 3 shows the dynamic test setup. Four accelerometers were mounted on

the surface of the beam. The beam was excited by hitting the beam at mid-span using the impact hammer. The accelerations were recorded using data acquisition system called Synergy box along with the instrumented hammer reading.

Drop weight test setup

Falling weight impact tests were conducted on the rubberized concrete beams used in the impact hammer tests by dropping a 70 mm (2.8 in) diameter, 23 kg (50 lb) steel cylinder from prescribed heights into the mid span of the beams. The beams were simply supported and the uplift was prevented at the supports while allowing rotations, as illustrated in Figure 4. The weight was dropped inside a guiding PVC pipe to ensure the impact occurred in the mid span and perpendicular to the beams. A 13-mm (0.5 in) thick neoprene plate with the same diameter of the cylinder was attached to the end of the cylinder to reduce the amount of vibration after the impact with the beams. The weight was held in position prior to each drop by a pulley system at the required drop height. The tests were performed on the two beams sets using three different drop heights. The weight was first dropped from a height of 75 mm (3 in) to measure the dynamic response with the attached accelerometers; similar to the impact hammer tests. The drop height was then increased to 150 mm (6 in) and 225 mm (9 in), at which the beams failed, to measure the fracture energy of the beams. The data was collected using the synergy box with a high sampling rate of 500,000 samples per second to ensure adequate representation of the impact.

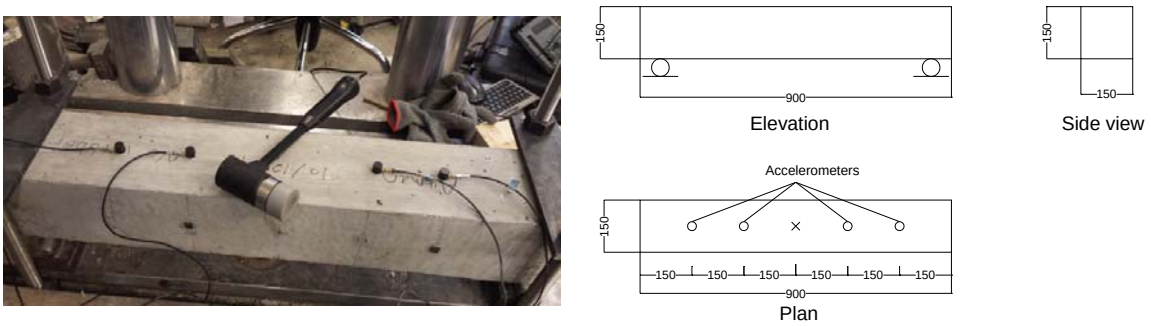

Figure 3 -- Impact hammer test setup (dimensions in mm: 1 inch = 25.4 mm)

To measure the deflection of the beams, a linear potentiometer with a 50-mm (2 in) stroke was secured at the bottom of the beam. To obtain the impact force on the beams, the data from the load cell incorporated by Tabatabaei et al. (2014) using the same test setup used in the current study. This load cell consisted of four individual dynamic load cells built by "PCB Piezotronics", each capable of measuring up to 89 kN (20,000 lb) in compression under dynamic load. The combined load cell was constructed using machined steel discs; allowing a total capacity of 359 kN (80,00 lb). The impact loads are dependent on the height of drop under free fall and are normally not affected by the impact objects [Banthia et al. (1989); Fujikake et al. (2009)]. This assumption was verified by examining all the impact loads at the same heights performed by Tabatabaei et al. (2014) and differenced of less than 5% were found; mainly due to the friction between the weight and the guiding PVC tube.

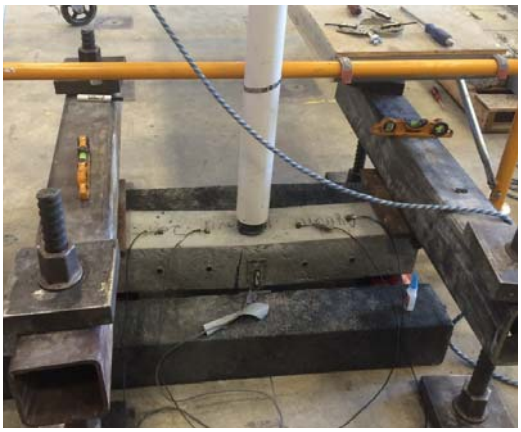

Figure 4 -- Drop weight test setup

Microstructure features test setup

Scanning electron microscope (SEM) was employed to investigate the microstructure features of rubberized concrete. The SEM was used to analyze the crystal structure of Calcium Silicate Hydrate (C-S-H) and Calcium Hydroxide (CH) in the interfacial layers of the aggregate to cement paste and rubber particles to cement paste. A thin disk with a thickness of 12.5 mm was cut from rubberized concrete cylinders and was broken down into smaller pieces to fit inside the SEM machine, as shown in Figure 5. The specimens tested represented the 20% rubber replacement for both the CS and the VS mixes. The specimens were prepared according to ASTM C1723 ASTM C1723 (2010). The specimens were air dried for 24 hours before the test. The oven drying was avoided because it can have a destructive effect that includes dehydration of hydrous phases and micro cracking. Specimen surface was coated by Edwards S150 sputter coater to get high quality interface images. Elemental analyses were performed on the samples using energy-dispersive X-ray spectroscopy (EDX) attached in the SEM. The EDX uses X-ray source to quantify the elements of the selected areas.

Figure 5 -- Test specimen for SEM analysis

Experimental results and discussion

Compressive strength

The compressive behavior of VS and CS mixtures was determined at 56 days according to ASTM C192 (2013), as illustrated in Figure 6. The Figure shows the average and range of compressive strength of concrete cylinders subjected to axial monotonic loading and cyclic loading at 56 days (six cylinders for each rubber content). The figure shows higher compressive strengths for the CS mix compared to the VS mix. For CS series and unlike the 7 days stress, replacing any percentage of sand resulted in a significant reduction in strength. Replacing up to 15% of sand with rubber resulted in a strength reduction of approximately 10%. At 30% replacement, the strength reduction was approximately 32%. Three cylinders were used for determination of the compressive strength of each rubber content. The standard deviation for the VS mix was higher than

that of the CS mix. This difference was caused by the non-uniform distribution of the rubber particles in the VS mix compared to the CS mix. A model to predict the compressive strength of the high strength rubberized concrete ($f_R^{'}$) based on the concrete compressive strength and the rubber content was developed as:

$$f_R^{'} = f_c^{'} - 1.20R - 0.012R^2 \quad (1)$$

where $f_R^{'}$ is the rubberized concrete compressive strength, $f_c^{'}$ is the compressive strength of concrete without rubber, and R is the replacement percentage by volume of the fine aggregate with rubber. The same model was used for both mixes as it provided good agreement with the experimental results.

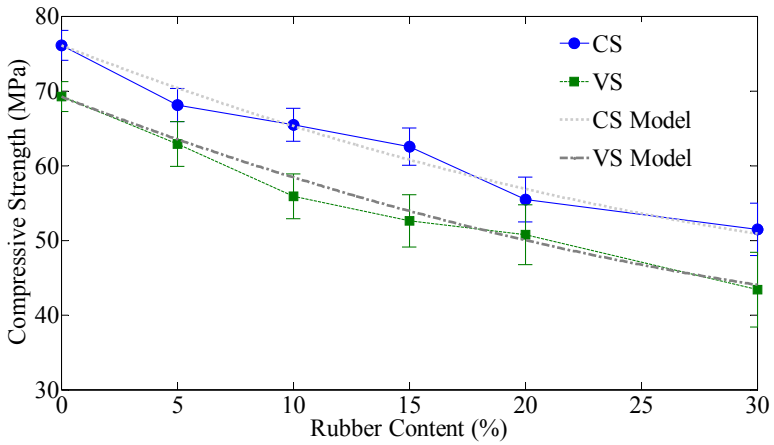

Figure 6 -- Compressive stress for VS and CS cylinders (1 MPa = 145 psi)

Hysteresis damping results

The hysteresis is the property of systems to follow different loading and unloading paths. The hysteresis damping for the cyclic testing is calculated from the specific damping capacity (Y), which is the ratio between the energy dissipated per unit

volume of the material, E_D, and the strain energy per unit volume stored in a linear elastic system, E_{S0}, as shown in eq. 2.

$$Y = \frac{E_D}{E_{S0}} \tag{2}$$

A graphical representation of E_D and E_{S0} is shown in Figure 7.

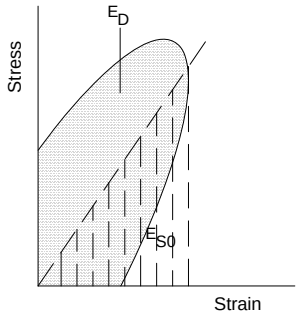

Figure 7 -- Dissipated energy per unit volume of the material, E_D and elastic strain energy, E_{S0}

The energy dissipated per cycle per unit volume, E_D, is measured as the area enclosed by a hysteresis loop drawn on axes of stress and strain. This area can be obtained as the integral of the area under the curve and it can be calculated mathematically using eq. 3.

$$E_D = \sum_{i=1}^{n-1} \left(\frac{F_{i+1} + F_i}{2} \right) \left(\Delta_{i+1} - \Delta_i \right) \tag{3}$$

where, E_D is the dissipated energy (J), n is the total number of stress or strain points, F_i is the force at point i (N), and Δ_i is the displacement at point I (m).

The hysteresis damping can be expressed as the equivalent viscous damping and is calculated from the specific damping capacity using eq. 4.

$$\zeta_{eq} = \frac{1}{2\pi} Y \tag{4}$$

Samples of the stress-strain curves for the normal concrete and the rubberized concretes are illustrated in Figure 8. The energy dissipated per cycle per unit volume, E_D, can be calculated for each of the stress-strain curves using eq. 3. Since the loading was displacement controlled, it is more representative to plot E_D versus the strain of the test specimen. Figure 9 shows the cumulative energy dissipation of the different mixtures. As shown in the figure, the cumulative energy dissipation for the rubberized concrete is much higher than the normal concrete, especially for 20% and 30% replacements.

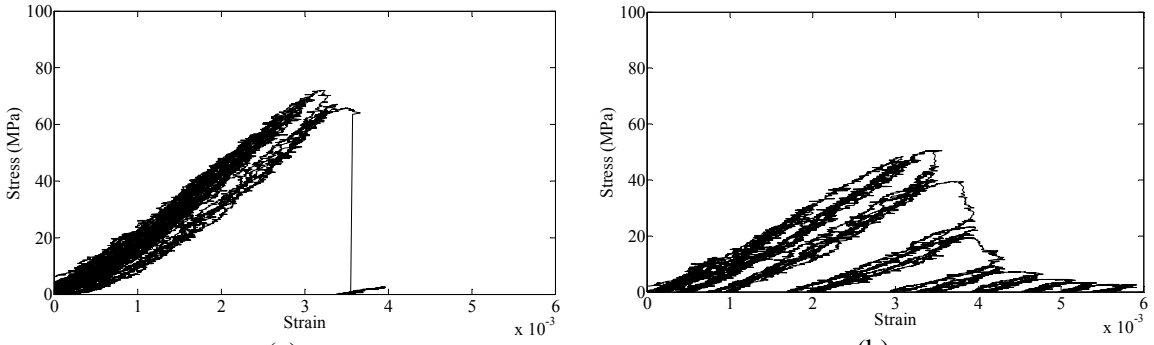

Figure 8 -- Sample stress-strain curves of a) normal concrete, b) rubberized concrete (1 MPa = 145 psi)

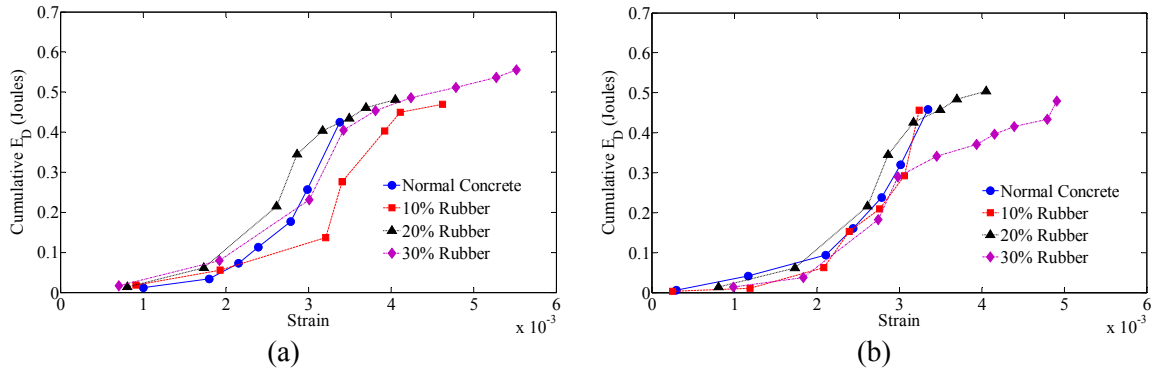

Figure 9 -- Cumulative dissipated energy for a) VS and b) CS (1 J = 8.85 lb.in)

The hysteresis damping is calculated using eq. 4 for each cycle. Figure 10 shows the hysteresis damping vs. axial compressive strain for each mixture for both sets. The figure shows that the average hysteresis damping increases with the increase of rubber content. For 20% and 30% rubber replacement the equivalent viscose damping reach approximately four times the equivalent viscous damping of normal concrete. The increase in damping is higher than that observed by Hernandez-Olivares et al. (2002) and Bowland (2011) because of the higher replacement ratios.

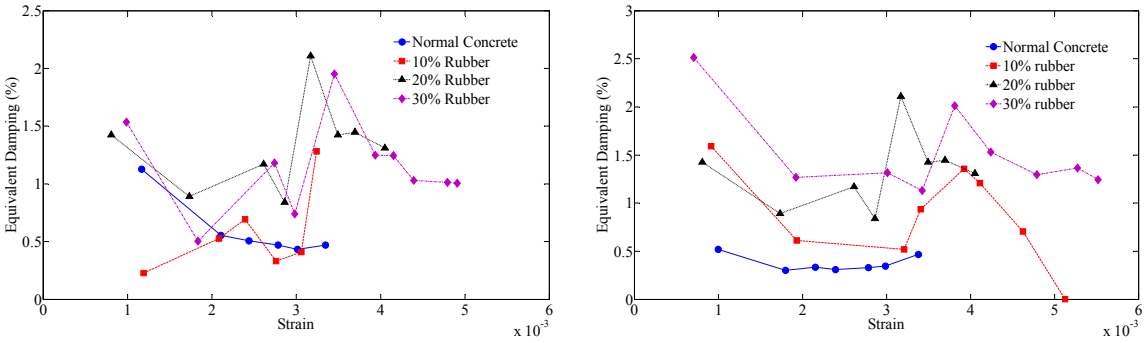

(a) (b)

Figure 10 -- Hysteresis damping for different rubber contents for a) VS and b) CS

Impact hammer results

Damping ratio

The viscous damping ratio can be calculated using free vibration tests of structural elements using the logarithmic decrement method [Yan et al. (2000)]. The accelerations amplitudes were recorded for the impact hammer and drop weight tests and the values of the damping ratio can be calculated using eq. 5.

$$\zeta = \frac{1}{2n\pi} \ln\left(\frac{A_0}{A_n}\right) \quad (5)$$

where, A_0 is the initial amplitude and A_n is the amplitude after n cycles.

A typical damping curve is shown in Figure 11 for the measured signals. The figure shows that the actual response of the beams is not strictly exponential; hence, variation in the value of damping ratio occurs with the change in the number of cycles used to calculate the damping. In the current study, a base of 10 cycles is used to define the damping ratio and is denoted by ζ_{10}.

The change in with the rubber content is shown in Figure 12. The figure shows an increasing trend of the damping ratio with the increase in rubber content for both CS and VS mixes. The increase in the damping ratio for VS mixture was 5.3%, 19.8%, and 22.9% for 10%, 20%, and 30% replacement, respectively. For the CS mixture, the increase was 12.5%, 29.4%, and 32.5% for 10%, 20%, and 30% replacement, respectively. The larger increase in the CS mix can be attributed to the higher workability of CS leading to a uniform distribution of the rubber particles as opposed to concentration of rubber in some places like the bottom surface and the corners. The results of the viscous damping are of good agreement with the results by Zheng et al. (2008) for normal strength concrete.

Effect of number of vibration cycles

It has been shown by several researchers that the calculated damping value depends on the number of cycles used in the calculations, i.e. n parameter in eq. 5. Figure 13 shows the change in damping ratio with changing the number of vibration cycles. As

shown in the figure, the damping calculations are sensitive to the number of vibration cycles up to 10 cycles, beyond that the results are independent of the number of vibration cycles.

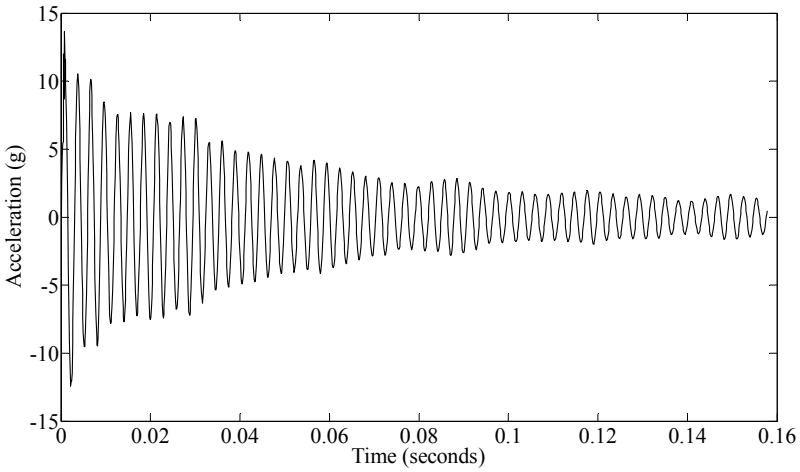

(a)

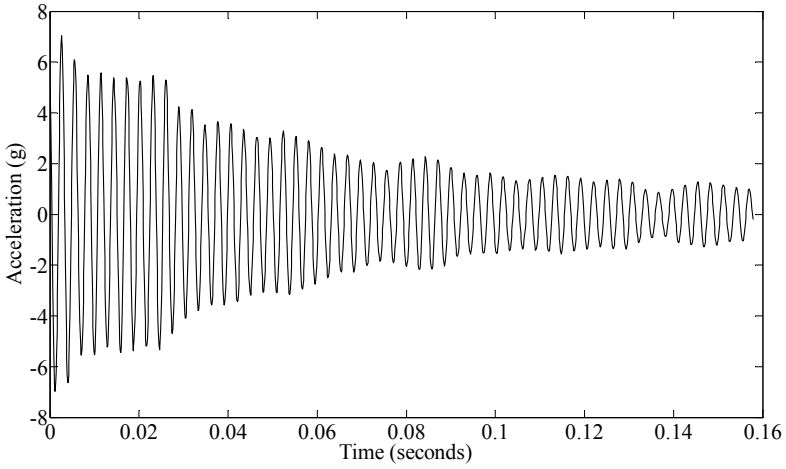

(b)

Figure 11 -- Typical damping curve in time domain for a) normal concrete, and b) rubberized concrete

Effect of the energy imposed on the system on the damping ratio

The effect of the energy imposed on the system on the damping ratio can be expressed by the effects of the maximum amplitude of the received signals on the damping ratio, as illustrated in Figure 14. As depicted in the figure, the conventional concrete is not very sensitive to the induced energy. The rubberized concrete, on the other

hand, is more affected by the energy induced on the system and the damping ratio is increased by the increase of the induced energy.

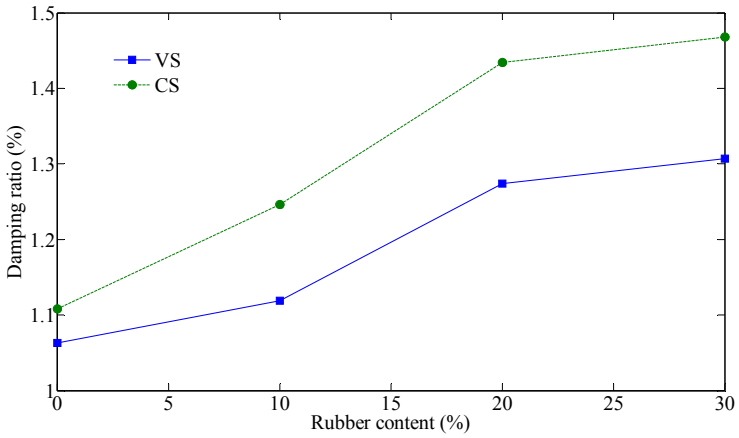

Figure 12 -- Damping ratio (ζ_{10}) for different rubber contents

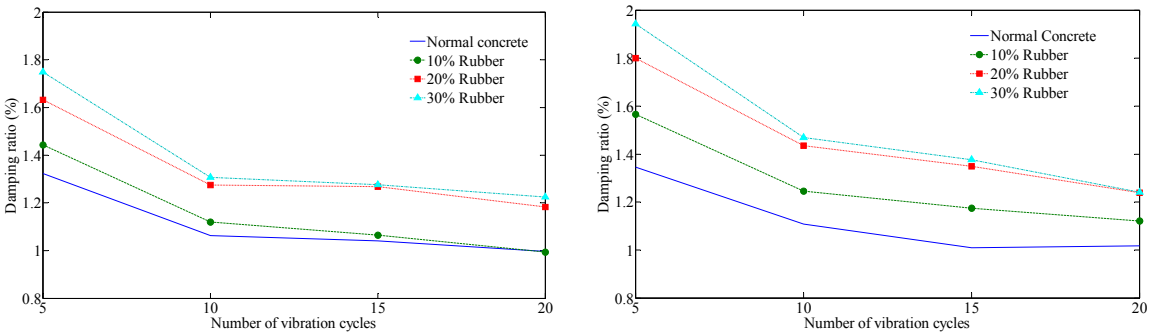

(a) (b)

Figure 13 -- Effect of the number of vibration cycles on the damping ratio for a) VS, and b) CS

Repeatability of the test

The effectiveness of the dynamic testing is determined by its repeatability. In this section, the repeatability of the test is examined when fixing the other parameters. For instance, the repeatability is checked at the same range of energy induced in the system and for different number of cycles. Figure 15 shows the damping ratios for different signals having the same range of maximum amplitude. The figure shows very good

repeatability for the normal concrete beams and a good repeatability for the rubberized concrete beams. The reason for the more diversity in the rubberized concrete is the difficulty in eliminating the effect of amplitude in such a test where is load is applied manually by a hammer. Nevertheless, the results are still showing good repeatability with less than 10% difference in a range of ± 1 g.

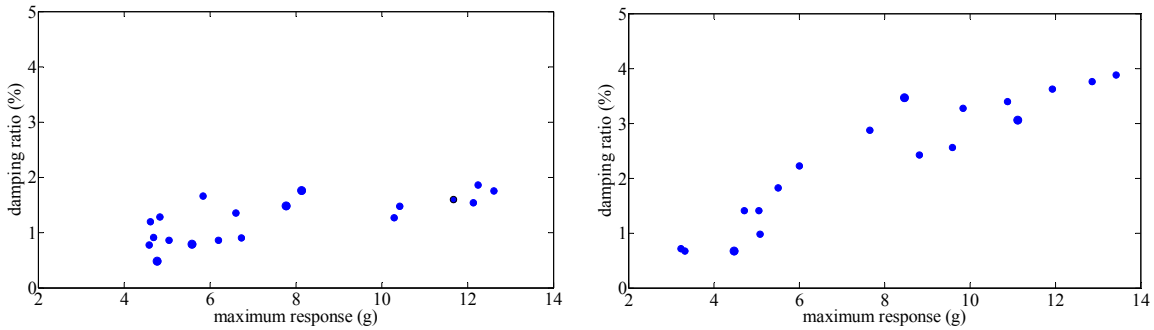

(a) (b)

Figure 14 -- Effect of amplitude on the damping ratio for a) normal concrete, and b) rubberized concrete

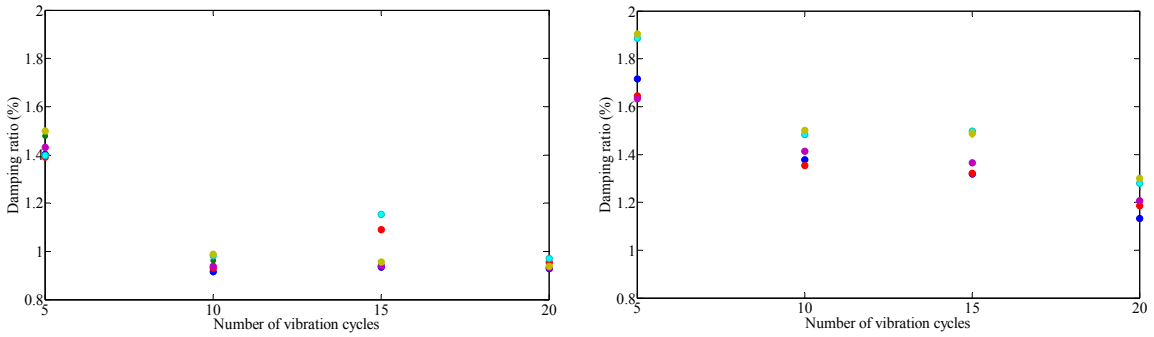

(a) (b)

Figure 15 -- Repeatability of the tests for a) normal concrete, and b) rubberized concrete

Natural frequency

The natural frequencies for the beams were calculated from the received signals by the fast Fourier transform (FFT). The result of the natural frequencies for the normal concrete and rubberized concrete are shown in Figure 16. The figure depicts a decrease in

the natural frequency with the addition of rubber. This increase is not significantly affected by the rubber content.

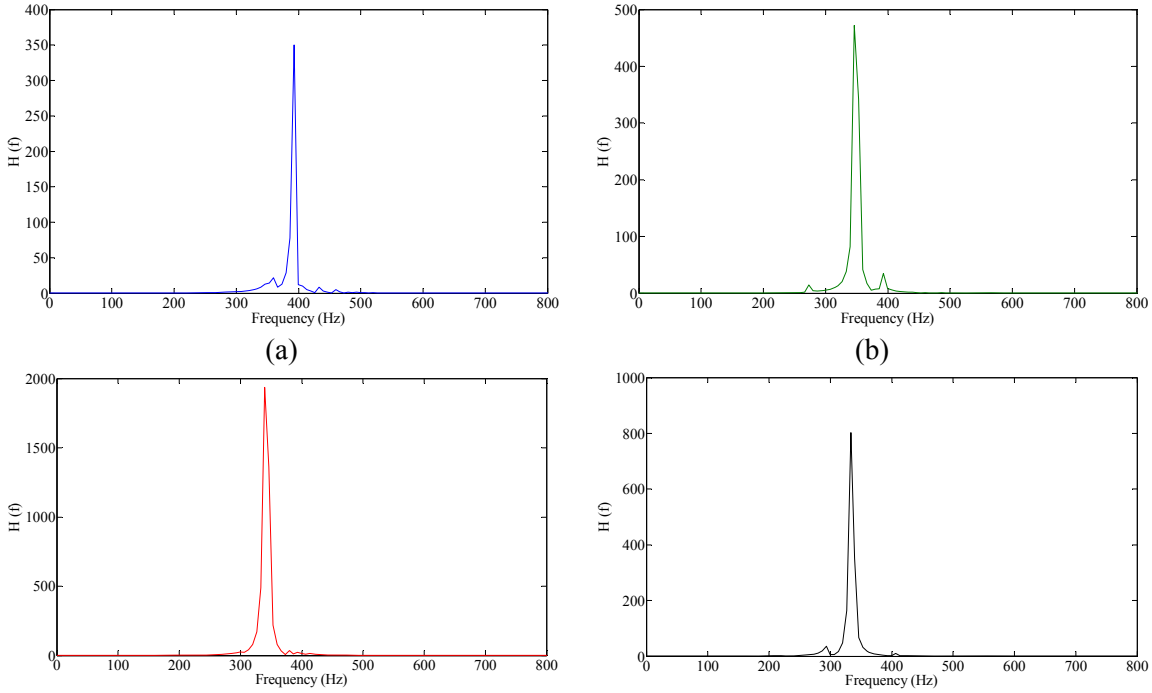

Figure 16 -- Natural frequencies for beams: a) normal concrete, b) 10% rubber, c) 20% rubber, and d) 30% rubber replacement

Dynamic and static modulus of elasticity

The dynamic modulus of elasticity of rubberized concrete was determined by using the experimental data obtained from the flexural beam vibration test under impact hammer. The relationship between dynamic modulus of elasticity and natural frequency is given in eq. 6. Re-arranging eq. 6, the E_D can be calculated given the natural frequency as shown in eq. 7.

$$f_n = \frac{\pi n^2}{2}\sqrt{\frac{EI}{ml^4}} \tag{6}$$

$$E_d = \frac{4mf_n^2 l^4}{I\pi^2 n^4} \tag{7}$$

where, m is the mass of the beam member in unit length, l is the length of the beam, I is the moment of inertia of the cross section, n is the number of the mode. To determine the dynamic modulus of elasticity of the beam from the natural frequency, n=1, and f is the natural frequency. The natural frequency can be determined experimentally by calculating the fast Fourier transform (FFT) of the received signals.

The static modulus of elasticity was computed from the monotonic testing of the cylinders according to ASTM C469 (2010) as the chord modulus of elasticity from 50μ strain to the point of 40% of the compressive strength. Figure 17 shows the change in the dynamic and static modulus of elasticity with rubber content. Both the dynamic and static modulus of elasticity decreased with the increase in rubber content. The dynamic modulus of elasticity is more influenced by the replacement of rubber as seen in replacement of 10%, but with the increase in rubber content the dynamic modulus of elasticity does not change much.

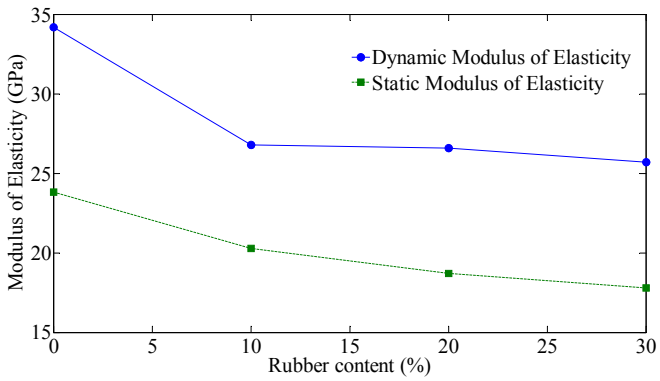

Figure 17 -- Comparison between dynamic and static modulus of elasticity with different rubber contents

Drop weight test results

Damping ratio

The viscous damping ratio for the drop weight test can be calculated using eq. 5 for the measured accelerations at 75 mm (3 in) drop height. The change in the damping ratio (ζ_{10}) with the rubber content is illustrated in Figure 18. The figure shows an increasing trend of the damping ratio with the increase in rubber content for both CS and VS mixes. The increase in the damping ratio for VS mixture was 9.0%, 26.3%, and 31.0% for 10%, 20%, and 30% replacement, respectively. For the CS mixture, the increase was 18.8%, 38.8%, and 42.6% for 10%, 20%, and 30% replacement, respectively. The larger increase in the CS mix can be attributed to the higher workability of CS leading to a uniform distribution of the rubber particles as opposed to concentration of rubber in some places like the bottom surface and the corners. The figure also shows a very large increase in the damping ratio for the drop weight test as compared to the impact hammer test [Figure 12]. This indicates the effect of the excitation amplitude on the damping; especially for the rubberized concrete that is much more affected by this increase.

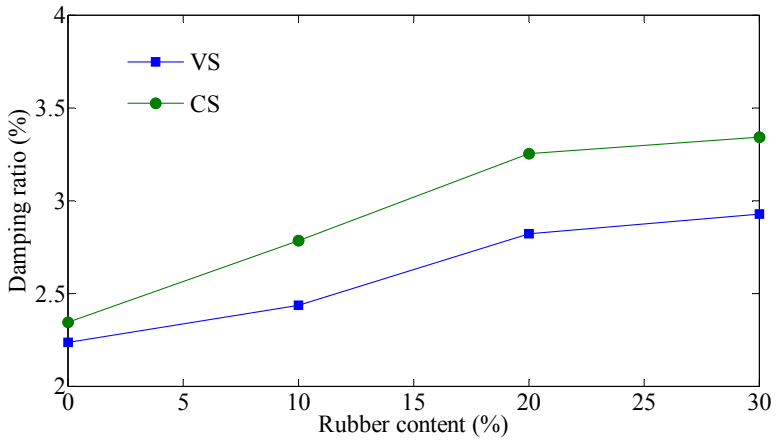

Figure 18 -- Damping ratio (ζ_{10}) for different rubber contents for drop weight test

Fracture energy

The impact load of the cylinder is not the true stressing or the true bending load owing to the inertial effects of the tested specimens [Venzi et al. (1970); Server (1978)]. This load (P_t) is the summation of the inertial load (P_i) and the bending load (P_b) acting on the specimen [Banthia et al. (1989)]. Hence, the bending load is calculated using eq. 8.

$$P_b = P_t - P_i \tag{8}$$

where, P_t is the measured load and P_i is the inertial load.

The inertial load (P_i) can be calculated from the measured accelerations using eq. 9. [Banthia et al. (1989)].

$$P_i = \rho A \ddot{u}_0(t)\left[\frac{L}{3} + \frac{8}{3}\frac{h^3}{L^2}\right] \tag{9}$$

where, ρ is the mass density of concrete, A is the cross sectional area of the beam, L is the length of the beam, h is the overhanging length outside the support, and $\ddot{u}_0(t)$ is the acceleration at the mid-span of the beam.

The acceleration at the mid-span of the beam was linearly extrapolated from the measurements of the four accelerometers mounted across the beam length.

The fracture energy (E_{fr}) of each beam can be calculated by integrating the load-deflection curve using eq. 10.

$$E_{fr} = \int P_b \delta \tag{10}$$

where, δ is the mid-span deflection measured by the linear potentiometer.

The bending load - mid-span deflection curves for the VS and CS mixes under drop weight tests are illustrated in Figures 19 and 20, respectively. The bending load was decreased by the increase of rubber content. This can be attributed to the increase of the inertial load of the rubberized concrete caused by the increase in the flexibility of the concrete, while the impact load was kept constant. However, this decrease was not significant and the maximum reduction in the bending load was 12%. The figures also show an increase of the mid-span deflection with the increase of rubber content. The increase in deflection is larger in the CS mix compared to the VS mix. This can be attributed to the better dispersion of the rubber particles in the CS mix, resulting in larger deformability as the cracks are forced to propagate through shorter distances which would have rubber particles with higher ductility. The increases of mid-span deflections were significant and the rubberized beams with 20% and 30% replacement in the CS mix had twice the deformation capacity.

The fracture energy (E_{fr}) of each beam was calculated by integrating the load-deflection curve using eq. 10. The fracture energy for the two mixes is illustrated in Figure 21. The figure shows an increasing trend of the damping ratio with the increase in rubber content up to 20% replacement for both CS and VS mixes. No increase in the fracture energy was observed between 20% and 30% replacement. The increase in the fracture energy for VS mixture was 30.3%, 62.4%, and 54.1% for 10%, 20%, and 30% replacement, respectively. For the CS mixture, the increase was 41.9%, 88.7%, and

85.2% for 10%, 20%, and 30% replacement, respectively. The larger increase in the CS mix can be attributed to the higher workability of CS leading to a uniform distribution of the rubber particles as opposed to concentration of rubber in some places like the bottom surface and the corners. This uniform distribution increases the chance of the cracks propagating towards rubber particles with higher ductility that manage to absorb the energy and produce larger deformations.

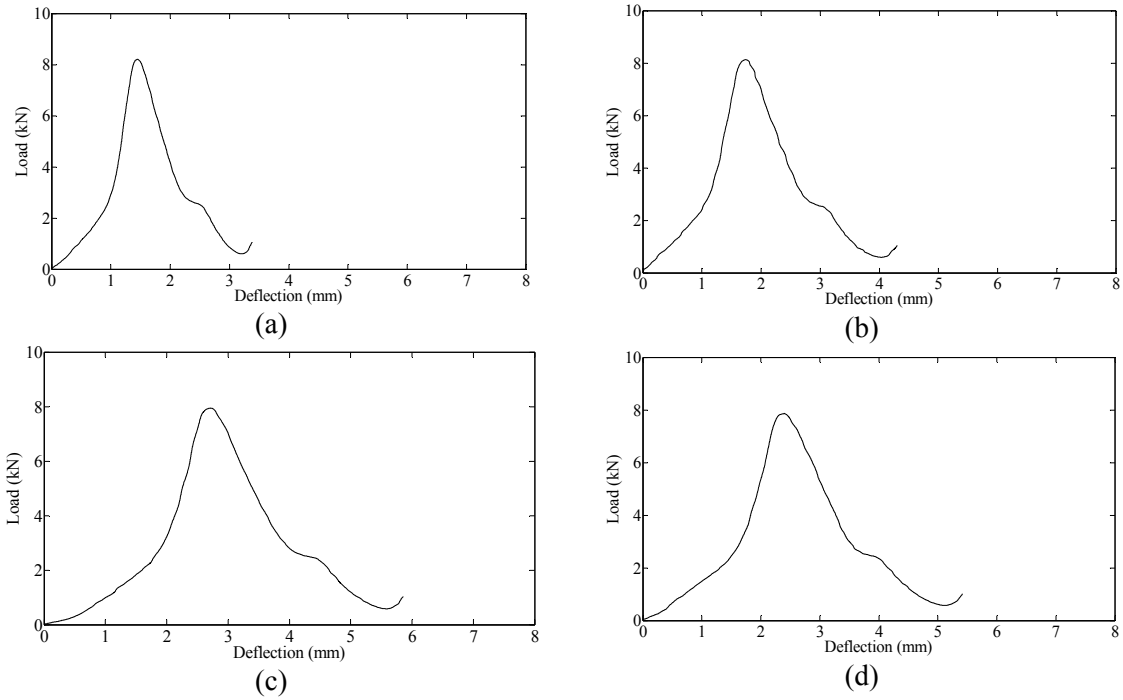

Figure 19 -- Load-deflection curves for the VS mix for: a) normal concrete, b) 10% rubber, c) 20% rubber, and d) 30% rubber replacement [1 kip = 4.45 kN]

Microstructure features test results

SEM was employed to investigate the microstructure features of rubberized concrete. The interaction between the aggregate (Agg) and cement paste (CP) and the rubber particle (Ru) and CP for the VS and CS mixes is illustrated in Figures 22 and 23, respectively. The VS mix had micro-cracks in the CP around the Ru, while this was not

observed in the CS mix. This VS mix also had larger voids in the CP than the CS mix. This can be attributed to the non uniform distribution of the rubber particles in the VS mix causing congested spots of rubber particles that have fewer bonds with the CP and no reactivity causing the reduction of hydration products around the rubber particles.

The interfacial transition zone (ITZ) between the Agg and CP and between the Ru and CP is illustrated in Figure 24. Higher bond between the Agg and CP can be observed compared to the bond between the Ru and CP. Poor bond and voids are observed in Figure 26b between the Ru and CP.

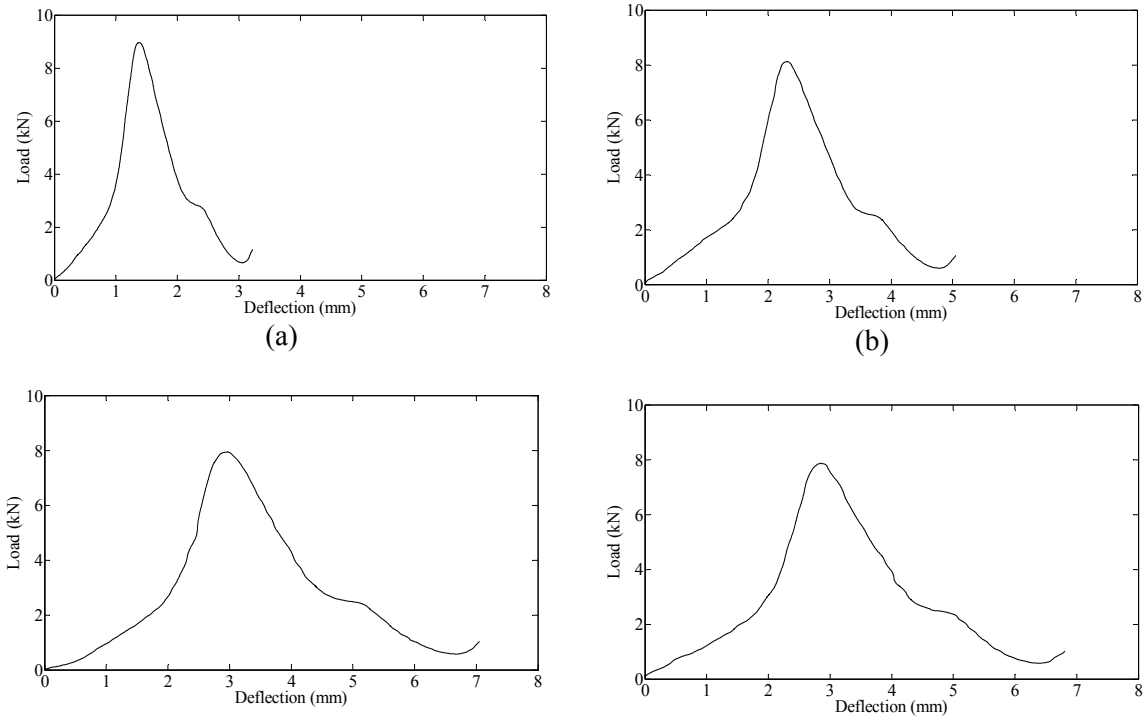

Figure 20 -- Load-deflection curves for the CS mix for: a) normal concrete, b) 10% rubber, c) 20% rubber, and d) 30% rubber replacement [1 kip = 4.45 kN]

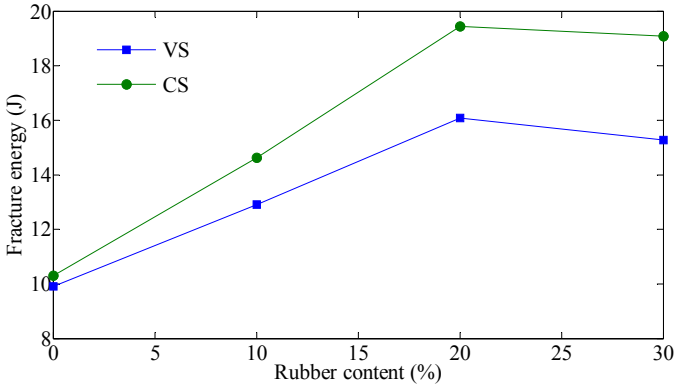

Figure 21 -- Fracture energy for different rubber contents for drop weight test (1 J = 8.85 lb.in)

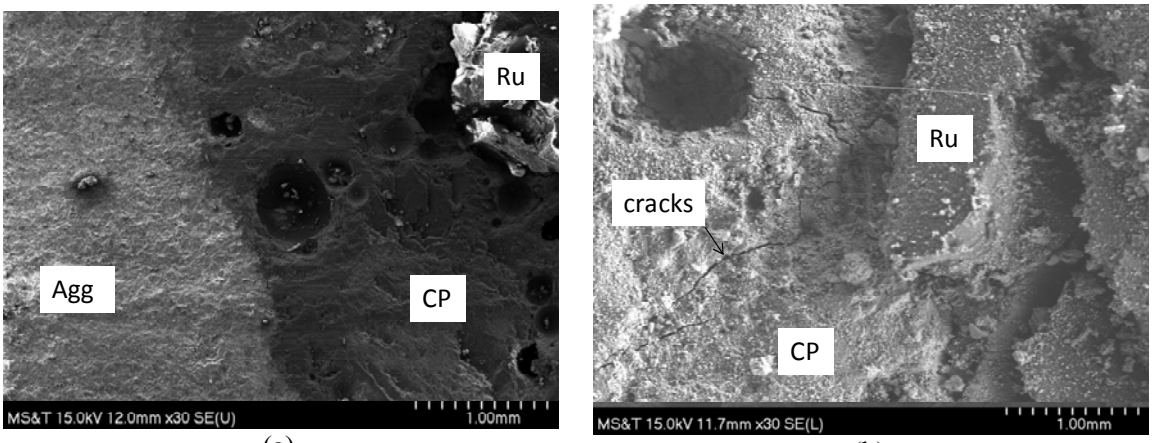

(a) (b)

Figure 22 -- Interaction between: a) aggregate - cement paste and b) rubber particle - cement paste for the VS mix

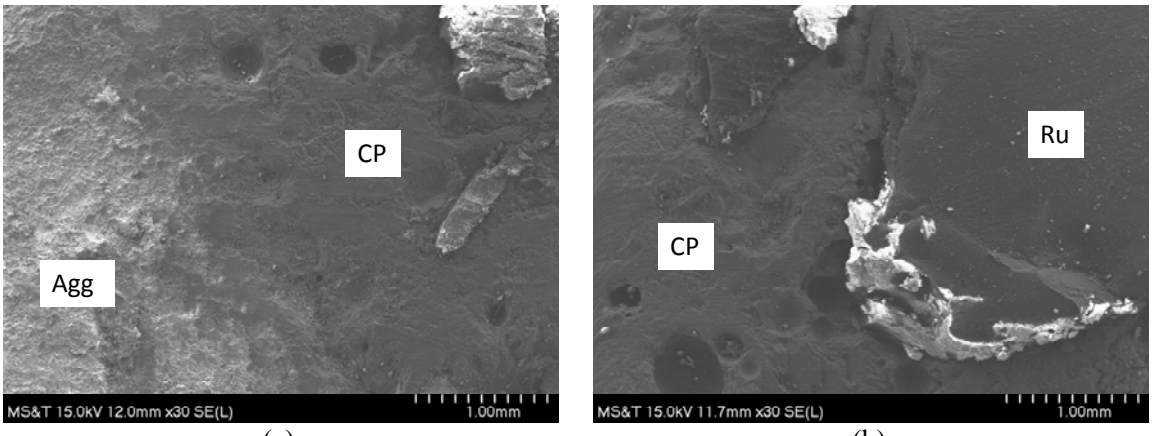

(a) (b)

Figure 23 -- Interaction between: a) aggregate - cement paste and b) rubber particle - cement paste for the CS mix

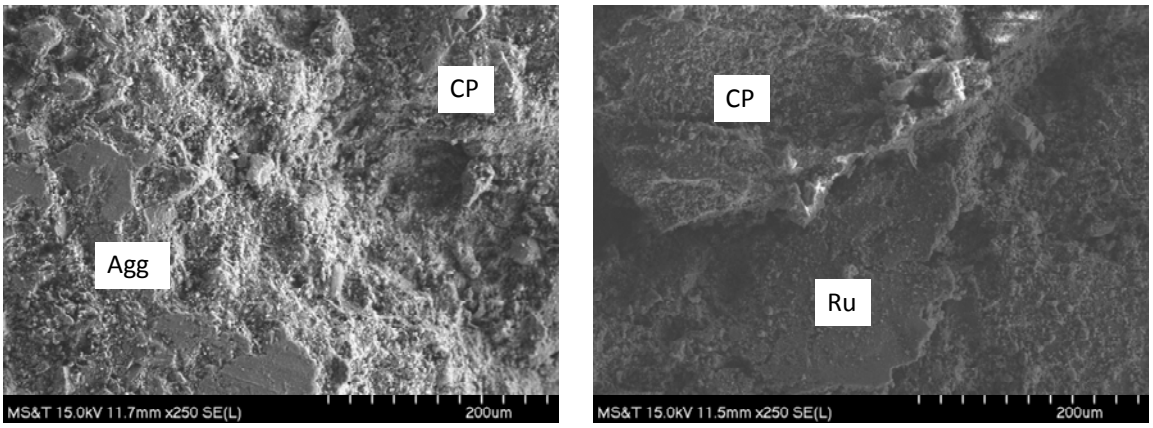

(a) (b)

Figure 24 -- Interfacial transition zone between: a) aggregate - cement paste and b) rubber particle - cement paste

The EDX was utilized to perform elemental analysis at the interfaces between the Agg and CP and between the Ru and CP. The elements of interest for the bond at the interface are the calcium (Ca) and silica (Si) as the ratio of Ca/Si gives an indication of the bond strength. The ITZ is considered to have a high bond strength when Ca/Si < 1.5 [Xincheng (2012); Kunther et al. (2015)]. This high bond strength results because for low Ca/Si ratios, the degree of polycondensation of the silicon-oxygen chain is much higher than high Ca/Si ratios [Xincheng (2012)]. The elemental analyses for the ITZ between the Agg and CP and between the Ru and CP for both mixes are illustrated in Figure 25. The Ca/Si ratios were 0.37, 1.15, and 1.62 for the ITZ between Agg and CP, Ru and CP for the CS mix, and Ru and CP for the VS mix. The very low ratio for the Ca/Si ratio for the ITZ between Agg and CP indicate a very strong bond between the two. The ratio for the VS mix is higher than the CS mix indicating the lower bond that resulted from the congestions of rubber particles reducing the hydration products and also the micro-cracks formed reduced the bond significantly. Sectional EDX analyses for sections passing through Agg and CP and through Ru and CP are illustrated in Figure 26. The figure shows the change in components throughout the ITZ.

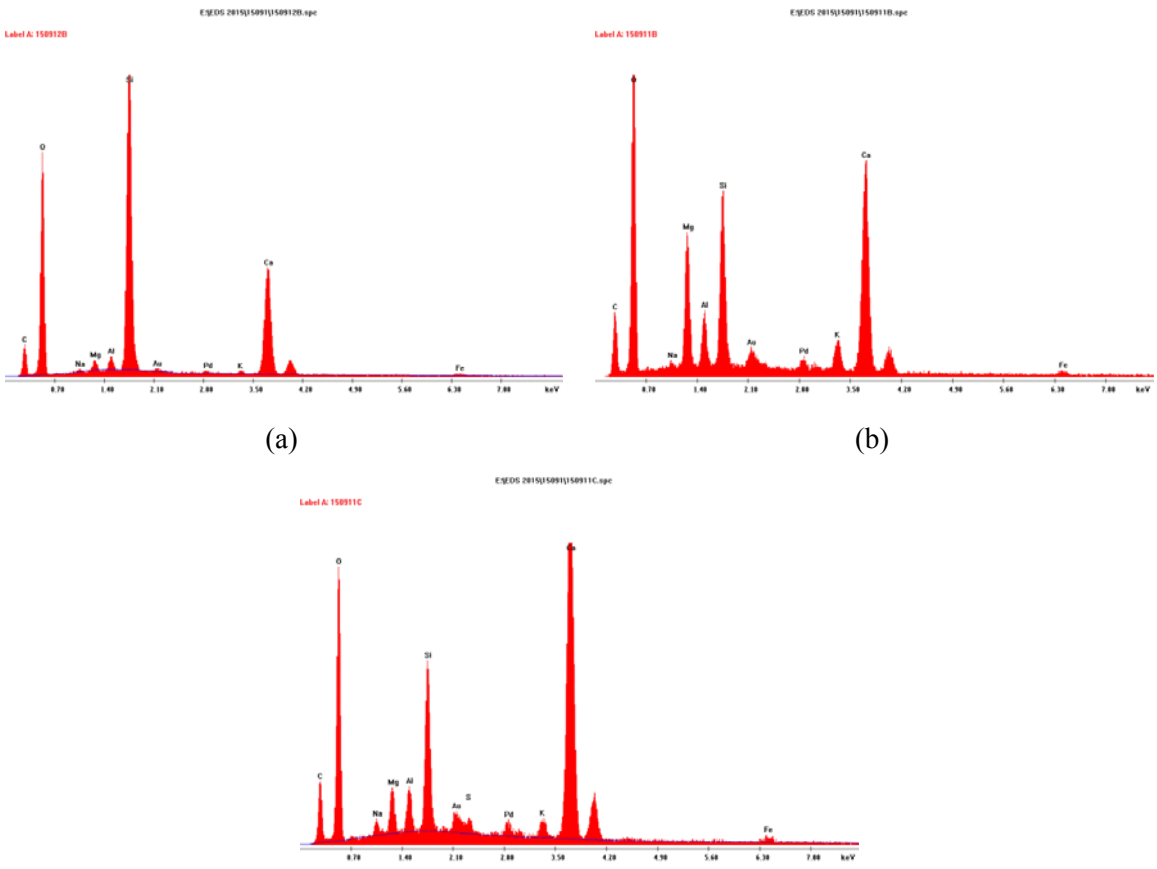

(a) (b)

(c)

Figure 25 -- Element analysis for the interfacial transition zone between: a) aggregate - cement paste, b) rubber particle - cement paste for CS mix, and c) rubber particle - cement paste for VS mix

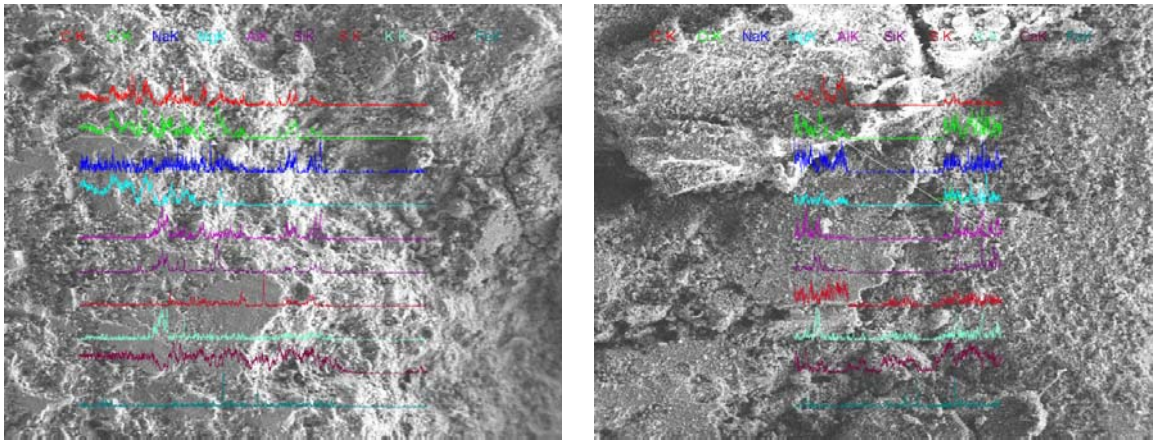

(a) (b)

Figure 26 -- Cross section of element analysis for the interfacial transition zone between: a) aggregate - cement paste, and b) rubber particle - cement paste

Conclusions

This study is the first to investigate the dynamic properties of high strength concrete with scrap tires. Two different rubberized concrete mixtures, VS and CS, were designed. The first set, VS was designed to maintain the mix design with sand replacement by rubber as the only variable. The other set was designed to keep the workability the same by changing the amount of the added superplasticizer along with sand replacement with rubber. The compressive strength was found to be reduced with the increase of rubber content. An analytical model was proposed for the estimation of the compressive strength of the rubberized concrete. The dynamic properties were investigated using three different methods; hysteresis analysis, free vibration tests with impact hammer on simply supported beams, and drop weight tests. The hysteresis damping was found to increase with the increase of rubber content. For both impact hammer test and drop weight test, the viscous damping was found to generally increase with increasing the rubber content up to 20% replacement. The change in viscous damping between 20% and 30% replacements is insignificant. The increase of viscous damping in the CS set was higher due to the more uniform distribution of the rubber particles in the beams. The induced energy is highly effective on the damping properties of rubberized concrete. It had less effect on conventional concrete. The fracture energy was increased by the increase of rubber content up to 20% then a small reduction was noticed when the rubber content was increased to 30%. The microstructure analysis showed higher bond of aggregate to cement paste compared to the bond between rubber particles and cement paste. The bond between the rubber and cement paste was higher in the CS mix compared to the VS mix.

This research had shown that the mix design for the CS set had better dynamic properties compared to both the VS mix and the conventional concrete. It shows the importance of maintaining the workability of concrete for better dispersion of rubber particles in the concrete rather than being a fresh property. It is recommended to replace up to 20% of fine aggregate with scrap tire rubber to achieve both lower reduction of compressive strength and enhanced dynamic properties compared to 30% replacement. The CS mix is recommended for further testing to be used in structural elements constructed out of rubberized concrete.

References

ASTM C192 (2013). C 192M-13: Standard practice for making and curing concrete test specimens in the laboratory.

ASTM C469 (2010). C 469M-10: Standard Test Method for Static Modulus of Elasticity and Poisson's Ratio of Concrete in Compression.

ASTM C1723. (2010). "Standard Guide for Examination of Hardened Concrete Using Scanning Electron Microscopy."

Banthia, N., Mindess, S., Bentur, A. and Pigeon, M. (1989). "Impact testing of concrete using a drop-weight impact machine." Experimental Mechanics 29(1): 63-69.

Benazzouk, A., Douzane, O., Langlet, T., Mezreb, K., Roucoult, J. and Quéneudec, M. (2007). "Physico-mechanical properties and water absorption of cement composite containing shredded rubber wastes." Cement and Concrete Composites 29(10): 732-740.

Bowland, A. G. (2011). Comparison and Analysis of the Strength, Stiffness, and Damping Characteristics of Concrete with Rubber, Latex, and Carbonate Additives, Virginia Polytechnic Institute and State University.

Eldin, N. N. and Senouci, A. B. (1993). "Rubber-tire particles as concrete aggregate." Journal of Materials in Civil Engineering 5(4): 478-496.

Emiroğlu, E. and Yıldız, S. (2008). "An İnvestigation on its microstructure of the concrete containing waste vehicle tire."

Fujikake, K., Li, B. and Soeun, S. (2009). "Impact response of reinforced concrete beam and its analytical evaluation." Journal of structural engineering 135(8): 938-950.

Hernandez-Olivares, F., Barluenga, G., Bollati, M. and Witoszek, B. (2002). "Static and dynamic behaviour of recycled tyre rubber-filled concrete." Cement and concrete research 32(10): 1587-1596.

Khatib, Z. K. and Bayomy, F. M. (1999). "Rubberized Portland cement concrete." Journal of materials in civil engineering 11(3): 206-213.

Kunther, W., Lothenbach, B. and Skibsted, J. (2015). "Influence of the Ca/Si ratio of the C–S–H phase on the interaction with sulfate ions and its impact on the ettringite crystallization pressure." Cement and Concrete Research 69: 37-49.

Moustafa, A. and ElGawady, M. A. (2015). "Mechanical properties of high strength concrete with scrap tire rubber." Construction and Building Materials 93: 249-256.

Moustafa, A. and ElGawady, M. A. (2016). "Strain Rate Effect on Properties of Rubberized Concrete Confined with Glass Fiber–Reinforced Polymers." Journal of Composites for Construction: 04016014.

Reda Taha, M. M., El-Dieb, A., Abd El-Wahab, M. and Abdel-Hameed, M. (2008). "Mechanical, fracture, and microstructural investigations of rubber concrete." Journal of materials in civil engineering 20(10): 640-649.

Rubber Manufacturers Association (2014). Tire industry facts, Rubber Manufacturers Association.

Server, W. (1978). "Impact three-point bend testing for notched and precracked specimens." Journal of Testing and Evaluation 6(1): 29-34.

Siddique, R. and Naik, T. R. (2004). "Properties of concrete containing scrap-tire rubber–an overview." Waste management 24(6): 563-569.

Tabatabaei, Z. S., Volz, J. S., Keener, D. I. and Gliha, B. P. (2014). "Comparative impact behavior of four long carbon fiber reinforced concretes." Materials & Design 55: 212-223.

Topcu, I. B. (1995). "The properties of rubberized concretes." Cement and Concrete Research 25(2): 304-310.

Toutanji, H. (1996). "The use of rubber tire particles in concrete to replace mineral aggregates." Cement and Concrete Composites 18(2): 135-139.

Venzi, S., Priest, A. and May, M. (1970). Influence of inertial load in instrumented impact tests. Impact Testing of Metals, ASTM International.

Xincheng, P. (2012). Super-High-Strength High Performance Concrete, CRC Press.

Yan, L., Jenkins, C. and Pendleton, R. (2000). "Polyolefin fiber-reinforced concrete composites: Part I. Damping and frequency characteristics." Cement and concrete research 30(3): 391-401.

Youssf, O., ElGawady, M. A. and Mills, J. E. (2015). "Experimental Investigation of Crumb Rubber Concrete Columns under Seismic Loading." Structures 3: 13-27.

Youssf, O., ElGawady, M. A. and Mills, J. E. (2016). "Static Cyclic Behaviour of FRP-confined Crumb Rubber Concrete Columns." Engineering Structures.

Youssf, O., ElGawady, M. A., Mills, J. E. and Ma, X. (2014). "An experimental investigation of crumb rubber concrete confined by fibre reinforced polymer tubes." Construction and Building Materials 53(0): 522-532.

Zheng, L., Sharon Huo, X. and Yuan, Y. (2008). "Experimental investigation on dynamic properties of rubberized concrete." Construction and Building Materials 22(5): 939-947.

III. STRAIN RATE EFFECT ON PROPERTIES OF RUBBERIZED CONCRETE CONFINED WITH GLASS FIBER REINFORCED POLYMERS

Ayman Moustafa[1] and Mohamed ElGawady[2]

Abstract

Rubberized concrete possesses viscous damping that is higher than that of conventional concrete, making it a promising candidate for construction in high seismic regions. Confining rubberized concrete with glass fiber reinforced polymers (GFRP) may result in superior performance. This paper investigates the behavior of rubberized concrete filled fiber reinforced polymer tubes (RCFFT) under different strain rates. The rubberized concrete had 0%, 10%, and 20% volume replacement of fine aggregate with shredded rubber. Each test specimen's behavior was compared to that of conventional concrete filled fiber reinforced polymer tubes (CFFT). The GFRP tubes were fabricated using wet-layup with different numbers of GFRP layers. Three different strain rates (representing static, earthquake, and severe earthquakes) were used to test these specimens under cyclic axial loading. The RCFFT behaved in a manner that was similar to conventional CFFTs. The rubberized concrete's confinement limited the reduction in the confined compressive strength more than it did in the unconfined compressive strength. The confinement of both conventional and rubberized concrete resulted in an increase in both the compressive strength and the ductility. The increase in the strain rate by two and three orders of magnitude resulted in increases in the compressive strength and ductility of both the

[1] Graduate research assistant, Department of Civil, Architectural, and Environmental Engineering, Missouri University of Science and Technology, USA E-mail: ampyf@mst.edu
[2] Benavides Associate professor, Department of Civil, Architectural, and Environmental Engineering, Missouri University of Science and Technology, USA E-mail: elgawadym@mst.edu

CFFT and RCFFT. High increases in the modulus of elasticity of both CFFT and RCFFT were observed with the increase of strain rates. The strain rate changed the behavior of the concrete that was confined with a lower confinement ratio. This effect was reduced when the confinement ratio was increased. The plastic dilation was also investigated. The addition of rubber resulted in a smooth transition in the dilation of concrete.

Keywords: Rubberized concrete, confinement, strain rate, self consolidating concrete, fiber reinforced polymers, dilation parameter

Introduction

The use of scrap tires in concrete, producing what is known as rubberized concrete, represents a beneficial option for the concrete industry. Replacing virgin materials with waste materials reduces the amount of waste materials going to landfills. If improperly handled, scrap tire piles can be easily set on fire. These fires are difficult to extinguish. They also produce both heavy smoke and toxic run off. Exposed scrap tires can be a breeding space for mosquitoes that carry disease (Rubber Manufacturers Association 2014).

Recent research has shown that rubberized concrete possesses a viscous damping that is significantly higher than conventional concrete, making it a good candidate for concrete structures subjected to dynamic loads such as earthquake ground motions (Reda Taha et al. 2008, Xue and Shinozuka 2013, Moustafa and ElGawady 2015). Rubberized concrete, however, displays strength that is smaller than its counterpart conventional

concrete. This drawback can be overcome by confining rubberized concrete (Youssf et al. 2014).

Research Significance

Significant amount of the research that showed the superior ductility, damping, and energy dissipation of unconfined and FRP confined rubberized concrete compared to the corresponding conventional concrete were carried out under pseudo static loads (Siddique and Naik 2004; Khaloo et al. 2008; Youssf et al. 2014; Moustafa and ElGawady 2015). However, rubberized concrete niche would be structural dynamic applications, such as earthquakes, where the constitutive material including rubber will be subjected to high strain rates. Rubber is a viscoelastic material sensitive to strain rate effects. Hence, investigating the effects of strain rate on rubberized concrete is required. Similarly, the niche application of conventional concrete encased in FRP is seismic application. The mechanical properties of both the CFFT and the RCFFT under different strain rates, to the best knowledge of the authors, have not been studied yet.

This article investigates the mechanical properties of six CFFT specimens and twelve RCFFT specimens subjected to cyclic axial loading under different strain rates representing static, earthquake, and severe earthquake (e.g. near fault ground motion) loadings. Various percentages of fine aggregate replacement (0, 10%, and 20% by volume) were used to produce the rubberized concrete.

Rubberized Concrete

The mechanical properties of rubberized concrete were investigated extensively under static loading. Others have concluded that replacing a high percentage of mineral

aggregates with shredded rubber reduces the concrete's compressive strength and workability. The amount of reduction depends on the percentage and type of aggregate to be replaced (either coarse or fine aggregate) as well as the size and distribution of the rubber particles (Eldin and Senouci 1993; Topcu 1995; Khatib and Bayomy 1999; Hernandez-Olivares et al. 2002; Siddique and Naik 2004; Youssf et al. 2014). Rubberized concrete, however, displays a more ductile behavior, better impact resistance, and stronger energy dissipation than conventional concrete. Zheng et al. 2008 measured viscous damping values ranging from 0.68% to 1.67% on small rubberized concrete cubes compared to viscous damping values ranging from 0.45% to 0.74% measured on conventional concrete cubes, i.e., rubberized concrete displayed about 75% higher viscous damping than that of the corresponding conventional concrete. Xue and Shinozuka 2013 investigated the seismic behavior of reinforced rubberized concrete columns. The columns displayed an average viscous damping coefficient of 7.7% compared to 4.75% for the corresponding columns constructed out of conventional concrete, i.e., rubberized concrete displayed 62% higher viscous damping than that of the conventional concrete. Reda Taha et al. 2008 found that rubberized concrete has an impact resistance that is 33% higher than conventional concrete at replacement ratios higher than 20%. An extensive literature review of the mechanical properties of rubberized concrete can be found in Youssf et al. 2014.

Confinement of Concrete with FRP

Confining conventional concrete with FRP increases the concrete's axial strength and ductility. The magnitude of the increase depends on the confinement ratio. This ratio is defined as the ratio of the lateral confinement pressure to the compressive strength (

$f_l / f_c^{'}$) (e.g. Fam et al. 2003; Lam et al. 2006; Zhu et al. 2006; ElGawady et al. 2010; ElGawady and Sha'lan 2010; Dai et al. 2011; Ozbakkaloglu and Lim 2013). The lateral confinement pressure is calculated as

$$f_l = \frac{2E_f t_f \varepsilon_f}{D} \quad (1)$$

where E_f is the GFRP's modulus of elasticity, t_f is the GFRP's thickness, ε_f is the GFRP's ultimate strain, and *D* is the CFFT's internal diameter.

Youssf et al. 2014 investigated the behavior of rubberized concrete encased in FRP tubes. As expected, confining rubberized concrete with FRP layers resulted in a significant overall increase in the confined specimens' compressive strength compared to the unconfined ones. Moreover, the strength increased as the FRP's stiffness increased. Confining rubberized concrete using FRP effectively negates the decrease in strength that occurs in rubberized concrete. It also retains the advantages of increased ductility and damping that arise from rubberized concrete. This finding has promising implications for the use of confined rubberized concrete in high seismic regions.

Effect of Strain Rate on Materials

The effect of the strain rate on materials is more effective when the strain rates are increased by an order of magnitude or more. Bischoff and Perry 1991 defined the strain rates that correspond to static loading to be between 0.5E-5 and 5E-5 (1/s). They also defined the earthquake loading to be corresponding to strain rates between 1E-3 and 1E-2 (1/s). The effects of strain rate on concrete, rubber, and FRP have been investigated extensively. The effects of strain rate on the CFFT's behavior, however, have not been

investigated yet. The behavior of RCFFT under high strain rates has also not been investigated.

The effect of strain rate on the mechanical properties of FRP was investigated extensively. In general, the FRP's tensile strength increased linearly with logarithmic increase in the strain rate (e.g. Davies and Magee 1975; Lifshitz 1976; Staab and Gilat 1995; Vashchenko et al. 2000; Okoli 2001; Jacob et al. 2004).

Rubber is an elastomeric material, and its properties are highly dependent on the strain rate. A high strain rate can increase rubber's strength by 50% (Song et al. 2004; Roland 2006; Tomita et al. 2008).

The effect of loading type is also inherent in concrete itself (Bischoff and Perry 1991; CEB-FIP 1993; Unified Facilities Criteria (UFC) 3-340-02 2008). Concrete compressive strength increases with increasing loading rate. This increase is caused by the inertial resistance of the materials through which the crack propagation path develops (Bischoff and Perry 1991). The propagation of the micro-cracks for the case of higher strain rates is delayed because as the stress level is increased with time, the micro-cracks also take a finite time to propagate to the equilibrium position corresponding to this stress level. Since the cracks have a certain propagation velocity, the delay in the micro-cracks propagation is achieved when the stress is increased in a higher rate than the time needed for the cracks to reach their new equilibrium position. Therefore, the cracking pattern experienced by concrete at higher strain rates will always be corresponding to a lower equivalent stress level that is experienced by concrete at lower strain rate at the same time because of this time delay. Furthermore, for high strain rates, cracks are likely to propagate in a straighter path through zones of higher strength such as aggregates

(Bischoff and Perry 1995). This contributes to higher stresses and less cracking. Rossi and Toutlemonde 1996 believed that pore water in the concrete along with additional water from wet conditions are the main contributor to the increase in the concrete parameters, especially the tensile capacity, at higher strain rates. They attributed the increase to the Stefan effect, which can be summarized as: when a thin film of a viscous liquid is trapped between two plates moving apart at a certain velocity, the film exerts a return force on the plates that is proportional to the velocity of separation. This effect can delay the creation of the micro-cracks and the propagation of the initial micro-cracks. Zheng and Li 2004 provided an explanation for the strain rate effect due to micro-cracks based on fracture mechanics by replacing the wide-spread micro-cracks by an equivalent single crack. They assumed that the increasing of dynamic macro-equivalent toughness for single crack can qualitatively explain the rate effect in concrete due to micro-crack nucleation, propagation and coalescence. Zheng et al. 2005 proposed a model for predicting the dynamic strength increase in concrete based on dynamic fracture mechanics for cracks growth based on the model by Kachanov 1987. They concluded that the failure process of concrete is sensitive to the strain rate. It may be due to higher unstable crack propagation speed and less time for stress release of crack tip at high loading rate. Georgin and Reynouard 2003 performed finite element simulation to capture the effect of strain rate on concrete. They associated the strain rate effect to the viscoplasticity of concrete at higher strain rates. They considered the viscoplastic model is the natural way to take into account the rate effect as it allows non-smooth multisurface criterion to be used between the cracks surfaces. The effect of strain rate on concrete has been extensively investigated (Yon et al. 1992; Ross et al. 1995; Grote et al. 2001;

Georgin and Reynouard 2003; Zheng et al. 2007). The effect of strain rate on the concrete strength is typically reported as a dynamic factor (DF). The DF could be as high as 7 for tension and 2 for compression at the strain rate of 102 (1/s) (Malvar and Ross 1998; Zheng et al. 2005). The DF for the range of earthquake strain rate is around 1.2 (Bischoff and Perry 1991; CEB-FIP 1993).

Experimental Investigation

Material Characteristics

Self consolidating concrete (SCC) was designed and used as a reference mixture during the course of this study. Both 10% and 20% of sand (by volume) were replaced with crumb rubber to design two different rubberized concrete mixtures. Variable amounts of superplasticizer were used to maintain the same workability of the fresh concrete, regardless of the rubber percentages. The characteristics of the concrete materials used in this study are listed in Tables 1 and 2; they are pictured in Figure 1.

Type I Portland cement that conformed to ASTM C150 specifications, limestone washed coarse aggregate with nominal maximum size of 19 mm, and Missouri river sand were used in each of the mixtures. The rubber used was crumb rubber with three different sizes denoted as R (8-14), R (14-30), and R (30-). The first number represents the sieve number of the passing particles and the second number represents the sieve number of the retained particles. Different trial mixtures, including different crumb rubber grading, were prepared. The grading that had the best workability and consistency was selected for this study.

The confinement was provided using unidirectional glass fiber reinforced polymers and Tyfo S epoxy by FYFE©. Three specimens of GFRP hoops were tested for each of the one and three layers according to ASTM D2290 2012. The average ultimate tensile strength in the fiber direction was 339 MPa and 352 MPa for the one layer and three layers, respectively. The elongation at break was 1.61% and 2.31% for the one layer and three layers, respectively. The increase of the elongation at break for the three layers can be attributed to the difference in the mode of failure. Single layer FRP displayed sudden rupture of the fibers for the one layer, while for the three layers when the fibers of one of the layers rupture, it keeps carrying load and keeps elongating until all the fibers along the thickness rupture.

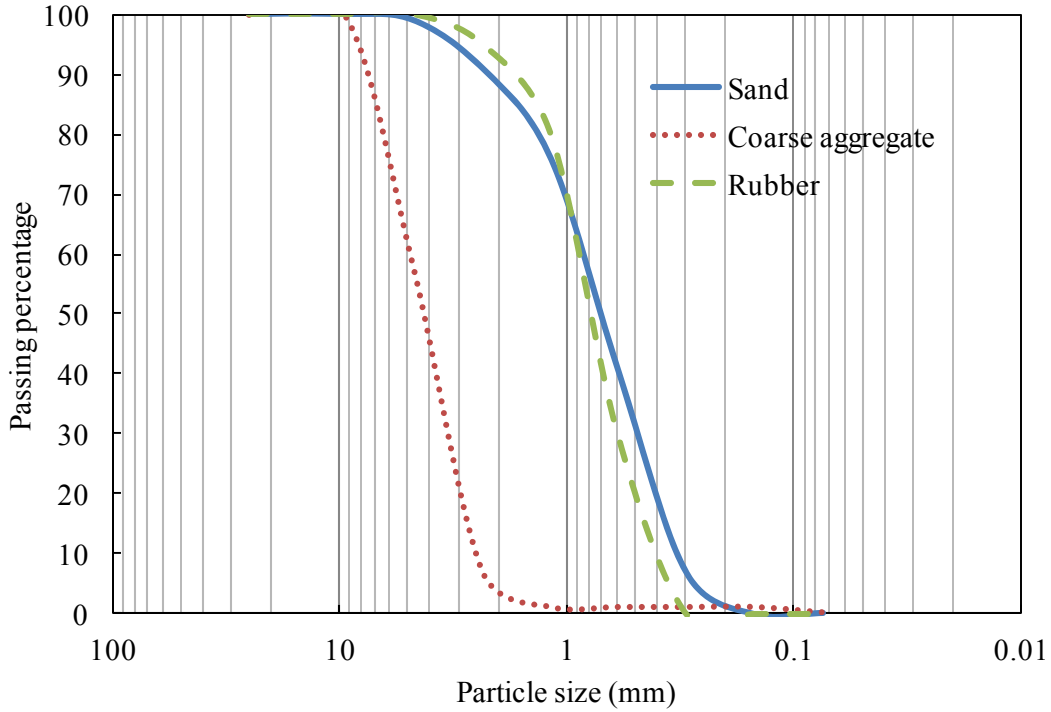

Figure 1. Grading of used aggregates and rubber

Test Specimens

A total of six CFFT specimens and twelve RCFFT specimens were prepared by wrapping epoxy saturated GFRP sheets around Sono-tubes. One continuous GFRP sheet was used for manufacturing the tubes having three layers of FRP. The GFRP overlap for each specimen was approximately $1/3^{rd}$ the perimeter of a test specimen. Each tube had a nominal outer diameter of 158 mm and a nominal height of 300 mm. The tubes were allowed to cure at room temperature for 7 days, and then concrete was poured inside the tubes. Six tubes for each percentage of rubber replacement were prepared (Table 3). One layer of GFRP was used to prepare three of these tubes. Three layers of GFRP were used to prepare the three remaining tubes. Six 100 mm x 200 mm cylinders for each mixture were cast the same day both the CFFT and the RCFFT tubes were prepared so that the concrete's compressive strength could be determined at 28 days. The cylinders were demolded after 24 hours; they were tested after moist curing in a controlled moisture room for 28 days according to ASTM C192 2013. The CFFT specimens were tested under three different strain rates: 2.8E-5, 2.8E-3 and 2.8E-2 (1/s) to simulate the loading rates associated with static loading, earthquakes, and severe earthquakes (e.g. near field ground motions), respectively.

Test Setup

An MTS machine (Figure 2) having a capacity of 2225 kN was used to test all the specimens under axial cyclic loading. The cyclic axial compressive load was applied according to a prescribed pattern of progressively increasing levels of axial displacements until failure occurred. Three cycles of loading/unloading were applied at each axial

displacement level. Two string potentiometers were placed on two opposite sides of each cylinder at a gauge length of one-third the specimen's height so that the average axial strain could be determined. A linear variable displacement transducer (LVDT) was used to measure the axial displacements which were used to obtain the average axial strains along a full specimen's height. Two horizontal strain gauges on opposite sides of each specimen were used to measure the hoop strains in the GFRP tube.

Figure 2. Test setup

Experimental Results

The specimens' strength and strain parameters are listed in Table 4. Here, $f_c^{'}$ is the unconfined compressive strength, ε_{c0} is the measured axial strain corresponding to $f_c^{'}$, $f_{cc}^{'}$ is the confined concrete compressive strength based on CFFT testing, and ε_{cu} is the axial strain corresponding to $f_{cc}^{'}$. The confinement ratio ($f_l / f_c^{'}$), and the confinement effectiveness; defined as the ratio between the confined compressive strength and the compressive strength ($f_{cc}^{'} / f_c^{'}$) are also presented.

The axial cyclic stress-strain curves for the unconfined concrete and CFFT are illustrated in Figures 3 and 4, respectively. The stress was obtained by dividing the axial load by the cross sectional area of the specific concrete specimen. The axial strain was obtained by dividing the displacement (measured by the LVDT) by the specimen's height.

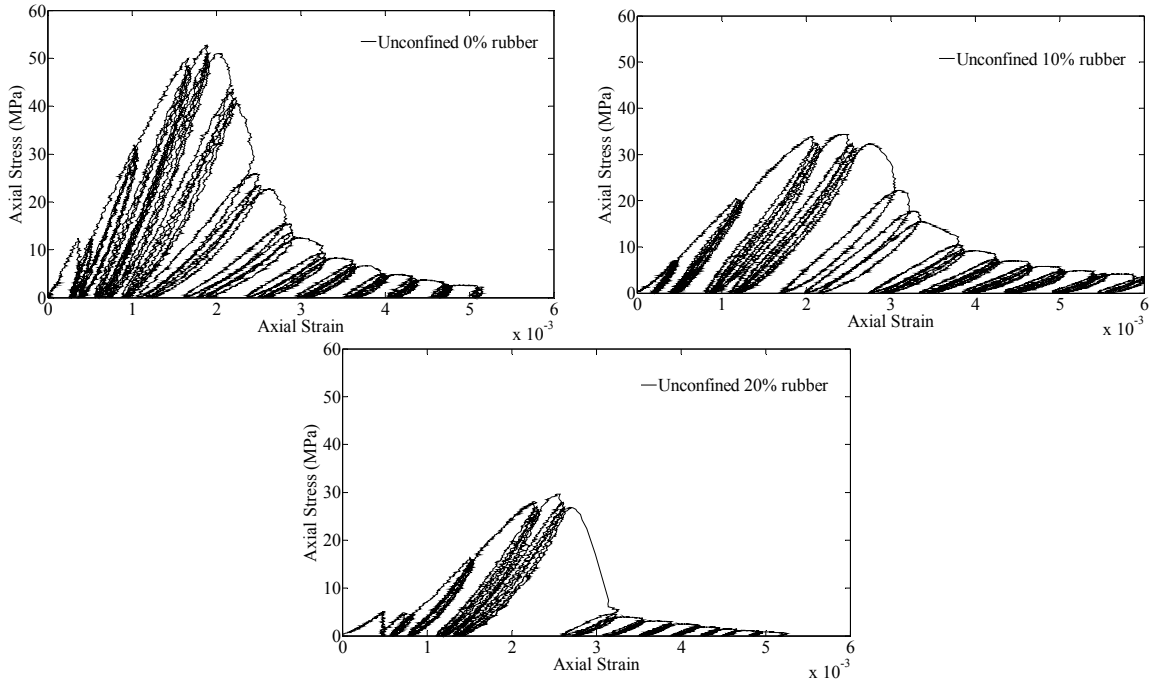

Figure 3. Axial cyclic stress-strain curves for unconfined specimens

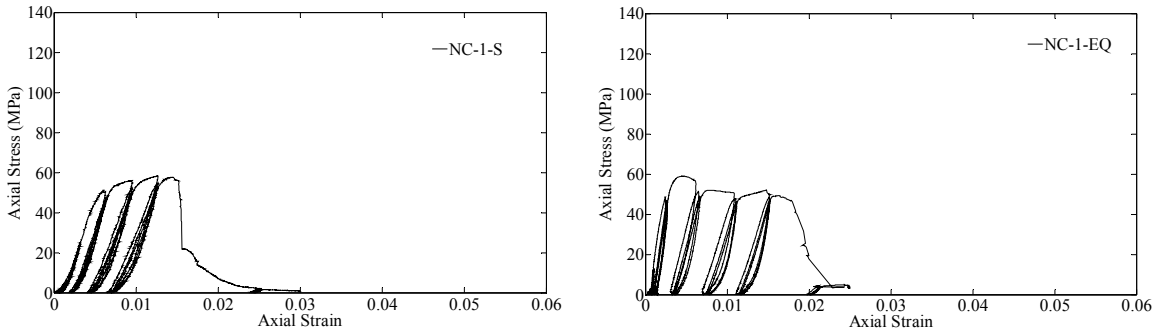

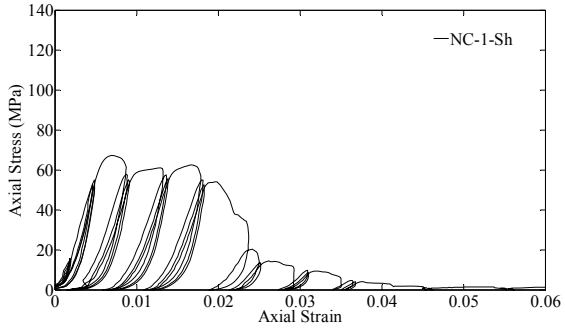
—NC-1-Sh
Axial Stress (MPa)
Axial Strain

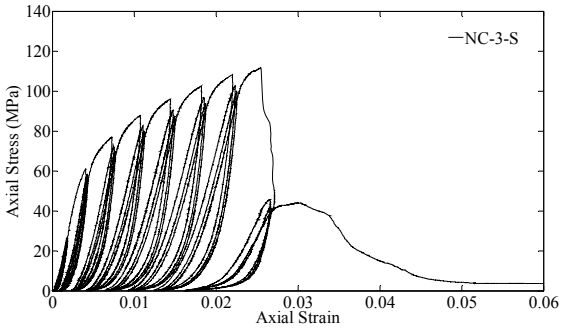
—NC-3-S
Axial Stress (MPa)
Axial Strain

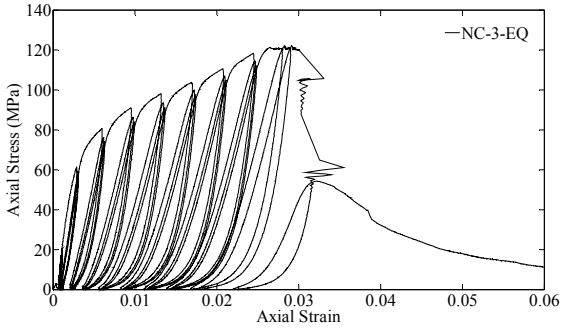
—NC-3-EQ
Axial Stress (MPa)
Axial Strain

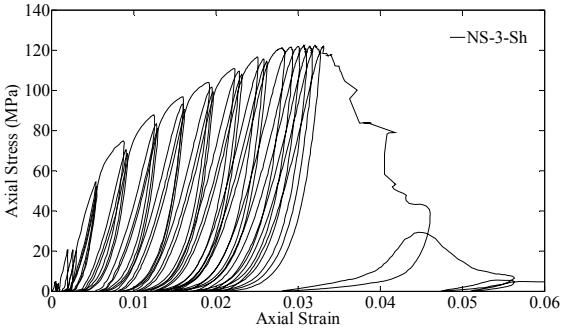
—NS-3-Sh
Axial Stress (MPa)
Axial Strain

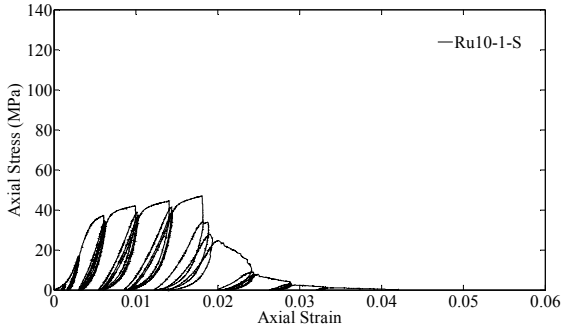
—Ru10-1-S
Axial Stress (MPa)
Axial Strain

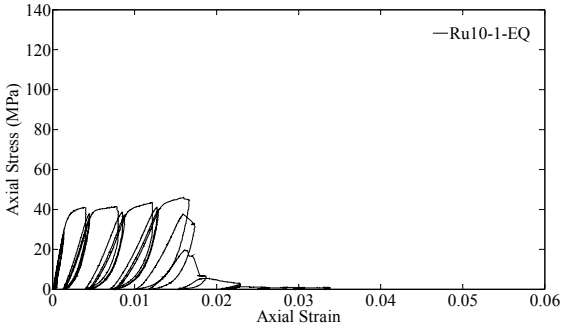
—Ru10-1-EQ
Axial Stress (MPa)
Axial Strain

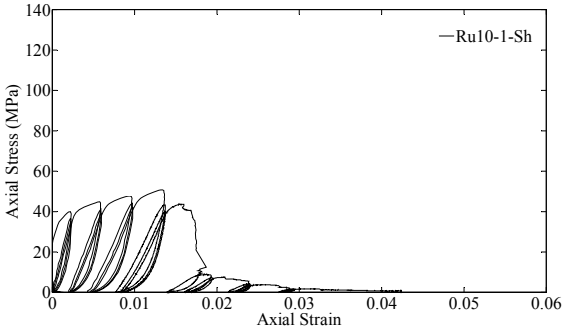
—Ru10-1-Sh
Axial Stress (MPa)
Axial Strain

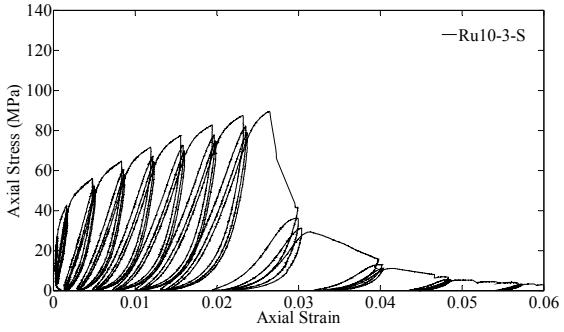
—Ru10-3-S
Axial Stress (MPa)
Axial Strain

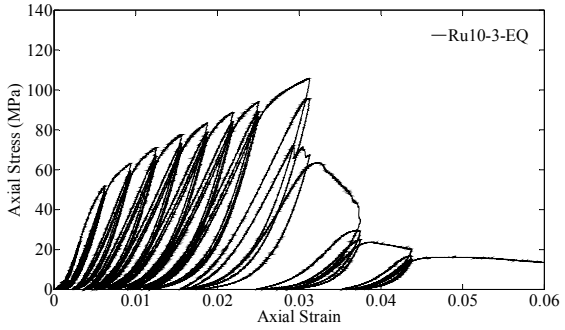
—Ru10-3-EQ
Axial Stress (MPa)
Axial Strain

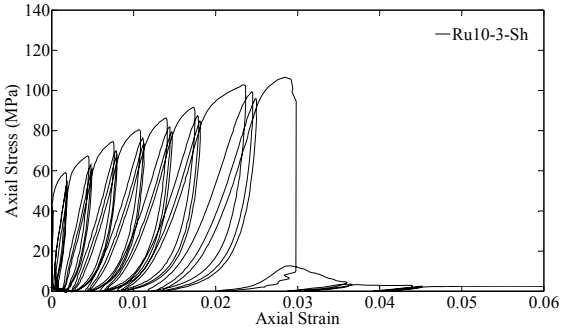
—Ru10-3-Sh
Axial Stress (MPa)
Axial Strain

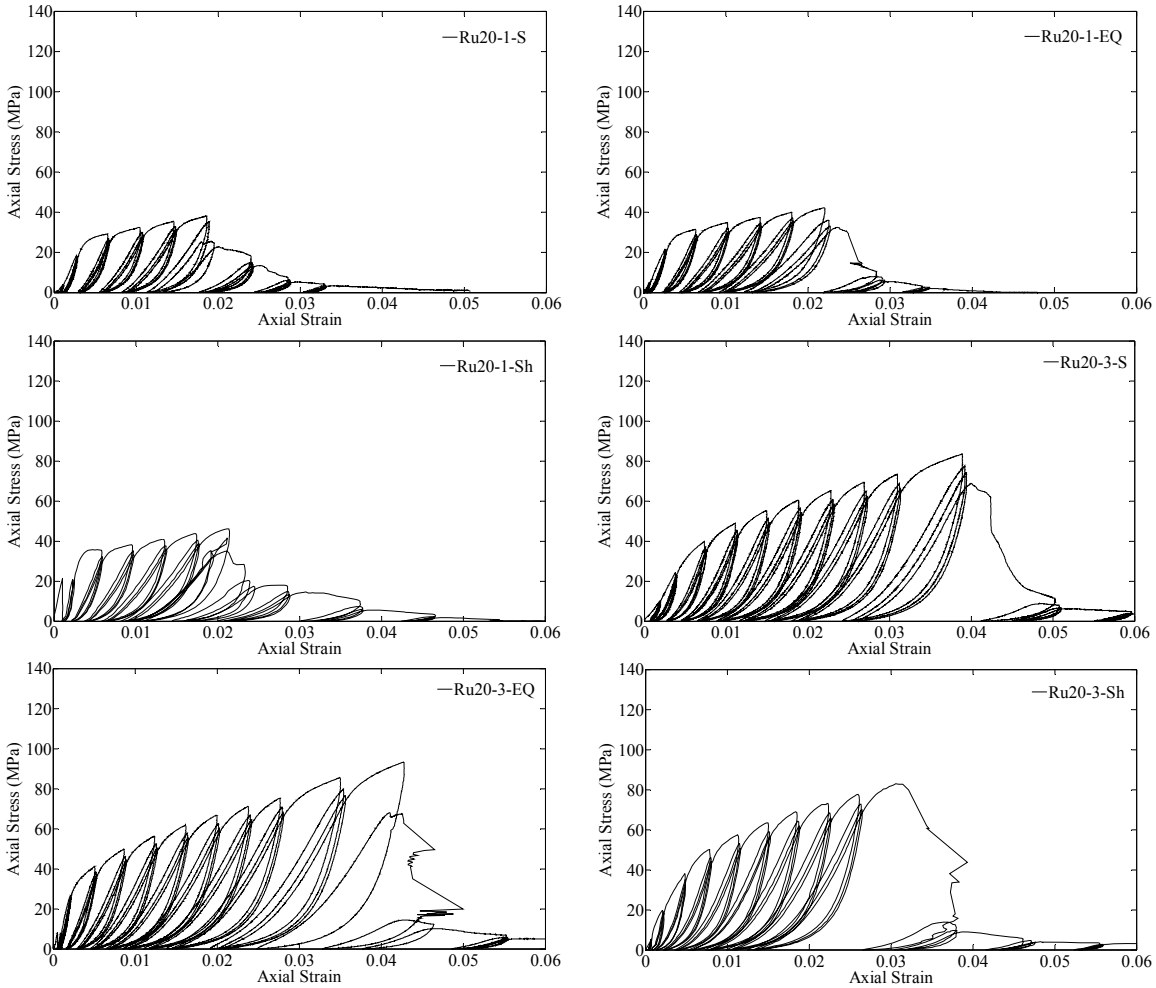

Figure 4. Axial cyclic stress-strain curves for CFFT and RCFFT specimens

Compressive Strength of Unconfined Concrete ($f_c^{'}$)

A comparison between the stress-strain curves of concrete with different rubber contents is illustrated in Figure 5. Figures 3 and 5 both show compressive strength reductions for the rubberized concrete of 32.6% and 41.9% for 10% and 20% rubber replacement, respectively. Increases in the axial strains at the maximum axial stress (ε_{c0}) of 26.7% and 33.8% for 10% and 20% rubber replacement, respectively, were measured. This indicates the stiffness of the rubberized SCC was reduced significantly as compared to the

reference concrete. The stiffness degradation and lower compressive strength of the rubberized concrete can be attributed to the lower stiffness of the rubber particles compared to the aggregate. This difference in stiffness also produces higher internal tensile stresses inside the concrete that cause early failure in the cement paste at the interfacial transition zone (ITZ) between the paste and the rubber particles. The ITZ was also affected by the poor bond between the rubber and the cement paste due to the high difference in the density of them. The poor bond led to a weaker ITZ which led to early failure of the rubberized concrete. Increases in the axial strains can be attributed to the higher deformation capacity of rubber particles as compared to aggregates.

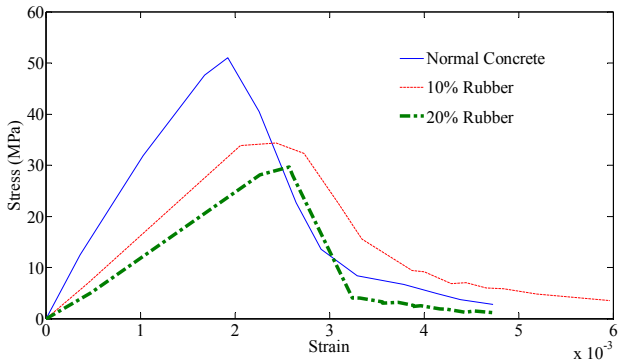

Figure 5. Stress strain envelope for unconfined concrete

Effect of Strain Rate on the Behavior of CFFT and RCFFT Specimens

The strain rate did not significantly affect the mode of failure. The GFRP tube ruptured near each specimen's mid-height in all of the specimens but NC-1-EQ and NC-1-Sh. This rupture caused both the CFFT and the RCFFT specimens to fail (Figure 6a). Failure occurred after the concrete core significantly dilated, leading to an excessive strain demand on the GFRP. This was followed by GFRP rupture and drop in the specimens' load carrying capacity. In general, the GFRP rupture was initiated at axial strains between

0.015 and 0.025. However, for specimens NC-1-EQ and NC-1-Sh having normal concrete confined by one layer of GFRP at higher strain rates, rupture of GFRP initiated at significantly lower axial strains, of approximately 0.004 to 0.005, compared to their counterpart CFFT specimen NC-1-S subjected to low strain rate loading. However, beyond this initial GFRP rupture, the specimens were still able to carry the applied load followed by gradual GFRP progressive rupture (Figure 6b).

(a) (b)

Figure 6. Failure mode of CFFT and RCFFT having a) three layers of GFRP, and b) one layer of GFRP

The visually observed difference in the mode of failure was also reflected on the test specimens' stress-strain. The envelope of the normalized axial stress versus the axial strain for each of the specimens confined using one layer of GFRP is illustrated in Figure 7. The normalized axial stress is defined as the measured stress of the CFFT specimen normalized by $f_c^{'}$ for each particular concrete mixture.

The concrete's behavior when confined with one layer of GFRP under different strain rates was significantly influenced by the concrete core behavior because the confinement ratio was relatively small between 0.144 and 0.248 (Table 4). As shown in Figure 7, the envelopes of the stress strain curves for the CFFT specimens having one

layer of GFRP can be approximated as an elasto-plastic behavior. A linear ascending first branch with high initial stiffness is observed followed by an ascending second branch with stiffness softening; then, significant stiffness degradation until failure occurred. The exceptions of this behavior are the CFFT normal concrete with one layer of GFRP under high strain rates (specimens NC-1-EQ and NC-1-Sh). The second ascending branch within these specimens occurred over a very small axial strain range and is directly followed by stiffness degradation. This can be attributed to the very low confinement ratio of 0.144. It can also be attributed to the fact that for concrete at high strain rates, the propagation of cracks is less, which caused less dilation of concrete. The GFRP confinement, which is a passive confinement, is basically not activated with that low confinement ratio and the concrete acted as unconfined concrete. The GFRP provided containment rather than confinement increasing the strain only. The increase in stress can be attributed to the strain rate effect on the concrete core. Unlike the normal concrete confined by one layer of GFRP, the rubberized concrete followed the elasto-plastic behavior for all strain rates. This can be attributed to the higher confinement ratios of 0.214 and 0.248, compared to 0.144 for the conventional concrete which led to confined concrete behavior.

Unlike the behavior of specimens confined with one layer of GFRP, the behavior of the specimens confined with three layers of GFRP was controlled by the GFRP tube, not the concrete. The elasto-plastic behavior occurred in all of the specimens due to the high confinement ratio that led to a conventional confined behavior. The envelopes of the stress strain curves for both the normal and the rubberized concrete are illustrated in Figure 8.

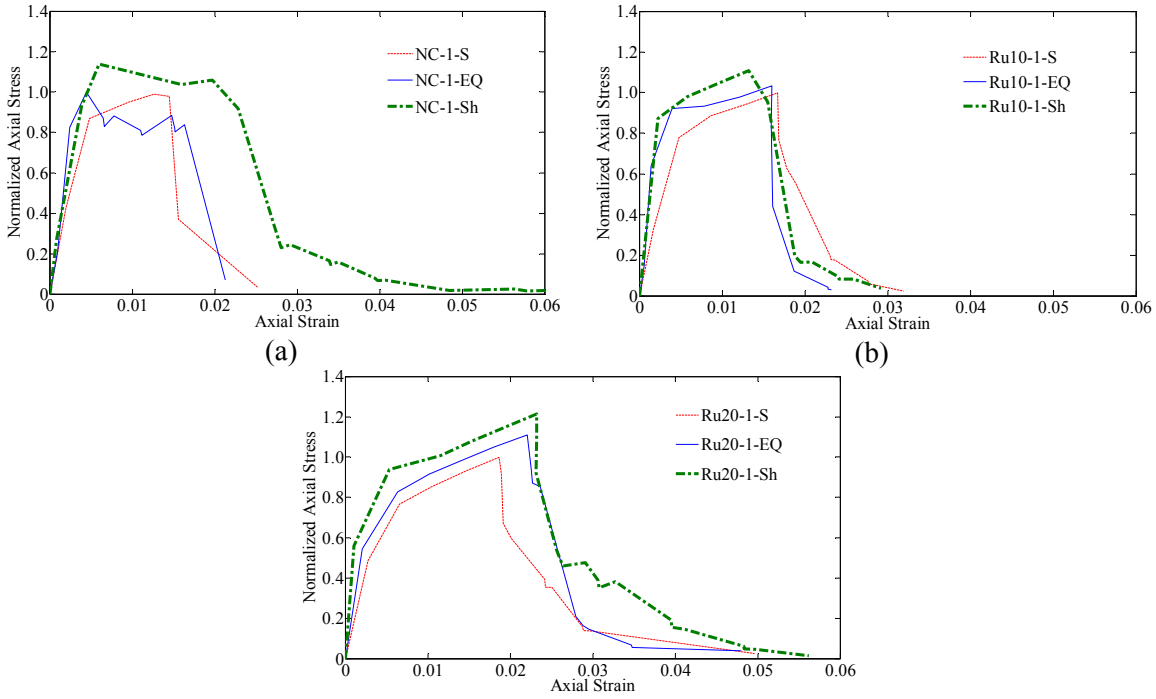

Figure 7. Normalized stress strain envelope for a) normal concrete, b) 10% rubber replacement and c) 20% rubber replacement confined with one layer of GFRP

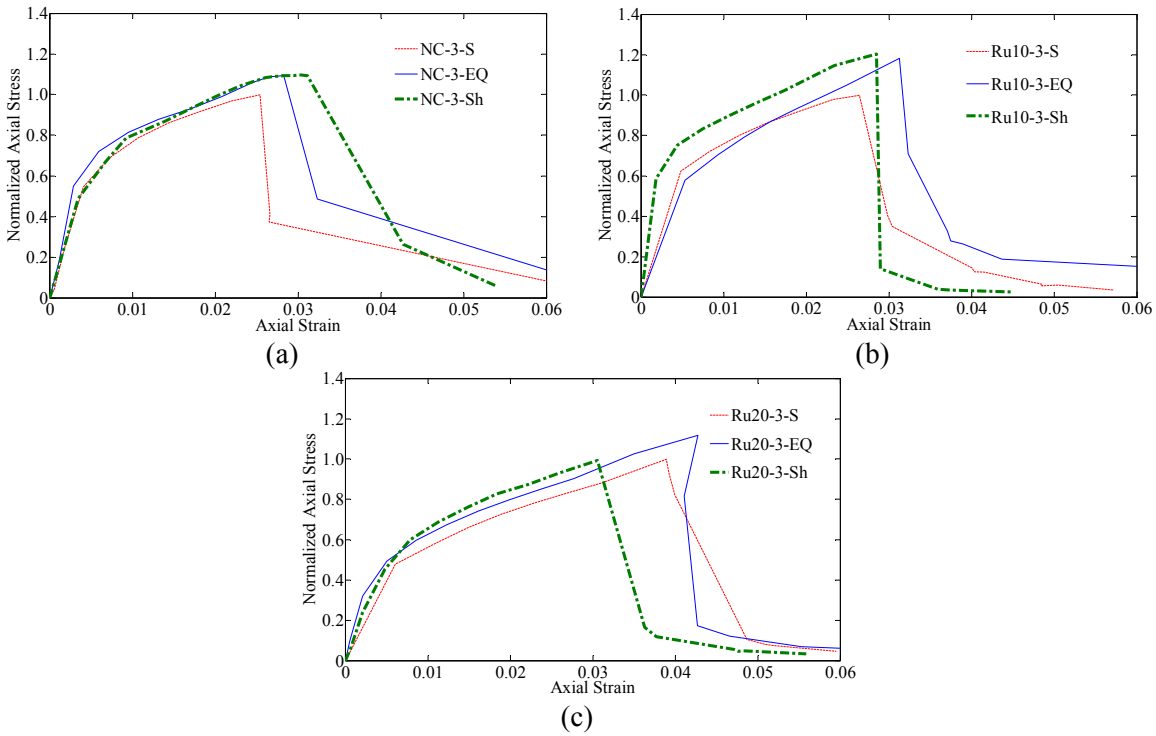

Figure 8. Normalized stress strain envelope for a) normal concrete, b) 10% rubber replacement and c) 20% rubber replacement confined with three layers of GFRP

Effect of Strain Rate on Confined Compressive Strength (f'_{cc})

The strain rate's effect on the confined compressive strength (f'_{cc}) in both the normal and the rubberized concrete is illustrated in Figure 9 with a semi log scale. Figure 9(a) shows an approximately linear increase in the strength of rubberized concrete confined with one layer of GFRP with the logarithmic increase in the strain rate. This behavior is similar to the linear relation observed by Vashchenko et al. 2000 for GFRP only. This indicates that the failure is controlled by the GFRP and the confinement is effective as discussed before. The confined compressive strength increased by 20%, further indicating the failure was governed by the GFRP's reaction to the strain rate effect. No increase in the strength was observed in concrete confined with one layer of GFRP until a strain rate of 2.8E-3 (1/s). An increase of 13.9% was observed beyond that rate. The non-linear behavior can again be interpreted by both the failure mode and the specimens' behavior discussed before. This behavior confirms that the increase in compressive strength was related to the strain rate effect on concrete because the low confinement ratio was ineffective. Thus, the concrete was acting as though it was unconfined.

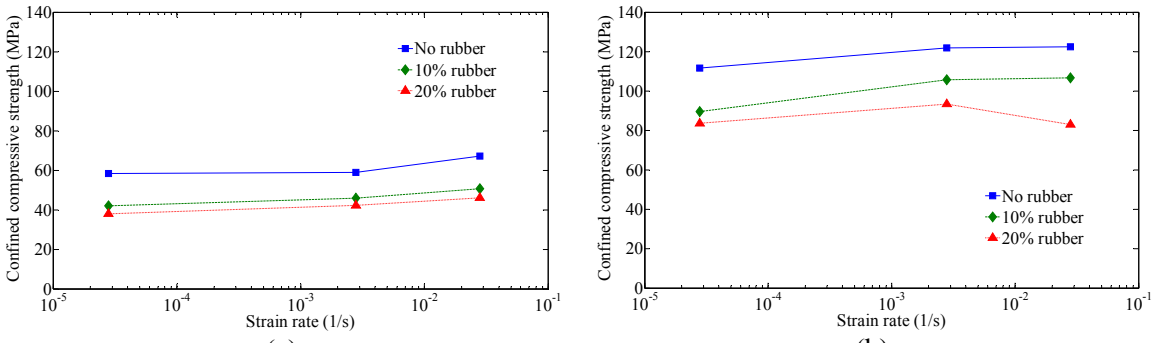

Figure 9. Strain rate effect on concrete confined with a) one layer, and b) three layers of GFRP

For CFFT with three layers of GFRP, shown in Figure 9(b), an increase is observed from the static rate of 2.8E-5 (1/s) to the dynamic rate of 2.8E-3 (1/s) and then

it stabilizes. This indicates the GFRP is used to its full capacity in confinement and the concrete reached its maximum strength. The $f_{cc}^{'}$ decreased in the 20% rubber replacement at a strain rate of 2.8E-2 probably due to earlier rupture of GFRP in the overlap zone. Determining where the rupture was initiated was made difficult by the high strain rate and the test's short duration.

The effect of rubber content on the confined compressive strength ($f_{cc}^{'}$) of the CFFT and RCFFT specimens can be observed when Figure 9 is interpreted vertically. The figure illustrates a compressive strength reduction for RCFFT compared to the corresponding CFFT specimens; this behavior is similar to what was observed for unconfined rubberized concrete. The confinement, however, was able to reduce the rate of compressive strength reduction compared to unconfined rubberized concrete. Using 10% rubber content resulted in a strength reduction of 32.6%, 28.5%, and 19.8% for confinement using zero, one, and three GFRP layers, respectively. Using 20% rubber content resulted in a strength reduction of 41.9%, 34.1%, and 25.1% for confinement using zero, one, and three GFRP layers, respectively. The lower reduction in the three layers of GFRP indicates higher confinement effectiveness as compared to the one layer. This reduction in the rate of strength decrease in the case of RCFFT occurred as for a given FRP stiffness, the confinement ratio was higher in the case of RCFFT than that of the case of the corresponding CFFT. Similar trend was observed in all loading rate cases.

Effects of Confinement on Behavior of Rubberized Concrete

The effect of confining the concrete with one and three layers of GFRP tubes for 0%, 10%, and 20% rubber replacement under static loading is illustrated in Figure 10. The

behavior of both normal and rubberized concrete was alike. The confinement effectiveness for the rubberized concrete was higher, however, than that observed in the normal concrete. The confinement effectiveness values for confinement with one layer of GFRP were 1.14, 1.37, and 1.28 for 0%, 10%, and 20% rubber replacement, respectively. Higher confinement effectiveness values of 2.19, 2.6, and 2.81 were achieved for confinement with three GFRP layers for 0%, 10%, and 20% rubber replacement, respectively. It should be noted that the number of layers for large scale columns will be higher; hence the confinement ratio ($f_l / f_c^{'}$) can be used as an indication of the increase in the compressive strength.

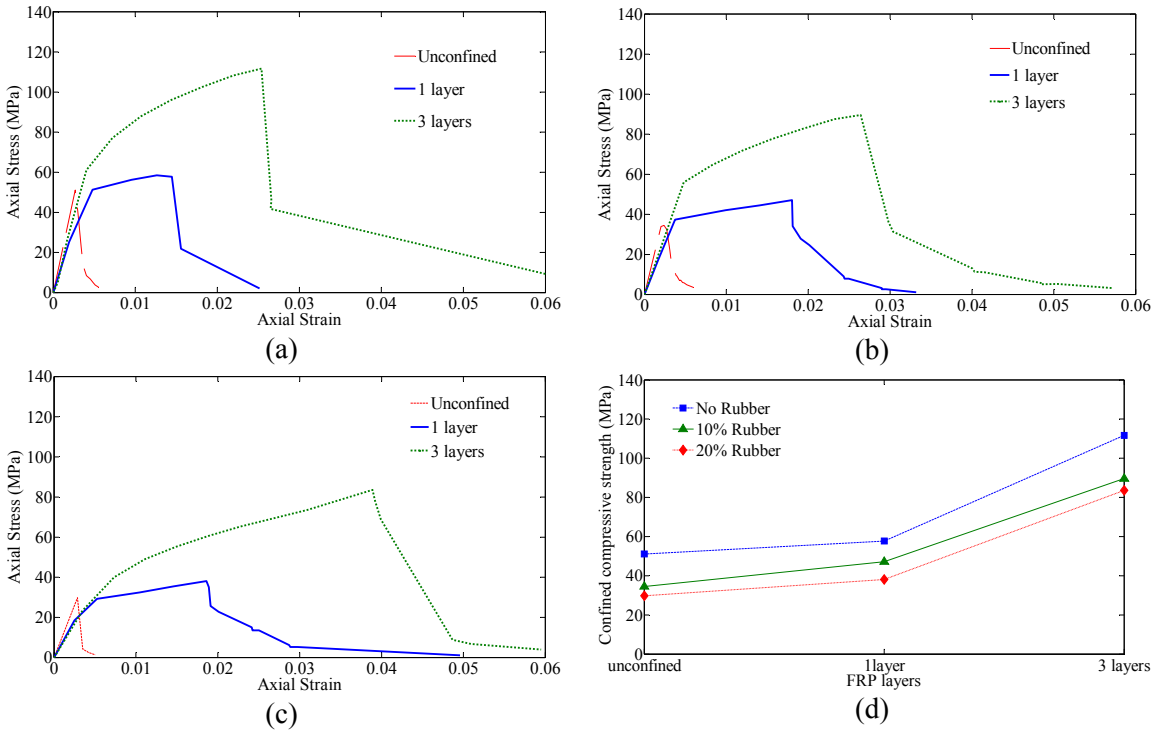

Figure 10. Effect of confinement on confined a) normal concrete, b) 10% rubber replacement, c) 20% rubber replacement, and d) confined compressive strength

Effect of Strain Rate on Modulus of Elasticity

The confined concrete's modulus of elasticity was computed according to ASTM C469 2010 as the chord modulus of elasticity from 50 micro strain to the point of 40% of the

compressive strength. The effect of strain rate on the confined concrete's modulus of elasticity is illustrated in Figure 11. The data in this figure indicate that the increase in the modulus of elasticity was quite large for a strain rate of 2.8E-3 when compared to 2.8E-5. The increase in the CFFT can be attributed to the micro-cracks that were unable to propagate fast enough, producing a higher apparent modulus of elasticity. The increase in the modulus of elasticity was higher in the RCFFT specimens because of the viscoelasticity of the rubber. The change in the modulus of elasticity between strain rates of 2.8E-3 and 2.8E-2 is much lower than the change between strain rates of 2.8E-5 and 2.8E-3. This indicates the stiffness of the CFFT tube was less affected by the higher velocity shocks.

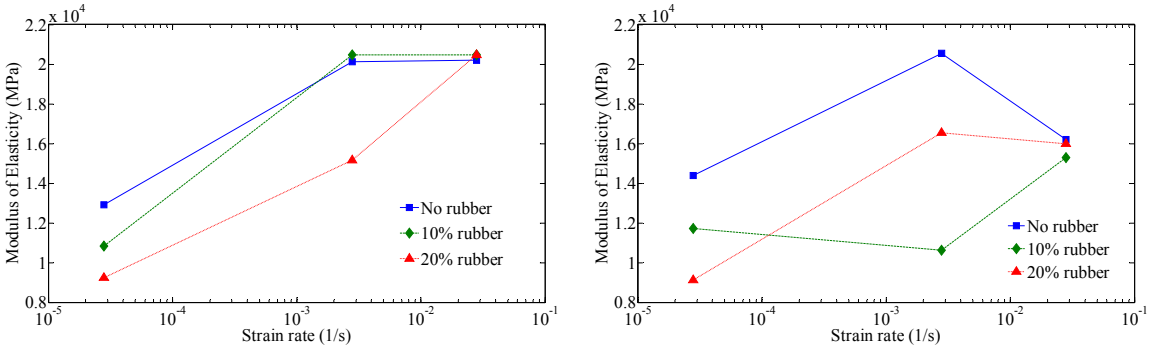

Figure 11. Strain rate effect on modulus of elasticity for a) one layer, and b) three layers of GFRP

Effect of Strain Rate on Ductility

Concrete ductility (μ) is defined as the ratio of concrete ultimate strain to its yield strain. The yield strain is defined as the strain that corresponds to a stress of 0.33-0.65 of the unconfined compressive strength ($f_c^{'}$) (Markovich et al. 2011). The yield strain chosen in this study corresponded to 0.65 $f_c^{'}$. The yield strain values were 1031, 1358, and 1553

micro-strain for 0%, 10%, and 20% rubber, respectively. The ultimate strain was determined when the GFRP ruptured and the strength decreased. The effect of strain rate on ductility is illustrated in Figure 12. The increase in ductility was more pronounced in the three layers than it was in the one layer for higher strain rates, with an increase of up to 16.7%. This can be attributed to the higher tensile strain capacity in the hoop direction, which then increased the axial strain. The ductility values were higher for the normal concrete because of the lower yield strain value. They were not produced by higher deformability.

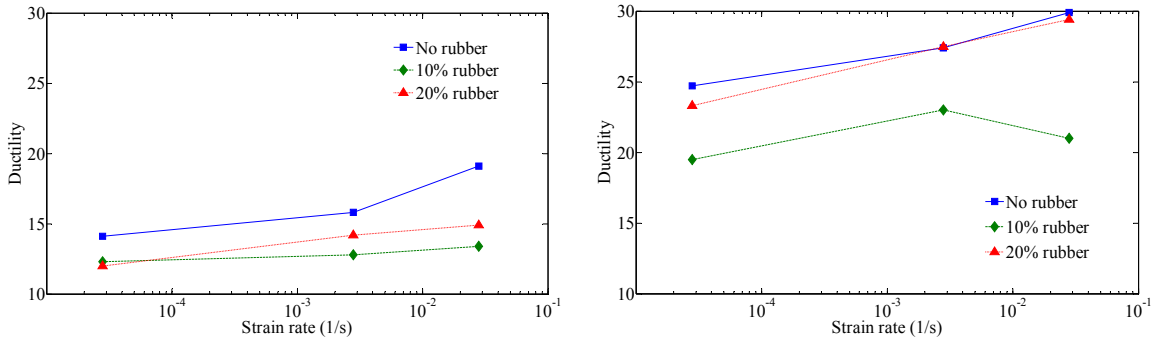

Figure 12. Strain rate effect on ductility for a) one layer, and b) three layers of GFRP

Effect of Strain Rate on Energy Dissipation and Hysteresis Damping

Hysteresis is the property of systems that follows different loading and unloading paths. Hysteresis damping for cyclic testing is calculated from the specific damping capacity (Y). The damping capacity is the ratio between the energy dissipated per unit volume of the material (E_D) and the strain energy per unit volume that is stored in a linear elastic system (E_{S0}) as shown in eq. 2.

$$Y = \frac{E_D}{E_{S0}} \tag{2}$$

A graphical representation of E_D and E_{S0} in terms of stress (σ) and axial strain (ε) is shown in Figure 13 (Chopra 2007).

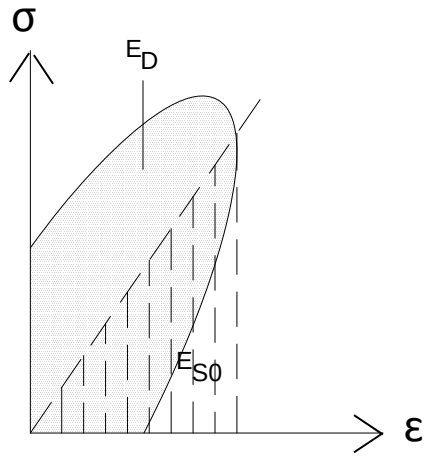

Figure13. Dissipated energy per unit volume of the material, E_D and elastic strain energy, E_{S0}

Hysteresis damping can be expressed as the equivalent viscous damping. It is calculated from the specific damping capacity using eq. 3.

$$\zeta_{eq} = \frac{1}{2\pi} Y \tag{3}$$

The cumulative dissipated energy for all specimens is illustrated in Figure 14. The CFFT's dissipated energy increased up to 27% as the strain rate increased. The addition of rubber increased the dissipated energy up to 60%. This can be attributed to the low stiffness of the rubber particles that allowed the rubberized concrete to have a relatively high flexibility, and thus absorb higher energy than normal concrete. As expected, the cumulative dissipated energy increased as the confinement ratio increased. Comparing

the curves in Figures 12 and 14 shows that using the energy dissipation is a more reliable criterion to present the trend of the results.

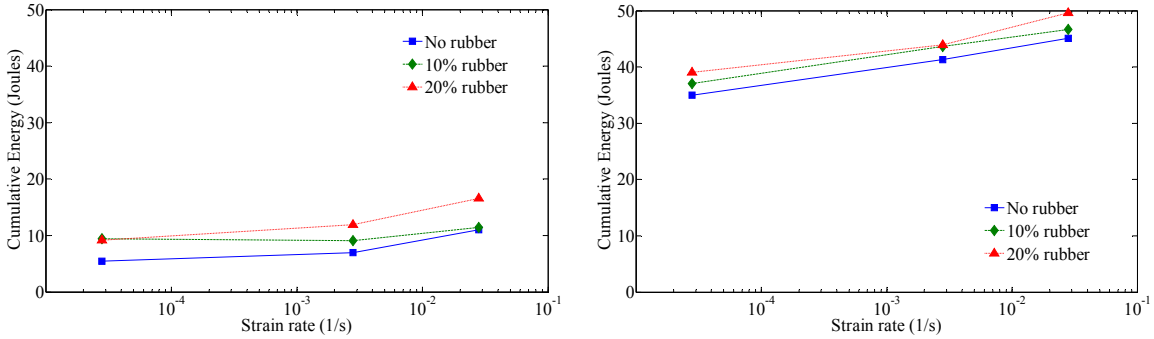

Figure 14. Strain rate effect on energy dissipated for a) one layer, and b) three layers of GFRP

The average equivalent damping for each specimen (calculated from eq. 3) is illustrated in Figure 15. The strain rate had a general increasing effect on hysteresis damping. The rubberized concrete's hysteresis damping values are relatively higher than those of normal concrete's damping for confinement with one layer of GFRP. This occurred because the rubberized concrete developed more micro cracks due to the stiffness mismatching between the rubber particles and the cement paste. For confinement with three layers of GFRP, the difference between the damping of the rubberized and conventional concrete is less pronounced because the higher confinement counteracted the micro-cracks' effect.

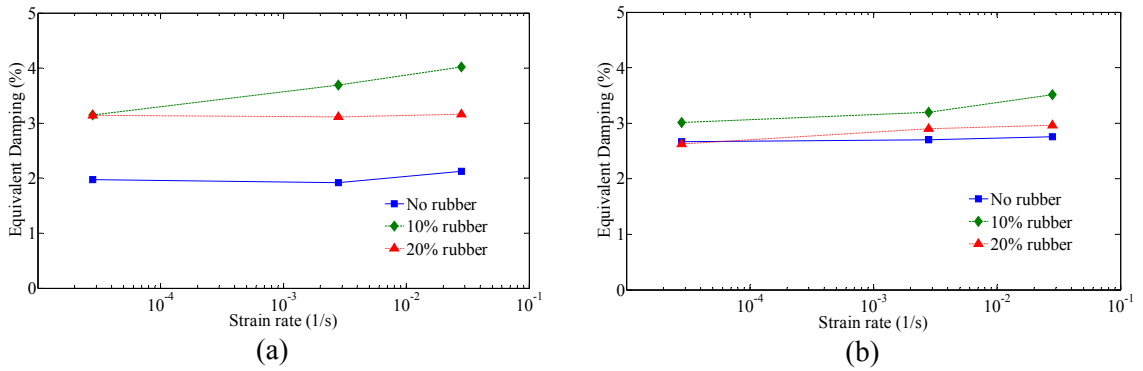

Figure 15. Strain rate effect on equivalent damping for a) one layer, and b) three layers of GFRP

Plastic Dilation of Concrete (α)

The plastic dilation parameter is a representation of the relationship that exists between plastic volumetric and shear strains. It provides information on the contraction and expansion of concrete inside a GFRP tube. It also indicates how the axial strain in the concrete and the hoop strain in the GFRP are related. The plastic volumetric strain is equal to the first invariant of the plastic strain tensor (I_1^p). It can be calculated using eq. 4 and the plastic shear strain is the square root of the second invariant of the plastic strain deviator ($\sqrt{I_{2D}^p}$), calculated by eq. 5. The plastic dilation parameter (α) is the slope of the I_1^p - $\sqrt{I_{2D}^p}$ curve. Thus, α is calculated using eq. 6.

$$I_1^P = \varepsilon_1^P + \varepsilon_2^P + \varepsilon_3^P \tag{4}$$

$$\sqrt{I_{2D}^P} = \sqrt{\frac{1}{6}\left[\left(\varepsilon_1^P - \varepsilon_2^P\right)^2 + \left(\varepsilon_2^P - \varepsilon_3^P\right)^2 + \left(\varepsilon_3^P - \varepsilon_1^P\right)^2\right]} \tag{5}$$

$$\alpha = \frac{dI_1^P}{d\sqrt{I_{2D}^P}} \tag{6}$$

The values of α are plotted versus the axial plastic strain for strain rates of 2.8E-5 and 2.8E-3 (1/s) (Figures 16 and 17). The negative values of α indicate contraction, and the positive values represent dilation. The values of α for a strain rate of 2.8E-2 (1/s) could not be calculated because the strain gages' data acquisition system was not capable of recording data at such high rate. The figure shows that for the confinement of conventional concrete with one layer of GFRP, the concrete displayed limited contraction at the beginning followed by rapid dilation. The dilation rate was then decreased but did not approach asymptote level. The rate of volumetric change decreased for rubberized concrete confined with one layer of GFRP. The existence of the rubber particles acted as

internal springs which reduced the contraction and dilation rates compared to those of corresponding conventional concrete.

The volumetric changes of the GFFT specimens having three layers of FRP were similar to those specimens having single layer of GFRP. Once the dilation parameter reached the peak dilation value, the dilation rate decreased until it approached an asymptote level at $\alpha = 0.3$, followed by GFRP rupture. The contraction values in the specimens confined with one layer of GFRP were smaller than those of specimens confined with three layers of GFRP since the confinement ratios were low in the case of one layer of GFRP. Thus, the GFRP was unable to prevent the concrete from expanding and lateral dilation occurred faster.

The increase in the strain rate changed the dilation behavior of the CFFT specimens confined with one layer of GFRP (Figure 17). However, the initial contraction was unaffected in all of the specimens. The dilation rate changed abruptly in the conventional concrete with no stabilization, which confirms that conventional concrete at high strain rate is acting more like unconfined concrete due to the low confinement ratio. It also explains the stiffness degradation after the first ascending branch for this specimen. The dilation in the rubberized concrete, however, was recovered leading to a softening second branch in the stress strain curve (the elasto-plastic behavior) which indicated higher confinement effects.

A higher initial contraction took place in the CFFT specimens that were confined by three layers of GFRP. This contraction was followed by concrete dilation. The dilation then approached an asymptote level at $\alpha = 0.5$ until failure occurred. The effect of the strain rate on the dilation of CFFT confined with three layers of GFRP was less

pronounced due to the higher confinement ratios. It did, however, increase the initial contraction, particularly for the rubberized concrete. It reduced the dilation rate change up to the stabilization point. It is worth noting that several studies utilize a single value of α for plasticity models; which is the stabilized value (dotted line). However, this is not necessarily true, especially for low confinement ratios like the CFFT specimens confined with one layer of GFRP.

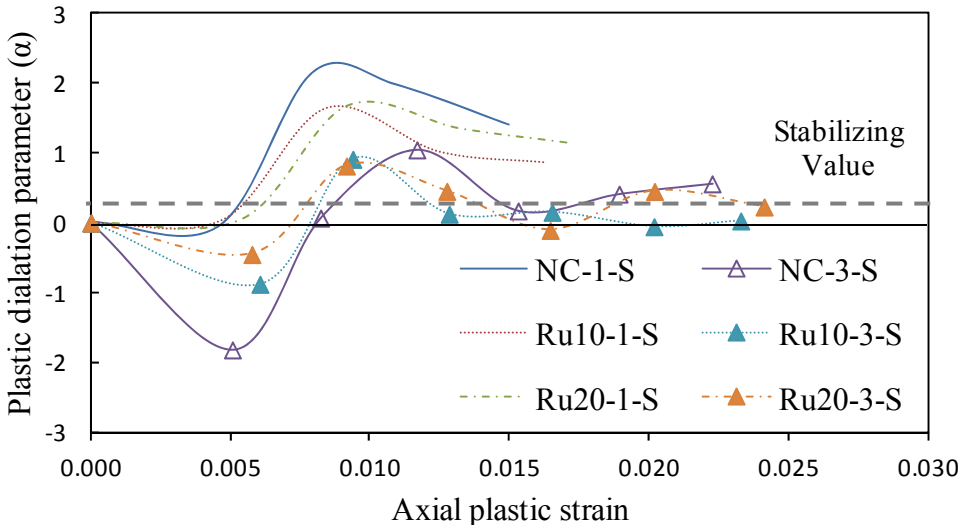

Figure 16. Plastic strain parameter (α) versus axial plastic strain for strain rate of 2.8E-5 (1/s)

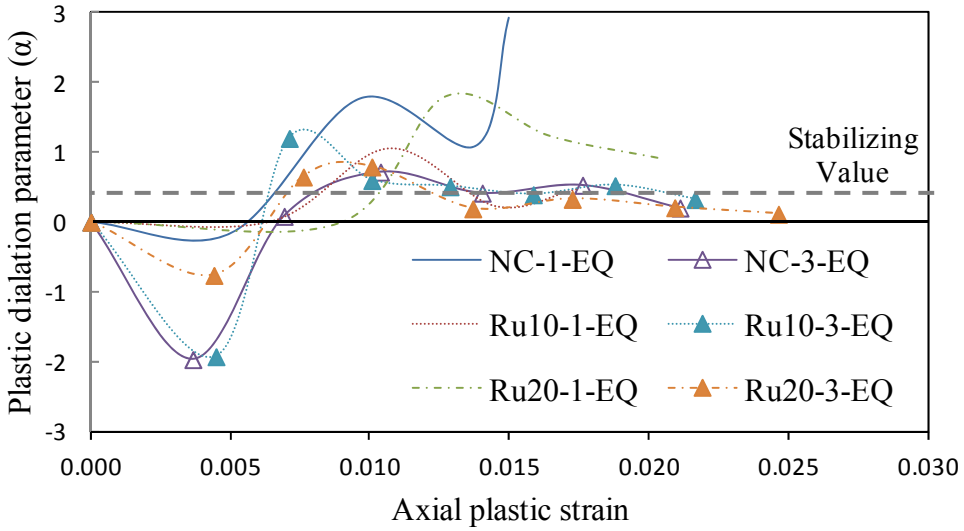

Figure 17. Plastic strain parameter (α) versus axial plastic strain for strain rate of 2.8E-3 (1/s)

Conclusions

Both CFFT and RCFFT specimens were tested under three different strain rates: 2.8E-5, 2.8E-3, and 2.8E-2 (1/sec) to simulate static loading, an earthquake, and a severe earthquake (like a near fault ground motion), respectively. The rubberized concrete's confinement provided a good solution to reducing of the compressive strength loss to 28.5% and 19.8% for 10% rubber replacement for one and three layers, respectively (compared to 32.6% reduction of unconfined concrete). The reductions were 34.1% and 25.1% for one and three layers, respectively, at a 20% rubber replacement (compared to 41.9% for the unconfined concrete). The increase in the strain rate by two and three orders of magnitude resulted in increases in CFFT's compressive strength of up to 20%, increases in ductility of up to 16.7%, and a high increase in the modulus of elasticity of up to 100%. The strain rate increase changed the behavior of the concrete confined with one layer of GFRP and the elasto-plastic behavior was not recognized. It did not, however, change the behavior of concrete confined with three layers. The CFFT's dissipated energy increased up to 27% as the strain rate increased. The addition of rubber increased the RCFFT's dissipated energy up to 60%. The strain rate had a general increasing effect on average equivalent damping. It is worth noting that despite the clear trends of the results provided in this article, more repetitions of the tests are preferred to eliminate the effect of variability of the properties of the used materials. The plastic dilation parameter (α) was also investigated for the different strain rates.

Table 1. Mixture proportions for the conventional and rubberized concrete

Materials (kg/m^3)	Water	Cement	Fly Ash	Coarse aggregate	Super-Plasticizer	VMA*	Sand	R(8-14)	R(14-30)	R(30-)
conventional Concrete	200	280	120	800	1.50	0.48	800	-	-	-
Ru 10	200	280	120	800	2.67	0.96	720	26.17	8.30	1.82
Ru 20	200	280	120	800	3.15	1.04	640	52.37	16.62	3.64

* VMA: viscosity modifying admixture

Table 2. Material characteristics

Material	Specific gravity	fineness	Unit weight (kg/m^3)
Sand	2.61	2.86	1440
Coarse Aggregate	2.69	N.A*	1552
Rubber	1.16	N.A*	640

* N.A = Not available

Table 3. Details of test specimens

Concrete type	Specimens nomenclature	Number of GFRP layers	Loading type
Normal Concrete	NC-1-S	1	Static
	NC-1-EQ		Earthquake
	NC-1-Sh		Severe Earthquake
	NC-3-S	3	Static
	NC-3-EQ		Earthquake
	NC-3-Sh		Severe Earthquake
Ru 10	Ru10-1-S	1	Static
	Ru10-1-EQ		Earthquake
	Ru10-1-Sh		Severe Earthquake
	Ru10-3-S	3	Static
	Ru10-3-EQ		Earthquake
	Ru10-3-Sh		Severe Earthquake
Ru 20	Ru20-1-S	1	Static
	Ru20-1-EQ		Earthquake
	Ru20-1-Sh		Severe Earthquake
	Ru20-3-S	3	Static
	Ru20-3-EQ		Earthquake
	Ru20-3-Sh		Severe Earthquake

Table 4. Ultimate conditions

Specimen nomenclature	$f_c^{'}$ (MPa)	ε_{c0}	$f_l / f_c^{'}$	$f_{cc}^{'}$ (MPa)	ε_{cu}	$f_{cc}^{'} / f_c^{'}$	$\varepsilon_{cu} / \varepsilon_{c0}$
NC-1-S	51	0.0019	0.144	58	0.0144	1.14	7.58
NC-1-EQ				59	0.0163	1.16	8.58
NC-1-Sh				67	0.0170	1.32	8.95
NC-3-S	51	0.0019	0.432	111	0.0255	2.19	13.42
NC-3-EQ				122	0.0292	2.40	15.37
NC-3-Sh				122	0.0321	2.40	16.90
Ru10-1-S	34	0.0024	0.214	46	0.0180	1.33	7.50
Ru10-1-EQ				47	0.0160	1.37	6.67
Ru10-1-Sh				51	0.0130	1.48	6.67
Ru10-3-S	34	0.0024	0.642	89	0.0265	2.60	11.04
Ru10-3-EQ				106	0.0313	3.08	13.04
Ru10-3-Sh				107	0.0285	3.10	11.88
Ru20-1-S	30	0.0026	0.248	38	0.0186	1.28	7.15
Ru20-1-EQ				42	0.0221	1.42	8.50
Ru20-1-Sh				46	0.0232	1.56	8.23
Ru20-3-S	30	0.0026	0.744	83	0.0389	2.82	14.96
Ru20-3-EQ				93	0.0427	3.15	16.42
Ru20-3-Sh				83	0.0312	2.79	12.00

References

ASTM C192 (2013). C 192M-13: Standard practice for making and curing concrete test specimens in the laboratory.

ASTM C469 (2010). C 469M-10: Standard Test Method for Static Modulus of Elasticity and Poisson's Ratio of Concrete in Compression.

ASTM D2290 (2012). "Standard Test Method for Apparent Hoop Tensile Strength of Plastic or Reinforced Plastic Pipe."

Bischoff, P. and Perry, S. (1991). "Compressive behaviour of concrete at high strain rates." Materials and structures 24(6): 425-450.

Bischoff, P. H. and Perry, S. H. (1995). "Impact Behavior of Plain Concrete Loaded in Uniaxial Compression." Journal of Engineering Mechanics 121(6): 685-693.

CEB-FIP, M. (1993). "90 (1993): Design of concrete structures. CEB-FIP-Model-Code 1990." British Standard Institution, London, UK.

Chopra, A. K. (2007). Dynamics Of Structures, 3/E, Pearson Education India.

Dai, J.-G., Bai, Y.-L. and Teng, J. (2011). "Behavior and modeling of concrete confined with FRP composites of large deformability." Journal of Composites for Construction 15(6): 963-973.

Davies, R. and Magee, C. (1975). "The effect of strain-rate upon the tensile deformation of materials." Journal of Engineering Materials and Technology 97(2): 151-155.

ElGawady, M., Booker, A. J. and Dawood, H. M. (2010). "Seismic behavior of posttensioned concrete-filled fiber tubes." Journal of Composites for Construction 14(5): 616-628.

ElGawady, M. A. and Sha'lan, A. (2010). "Seismic behavior of self-centering precast segmental bridge bents." Journal of Bridge Engineering 16(3): 328-339.

Fam, A., Flisak, B. and Rizkalla, S. (2003). "Experimental and analytical modeling of concrete-filled fiber-reinforced polymer tubes subjected to combined bending and axial loads." ACI Structural Journal 100(4).

Georgin, J. and Reynouard, J. (2003). "Modeling of structures subjected to impact: concrete behaviour under high strain rate." Cement and Concrete Composites 25(1): 131-143.

Grote, D., Park, S. and Zhou, M. (2001). "Dynamic behavior of concrete at high strain rates and pressures: I. experimental characterization." International Journal of Impact Engineering 25(9): 869-886.

Kachanov, M. (1987). "Elastic solids with many cracks: a simple method of analysis." International Journal of Solids and Structures 23(1): 23-43.

Khaloo, A. R., Dehestani, M. and Rahmatabadi, P. (2008). "Mechanical properties of concrete containing a high volume of tire–rubber particles." Waste Management 28(12): 2472-2482.

Khatib, Z. K. and Bayomy, F. M. (1999). "Rubberized Portland cement concrete." Journal of materials in civil engineering 11(3): 206-213.

Lam, L., Teng, J., Cheung, C. and Xiao, Y. (2006). "FRP-confined concrete under axial cyclic compression." Cement and Concrete composites 28(10): 949-958.

Lifshitz, J. M. (1976). "Impact strength of angle ply fiber reinforced materials." Journal of Composite Materials 10(1): 92-101.

Malvar, L. J. and Ross, C. A. (1998). "Review of strain rate effects for concrete in tension." ACI Materials Journal 95(6).

Markovich, N., Kochavi, E. and Ben-Dor, G. (2011). "An improved calibration of the concrete damage model." Finite Elements in Analysis and Design 47(11): 1280-1290.

Moustafa, A. and ElGawady, M. A. (2015). "Mechanical properties of high strength concrete with scrap tire rubber." Construction and Building Materials 93: 249-256.

Okoli, O. I. (2001). "The effects of strain rate and failure modes on the failure energy of fibre reinforced composites." Composite Structures 54(2): 299-303.

Ozbakkaloglu, T. and Lim, J. C. (2013). "Axial compressive behavior of FRP-confined concrete: Experimental test database and a new design-oriented model." Composites Part B: Engineering 55: 607-634.

Reda Taha, M. M., El-Dieb, A., Abd El-Wahab, M. and Abdel-Hameed, M. (2008). "Mechanical, fracture, and microstructural investigations of rubber concrete." Journal of materials in civil engineering 20(10): 640-649.

Roland, C. (2006). "Mechanical behavior of rubber at high strain rates." Rubber Chemistry and Technology 79(3): 429-459.

Ross, C. A., Tedesco, J. W. and Kuennen, S. T. (1995). "Effects of strain rate on concrete strength." ACI Materials Journal 92(1).

Rossi, P. and Toutlemonde, F. (1996). "Effect of loading rate on the tensile behaviour of concrete: description of the physical mechanisms." Materials and structures 29(2): 116-118.

Rubber Manufacturers Association (2014). Tire industry facts, Rubber Manufacturers Association.

Siddique, R. and Naik, T. R. (2004). "Properties of concrete containing scrap-tire rubber–an overview." Waste management 24(6): 563-569.

Song, B., Chen, W. and Cheng, M. (2004). "Novel model for uniaxial strain-rate–dependent stress–strain behavior of ethylene–propylene–diene monomer rubber in compression or tension." Journal of applied polymer science 92(3): 1553-1558.

Staab, G. H. and Gilat, A. (1995). "High strain rate response of angle-ply glass/epoxy laminates." Journal of Composite Materials 29(10): 1308-1320.

Tomita, Y., Azuma, K. and Naito, M. (2008). "Computational evaluation of strain-rate-dependent deformation behavior of rubber and carbon-black-filled rubber under monotonic and cyclic straining." International Journal of Mechanical Sciences 50(5): 856-868.

Unified Facilities Criteria (UFC) 3-340-02 (2008). "Structures to resist the effects of accidental explosions." Washington D.C.: U.S. Department of Defense: 50-70.

Vashchenko, A., Spiridonova, I. and Sukhovaya, E. (2000). "Deformation and fracture of structural materials under high-rate strain." Metalurgija 39(2): 89-92.

Xue, J. and Shinozuka, M. (2013). "Rubberized concrete: A green structural material with enhanced energy-dissipation capability." Construction and Building Materials 42: 196-204.

Yon, J.-H., Hawkins, N. M. and Kobayashi, A. S. (1992). "Strain-rate sensitivity of concrete mechanical properties." ACI Materials Journal 89(2).

Youssf, O., ElGawady, M. A., Mills, J. E. and Ma, X. (2014). "An experimental investigation of crumb rubber concrete confined by fibre reinforced polymer tubes." Construction and Building Materials 53(0): 522-532.

Zheng, D. and Li, Q. (2004). "An explanation for rate effect of concrete strength based on fracture toughness including free water viscosity." Engineering Fracture Mechanics 71(16): 2319-2327.

Zheng, D., Li, Q. and Wang, L. (2005). "A microscopic approach to rate effect on compressive strength of concrete." Engineering Fracture Mechanics 72(15): 2316-2327.

Zheng, D., Li, Q. and Wang, L. (2007). "Rate effect of concrete strength under initial static loading." Engineering fracture mechanics 74(15): 2311-2319.

Zheng, L., Sharon Huo, X. and Yuan, Y. (2008). "Experimental investigation on dynamic properties of rubberized concrete." Construction and Building Materials 22(5): 939-947.

Zhu, Z., Ahmad, I. and Mirmiran, A. (2006). "Seismic performance of concrete-filled FRP tube columns for bridge substructure." Journal of bridge engineering 11(3): 359-370.

IV. SEISMIC RESPONSE OF HIGH ENERGY DISSIPATING RUBBERIZED CONCRETE COLUMNS: SHAKING TABLE TESTING

Ayman Moustafa[1], Ahmed Gheni[2], and Mohamed ElGawady[3]

Abstract

This paper presents the first shake-table tests of a large-scale rubberized concrete column with scrap tire replacement of the fine aggregate. It compares the response to that of a conventional bridge column. Both columns had the same details and the only difference is the material used. Both columns were subjected to a sequence of scaled historical ground motion recorded in the Northridge-01 1994 earthquake with near-fault pulse-like characteristics. The conventional column formed a flexural plastic hinge with rebar fracture after 14 scaled test runs. The rubberized column experienced the rebar fracture after 19 test runs. The rubberized column achieved a capacity that is comparable to the conventional column with increased lateral drift. The dissipated energy of the rubberized column increased by 16.5% compared to the conventional column. The damping of the rubberized column also increased up to the rebar fracture.

Keywords: Bridge columns; rubberized concrete; scrap tires; seismic behavior; shaking table test.

[1] Graduate research assistant, Department of Civil, Architectural, and Environmental Engineering, Missouri University of Science and Technology, USA E-mail: ampyf@mst.edu
[2] Graduate research assistant, Department of Civil, Architectural, and Environmental Engineering, Missouri University of Science and Technology, USA E-mail: aagmr6@mst.edu
[3] Benavides Associate professor, Department of Civil, Architectural, and Environmental Engineering, Missouri University of Science and Technology, USA E-mail: elgawadym@mst.edu

Introduction

When reinforced concrete (RC) bridge columns are subjected to moderate to strong earthquakes, severe damage can occur due to energy dissipation mechanism consisting mainly of rebar yielding, rebar slip, concrete cracking, and concrete spalling [Gibson et al. 2002; Phan et al. 2007; Schoettler et al. 2012]. The near-fault ground motions can cause more damage to structures compared to the far-field ground motions due to their impulsive nature releasing a large amount of energy in a short period of time. However, most of current design standard were developed based on the characteristics of the far-field ground motions which differ from those of the more damaging near-fault ground motions. The near-fault ground motions have impulsive nature due to the forward directivity effect [Hall et al. 1995; Sasani and Bertero 2000; Zhang and Iwan 2002; Bray and Rodriguez-Marek 2004; Baker et al. 2011; Sehhati et al. 2011]. This impulsive nature imposes a large amount of energy into the nearby structures such as bridges. Hence, increasing the energy dissipation of bridge columns is desirable

The addition of rubber to concrete, producing what is called rubberized concrete, can change its mechanical properties as well as can increase concrete ductility, impact resistance, and potentially damping values compared to conventional concrete [Eldin and Senouci 1993; Toutanji 1996; Khatib and Bayomy 1999; Segre and Joekes 2000; Hernandez-Olivares et al. 2002; Güneyisi et al. 2004; Khaloo et al. 2008; Zheng et al. 2008; Bowland 2011; Al-Tayeb et al. 2013; Youssf et al. 2014; Moustafa and ElGawady 2015; Moustafa and ElGawady 2016]. Past research concluded that replacing up to 5% of mineral fine aggregates with rubber has insignificant effects on concrete strength and

workability. However, increasing the rubber content beyond this percentage reduces the compressive strength and workability of fresh concrete.

Results of energy dissipation of rubberized concrete material showed a significant scatter and contradiction. Replacing 3.5% to 30% of mineral aggregates with scrap rubber increased the energy dissipation and viscous damping by 23% to 30% [Zheng et al. 2008]. Beyond 30% replacement, the energy dissipation decreased. Moustafa and ElGawady 2015 measured rubberized concrete energy dissipation using different approach and reported an increase in energy dissipation, hysteresis damping, and viscous damping compared to conventional concrete. The increase ratio varies with the variation in the measuring approach. Xue and Shinozuka 2013 performed shaking table testing on two small-scale columns having dimensions of 40 mm x 40 mm x 500 mm with one rebar in the center. One column was constructed with conventional concrete and the other with rubberized concrete with 15% replacement of fine aggregates. However, the shaking table test results were not used to determine the damping of the columns, but rather free vibration testing of the columns using impact hammer were used to determine the damping ratio. Using the impact free vibration results, they reported an increase of damping ratio of 62% for the rubberized concrete compared to the conventional concrete. The shaking table tests were used to report a decrease in the peak seismic response acceleration by 27% for the rubberized column compared to the conventional column. Other researchers reported no increase in energy due to rubber replacement (Resende et al. 2003). Bowland 2011 tested two full-scale footbridges; one with conventional concrete and the other with 15% replacement of fine aggregate with ground rubber. No

significant change in damping between the two footbridges was reported. This may be attributed to the very low imposed excitations of only 0.05g.

Limited large scale testing of rubberized concrete columns has been carried out under pseudo static loading [Youssf et al. 2015; Youssf et al. 2016]. Youssf et al. 2015 investigated the behavior of a rubberized concrete column with 20% rubber replacement of fine aggregate under reversed cyclic loading. The energy dissipation and hysteresis damping were determined from the cyclic loading and the damping ratio was determined from snap-back tests. The rubberized column had an increase of 13% in hysteretic damping while the viscous damping was decreased by 49% compared to the conventional column. Youssf et al. 2016 investigated rubberized concrete columns confined with fiber reinforced polymers (FRP). The overall behavior of the FRP confined rubberized column was very similar to that of the FRP confined conventional concrete. The rubberized concrete had an insignificant effect on the energy dissipation and damping.

While these results provide an insight about the use of rubberized concrete as a structural component, the pseudo static nature of loading can be misleading with regard to the dynamic behavior of rubberized concrete columns. In this article, the dynamic behavior of rubberized concrete bridge columns is investigated under simulated ground motions to investigate the dynamic behavior of these columns.

Research Significance

Significant amount of research showed the superior ductility, damping, and energy dissipation of rubberized concrete compared to the corresponding conventional concrete were carried out under pseudo static loads [Siddique and Naik 2004; Khaloo et al. 2008; Youssf et al. 2015; Youssf et al. 2016]. However, rubberized concrete niche would be

structural dynamic applications, such as earthquakes. The dynamic effects on rubberized concrete in previous research have all been carried out on the material level using small scale specimens [Hernandez-Olivares et al. 2002; Zheng et al. 2008; Bowland 2011; Moustafa and ElGawady 2015; Moustafa and ElGawady 2016]. Shake table testing of small specimens by Xue and Shinozuka 2013 is still considered to regard material application.

Large divergences of the dynamic results on rubberized concrete from high increase in energy dissipation and damping to no effect at all, along with the need for an actual dynamic testing on rubberized concrete as a structural component motivated the current study. This article presents the first shaking table test of a large scale reinforced rubberized concrete column with scrap tire rubber as a substitution for fine aggregate. The behavior was compared to that of a conventional concrete column with the same details.

Experimental Program

Overview of the Test Specimens

Two ¼-scale cantilever columns having the same structural configuration were constructed. One column was constructed using conventional concrete and the other one using rubberized concrete. The columns' elevation and cross section along with the test setup are illustrated in Figure 1. Each column had a diameter of 300 mm. The columns' height measured from the top of the footing to the center of the mass was 1900 mm, resulting in an aspect ratio of approximately 6.33. The aspect ratio is defined as the height of the column divided by its diameter.

Each column had eight longitudinal #4 rebar (12.5 mm diameter) corresponding to a longitudinal reinforcement ratio of 1.4% and spiral reinforcement of #3 rebar (9 mm diameter) with a pitch of 75 mm for corresponding to transverse volumetric reinforcement ratio of 1.3%. The spiral reinforcement was extended in the entire depth of the footing and the column head.

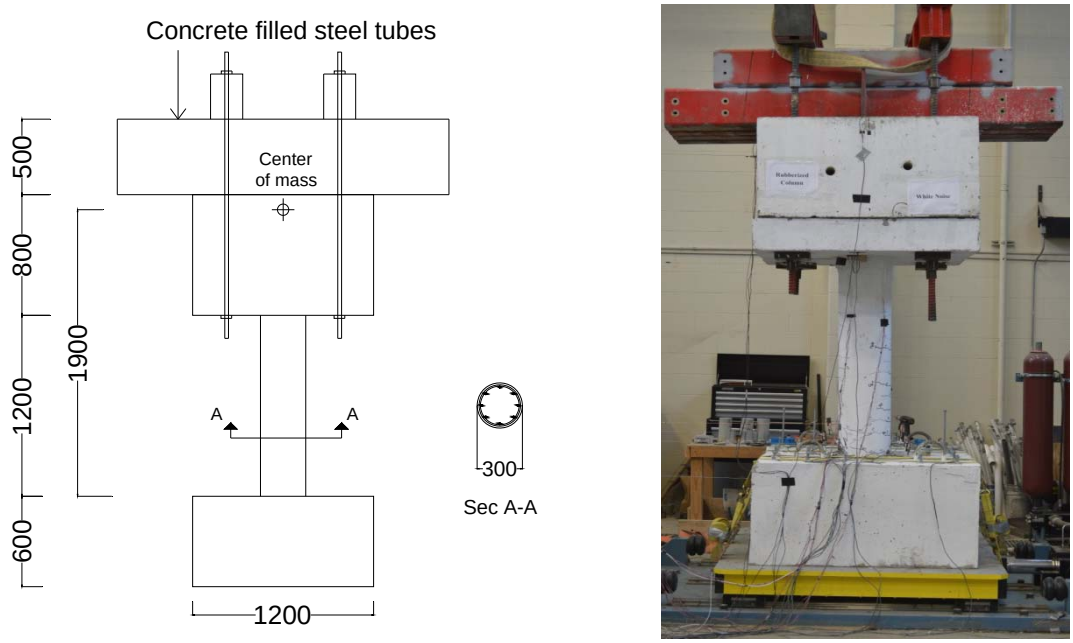

Figure 1. Configuration and dimensions of the columns (unit: mm)

Material Characteristics

The compositions of the concrete materials used in this study are listed in Table 1.The conventional concrete used for the RC column was a ready mix concrete with a compressive strength of 35 MPa at the day of testing. The rubberized concrete was designed by volumetric replacement of 20% of the fine aggregate with crumb rubber. The rubber replacement ratio was selected to result in a good combination of fresh and

hardened concrete properties (Moustafa and ElGawady 2015; Moustafa and ElGawady 2016).

Type I Portland cement that conformed to ASTM C150 specifications, limestone washed coarse aggregate with nominal maximum size of 19 mm, and Missouri river sand were used in each of the mixtures. The rubber used was crumb rubber with three different sizes denoted as R (8-14), R (14-30), and R (30-). The first number represents the sieve number of the passing particles and the second number represents the sieve number of the retained particles. The compressive strength of the rubberized concrete at the day of testing was 27 MPa.

The mixing procedure of the rubberized concrete was started by dry mixing the coarse aggregate, sand, and rubber for about 1 minute to ensure distribution of the aggregates and then the cement and fly ash were added and the concrete was dry mixed for another minute. The superplasticizer was added to the water and the water was then added to the mixture and the concrete was mixed for 2 minutes and then let stand for 1 minute; then, mixed for another two to three minutes until consistency was observed.

Table 1. Mixture proportions for the conventional and rubberized concrete

Materials (kg/m^3)	Water	Cement	Fly Ash	Coarse aggregate	Super-Plasticizer	VMA *	Sand	R(8-14)	R(14-30)	R(30-)
Conventional Concrete	200	280	120	800	1.50	0.48	800	-	-	-
Rubberized Concrete	200	280	120	800	3.15	1.04	640	52.37	16.62	3.64

* VMA: viscosity modifying admixture

Test Setup and Loading Sequence

The columns were fixed to a uni-axial shaking table using 36 all-threaded bars, each with a capacity of 45 kN. The shaking table is running using a closed loop controller that can

use either displacement or acceleration control. Six accelerometers were used to measure the horizontal accelerations on the shaking table, the center of the column head, and the center of mass. Eight string potentiometers were used to measure the horizontal displacements along the heights of the columns. Eight linear potentiometers were mounted on the column to measure the curvature along the bottom 187.5 mm (7.5 inches) of the column and one linear potentiometer to measure horizontal sliding between the column and the foundation. Seven strain gages were mounted on each of the north and south rebar; four of them along the bottom 225 mm above the footing and three at 100 mm into the footing to measure the potential strain penetration depth into the foundation. The mass atop the column was provided by a 1200 mm x 1200 mm x 800 mm column reinforced concrete stub and eight concrete filled steel tubes (CFTs) each having a cross section of 600 mm x 500 mm. Four of these CFTs each had a length of 2200 mm and the other four each had a length of 1925 mm. The tubes were post-tensioned to the column head with a total weight of 54 kN.

Each column was subjected to a sequence of a scaled Northridge-01 1994 earthquake at “Rinaldi Receiving Station” which is a near-fault pulse-like ground motion. The selected ground motion was scaled to the design spectrum (DE) shown in Figure 2 by matching the spectral acceleration at the column’s first mode (Sa(T1)) to the design response spectrum. Hereinafter, the DE will refer to the design spectrum used in the current study. The columns were assumed to be in a high seismic zone in San Francisco, California; where the prototype column is assumed. The input ground motion and the design response spectrum with a probability of excess of 10% in 50 years are illustrated in Figure 2.

The time coordinate of the input accelerations was compressed by a factor of $\sqrt{0.25} = 0.5$ for similitude according to the scale factor of 4. The columns were subjected to a sequence of the scaled ground motion starting at 10% of the DE to 200% of the DE with steps of 10% increments giving a total of 20 ground motions. A white noise test with duration of 75 s and 0.02g amplitude of acceleration was run after each ground motion excitation to determine the updated fundamental period of the column.

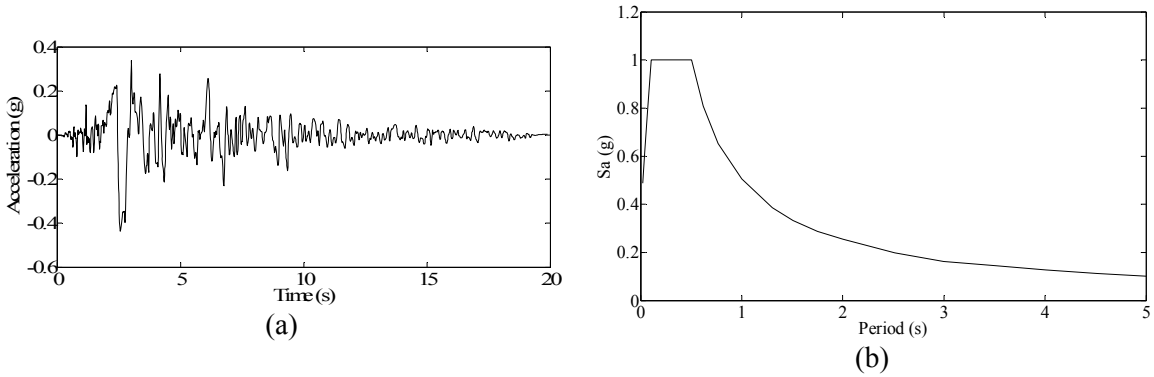

(a) (b)

Figure 2. a) Input ground motion and b) design earthquake spectrum

Experimental Results and Discussion

General Behavior

The RC column displayed the anticipated performance of well-designed columns. Visible cracks occurred at a drift of 1% during subjecting the column to 50% of the DE. Rebar yielding, as measured by the strain gages, was also initiated at that point. As the intensity of the earthquake was increased, existing cracks widen more and connect together to form larger cracks. Minor spalling started at a drift of 2.1% corresponding to 90% of the DE. The southern rebar was fractured at 140% of the DE and it was accompanied by a popping sound. Beyond that, the column displayed apparent residual drifts but the tests

proceeded until 200% of the DE and the test was terminated for safety purposes. The RC column suffered severe damages consisting of rebar fracture, buckling of rebar, concrete spalling, and large residual drifts. Images for the test specimens at the end of the test are shown in Figure 3.

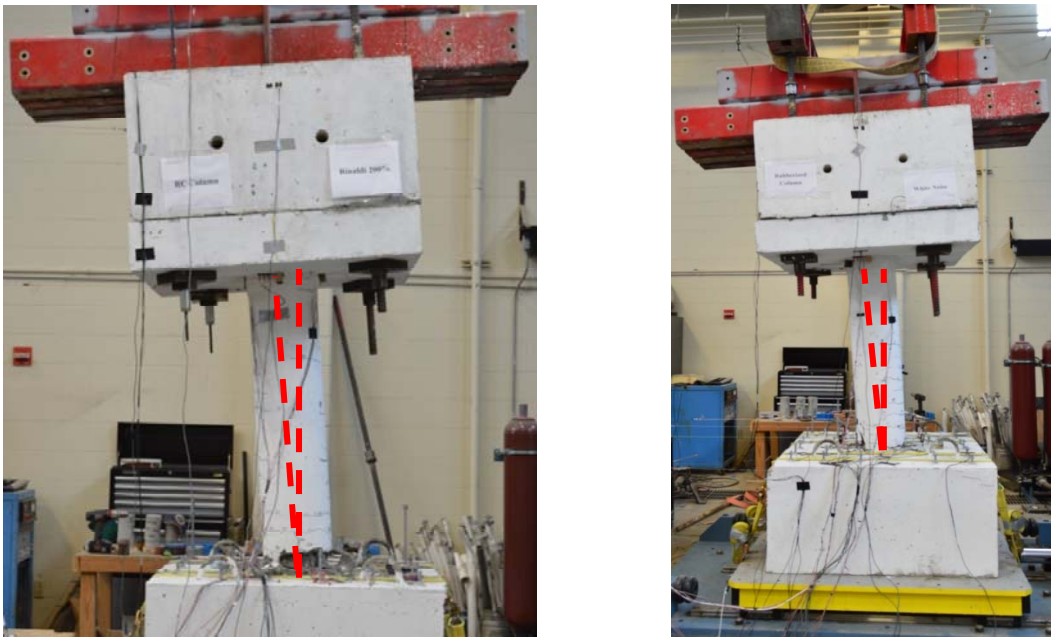

(a) (b)

Figure 3. Test specimens at the test end: a) RC column and b) rubberized column

The rubberized column's behavior generally outperformed that of the RC column. Visible cracks initiated at a drift of 1.8% corresponding to 70% of the DE and the spalling started at a drift of 2.9% corresponding to 110% of the DE. The major differences in the rubberized column were the delaying of the rebar yielding to a drift of 1.8% compared to 1% for the RC column and rebar fracture to be caused at 190% of the DE instead of 140% for the RC column. The delay of rebar fracture can be attributed to the higher energy dissipation of the rubberized concrete, resulting in lower demand on the rebar. The test was stopped at 200% of the DE. The rubberized concrete at the end of the

20 runs suffered damage similar to that of the RC column. It should be noted that the spalling of the rubberized concrete was less than the conventional concrete and the rubberized concrete remained intact. By the end of the test, the authors manually removed concrete chunks to examine rebar failure. The test specimens' crack patterns and plastic hinge extension along with the rebar fracture are illustrated in Figure 4.

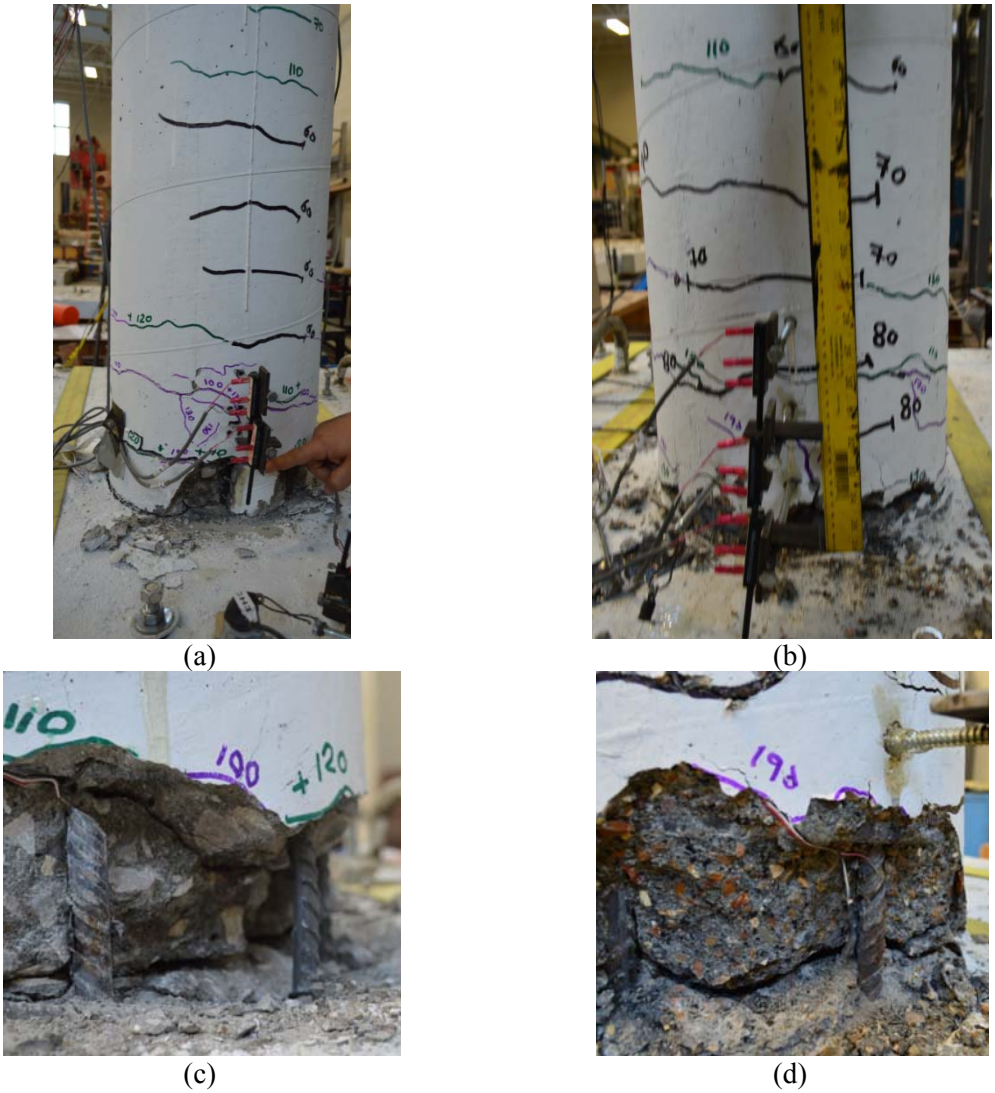

Figure 4. Damage in the test specimens at the test end: (a) RC crack pattern, (b) rubberized column crack pattern, c) RC rebar fracture, and d) rubberized column rebar fracture

Time Histories and Hysteretic Behavior

Samples of the lateral drifts and response accelerations for the test specimens are illustrated in Figures 5 and 6, respectively, at the DE and after rebar fracture in the RC column. The lateral displacements were obtained by subtracting the table displacement from the displacement at the center of mass; both recorded by the string pots. The drift was then obtained by dividing the lateral displacement by the height of the column from the top of the footing to the center of mass. Both the drift and acceleration responses are similar for the two columns at the DE. The rubberized column managed to achieve the same capacity and drift demand at the DE. However, after the rebar fracture in the RC column and at 150% of the DE, the response of the two columns became different. The RC column had a very large residual drift compared to the rubberized column. The rubberized column had the same maximum response acceleration and the RC column had a reduction of 15% in the response acceleration.

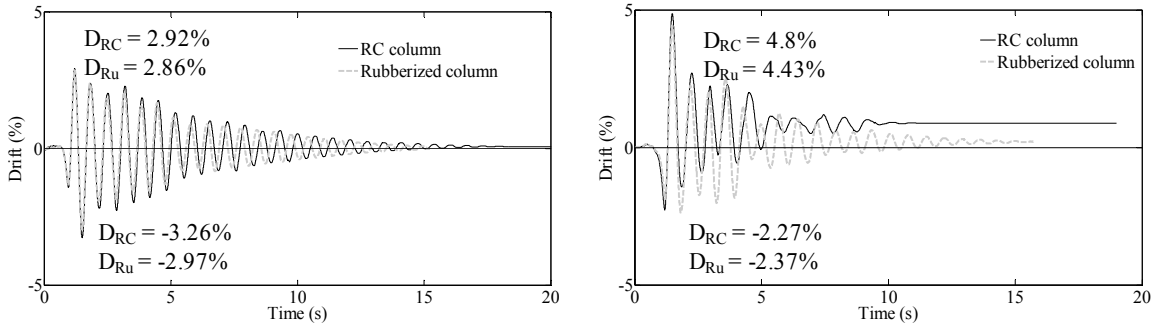

Figure 5. Drift time histories for the two specimens at: a) DE, and b) RC column rebar fracture

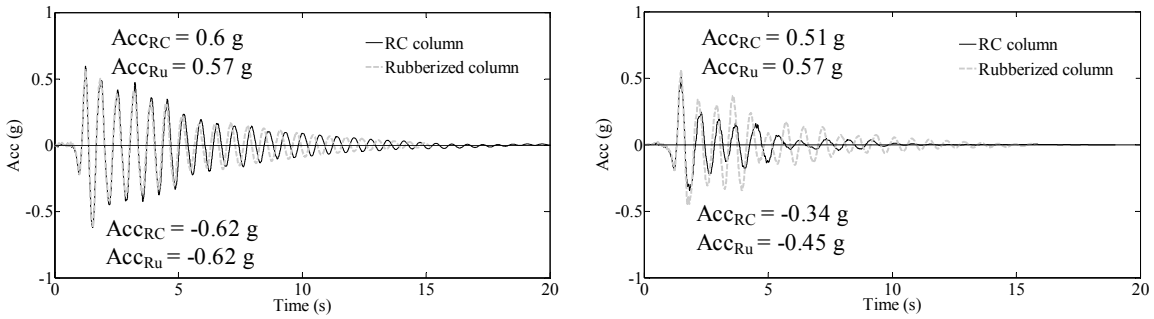

(a) (b)

Figure 6. Response acceleration time histories for the two specimens at: a) DE, and b) RC column rebar fracture

Samples of the lateral force versus lateral drifts for the RC and rubberized columns are illustrated in Figures 7 and 8, respectively, for different intensities of the simulated earthquakes as percentages of the DE. The lateral force was obtained by multiplying the mass on top of the column times the acceleration at the center of mass. The response of both columns was nearly symmetric at the elastic region which ended at 50% and 70% of the DE for the RC and rubberized columns, respectively. Beyond that the hysteretic became asymmetric due to bar yielding. This occurred since the input ground motion is asymmetric and has an impulsive nature. The RC column experienced higher residual drift at 150% of the DE compared to that of the rubberized concrete column due to the rebar fracture. The impulsive nature of the input motion was more dominant at 200% of the DE causing failure and the test was stopped.

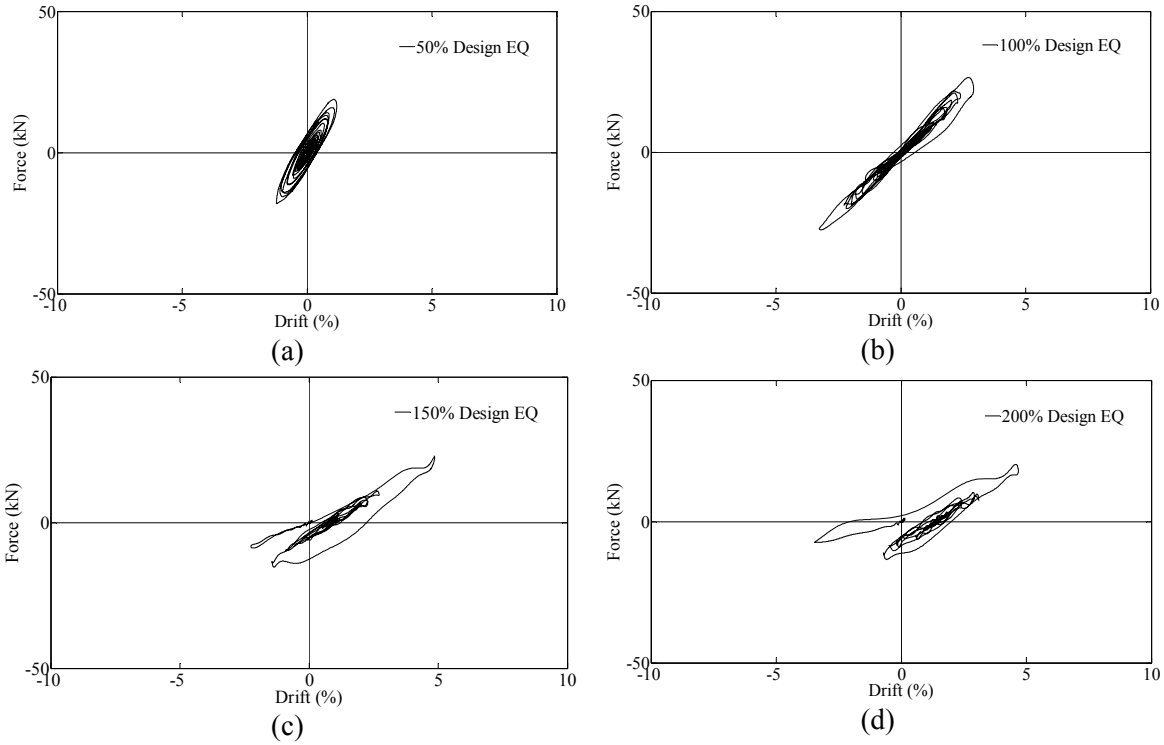

Figure 7. Measured forces versus drift ratios for the RC column at different stages of the test at: a) rebar yielding, b) DE, c) rebar fracture, and d) test end

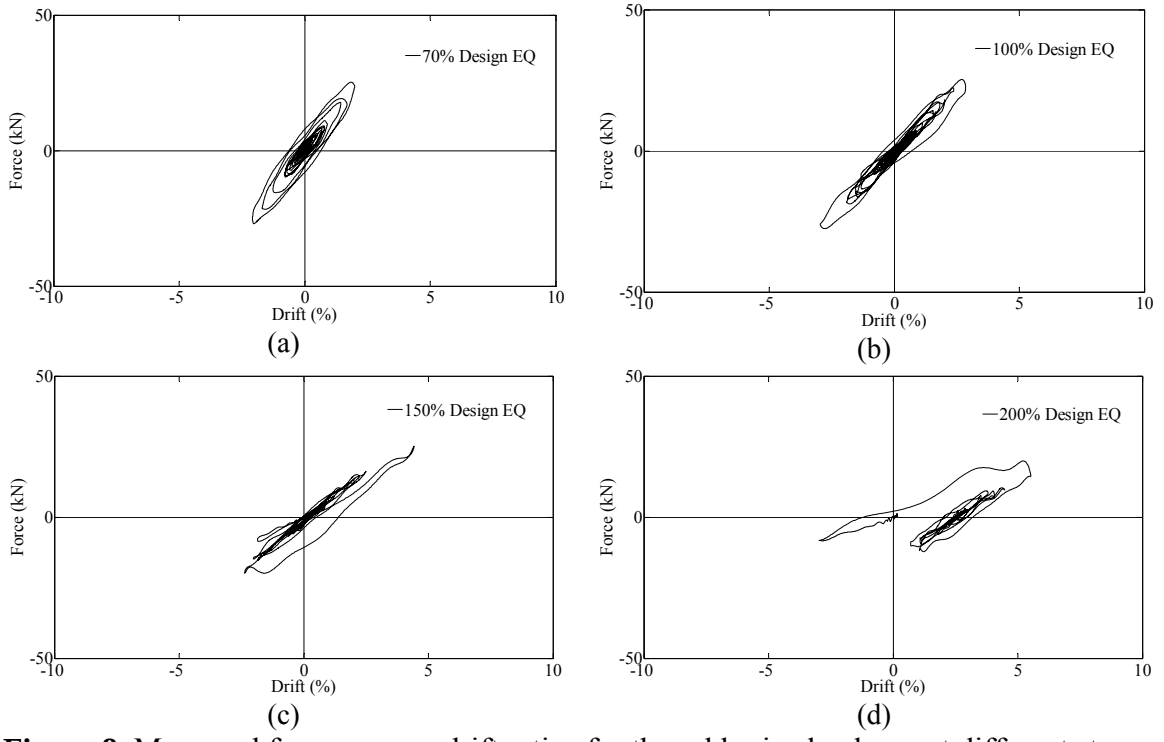

Figure 8. Measured forces versus drift ratios for the rubberized column at different stages of the test at: a) rebar yielding, b) DE, c) RC rebar fracture stage, and d) test end

The envelopes of the lateral force versus lateral drift, known as dynamic push over curve, for both columns are illustrated in Figure 9 for comparison. Each point on the curve represents the maximum force and the corresponding drift for one of the tests from the sequence of 10% to 200% of the DE. The capacity of the RC column and rubberized column were 27.5 kN and 26.6 kN, respectively representing a reduction in the strength of the rubberized concrete of only 3%. This can be attributed to the high confinement ratio in both columns negating the effect of rubberized concrete reduced compressive strength. This observation was also found in previous studies [Youssf et al. 2014; Moustafa and ElGawady 2016]. The loss in the RC column's capacity started at 3.4% drift and the column strength reduced by 20.6% of its capacity at 4.8% drift. This was attributed to rebar fracture which occurred at 4.25% drift during 140% of the DE. The rubberized column, on the other hand, was able to sustain the imposed ground motions up to 5.4% drift due to the delayed rebar fracture caused by the higher energy dissipation. The initial stiffness of the rubberized column, however, was 9.6% lower than that of the RC column due to the inherent reduced stiffness of the rubberized concrete caused by the lower stiffness of the rubber particles compared to the aggregate. The overall performance of the rubberized column was therefore more preferable compared to the RC column.

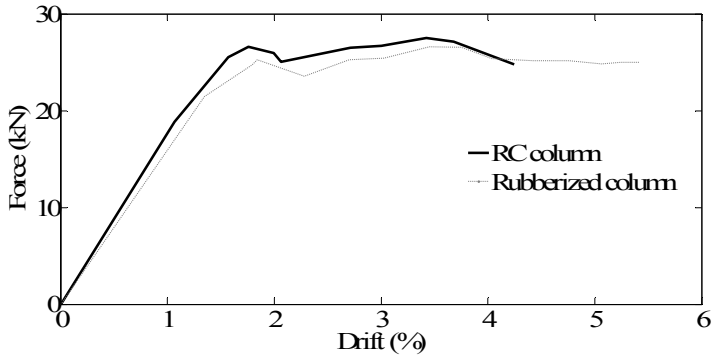

Figure 9. Envelopes of forces versus drift ratios

Peak and Residual Drift Ratios

The absolute residual drifts and residual drifts normalized after each test run for both columns are illustrated in Figure 10. The RC column started to experience residual drifts at earlier stages than the rubberized concrete. This was due to the earlier rebar fracture accompanied with heavy spalling of concrete. The rubberized column experienced residual drifts due to yielding of the rebar. The values of the residual drifts of the rubberized column increased with yielding but were less than their counterpart RC column drifts until rebar fracture of the rubberized column at 190% of the DE. At that stage, the residual drift of the rubberized column was higher than the RC column, probably due to the increased P-Δ effect due to the larger drift of the rubberized column.

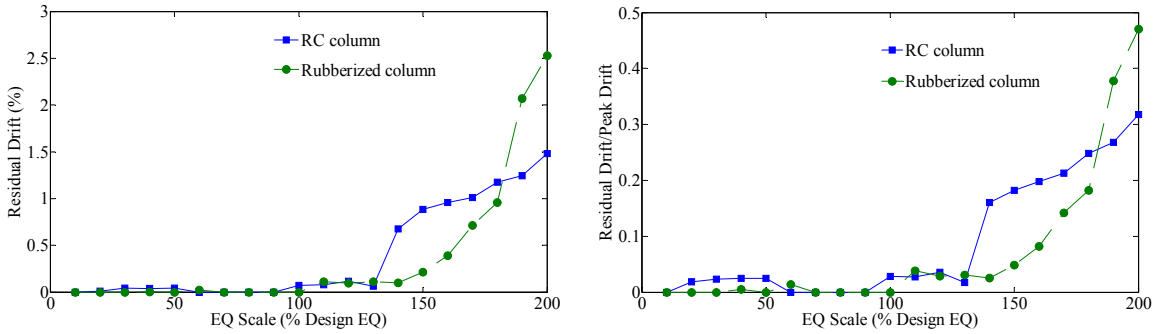

(a) (b)

Figure 10. Residual drifts at different stages: (a) absolute residual drift and (b) normalized residual drift

Fundamental Periods of the Columns

The fundamental period of a structure is one of the important dynamic properties as it affects the response of the structure to ground excitation. The fundamental periods for the two test specimens were calculated from the acceleration response of the specimens to the white noise excitation with the amplitude of 0.02 g that was applied before each test.

The fundamental periods for the two specimens are illustrated in Figure 11. At the beginning of the test at 10% of the DE, the fundamental period of the rubberized column was 7% higher than that of the RC column due to the lower stiffness of the rubberized column. As the tests progressed, the fundamental periods of both columns increased due to the reduction of columns' stiffness caused by damage. The period of the RC column at any stage was higher than its corresponding value for the rubberized column, which indicates more damage occurred in the conventional concrete, while the rubberized concrete was more intact. At 190% of the DE, the fundamental period of the RC column was 10% higher than that of the rubberized column.

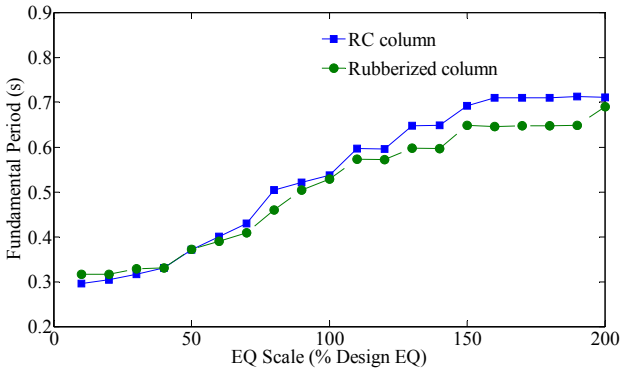

Figure 11. Fundamental periods of the specimens at different stages

Dissipated Energy and Hysteresis Damping

The hysteresis is the property of systems to follow different loading and unloading paths. The hysteresis damping for the cyclic testing is calculated from the specific damping capacity (Y), which is the ratio between the energy dissipated per unit volume of the material, E_D, and the strain energy per unit volume stored in a linear elastic system, E_{S0}, as shown in eq. 1.

$$Y = \frac{E_D}{E_{S0}} \tag{1}$$

A graphical representation of ED and ES0 is shown in Figure 12 [Chopra 2007].

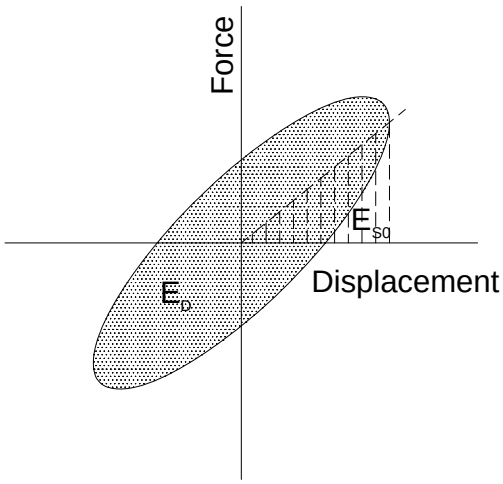

Figure 12. Dissipated energy per unit volume of the material, E_D and elastic strain energy, E_{S0}

The energy dissipated per cycle per unit volume, E_D, is measured as the area enclosed by a hysteresis loop drawn on axes of stress and strain. It can be calculated mathematically using eq. 2.

$$E_D = \sum_{i=1}^{n-1} \left(\frac{F_{i+1} + F_i}{2} \right) \left(\Delta_{i+1} - \Delta_i \right) \tag{2}$$

where, E_D is the dissipated energy (Joules), n is the total number of stress or strain points, F_i is the force at point i (N), and Δ_i is the displacement at point i (m).

The hysteresis damping can be expressed as the equivalent viscous damping and is calculated from the specific damping capacity using eq. 3.

$$\zeta_{eq} = \frac{E_D}{4\pi E_{S0}} \tag{3}$$

The cumulative dissipated energy for the two specimens is illustrated in Figure 13. The energy dissipated by the rubberized column at any stage was higher than its counterpart of the RC column. This can be attributed to the visco-elastic nature of the rubber particles allowing the rubberized concrete to absorb more energy than the conventional concrete. The cumulative dissipated energy was increased by 16.5% in the rubberized column compared to the RC column.

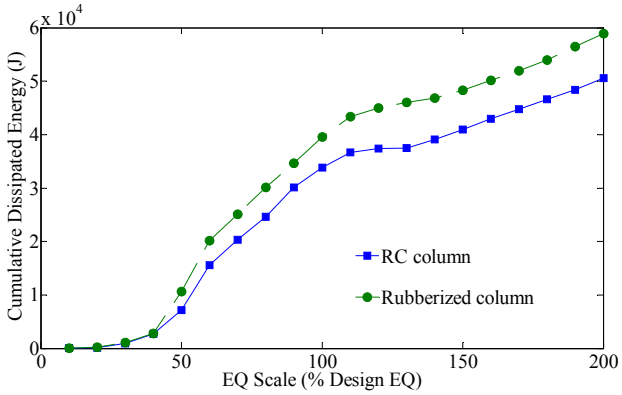

Figure 13. Cumulative dissipated energy for the test specimens at different stages

The hysteresis damping for the two columns (as calculated by Eq. 3) is illustrated in Figure 14. The rubberized column showed a higher average damping before the rupture of the rebar in the RC column. This occurred because the rubberized concrete developed more micro-cracks due to the stiffness mismatching between the rubber particles and the cement paste. These micro-cracks provided more damping for the rubberized column without affecting the integrity of the column (unlike the macro-cracks that develop from damage). After rebar yielding of the RC column, an extensive spalling occurred and higher damage accumulated resulting in the expected increase in the

damping with damage, while the rubberized column kept its integrity up to 190% of the DE; where rebar fractured and higher damage occurred leading to a large increase in damping.

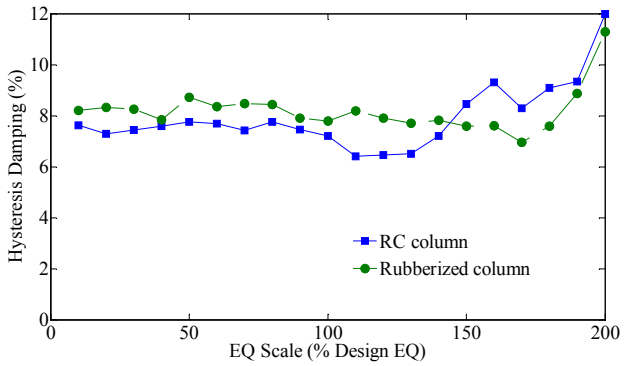

Figure 14. Hysteresis damping for the test specimens at different stages

Damping Ratio

The viscous damping ratio can be calculated using the logarithmic decrement method by Yan et al. 2000 for the measured accelerations. The value of the damping ratio can be calculated using Eq. 4.

$$\zeta = \frac{1}{2n\pi} \ln\left(\frac{A_0}{A_n}\right) \tag{4}$$

where, A_0 is the initial amplitude and A_n is the amplitude after n cycles.

A sample damping curve for each of the specimens is illustrated in Figure 15 for the measured signals. The change in the viscous damping is illustrated in Figure 16. The figure shows an increasing trend of the damping ratio with the increase in the ground motion amplitude. This increase was due to the increase of the driving force along with the damage. The viscous damping of the rubberized column was higher than that of the RC column due to the visco-elastic nature of the rubber. The rebar fracture in the RC

column at 140% of the DE caused the damping to increase significantly due to the reduction in column stiffness and the increased damage. After that, the damping ratio started to decrease due to the reduction of the driving force, which agrees with the force-drift curve shape. The rubberized column did not experience such behavior until 190% of the DE because the concrete spalling was much less and the rebar fracture was delayed leading to the increase in the viscous damping.

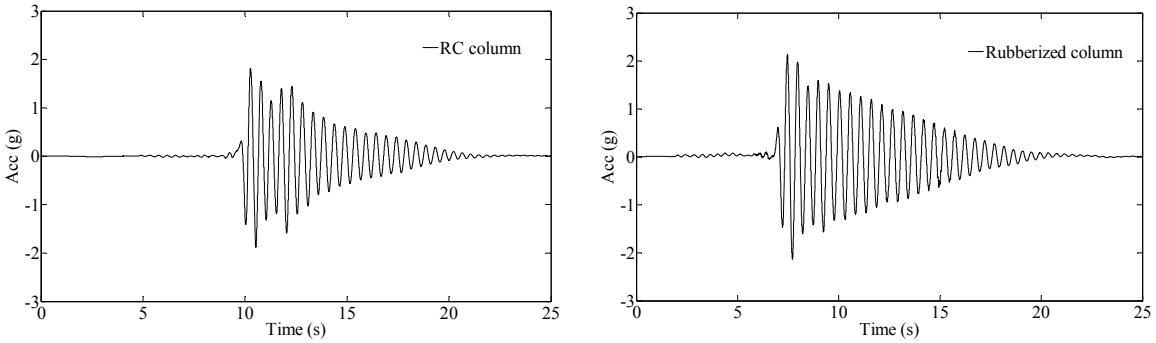

(a) (b)

Figure 15. Sample acceleration curve in time domain for a) RC column, and b) rubberized column

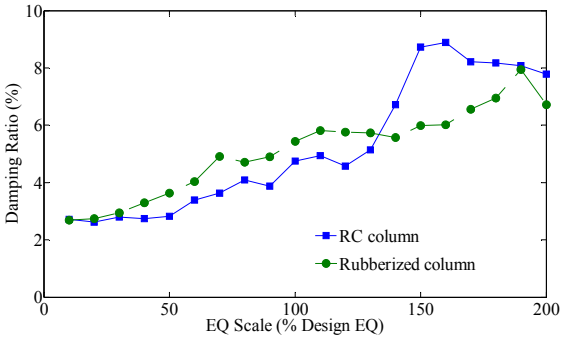

Figure 16. Damping ratio for the test specimens at different stages

Reinforcement Strains

The maximum reinforcement strains at each test for both columns are illustrated in Figure 17. The maximum strains distributions along the column height are illustrated in Figure

18. The RC column experienced yielding at a drift of 1% corresponding to 50% of the DE compared to 1.8% drift corresponding to 70% of the DE for the rubberized column. This could explain the delay of visible macro cracks in the rubberized column, as explained earlier. The RC column experienced a large strain increase at 130% of the DE followed by a larger increase in strain of almost 80,000 microstrain that led to the rupture of the rebar at 140% of the DE. The rupture of the rebar was already observed by the popping sound that accompanied it, as explained earlier. The rubberized column, on the other hand, experienced a smooth increase of strain up to the rupture of the rebar at 190% of the DE. This can be attributed to the higher ductility and greater energy dissipation of the rubberized concrete that delayed the concrete cover spalling and minimized the macro cracks compare to the conventional concrete, leading to the concrete being intact for a longer time during the tests. The delay of cracks and spalling of rubberized concrete was visually confirmed, as explained earlier. This smooth transition and delay of cracks was also observed by Youssf et al. 2015 during the static cyclic loading of rubberized columns. The effect is more obvious in the shaking table tests presented here due to the dynamic nature of loading.

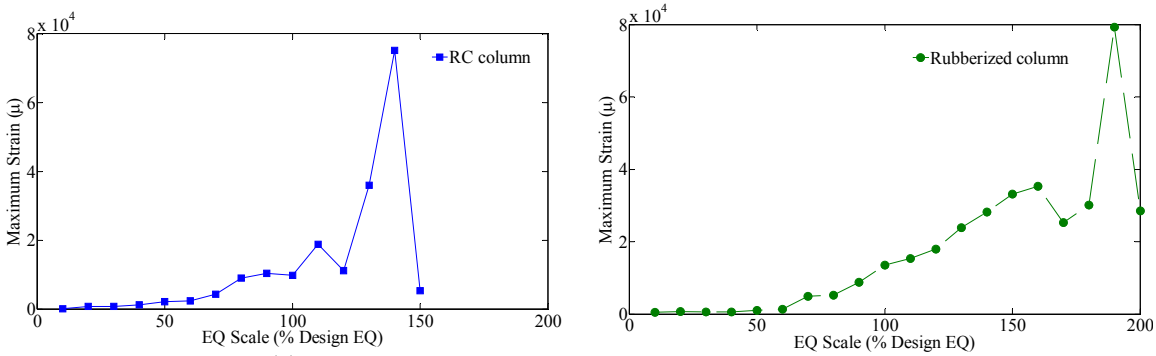

Figure 17. Maximum strains at different stages for a) RC column, and b) rubberized column

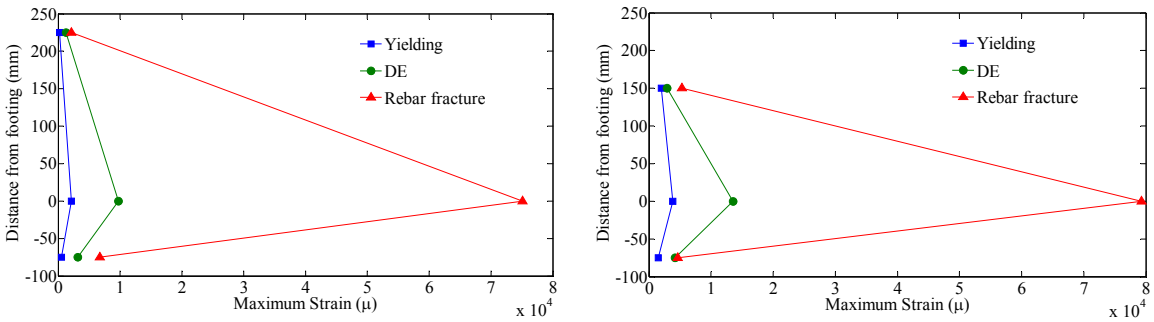

Figure 18. Maximum strains distribution along columns height at different stages for a) RC column, and b) rubberized column

Cross-Section Curvature of the Columns and Columns' Profiles

Six linear potentiometers (three on each side) were distributed up to a distance of 187.5 mm (7.5 inches) above the column foundation in order to measure the vertical displacements. The data from each pair of linear potentiometers was used to calculate the average curvature at that section using Eq. 5.

$$\Phi = \frac{\varepsilon_1 - \varepsilon_2}{S} \tag{5}$$

where, ε_1 is the average strain calculated from the linear potentiometer measurement on one side, ε_2 is the average strain calculated from the linear potentiometer measurement on the opposite side along the same plane, and S is the horizontal distance between the two potentiometers. The moment-curvature relationship for both columns is illustrated in Figure 19. The values shown in the figure are the maximum moment and maximum curvature during each test run. The distance in the legend refers to the distance of measurement above the foundation level. Most of the columns' curvatures occurred in the lower column segments at the plastic hinge, where most of the damage occurred. It

should be noted here that the ultimate curvature of the two columns cannot be compared because the concrete spalling in the RC column was too extensive that the linear potentiometers fixation became loose and had to be removed. This is indicated by the dotted line in Figure 19(a) to avoid misleading interpretation. The figure shows moment drop of 20.6% of the ultimate moment at a curvature of 0.0003 rad/mm for the RC column, while the rubberized column did not experience such drop and the curvature was accommodated by the viscoelasticity of the rubber and increased ductility. The drop in moment in the rubberized column happened at the last two test runs, where the linear potentiometers were removed to prevent their damage. The rate of curvature increase for the rubberized column was higher than that of the RC column. This can be attributed to the ability of rubberized concrete to delay and reduce the macro cracks along with the viscoelasticity of the rubber.

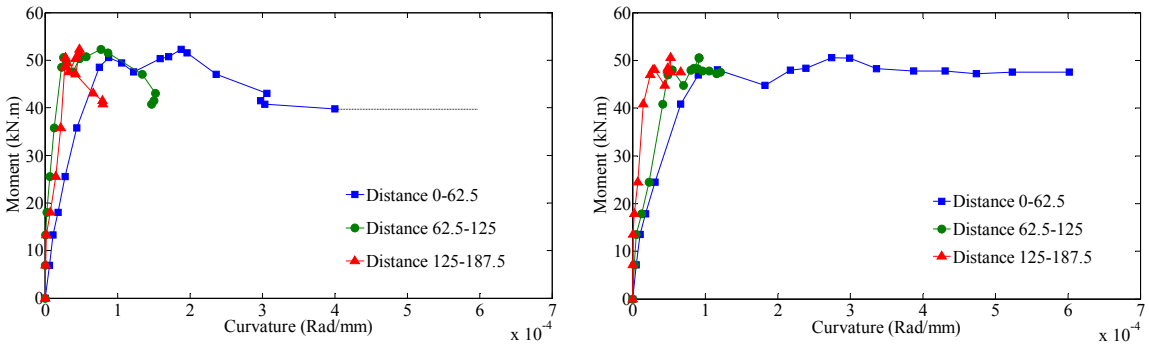

Figure 19. Moment versus curvature for a) RC column, and b) rubberized column

The distribution of the columns curvatures are illustrated at Figure 20 at different stages of the test. The curvature of each column increased with the increase of the ground motion intensity. In addition, the curvature decreases with the increase of height with most of the curvature concentrated at the bottommost portion of the columns. The higher the excitation, the larger the difference between the average curvatures at the first height

of measurement compared to the second one. The exception for the RC column at 150% of the DE, where the curvature at the second potentiometers plane were almost half of the first one, resulted from the rebar fracture at 140% of the DE. The curvature of the rubberized column at any stage was higher than its counterpart of the RC column. Again, this can be attributed to the ability of rubberized concrete to delay and reduce the macro cracks along with the viscoelasticity of the rubber.

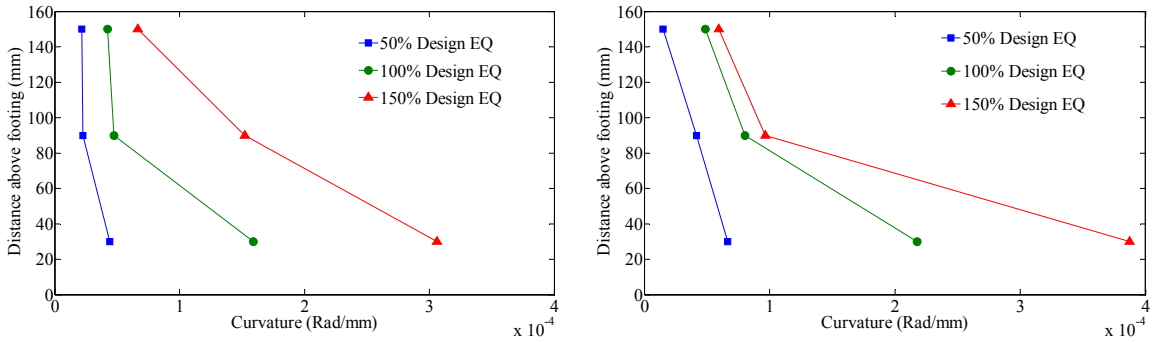

Figure 20. Curvature distribution along the height of the columns at different stages for a) RC column, and b) rubberized column

The columns' profiles are illustrated at Figure 21 at different stages of the test. The figure shows the global behavior of the columns as opposed to the local behavior in Figure 17. The smaller drifts at the bottom of the column resulted from the curvatures at these sections. The columns drifted in a rigid body motion above the plastic hinge region. The rubberized column drifts increased throughout the experiments indicating less damage than the RC column, where the column could not maintain its drift capacity after rebar fracture.

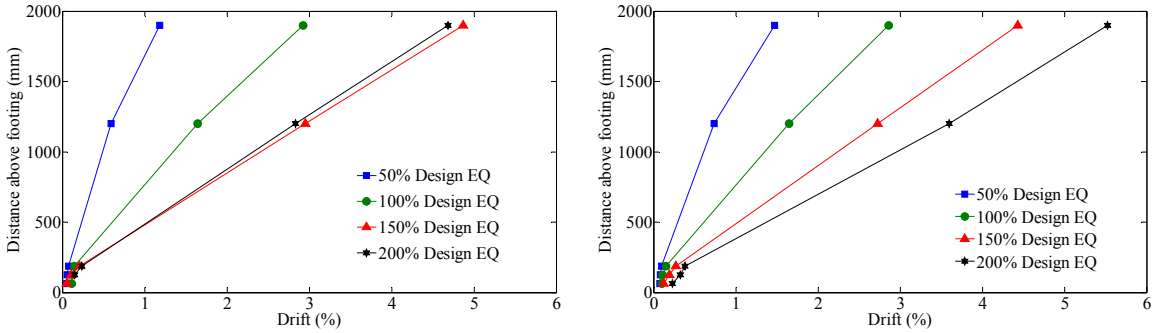

Figure 21. Columns profiles along the height at different stages for a) RC column, and b) rubberized column

Analysis of the Columns' Behavior

The behavior of the columns was mainly governed by two factors: 1) the reduction of the concrete compressive strength in the rubberized column and 2) the dynamic properties of the rubberized concrete. The latter was considered to be dominant due to the viscoelasticity nature of the rubber that would result in the change in behavior. However, it was not possible to separate the effects of the two factors experimentally. This section provides analytical studies of the effects of the two factors on the behavior of the columns. Cross-sectional analyses using XTRACT 3.0.8 were performed to investigate the effect of the concrete compressive strength on the behavior. An OpenSees model (Mazzoni et al. 2006) was developed under the same sequence of ground motions as the experimental investigation to isolate the two effects.

Cross-Sectional Analyses

Cross-sectional analyses of the two columns with the variation of the compressive strength only were performed using XTRACT. The results of the analyses are illustrated in Table 2. The table shows practically no differences between the moment-curvature

behaviors of the two columns due to compressive strength reduction. This can be attributed to the high confinement for both columns leading to failure and termination of the analysis due to rebar fracture so the behavior was not governed by the concrete.

Table 2. Cross-sectional analyses results

Column	$f_c^{'}$	M_y (kN.m)	Φ_y (rad/mm)	M_u (kN.m)	Φ_u (rad/mm)
RC	35	29.79	1.10E-5	56.87	3.84E-4
Ru	27	29.79	1.10E-5	56.76	3.85E-4

OpenSees Models

Two-dimensional (2D) analytical finite element models were developed using the OpenSees platform, which considers both geometrical and material nonlinearities. The OpenSees models were used to conduct nonlinear time history analysis to evaluate the effects of compressive strength and damping on the columns' behavior. The damping was used to simulate the viscoelastic properties of rubberized concrete. Despite this approach was not completely accurate as it only represented the change in damping due to the use of rubberized concrete, not the viscoelastic properties, this approximation should be satisfactory to provide an insight on the change in behavior.

For modeling of the columns, nonlinear beam column elements with fiber-defined cross sections were considered. In the fiber sections, each of the unconfined and confined concrete, and the reinforcing steel, was defined in the precise coordinates of the cross section. The constitutive behavior for the concrete was modeled using Concrete01 model. The reinforcing steel was modeled using the Reinforcing Steel material. In this material model, the fatigue and buckling behavior of steel during loading is included, which is

ignored in other available material models (e.g. Steel01 or 02). This model was chosen because the low cyclic fatigue governed the rebar fracture in the experimental study. The model was subjected to the same sequence as the experimental study starting from 10% of the DE up to 200% of the DE with increments of 10%.

The force-drift envelopes for the experimental versus the OpenSees model for the RC column are illustrated in Figure 22. There is a good agreement between the model and the experimental results. It should be noted that the experimental results in the figure were included after the failure, defined as the loss of capacity of larger than 20%, to provide an overview of the model versus experimental results.

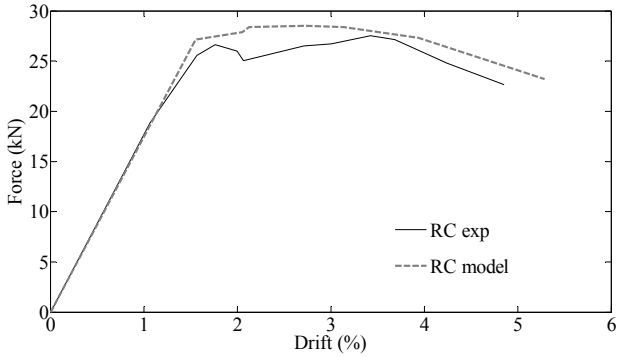

Figure 22. Experimental versus model envelopes of forces versus drift ratios for the RC column

The strains in the rebar for the experimental versus model are illustrated in Figure 23 for the RC column. The model was able to accurately predict the strains in the rebar up to failure due to the use of the Reinforcing Steel material, as explained before.

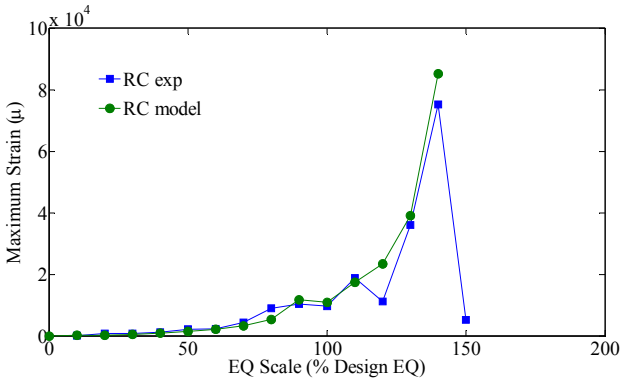

Figure 23. Experimental versus model reinforcement strain for the RC column

The force-drift envelopes for the experimental versus the OpenSees model for the rubberized column are illustrated in Figure 24. The column was modeled twice; the first one changing the compressive strength without changing the damping, and the second one by changing both the compressive strength and the damping to investigate the effect of damping and simulate the rubberized concrete effect. The model without changing the damping showed earlier loss of capacity compared to the experimental results. The model with changing the damping had a similar behavior to the experimental results. It showed lower ultimate drift, which can be attributed to the effect of the viscoelastic behavior of rubberized concrete not included. The models showed the dominant effect of the rubberized concrete over the effect of compressive strength.

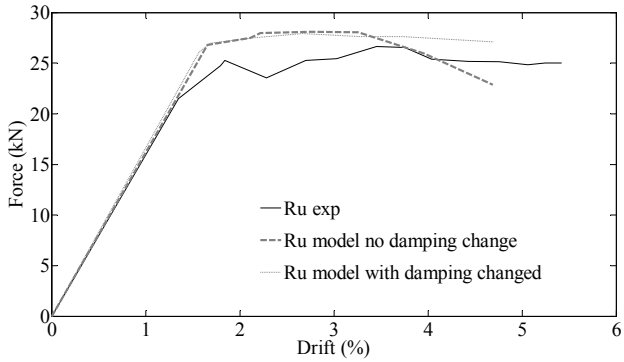

Figure 24. Experimental versus model envelopes of forces versus drift ratios for the rubberized column

The strains in the rebar for the experimental versus model are illustrated in Figure 25 for the rubberized column. The model without change in damping estimated an early rebar fracture at 140% of the DE, which was similar to the RC column. The model with damping change estimated rebar fracture at 170% of the DE compared to 190% of the DE for the experimental study. This can be attributed to the viscoelastic behavior of the rubberized concrete in the experimental study delaying the rebar fracture, as explained in the experimental results and discussion.

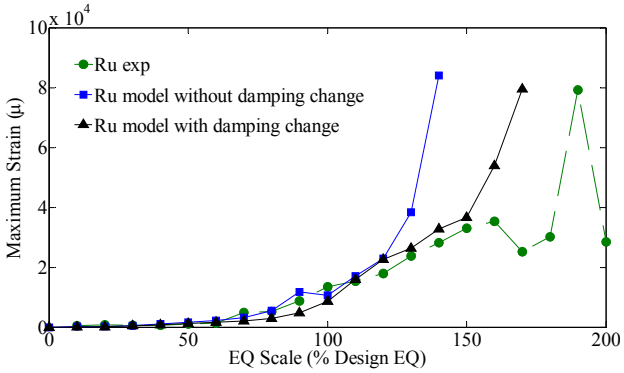

Figure 25. Experimental versus model reinforcement strain for the rubberized column

Conclusion

This paper presented the first shake-table test of a large-scale rubberized column and compared its behavior to that of a conventional column with identical dimensions. Both columns were subjected to a sequence of scaled ground motions of the Northridge-01 1994 earthquake at Rinaldi receiving station. The ground motion scales started from 10% of the DE up to 200% of the DE with increments of 10%. The rebar fracture in the RC column occurred at 140% of the DE. The use of rubberized concrete delayed the rebar fracture to 190% of the DE. The RC column started losing its capacity at 3.4% drift and it lost 20.6% of its capacity at 4.8% drift. This can be attributed to the earlier rebar fracture.

The rubberized column, on the other hand, was able to maintain its integrity up to 5.4% drift due to the delayed rebar fracture caused by the higher energy dissipation. The rubberized column reached a peak drift of 5.4% as compared to 4.8% in the RC column with an increase of 12.5%. The cumulative dissipated energy was increased by 16.5% in the rubberized column compared to the RC column. The rubberized column showed a higher average hysteresis damping before the rebar fracture in the RC column. The viscous damping of the rubberized column was higher than that of the RC column due to the visco-elastic nature of the rubber. The rebar fracture in the RC column at 140% of the DE caused the damping to increase significantly due to the reduction in column stiffness and the increased damage. The improved performance of the rubberized column along with the ease of use because of maintaining the construction technique makes the rubberized columns a superior candidate for bridge columns in high seismic regions.

References

Al-Tayeb, M. M., Bakar, B. A., Ismail, H. and Akil, H. M. (2013). "Effect of partial replacement of sand by recycled fine crumb rubber on the performance of hybrid rubberized-normal concrete under impact load: experiment and simulation." Journal of Cleaner Production 59: 284-289.

Baker, J. W., Lin, T., Shahi, S. K. and Jayaram, N. (2011). New ground motion selection procedures and selected motions for the PEER transportation research program, Pacific Earthquake Engineering Research Center.

Bowland, A. G. (2011). Comparison and Analysis of the Strength, Stiffness, and Damping Characteristics of Concrete with Rubber, Latex, and Carbonate Additives, Virginia Polytechnic Institute and State University.

Bray, J. D. and Rodriguez-Marek, A. (2004). "Characterization of forward-directivity ground motions in the near-fault region." Soil dynamics and earthquake engineering 24(11): 815-828.

Chopra, A. K. (2007). Dynamics Of Structures, 3/E, Pearson Education India.

Eldin, N. N. and Senouci, A. B. (1993). "Rubber-tire particles as concrete aggregate." Journal of Materials in Civil Engineering 5(4): 478-496.

Gibson, N., Filiatrault, A. and Ashford, S. A. (2002). "Impulsive seismic response of bridge column-cap beam joints." Structural Journal 99(4): 470-479.

Güneyisi, E., Gesoğlu, M. and Özturan, T. (2004). "Properties of rubberized concretes containing silica fume." Cement and Concrete Research 34(12): 2309-2317.

Hall, J. F., Heaton, T. H., Halling, M. W. and Wald, D. J. (1995). "Near-source ground motion and its effects on flexible buildings." Earthquake spectra 11(4): 569-605.

Hernandez-Olivares, F., Barluenga, G., Bollati, M. and Witoszek, B. (2002). "Static and dynamic behaviour of recycled tyre rubber-filled concrete." Cement and concrete research 32(10): 1587-1596.

Khaloo, A. R., Dehestani, M. and Rahmatabadi, P. (2008). "Mechanical properties of concrete containing a high volume of tire–rubber particles." Waste Management 28(12): 2472-2482.

Khatib, Z. K. and Bayomy, F. M. (1999). "Rubberized Portland cement concrete." Journal of materials in civil engineering 11(3): 206-213.

Moustafa, A. and ElGawady, M. A. (2015). "Mechanical properties of high strength concrete with scrap tire rubber." Construction and Building Materials 93: 249-256.

Moustafa, A. and ElGawady, M. A. (2016). "Strain Rate Effect on Properties of Rubberized Concrete Confined with Glass Fiber–Reinforced Polymers." Journal of Composites for Construction: 04016014.

Phan, V., Saiidi, M. S., Anderson, J. and Ghasemi, H. (2007). "Near-fault ground motion effects on reinforced concrete bridge columns." Journal of structural engineering 133(7): 982-989.

Resende, F., Roitman, N., Magluta, C. and Toledo Filho, R. (2003). "Influence of Scrap Rubber Tires and Steel Fibers on the Damping Characteristics of Normal Concrete." Civil Engineering Department, COPPE/Federal University of Rio de Janeiro, Rio de Janeiro, Brazil.

Sasani, M. and Bertero, V. (2000). Importance of severe pulse-type ground motions in performance-based engineering: historical and critical review, WORLD CONFERENCE ON EARTHQUAKE ENGINEERING.

Schoettler, M., Restrepo, J., Guerrini, G., Duck, D. and Carrea, F. (2012). "A full-scale, single-column bridge bent tested by shake-table excitation." Las Vegas, NV: Center for Civil Engineering Earthquake Research, Department of Civil Engineering, University of Nevada.

Segre, N. and Joekes, I. (2000). "Use of tire rubber particles as addition to cement paste." Cement and Concrete Research 30(9): 1421-1425.

Sehhati, R., Rodriguez-Marek, A., ElGawady, M. and Cofer, W. F. (2011). "Effects of near-fault ground motions and equivalent pulses on multi-story structures." Engineering Structures 33(3): 767-779.

Siddique, R. and Naik, T. R. (2004). "Properties of concrete containing scrap-tire rubber–an overview." Waste management 24(6): 563-569.

Toutanji, H. (1996). "The use of rubber tire particles in concrete to replace mineral aggregates." Cement and Concrete Composites 18(2): 135-139.

Xue, J. and Shinozuka, M. (2013). "Rubberized concrete: A green structural material with enhanced energy-dissipation capability." Construction and Building Materials 42: 196-204.

Yan, L., Jenkins, C. and Pendleton, R. (2000). "Polyolefin fiber-reinforced concrete composites: Part I. Damping and frequency characteristics." Cement and concrete research 30(3): 391-401.

Youssf, O., ElGawady, M. A. and Mills, J. E. (2015). "Experimental Investigation of Crumb Rubber Concrete Columns under Seismic Loading." Structures 3: 13-27.

Youssf, O., ElGawady, M. A. and Mills, J. E. (2016). "Static Cyclic Behaviour of FRP-confined Crumb Rubber Concrete Columns." Engineering Structures.

Youssf, O., ElGawady, M. A., Mills, J. E. and Ma, X. (2014). "An experimental investigation of crumb rubber concrete confined by fibre reinforced polymer tubes." Construction and Building Materials 53(0): 522-532.

Zhang, Y. and Iwan, W. D. (2002). "Active interaction control of tall buildings subjected to near-field ground motions." Journal of Structural Engineering 128(1): 69-79.

Zheng, L., Sharon Huo, X. and Yuan, Y. (2008). "Experimental investigation on dynamic properties of rubberized concrete." Construction and Building Materials 22(5): 939-947.

V. SHAKING TABLE TESTING OF DAMAGE-RESISTANT SEGMENTAL DOUBLE-SKIN BRIDGE COLUMNS

Ayman Moustafa[1] and Mohamed ElGawady[2]

Abstract

This paper presents the shake-table tests of three proposed damage-resistant segmental double-skin bridge columns with post-tensioned unbonded strands. One column without energy dissipaters and two with external energy dissipaters' details were investigated. It also compares the response to that of a conventional reinforced concrete (RC) column under the same conditions. The cross section is a double-skin section composed of an outside glass fiber reinforced polymer tube (GFRP), an inside steel tube, and concrete cast in between the two. The columns combine the advantages of accelerated bridge construction and self centering due to rocking with high energy dissipation from the steel bars. All columns were subjected to a sequence of scaled near-fault pulse-like ground motions. The double-skin segmental columns sustained no noticeable damage and no residual drift after the sequence of motions up to 250% of the design earthquake, which caused a peak drift ratio of 8.85%. On the other hand, the counterpart conventional column suffered severe damage with rebar fracture and extensive concrete spalling. The accumulated residual drift of the conventional column was 1.5% after the sequence of motions up to 200% of the design earthquake, which caused a peak drift ratio of 4.8%.

[1] Graduate research assistant, Department of Civil, Architectural, and Environmental Engineering, Missouri University of Science and Technology, USA E-mail: ampyf@mst.edu
[2] Benavides Associate professor, Department of Civil, Architectural, and Environmental Engineering, Missouri University of Science and Technology, USA E-mail: elgawadym@mst.edu

The energy dissipated by the segmental columns and the damping were comparable to those of the conventional RC column along the tests.

Key words: Bridge columns, energy dissipation, seismic design, segmental columns, seismic resistant columns, self centering, shaking table test.

Introduction

Current seismic design provisions are intended to prevent bridges collapse under maximum considered earthquake (FEMA 2006) while allowing some damage during a design earthquake (DE) in the form of rebar yielding and concrete spalling (Caltrans 2010). Larger damage would accumulate in a reinforced concrete (RC) column under near-fault pulse-like ground motions compared to that of equal magnitude near-fault motions without pulse (Gibson et al. 2002; Phan et al. 2007; Sehhati et al. 2011). This damage results in excessive residual drift which may inhibit bridge repair (Jeong et al. 2008). For example, the Japanese seismic design specifications are limiting the residual drifts of columns to 1% (Japan Road Association 2002).

Unbonded post-tensioned rocking columns (PTRC) have been investigated to reduce excessive residual drift. PTRCs can consist of a single-segment (Palermo et al. 2007; Shim et al. 2008; Marriott et al. 2009; Trono et al. 2014) or multi-segments (Chang et al. 2002; Chou and Chen 2006; ElGawady et al. 2010; Ichikawa et al. 2016). PTRCs are typically designed so the PT tendons remain elastic under earthquake ground motions; hence, PTRCs dissipate energy through viscous and radiation damping. Therefore, multi-segment columns generally displayed relatively higher energy dissipation than single-

segment due to the increase in the number of interface joints where rocking can take place (Hewes 2000). However, both systems showed limited energy dissipation compared to that of counterparts conventional RC columns.

Internal bonded mild steel bars (Palermo et al. 2007; Wang et al. 2008; Ou et al. 2010) and external energy dissipaters in the form of steel bars or angles (Chou and Chen 2006; Marriott et al. 2009; ElGawady et al. 2010; ElGawady and Sha'lan 2010) were successfully employed to increase the energy dissipation of PTRCs. Large variations in the increase of energy dissipation results were reported. Internal dissipaters are protected against vandalism and environmental effects; however, it is impractical to replace them when damaged post an earthquake. External dissipaters are easy to replace post an earthquake; however, they need careful architectural considerations to not affect the appearance of the columns. Also, they need protection against vandalism and environmental effects. Marriott et al. 2009 used mild steel as external energy dissipaters with grouted steel tube casing to prevent their buckling. This connection is promising because it provided a simple connection with ease of construction and high energy dissipation. However, rupture of the external energy dissipaters occurred due to low cyclic fatigue resulting from the bond between the bars and grout making it a bonded connection despite the design was for an unbonded connection. It should be noted that the tests were performed up to a small lateral drift of 3.5% and under static cyclic loading.

The majority of PTRCs were investigated under static cyclic loading (Mander and Cheng 1997; Hewes and Priestley 2002; Chou and Chen 2006; Palermo et al. 2007; Shim et al. 2008; Wong et al. 2008; Marriott et al. 2009; Solberg et al. 2009; Ou et al. 2009; ElGawady et al. 2010; ElGawady and Sha'lan 2010; Kim et al. 2010; Ou et al. 2010;

Ichikawa et al. 2016). During these static cyclic tests, peak drifts ranging from 3.5% to 11% and residual drifts of less than 1% were reported. Limited number of studies investigated the dynamic characteristics of PTRC having 1/5 to 1/3 scales under shaking table tests. The tests showed the viability of using PTRC in high seismic regions. However, these tests used shear keys and wet-joints, a monolithic first segment, or heavily reinforced first segment which would increase the column construction time and compromise the accelerating construction nature of PTRC.

PTRC columns with conventional rebar and transverse reinforcement experienced concrete spalling, and rebar buckling (Trono et al. 2014). Confinement in forms of steel jackets (Jeong et al. 2008) or fiber reinforced polymer (FRP) jackets (ElGawady et al. 2010; ElGawady and Sha'lan 2010) were adapted to overcome these issues. Recently, researchers investigated combining steel confinement jackets with hollow-core sections (Guerrini and Restrepo 2013).

During the last few decades, researchers have attempted to develop hollow-core double-skin columns that can display low damage and ductile behavior. Generally, a double-skin section includes generally concentric outer tube, inner tube, and concrete shell in between the two tubes. Montague 1978 used an outer and inner steel tubes while Teng et al. 2005 used inner steel tube and outer FRP tube. Several experimental and finite element studies were conducted on the hollow-core double-skin columns under different static and cyclic loading conditions (Teng et al. 2007; Wong et al. 2008; Han et al. 2010; Ozbakkaloglu and Idris 2014; Abdelkarim and ElGawady 2014). However, the use of such cross-section in segmental construction, to the knowledge of the authors, has not been investigated yet.

Both analytical and finite element models PTRC were also developed for segmental columns (Pampanin et al. 2001; Palermo et al. 2007; Dawood et al. 2011; ElGawady and Dawood 2012; Chou et al. 2013; Zhang and Alam 2015; Leitner and Hao 2016). The models were able to predict the capacity of the investigated columns under static cyclic loading.

Research Significance

The apparently simple nature of free rocking motion reveals complex dynamic behavior along with chaotic and butterfly effect. That is, a minute perturbation can cause significant effects on the rocking response. This behavior is attributed to the sensitive dependence of the solution on the initial conditions. Hence, the behavior of PTRC needs to be investigated under dynamic load. Currently, the literature includes very limited number of dynamic tests on segmental columns. Furthermore, none of these tests were conducted under the effects of near-fault ground motion. This manuscript investigates the behavior of segmental columns subjected to near-fault ground motion. The segments in this manuscript had hollow-core fiber reinforced polymer concrete steel cross (HC-FCS) sections. HC-FCS consists of an outer FRP tube, inner steel tube, and a concrete shell sandwiched between the two tubes.

Experimental Program

Overview of the Test Specimens

Four columns were experimentally investigated including a reference RC column, a segmental double-skin column, hereinafter denoted as SEG, and two segmental double-

skin columns with two external energy dissipation details, hereinafter denoted as SEG-ED1, and SEG-ED2. The SEG column had no reinforcement other than the internal unbonded post-tension (PT) strands. The SEG-ED1 was designed for moderate seismic response to dissipate higher energy at the DE level through yielding of the external energy dissipaters. The SEG-ED2 was designed to sustain the maximum considered earthquake (MCE) without rupture of the external energy dissipaters.

The columns' elevations and cross sections along with the test setup are illustrated in Figures 1 and 2 for the RC and the segmental columns, respectively. The columns' height measured from the top of the footing to the center of the mass was 1800 mm, resulting in an aspect ratio of approximately 6, except for the RC column, where the height slightly increased to 1900 mm as a slab was monolithically cast with the column to enable attaching the column head. The aspect ratio is defined as the height of the column divided by its diameter. The RC column was a monolithic while the segmental columns consisted of four segments of 300 mm high each.

All columns had identical outside diameter of 300 mm. The double-skin columns had identical inside diameter of 175 mm. The reinforcement of the RC column consisted of eight longitudinal #4 rebar (12.5 mm diameter) corresponding to a longitudinal reinforcement ratio of 1.4% and spiral reinforcement of #3 rebar (9 mm diameter) with a pitch of 75 mm corresponding to transverse volumetric reinforcement ratio of 1.3%. The spiral reinforcement was extended in the entire depth of the footing and the column head. Each segmental column had four 12.7 mm diameter seven wire strands PT, each with a cross sectional area of 99 mm^2 as the main reinforcement of the column. Column SEG-ED1 had two external A36 steel bars with a diameter of 6 mm and unbonded length of 50

mm at the north and south directions of the column. Column SEG-ED2 had two external A36 steel bars with a diameter of 8 mm and unbonded length of 150 mm at the north and south directions of the column. These bars were fixed to the foundation using a stiff angle bolted in the foundation using three epoxy glued anchor wedges with a diameter of 16 mm each. The tension only bars were connected from one end to the segments through a rigid thick plate attached to the second segment with the bars passing through the plate. The bars were threaded at the ends and thick washers and double nuts were used to tighten the bars and to allow tension only. The rigid plates with oval shaped holes were able to slide without friction in compression. The bars were lathed from a diameter of 15.6 mm to the desired diameter at the specified unbonded lengths (Figure 3). The energy dissipaters were connected to the second segment providing controlled rocking for the bottom two segments, where most of the rocking is expected.

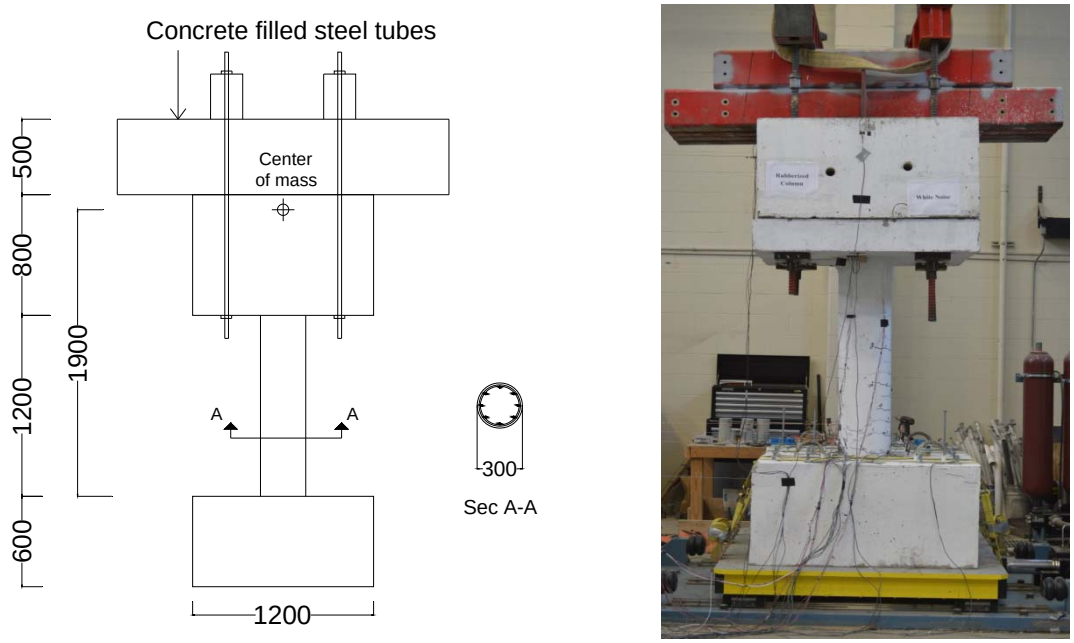

Figure 1. Configuration and dimensions of the RC column (unit: mm)

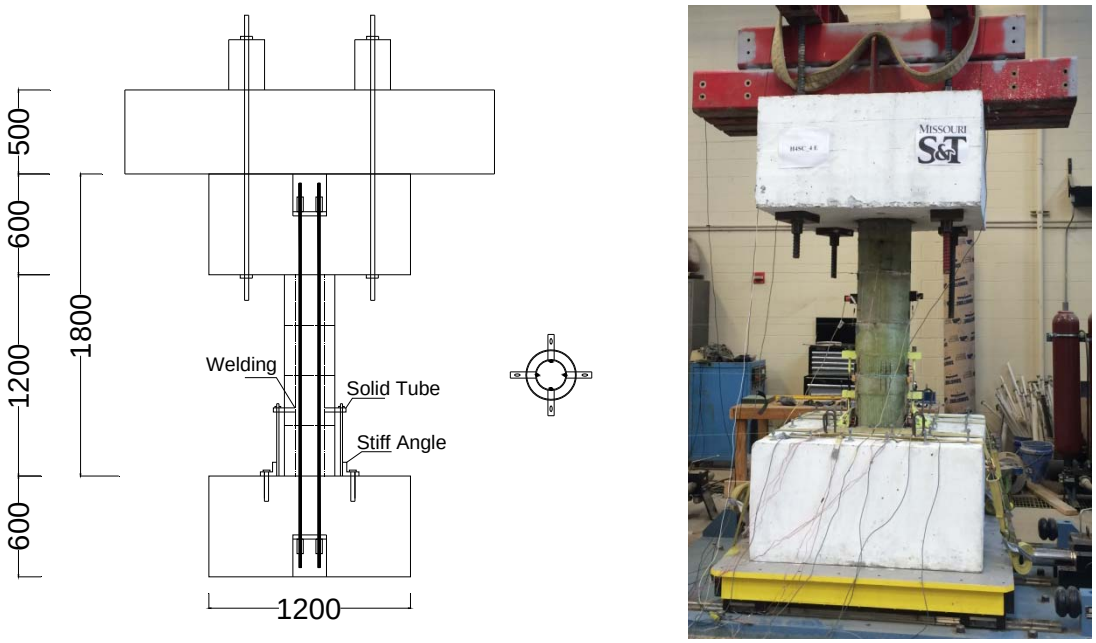

Figure 2. Configuration and dimensions of the segmental columns (units: mm)

(a) (b)

Figure 3. External energy dissipaters for: a) SEG-ED1 and b) SEG-ED2 with connection

Material Characteristics

The concrete compressive strength was 35 MPa. The inner steel tube thickness was 4.7 mm. The outer tube consisted of four layers of unidirectional glass fiber reinforced polymers and Tyfo S epoxy by FYFE© with a total thickness of 5 mm. Three specimens of GFRP hoops were tested according to ASTM D2290 2012. The average ultimate tensile strength in the fiber direction was 352 MPa. The elongation at break was 2.31%. The strands were distributed along the edge of the hollow part of the cross section to maximize the distance of the strands to the neutral axis. The PT strands had a diameter of 12.7 mm, a yield stress of 1675 MPa, and an ultimate strength of 1861 MPa. The external energy dissipaters were low carbon A36 steel bars. The stress-strain curves for three specimens of the A36 steel are illustrated in Figure 4.

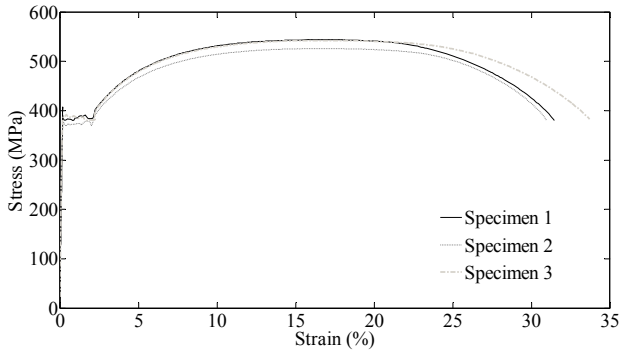

Figure 4. Stress-strain curves for the external energy dissipaters

Test Setup and Loading Sequence

The columns were fixed to a uni-axial shaking table using 36 all-threaded bars, each with a capacity of 45 kN. The shaking table is running using a closed loop controller that can use either displacement or acceleration control. Six accelerometers were used to measure the horizontal accelerations on the shaking table, the center of the column head, and the

center of mass. Eight string potentiometers were used to measure the horizontal displacements along the heights of the columns. For the RC column, eight linear potentiometers were mounted on the column to measure the curvature along the bottom 187.5 mm of the column and one linear potentiometer to measure horizontal sliding between the column and the foundation. Seven strain gages were mounted on each of the north and south rebar; four of them along the bottom 225 mm above the footing and three at 100 mm into the footing to measure the potential strain penetration depth into the foundation. For the segmental columns, twelve linear potentiometers were mounted on the column to measure the vertical openings and horizontal sliding between the segments. Load cells were placed at the north and south strands to measure the forces in the strands. Strain gages were attached to the external energy dissipaters at the unbonded length.

The mass atop the column was provided by a 1200 mm x 1200 mm x 800 mm column reinforced concrete stub and eight concrete filled steel tubes (CFTs) each having a cross section of 600 mm x 500 mm. Four of these CFTs each had a length of 2200 mm and the other four each had a length of 1925 mm. The tubes were post-tensioned to the column head with a total weight of 54 kN.

Each column was subjected to a sequence of a scaled Northridge-01 1994 earthquake at “Rinaldi Receiving Station” which is a near-fault pulse-like ground motion. The selected ground motion was scaled to the design spectrum (Figure 5), by matching the spectral acceleration at the column’s first mode (Sa(T1)) to the design response spectrum. Hereinafter, the DE will refer to the design earthquake spectrum used in the current study. The columns were assumed to be in a high seismic zone in San Francisco, California, soil class D; where the prototype column is assumed. The design response

spectrum (DE) with a probability of excess of 10% in 50 years and the maximum considered earthquake (MCE) response spectrum with a probability of excess of 2% in 50 years are illustrated in Figure 5.

The time coordinate of the input accelerations was compressed by a factor of $\sqrt{0.25} = 0.5$ for similitude according to the scale factor of 4. The columns were subjected to a sequence of the scaled ground motion starting at 10% of the DE to 250% of the DE with steps of 10% increments giving a total of 25 ground motions, except for the RC column loaded up to 200% of the DE for safety and SEG-ED1 loaded up to 120% of the DE due to external dissipaters fracture. A white noise test with duration of 75 s and 0.02g amplitude of acceleration was run after each ground motion excitation to determine the updated fundamental period of the column.

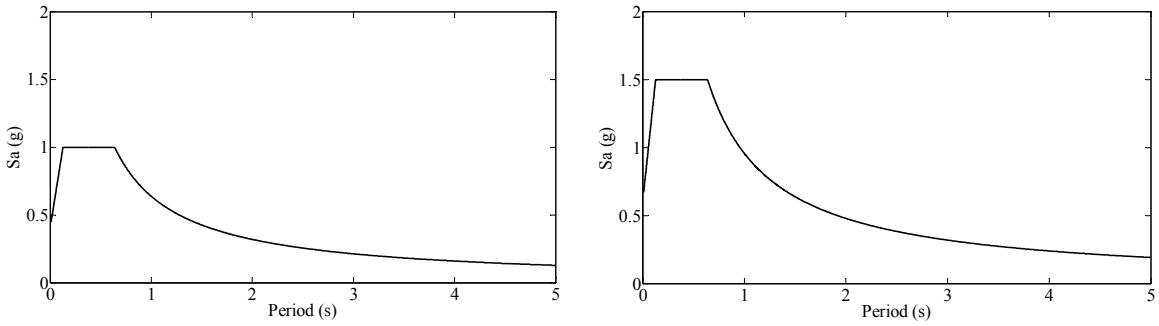

(a) (b)

Figure 5. a) Design earthquake spectrum and b) maximum considered earthquake spectrum

Experimental Results and Discussion

General Behavior

The RC column displayed the anticipated performance of well-designed columns. Visible cracks occurred at a drift of 1% during subjecting the column to 50% of the DE. Rebar yielding, as measured by the strain gages, was also initiated at that point. As the intensity

of the earthquake was increased, existing cracks widen more and connect together to form larger cracks. Minor spalling started at a drift of 2.1% corresponding to 90% of the DE. The southern rebar was fractured at 140% of the DE and it was accompanied by a popping sound. Beyond that, the column displayed apparent residual drifts but the tests proceeded until 200% of the DE and the test was terminated for safety purposes. The RC column suffered severe damages consisting of rebar fracture, buckling of rebar, concrete spalling, and large residual drifts (Figure 6). These damages were accompanied by loss of capacity as the test progressed.

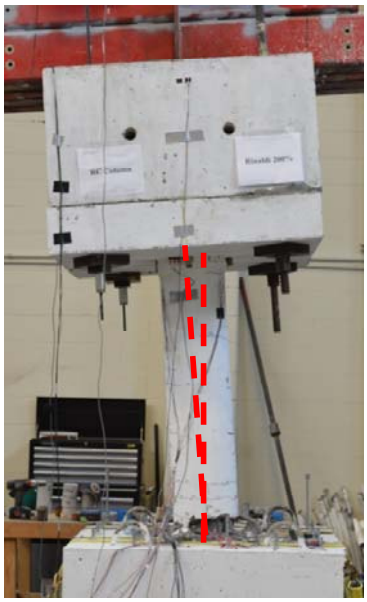

(a)

(b)

Figure 6. RC column at the test end: a) residual drift and b) rebar fracture, buckling, and concrete spalling

The column SEG displayed a different behavior with rocking at the interface between the first segment and the foundation being the most observed behavior during the tests. No apparent residual drifts were observed at all during the tests. No damage in the GFRP was noticed and the damage of the core concrete was examined after the test and was found to be minor. The column was able to resist the full sequence of the scaled

earthquakes up to the 250% of the DE, where the test was terminated because the maximum velocity of the shaking table was reached. However, the analysis of the results showed yielding of the PT strands occurred at 160% of the DE, as will be shown in a later section. It should be noted that this exceeded the MCE, which corresponds to 150% of the DE.

The column SEG-ED1 behaved in rocking resulting in yielding of the external energy dissipaters at 50% of the DE and visually apparent permanent strains at the DE indicating the desired large yielding at the DE was achieved. The test was continued up to 120% of the DE, where rupture of the two energy dissipaters occurred.

The column SEG-ED2 outperformed the other columns. The column was able to sustain the full sequence of the scaled earthquakes up to the maximum of 250% of the DE without any noticeable damage or residual drift. As designed, the external energy dissipaters yielded to improve the energy dissipation. These dissipaters can be easily replaced after a major earthquake of an intensity of the MCE or higher. The PT yielding was avoided in this column by reducing the initial PT force and relying on the energy dissipaters to supply the difference in capacity. The initial PT force was reduced from 54% to 44% of the ultimate strength. This initial PT is still in the economic range.

Time Histories and Hysteretic Behavior

All columns were designed to have the same yielding capacity for comparison. For the segmental columns, this was achieved by adjusting the initial PT force and adding the energy dissipaters. The initial PT forces were 100 kN, 89 kN, and 81 kN in each strand resulting in a total force of 400 kN, 356 kN, and 324 kN for columns SEG, SEG-ED1,

and SEG-ED2, respectively. Samples of the lateral drifts and response accelerations for the test specimens are illustrated in Figures 7 and 8, respectively, at the DE and at the end of the RC column test. The lateral displacements were obtained by subtracting the table displacement from the displacement at the center of mass; both recorded by the string pots. The drift was then obtained by dividing the lateral displacement by the height of the column from the top of the footing to the center of mass. At the DE, the drift demand on the RC column is 50%, 40%, and 55% higher than the SEG, SEG-ED1, and SEG-ED2 columns, respectively, while the acceleration response; hence the force, is similar. This low drift demand at the DE level for the segmental columns is favorable since it reduces the demand on the superstructure and its joints. It resulted from the PT force increasing the stiffness of the segmental columns and allowing low amplitude rocking. The SEG-ED1 column test was terminated at 120% of the DE. At the RC column test end at 200% of the DE, the RC column had a very large residual drift of 1.5% while the segmental columns showed no residual drift. Unlike the segmental columns, both the drift and acceleration of the RC column highly differ in the positive and negative direction. This is attributed to the fact that the input ground motion is asymmetric pulse-like wave and the RC column with its ruptured rebar and large damage was unable to recover the drift in the negative direction. The segmental columns had symmetric response in the positive and negative directions indicating a favorable response with the columns rocking in both directions to accommodate the asymmetric impulsive nature of the input motion. The acceleration of the SEG column is lower than that of the SEG-ED2 column due to yielding of the PT strands.

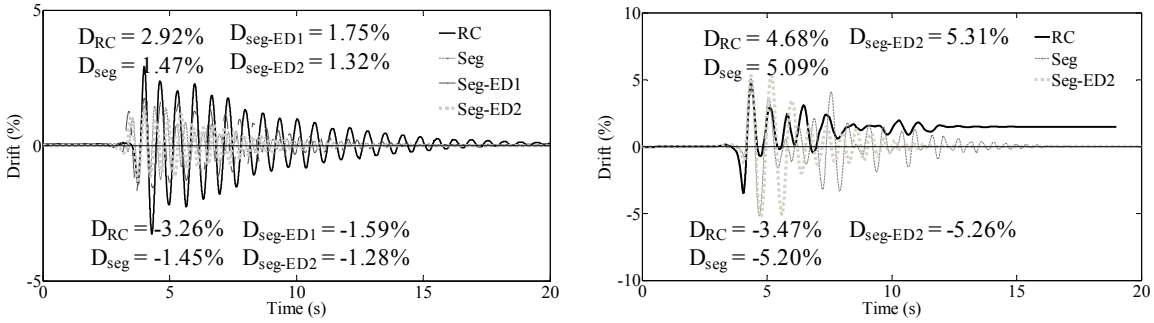

(a) (b)

Figure 7. Drift time histories for the specimens at: a) DE, and b) RC column test end

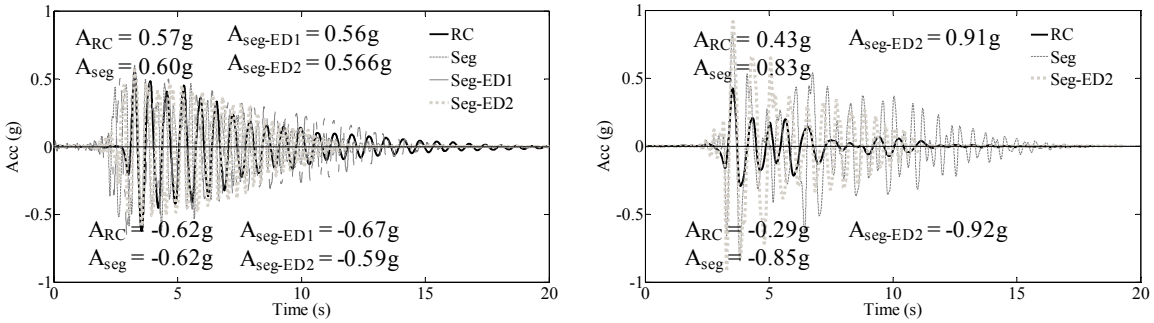

(a) (b)

Figure 8. Response acceleration time histories for the specimens at: a) DE, and b) RC column test end

Samples of the lateral force versus lateral drifts for the RC, SEG, SEG-ED1, and SEG-ED2 columns are illustrated in Figures 9, 10, 11, and 12, respectively, for different intensities of the simulated earthquakes as percentages of the DE. The lateral force was obtained by multiplying the mass on top of the column times the acceleration at the center of mass. The response of the RC column was nearly symmetric at the elastic region which ended at 50% of the DE. Beyond that the hysteretic became asymmetric due to rebar yielding since the input ground motion is asymmetric and has an impulsive nature, as explained earlier. The segmental columns maintained the nearly symmetric response throughout the tests despite the yielding of the PT strands in the SEG column. The yielding of the PT strands led to losses in the PT force due to the inelastic response

(Priestley and Tao 1993). However, the column still responded in the normal rocking mode but with lower PT force. The RC column experienced high residual drifts at 150% of the DE due to the rebar fracture. The impulsive nature of the input motion was more dominant at 200% of the DE causing failure and the test was stopped. The segmental columns had no measurable residual drifts. The drift at zero force for the maximum force and large amplitude cycles was higher in the SEG-ED2 column compared to the SEG column due to yielding of the energy dissipaters. This drift at zero force was recovered in both columns by the PT force.

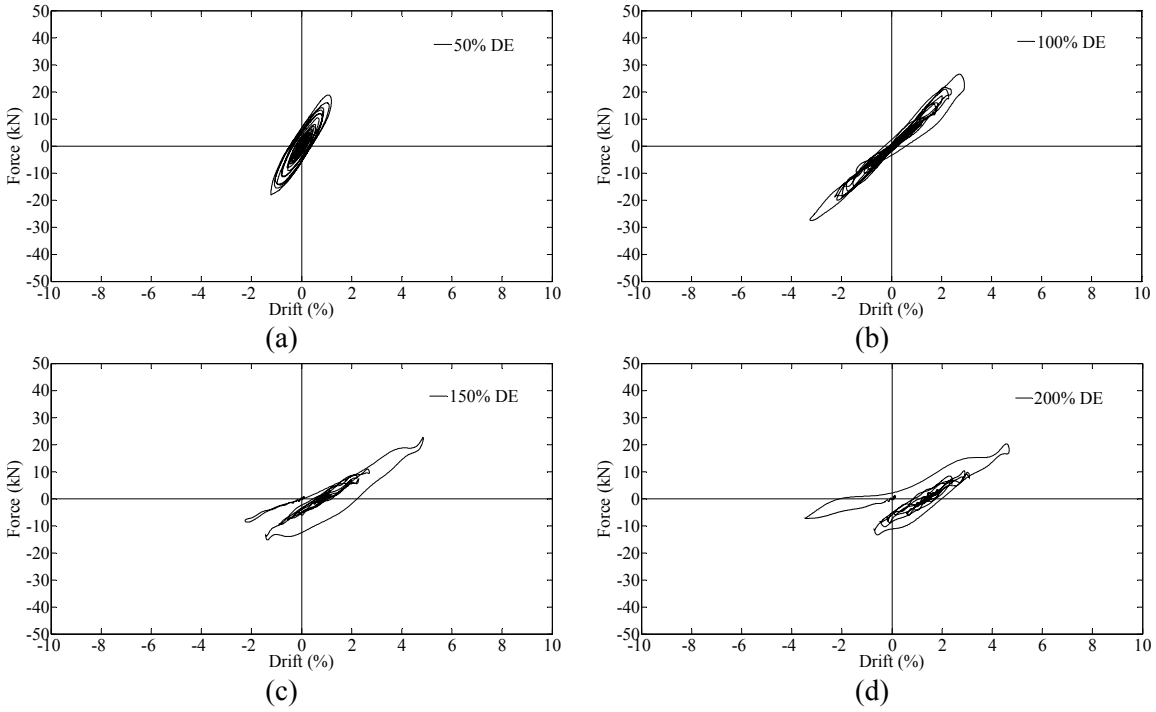

Figure 9. Measured forces versus drift ratios for the RC column at different stages of the test at: a) rebar yielding, b) DE, c) rebar fracture, and d) test end

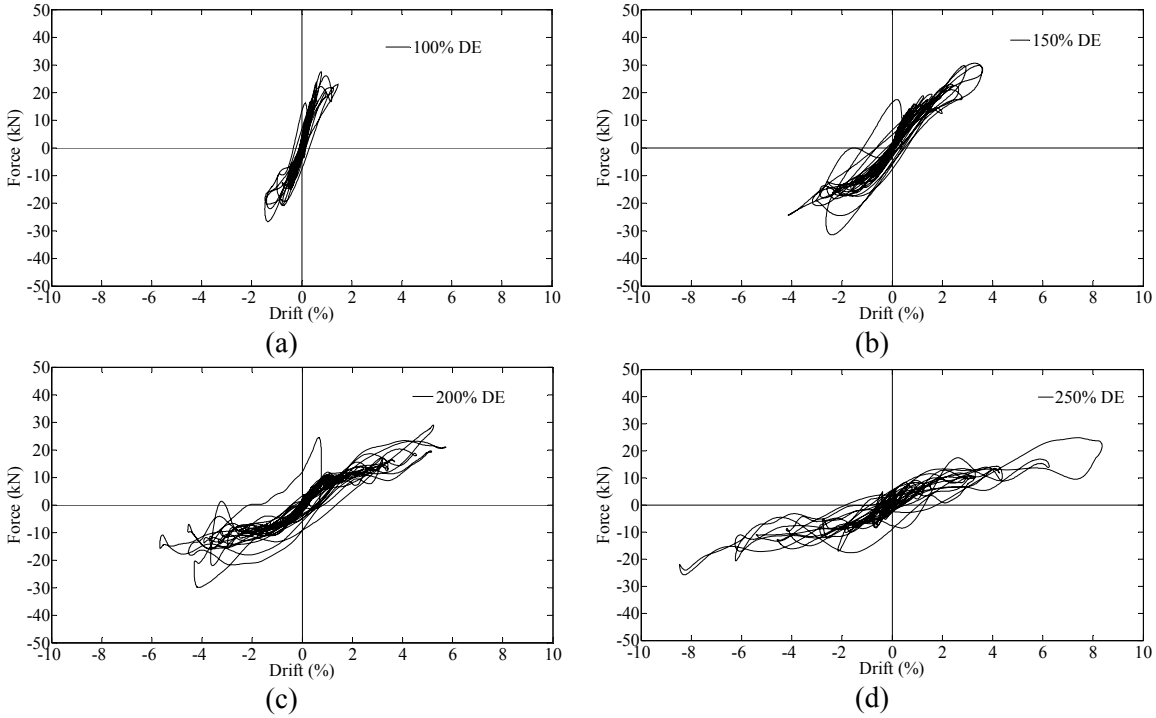

Figure 10. Measured forces versus drift ratios for the SEG column at different stages of the test at: a) DE, b) MCE, c) RC column test end, and d) SEG column test end

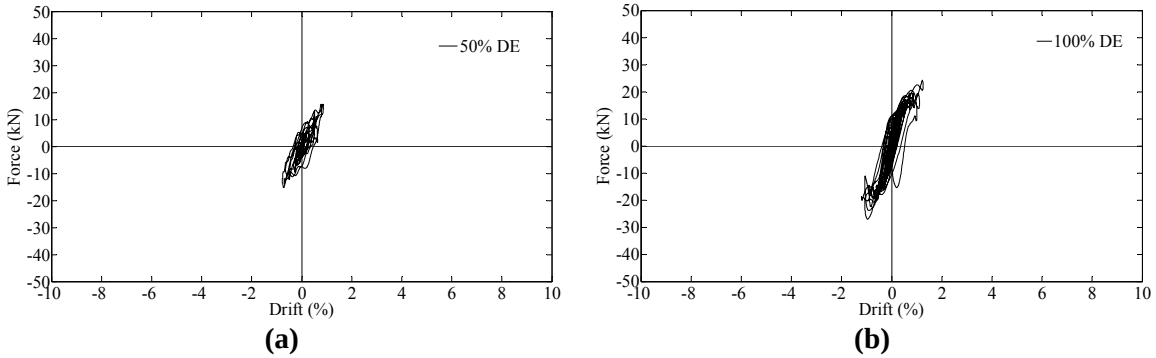

Figure 11. Measured forces versus drift ratios for the SEG-ED1 column at different stages of the test at: a) energy dissipaters yielding, b) DE

The envelopes of the lateral force versus lateral drift, known as dynamic push over curve, for all columns are illustrated in Figure 13 for comparison. Each point on the curve represents the maximum force and the corresponding drift for one of the tests from the sequence of 10% to 250% of the DE. The yield point in the RC column and the corresponding nonlinear point for the segmental columns occurred at forces of 25.55 kN,

29.12 kN, 26.25, and 26.27 kN for the RC, SEG, SEG-ED1, and SEG-ED2 columns, respectively. The behavior beyond that point is totally different between the RC and segmental columns resulting in capacities of 27.5 kN, 34.4 kN, 33.6 kN, and 34.7 kN for the RC, SEG, SEG-ED1, and SEG-ED2 columns, respectively, representing an increase of the strength of 25%, 22.2%, and 26.2% for the SEG, SEG-ED1, and SEG-ED2 columns compared to the RC column, respectively. This gain of strength, post yielding, is a favorable characteristic for the segmental columns. The loss in the RC column's capacity started at 3.4% drift and the column strength reduced by 20.6% of its capacity at 4.8% drift. This was attributed to rebar fracture which occurred at 4.25% drift during 140% of the DE. The SEG column was able to sustain the imposed ground motions up to 4.55% drift followed by a reduction of strength of 22% at 160% of the DE due to yielding of the PT strands. It should be noted that the SEG column was still able to sustain the ground motions up to 250% of the DE with the modified strength due to PT losses. The maximum drift for the SEG column was 8.25% with an increase in drift of 72% compared to the RC column. The SEG-ED2 column, on the other hand, outperformed the other columns with a small reduction in capacity of only 6% at 180% of the DE due to stress softening of the energy dissipaters. The use of external energy dissipaters in this study enables their replacement which would result in restoring the capacity of the column. The ultimate drift of the SEG-ED2 column was 8.85% with an increase of 84% compared to the RC column. The initial stiffness of the segmental columns was much higher than that of the RC column due to the PT force. However, unlike the conventional RC columns, this increase of stiffness does not come with the price of low ductility but rather is favorable to reduce the drifts up to the DE and provide the ductility through

rocking. The drawback of such high stiffness is the lower energy dissipation which is investigated in this article and the external energy dissipaters are proposed as a solution to this problem.

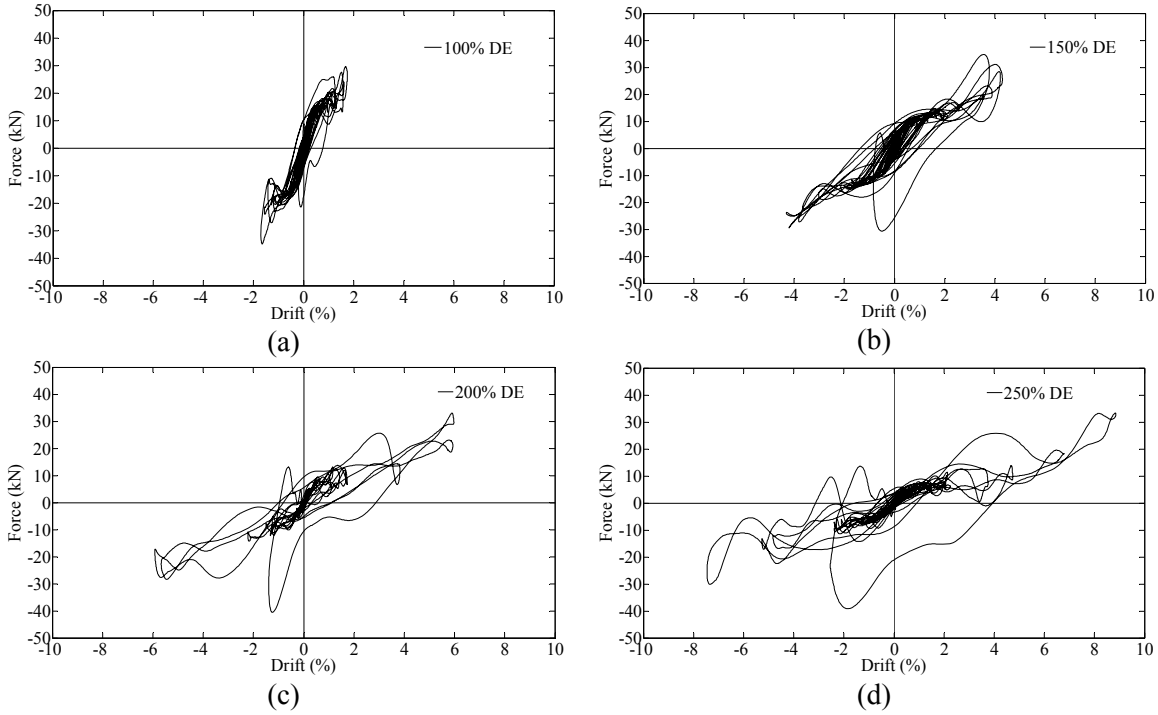

Figure 12. Measured forces versus drift ratios for the SEG-ED2 column at different stages of the test at: a) DE, b) MCE, c) RC column test end, and d) SEG-ED2 column test end

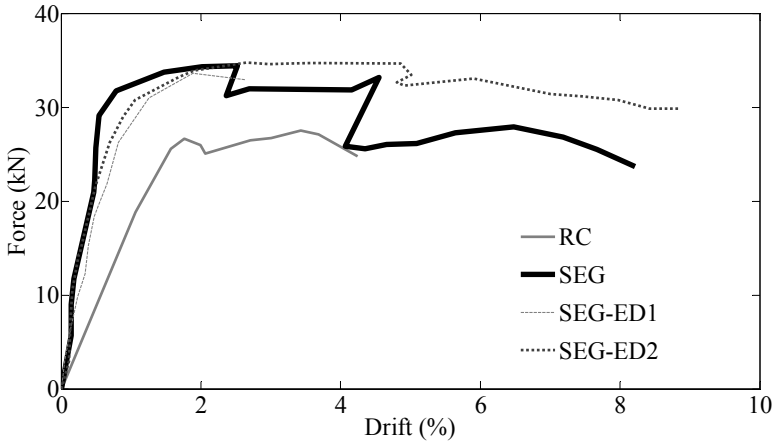

Figure 13. Envelopes of forces versus drift ratios

Post-Tension Forces

Two load cells; one with a capacity of 220 kN and the other with a capacity of 440 kN were installed in the direction of loading on the southern and the northern PT strands, respectively, to monitor the progress of the PT force during the tests. The strands had a yield force of 165.3 kN and an ultimate strength of 183.7 kN. The maximum PT load progress during the tests is illustrated in Figure 14. The figure shows yielding at 160% of the DE for the SEG column followed by a drop in the maximum PT force and then an increase of the force in the inelastic region up to 179.2 kN at 250% of the DE at the test end. For the SEG-ED2 column, the external energy dissipaters provided an extra support with the controlled rocking reducing the maximum PT force to 155.7 kN at 250% of the DE. This reduction in the maximum PT force was achieved by reducing the initial PT force from 54% to 44% of the ultimate strength along with the external energy dissipaters.

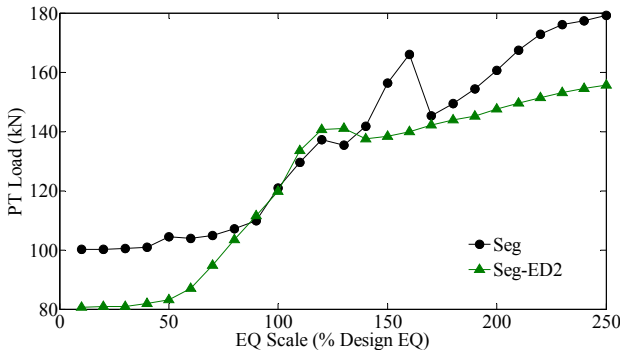

Figure 14. Maximum PT force for columns SEG and SEG-ED2 at different stages of the test

Peak and Residual Drift Ratios

The absolute residual drifts and residual drifts normalized after each test run for all columns are illustrated in Figure 15. The RC column started to experience residual drifts

at early stages starting at the DE level. The residual drift was increased by the rebar fracture at 140% of the DE accompanied with heavy spalling of concrete. The maximum residual drift at the test end was 1.5%. This highly exceeded the 1% limit set by the Japanese seismic design specifications for column demolition (Japan Road Association 2002). All the segmental columns had no significant residual drift with the maximum residual drift of 0.08% in the SEG column, which can be ignored.

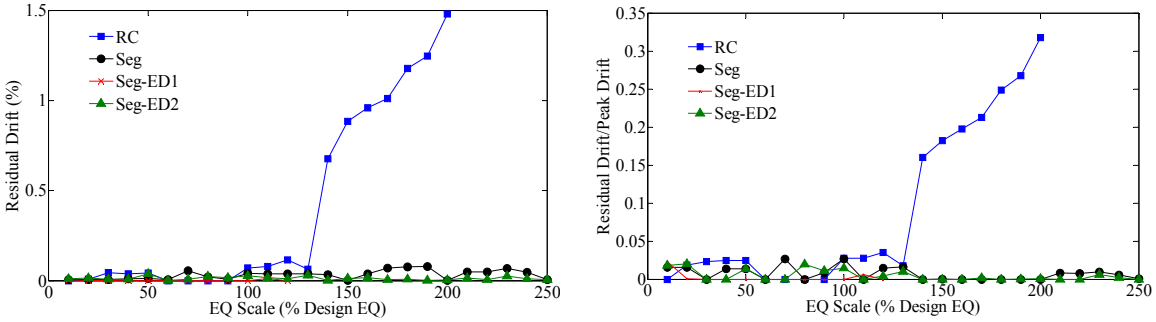

(a) (b)

Figure 15. Residual drifts at different stages: (a) absolute residual drift and (b) normalized residual drift

Fundamental Periods of the Columns

The fundamental period of a structure is one of the important dynamic properties as it affects the response of the structure to ground excitation. The fundamental period here is used as an indication of damage in the columns. The occurrence of damage increases the fundamental period. The fundamental periods for the test specimens were calculated from the acceleration response of the specimens to the white noise excitation with the amplitude of 0.02 g that was applied before each test (Figure 16). At the beginning of the test at 10% of the DE, the fundamental period of the SEG column was lower than that of the RC and SEG-ED2 columns due to the higher stiffness of the SEG column because of the larger PT force. It should be noted here that the stiffness affecting the periods of the

segmental columns was due to the PT force only without a contribution from the external energy dissipaters due to the very low amplitude of the white noise not causing rocking. This explains why the period of the SEG column is lower than that of the SEG-ED2 column, while the overall stiffness of both columns is almost equal, as shown previously (Figure 13). As the tests progressed, the fundamental periods of the RC column increased due to the reduction of column's stiffness caused by damage in the concrete and rebar yielding till fracture. The fundamental period of the SEG columns was not affected much up to 160% of the DE, where the PT strands yielded, and then the fundamental period was almost constant again indicating the column reached a new steady state with the new PT force. The fundamental period of the SEG-ED1 and SEG-ED2 columns was not much affected by the test runs indicating no major damage. The constant fundamental period of the segmental columns is due to the PT force returning the column to the original position after each test run.

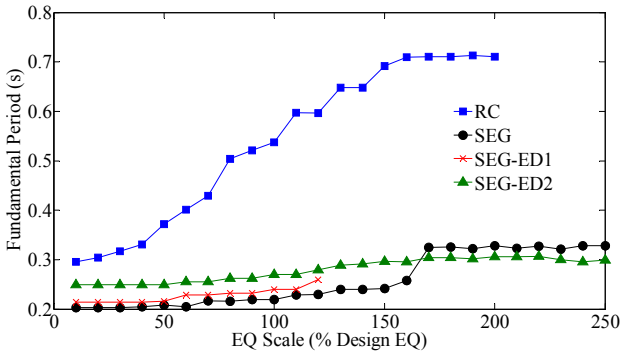

Figure 16. Fundamental periods of the specimens at different stages

Curvatures and Rotations of the RC Columns

The RC column formed a plastic hinge at its base which produced the lateral drift. Six linear potentiometers (three on each side) were distributed up to a distance of 187.5 mm (7.5 inches) above the column foundation in order to measure the vertical displacements.

The data from each pair of linear potentiometers was used to calculate the average curvature at that section using Eq. 1.

$$\Phi = \frac{\varepsilon_1 - \varepsilon_2}{S} \quad (1)$$

where, ε_1 is the average strain calculated from the linear potentiometer measurement on one side, ε_2 is the average strain calculated from the linear potentiometer measurement on the opposite side along the same plane, and S is the horizontal distance between the two potentiometers. The moment-curvature relationship is illustrated in Figure 18. The values shown in the figure are the maximum moment and maximum curvature during each test run. The distance in the legend refers to the distance of measurement above the foundation level. Most of the column's curvatures occurred in the lower column segments at the plastic hinge, where most of the damage occurred. The figure shows moment drop of 20.6% of the ultimate moment at a curvature of 0.0003 rad/mm.

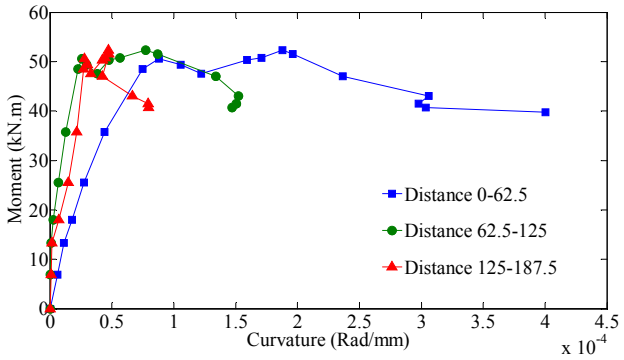

Figure 17. Moment versus curvature for the RC column

The distribution of the column's curvature is illustrated at Figure 18 at different stages of the test. The curvature of the column increased with the increase of the ground

motion intensity. In addition, the curvature decreases with the increase of height with most of the curvature concentrated at the bottommost portion of the columns. The higher the excitation, the larger the difference between the average curvatures at the first height of measurement compared to the second one. At 150% of the DE, the curvature at the second potentiometers plane which was almost half of the first one resulted from the rebar fracture at 140% of the DE.

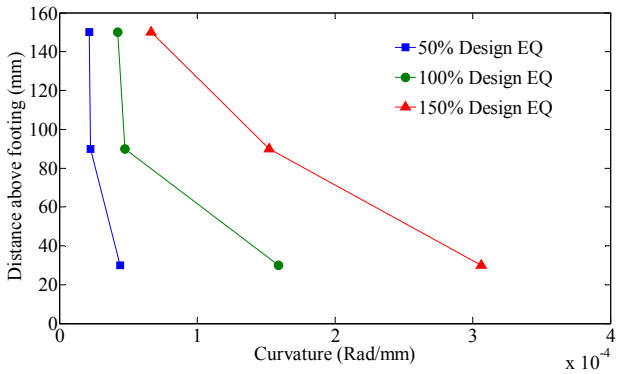

Figure 18. Curvature distribution along the height of the RC column at different stages

The column's profile is illustrated at Figure 19 at different stages of the test. The figure shows the global behavior of the columns as opposed to the local behavior in Figure 18. The smaller drifts at the bottom of the column resulted from the curvatures at these sections. The column drifted in a rigid body motion above the plastic hinge region.

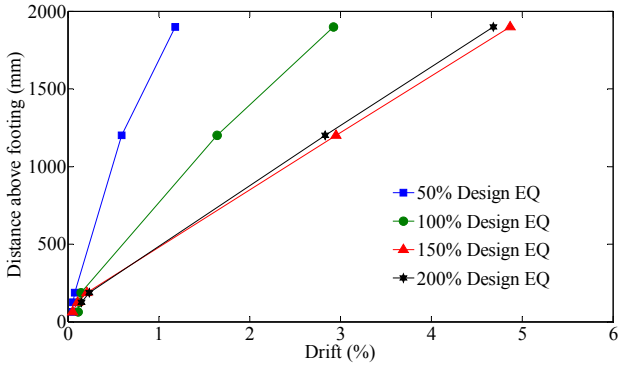

Figure 19. RC column profiles along the height at different stages

Rigid Body Motions

Unlike the RC column, rocking is the dominant mode in the segmental columns. The lateral drift of these columns consists of elastic deformations and rigid body rotations producing lateral drift, as illustrated in Figure 20.

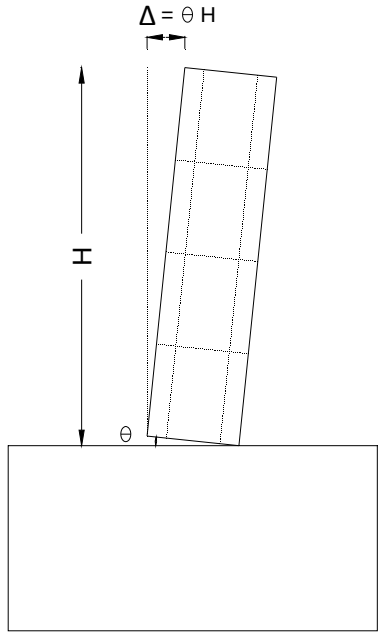

Figure 20. Rigid body motion lateral drift

The contributions of the rigid body motions of the bottommost segment, the second segment, and elastic deformations are illustrated in Figures 21 and 22 for the SEG and SEG-ED2 columns, respectively. The drift at each test run is normalized by the maximum drift at that run. For both columns, the elastic drift was dominant at the small percentages of the DE giving the expected elastic response without noticeable rocking. After that stage, the rocking started to become more dominant and the elastic deformations became less pronounced. For the SEG column with free rocking, the contribution of the second segment rocking was significant between 50% and 120% of the DE. After that, the rocking from the first segment produced more than 80% of the

lateral drift. For the SEG-ED2 column where the rocking of the first two segments was controlled by the energy dissipaters, the contribution of the second segment rocking was very low and the elastic deformation effect was more pronounced due to yielding of the energy dissipaters contributing to it.

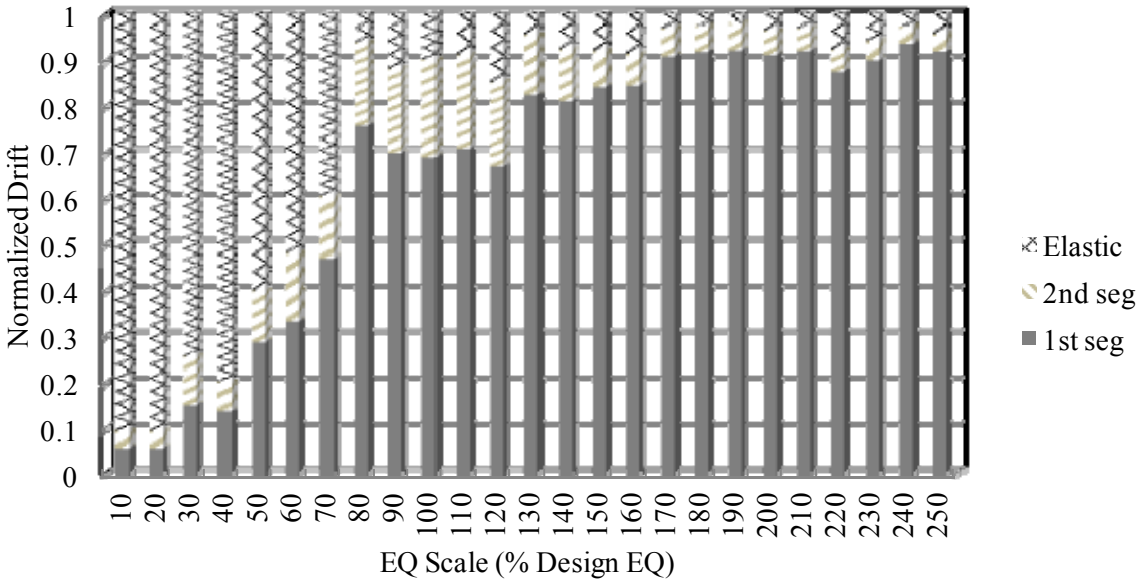

Figure 21. Drift contributions from rigid body motions and elastic deformations for the SEG column

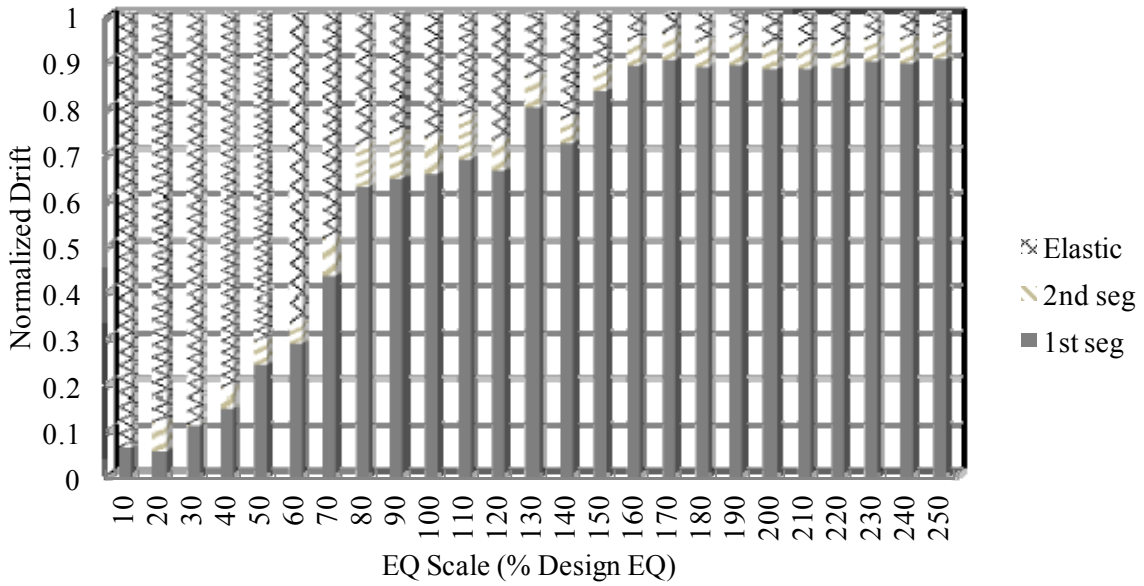

Figure 22. Drift contributions from rigid body motions and elastic deformations for the SEG-ED2 column

Rebar and Energy Dissipaters' Strains

The maximum rebar strains for the RC column and the energy dissipaters' strains for the SEG-ED1, and SEG-ED2 columns at each test are illustrated in Figure 23. The RC column experienced yielding at a drift of 1% corresponding to 50% of the DE. The RC column experienced a large strain increase at 130% of the DE followed by a larger increase in strain of almost 80,000 microstrain that led to the rupture of the rebar at 140% of the DE. The rupture of the rebar was already observed by the popping sound that accompanied it, as explained earlier. For the SEG-ED1 column, due to the short unbonded length of 50 mm chosen, the energy dissipaters yielded at a drift of 0.4% corresponding to 50% of the DE and a large strain was achieved at the DE level followed by rupture of the energy dissipaters with a strain of 256,800 microstrain at a drift of 2.6% corresponding to 120% of the DE. For the SEG-ED2 column, the energy dissipaters yielded at a drift of 0.7% corresponding to 70% of the DE. The strain was limited due to the large unbonded length of 150 mm and no rupture occurred. It is clear that the use of external energy dissipaters is advantageous due to the flexibility of tailoring the unbonded length to achieve the desired performance and because of the possibility of replacing these energy dissipaters after an earthquake. The use of unbonded energy dissipaters also increased the rupture strain for the SEG-ED1 column compared to the bonded rebar in the RC column, where the low cyclic fatigue highly reduced the rupture strain. The use of tension only energy dissipaters in the SEG-ED2 column allowed for energy dissipation in the large cycles only and the bars are not engaged in the lower cycles which reduced the number of yield cycles and prevented the low cyclic fatigue.

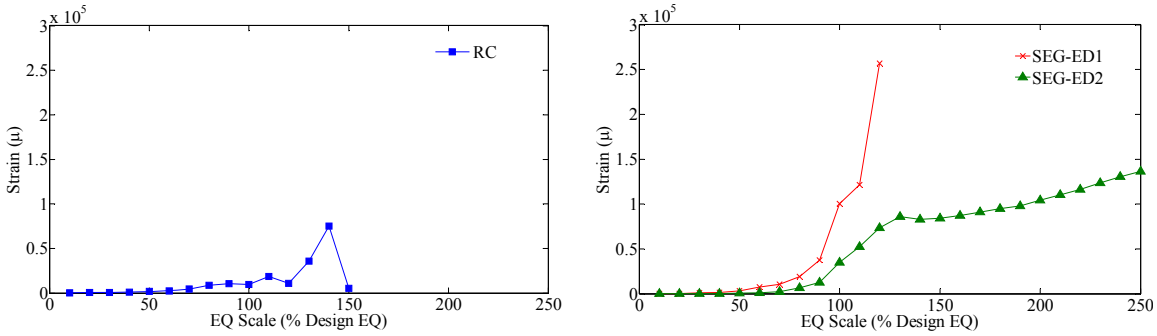

Figure 23. Maximum strains at different stages for a) RC column rebar, and b) external energy dissipaters

Dissipated Energy and Hysteresis Damping

The hysteresis is the property of systems to follow different loading and unloading paths. The hysteresis damping for the cyclic testing is calculated from the specific damping capacity (Y), which is the ratio between the energy dissipated per unit volume of the material, E_D, and the strain energy per unit volume stored in a linear elastic system, E_{S0}, as shown in eq. 2.

$$Y = \frac{E_D}{E_{S0}} \tag{2}$$

A graphical representation of ED and ES0 is shown in Figure 24 (Chopra 2007).

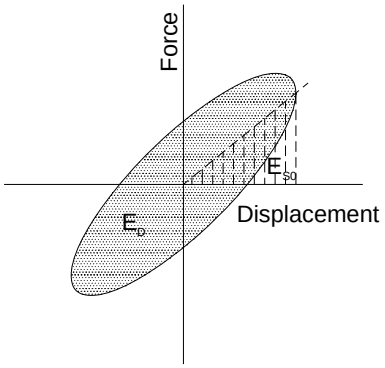

Figure 24. Dissipated energy per unit volume of the material, E_D and elastic strain energy, E_{S0}

The energy dissipated per cycle per unit volume, E_D, is measured as the area enclosed by a hysteresis loop drawn on axes of stress and strain. It can be calculated mathematically using eq. 3.

$$E_D = \sum_{i=1}^{n-1} \left(\frac{F_{i+1} + F_i}{2} \right) \left(\Delta_{i+1} - \Delta_i \right) \tag{3}$$

where, E_D is the dissipated energy (Joules), n is the total number of stress or strain points, F_i is the force at point i (N), and Δ_i is the displacement at point i (m).

The hysteresis damping can be expressed as the equivalent viscous damping and is calculated from the specific damping capacity using eq. 4.

$$\zeta_{eq} = \frac{E_D}{4\pi E_{S0}} \tag{4}$$

The cumulative dissipated energy for the test specimens is illustrated in Figure 25. The energy dissipated by the RC column at any stage was higher than its counterpart of the segmental columns. This was expected since the segmental columns have the deficiency of lower energy dissipation due to their flag shaped hysteresis that dissipates energy through rocking. However, the use of external energy dissipaters highly increased the energy dissipation in the SEG-ED2 column throughout the test runs, while the energy dissipation of the SEG column was much lower until yielding of the PT strands occurred resulting in higher energy dissipation. The cumulative dissipated energy of the RC column was 37% higher than the SEG column at the RC column test end at 200% of the DE. This ratio was reduced to 17% only when comparing the RC and SEG-ED2 columns. However, it should be noted that the energy dissipation of the RC column was achieved

by rebar yielding, fracture, and concrete spalling all generating damages that cannot be restored, while the energy dissipation of the SEG-ED2 column was achieved by rocking which was retrieved during the tests and yielding of the external energy dissipaters which can be easily replaced after a major earthquake.

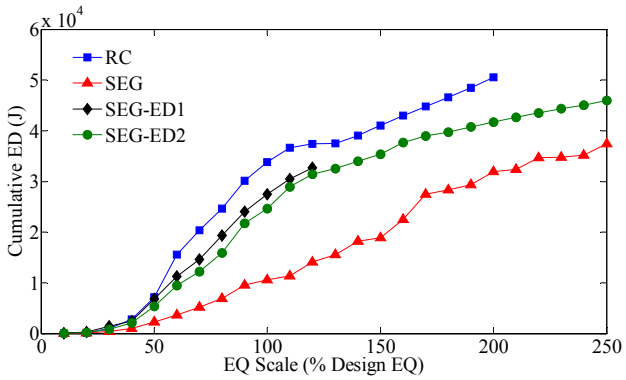

Figure 25. Cumulative dissipated energy for the test specimens at different stages

The hysteresis damping for the columns (as calculated by Eq. 4) is illustrated in Figure 26. The RC column showed a higher average damping that was highly increased after the rupture of the rebar. The average hysteresis damping of the SEg-ED2 column was higher than that of the SEG column due to the larger energy dissipation.

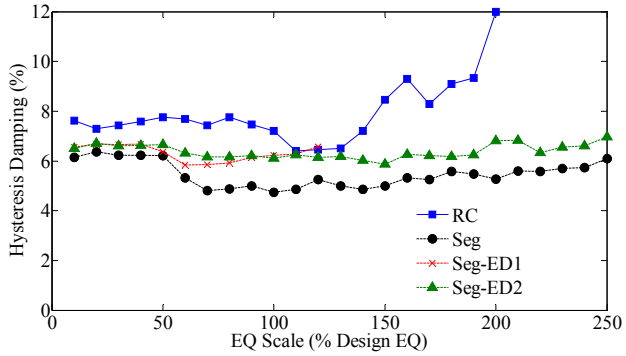

Figure 26. Hysteresis damping for the test specimens at different stages

Conclusion

This paper presented shake-table testing of three proposed damage-resistant segmental double-skin bridge columns with and without external energy dissipaters and an RC column as a reference. The double-skin segmental posttensioned column inherited the combined advantages of all its components as follows: the column benefited from the confinement of the FRP from the double skin section. The columns also utilized the re-centering capability of the unbonded posttensioned system. In addition, the columns accelerate the bridge construction due to the segmental nature and light weight because of the hollow cross section. Energy dissipation was provided by external replaceable bars for columns SEG-ED1 and SEG-ED2.

The columns were subjected to a sequence of scaled ground motions of the Northridge-01 1994 earthquake at Rinaldi receiving station. The ground motion scales started from 10% of the DE up to 250% of the DE with increments of 10%. The rebar fracture in the RC column occurred at 140% of the DE and the column started losing its capacity at 3.4% drift and it lost 20.6% of its capacity at 4.8% drift. The column SEG was able to sustain up to 250% of the DE. However, yielding of the PT strands occurred at 160% of the DE. This yielding was avoided in the column SEG-ED2 by reducing the initial PT force from 54% to 44% of the ultimate strength. The addition of the external energy dissipaters was able to make up for the difference in capacity. It is recommended to maintain the initial PT force under 40% of the ultimate strength to avoid yielding of the PT strands at large drifts.

All the segmental columns exhibited an excellent re-centering capability with only 0.08% maximum residual drift after being subjected to the sequence of ground

motions while the RC column suffered 1.5% residual drift. The SEG-ED2 column was able to achieve energy dissipations and damping close to the reference RC column.

The addition of external energy dissipaters resulted in a favorable behavior with the possibility of replacement after a major earthquake, the possibility to tailor them according to the seismic zone and the required performance, and the control of the unbonded length along with the tension only detail which prevent low cyclic fatigue.

The SEG-ED2 column outperformed the rest of the columns providing a superior candidate for damage-resistant columns in high seismic zones.

Acknowledgments

The authors acknowledge AMSYSCO Post Tensioning corporate for their generous donations of materials used in the tests.

References

Abdelkarim, O. I. and ElGawady, M. A. (2014). "Analytical and Finite-Element Modeling of FRP-Concrete-Steel Double-Skin Tubular Columns." Journal of Bridge Engineering.

ASTM D2290 (2012). "Standard Test Method for Apparent Hoop Tensile Strength of Plastic or Reinforced Plastic Pipe."

Caltrans, S. (2010). Caltrans Seismic Design Criteria, Version.

Chang, K., Loh, C., Chiu, H., Hwang, J., Cheng, C. and Wang, J. (2002). "Seismic behavior of precast segmental bridge columns and design methodology for applications in Taiwan." Taiwan Area National Expressway Engineering Bureau, Taipei, Taiwan in Chinese.

Chopra, A. K. (2007). Dynamics Of Structures, 3/E, Pearson Education India.

Chou, C.-C., Chang, H.-J. and Hewes, J. T. (2013). "Two-plastic-hinge and two dimensional finite element models for post-tensioned precast concrete segmental bridge columns." Engineering Structures 46: 205-217.

Chou, C. C. and Chen, Y. C. (2006). "Cyclic tests of post-tensioned precast CFT segmental bridge columns with unbonded strands." Earthquake engineering & structural dynamics 35(2): 159-175.

Dawood, H., ElGawady, M. and Hewes, J. (2011). "Behavior of Segmental Precast Posttensioned Bridge Piers under Lateral Loads." Journal of Bridge Engineering 17(5): 735-746.

ElGawady, M., Booker, A. J. and Dawood, H. M. (2010). "Seismic behavior of posttensioned concrete-filled fiber tubes." Journal of Composites for Construction 14(5): 616-628.

ElGawady, M. A. and Dawood, H. M. (2012). "Analysis of segmental piers consisted of concrete filled FRP tubes." Engineering Structures 38: 142-152.

ElGawady, M. A. and Sha'lan, A. (2010). "Seismic behavior of self-centering precast segmental bridge bents." Journal of Bridge Engineering 16(3): 328-339.

FEMA, A. (2006). 445, Next-generation performance-based seismic design guidelines-program plan for new and existing buildings, Redwood City.

Gibson, N., Filiatrault, A. and Ashford, S. A. (2002). "Impulsive seismic response of bridge column-cap beam joints." ACI Structural Journal 99(4).

Guerrini, G. and Restrepo, J. (2013). Seismic response of composite concrete-dual steel shell columns for accelerated bridge construction. Proc., 7th National Seismic Conf. on Bridges and Highways, MCEER.

Han, L.-H., Tao, Z., Liao, F.-Y. and Xu, Y. (2010). "Tests on cyclic performance of FRP–concrete–steel double-skin tubular columns." Thin-Walled Structures 48(6): 430-439.

Hewes, J. T. (2000). Seismic response of unbonded post-tensioned precast concrete segmental bridge columns, University of California, San Diego.

Hewes, J. T. and Priestley, M. N. (2002). Seismic design and performance of precast concrete segmental bridge columns.

Ichikawa, S., Matsuzaki, H., Moustafa, A., ElGawady, M. A. and Kawashima, K. (2016). "Seismic-Resistant Bridge Columns with Ultrahigh-Performance Concrete Segments." Journal of Bridge Engineering: 04016049.

Japan Road Association (2002). "Design specifications of highway bridges, Part V seismic design." Maruzen, Tokyo, Japan.

Jeong, H., Sakai, J. and Mahin, S. A. (2008). "Shaking table tests and numerical investigation of self-centering reinforced concrete bridge columns." Pacific Earthquake Engineering Research Center. University of California, Berkeley. Public Works Research Institute, Tsukuba, Japan.

Kim, T.-H., Lee, H.-M., Kim, Y.-J. and Shin, H. (2010). "Performance assessment of precast concrete segmental bridge columns with a shear resistant connecting structure." Engineering Structures 32(5): 1292-1303.

Leitner, E. J. and Hao, H. (2016). "Three-dimensional finite element modelling of rocking bridge piers under cyclic loading and exploration of options for increased energy dissipation." Engineering Structures 118: 74-88.

Mander, J. B. and Cheng, C.-T. (1997). Seismic design of bridge piers based on damage avoidance design, National Center for Earthquake Engineering Research, State Univ. of New York at Buffalo, Buffalo, NY.

Marriott, D., Pampanin, S. and Palermo, A. (2009). "Quasi-static and pseudo-dynamic testing of unbonded post-tensioned rocking bridge piers with external replaceable dissipaters." Earthquake Engineering & Structural Dynamics 38(3): 331-354.

Montague, P. (1978). "The experimental behaviour of double-skinned, composite, circular cylindrical shells under external pressure." Journal of Mechanical Engineering Science 20(1): 21-34.

Ou, Y.-C., Wang, P.-H., Tsai, M.-S., Chang, K.-C. and Lee, G. C. (2009). "Large-scale experimental study of precast segmental unbonded posttensioned concrete bridge columns for seismic regions." Journal of structural engineering 136(3): 255-264.

Ou, Y. C., Tsai, M. S., Chang, K. C. and Lee, G. C. (2010). "Cyclic behavior of precast segmental concrete bridge columns with high performance or conventional steel reinforcing bars as energy dissipation bars." Earthquake Engineering & Structural Dynamics 39(11): 1181-1198.

Ozbakkaloglu, T. and Idris, Y. (2014). "Seismic behavior of FRP-high-strength concrete–steel double-skin tubular columns." Journal of Structural Engineering 140(6): 04014019.

Palermo, A., Pampanin, S. and Marriott, D. (2007). "Design, modeling, and experimental response of seismic resistant bridge piers with posttensioned dissipating connections." Journal of Structural Engineering 133(11): 1648-1661.

Pampanin, S., Nigel Priestley, M. and Sritharan, S. (2001). "Analytical modelling of the seismic behaviour of precast concrete frames designed with ductile connections." Journal of Earthquake Engineering 5(3): 329-367.

Phan, V., Saiidi, M. S., Anderson, J. and Ghasemi, H. (2007). "Near-fault ground motion effects on reinforced concrete bridge columns." Journal of structural engineering 133(7): 982-989.

Priestley, M. N. and Tao, J. R. (1993). "Seismic response of precast prestressed concrete frames with partially debonded tendons." PCI Journal 38(1): 58-69.

Sehhati, R., Rodriguez-Marek, A., ElGawady, M. and Cofer, W. F. (2011). "Effects of near-fault ground motions and equivalent pulses on multi-story structures." Engineering Structures 33(3): 767-779.

Shim, C. S., Chung, C.-H. and Kim, H. H. (2008). "Experimental evaluation of seismic performance of precast segmental bridge piers with a circular solid section." Engineering Structures 30(12): 3782-3792.

Solberg, K., Mashiko, N., Mander, J. and Dhakal, R. (2009). "Performance of a damage-protected highway bridge pier subjected to bidirectional earthquake attack." Journal of structural engineering 135(5): 469-478.

Teng, J., Yu, T., Wong, Y. and Dong, S. (2005). "Innovative FRP-steel-concrete hybrid columns." Advances in Steel Structures 1: 545-554.

Teng, J., Yu, T., Wong, Y. and Dong, S. (2007). "Hybrid FRP–concrete–steel tubular columns: concept and behavior." Construction and Building Materials 21(4): 846-854.

Trono, W., Jen, G., Panagiotou, M., Schoettler, M. and Ostertag, C. P. (2014). "Seismic response of a damage-resistant recentering posttensioned-HYFRC bridge column." Journal of Bridge Engineering 20(7): 04014096.

Wang, J. C., Ou, Y. C., Chang, K. C. and Lee, G. C. (2008). "Large-scale seismic tests of tall concrete bridge columns with precast segmental construction." Earthquake Engineering & Structural Dynamics 37(12): 1449-1465.

Wong, Y., Yu, T., Teng, J. and Dong, S. (2008). "Behavior of FRP-confined concrete in annular section columns." Composites Part B: Engineering 39(3): 451-466.

Zhang, Q. and Alam, M. S. (2015). "Evaluating the Seismic Behavior of Segmental Unbounded Posttensioned Concrete Bridge Piers Using Factorial Analysis." Journal of Bridge Engineering 21(4): 04015073.

VI. SEISMIC BEHAVIOR OF DAMAGE-RESISTANT SEGMENTAL HOLLOW-CORE BRIDGE COLUMNS FOR ACCELERATED BRIDGE CONSTRUCTION

Ayman Moustafa[1] and Mohamed ElGawady[2]

Abstract

This paper investigates the seismic behavior of a proposed damage-resistant segmental hollow-core bridge column system for accelerated bridge construction. The system is investigated with and without external energy dissipaters using two columns. The cross section is a double-skin section composed of an outside glass fiber reinforced polymer tube (GFRP), an inside steel tube, and concrete cast in between the two. The columns combine the advantages of accelerated bridge construction and self centering due to rocking with high energy dissipation from the steel bars. The columns were subjected to a sequence of scaled near-fault pulse-like ground motions. The columns sustained no noticeable damage and no residual drift after the sequence of motions up to 250% of the design earthquake, which caused a peak drift ratio of 8.85%. The apparently simple nature of free rocking motion reveals complex dynamic behavior along with chaotic and butterfly effect. That is, a minute perturbation can cause significant effects on the rocking response. The energy of the system is investigated to better comprehend the dynamic behavior of rocking under forced vibrations. An analytical model is developed to predict the dynamic capacity of the segmental hollow-core bridge columns.

[1] Graduate research assistant, Department of Civil, Architectural, and Environmental Engineering, Missouri University of Science and Technology, USA E-mail: ampyf@mst.edu
[2] Benavides Associate professor, Department of Civil, Architectural, and Environmental Engineering, Missouri University of Science and Technology, USA E-mail: elgawadym@mst.edu

Key words: Bridge columns, energy dissipation, seismic design, segmental columns, seismic resistant columns, self centering, shaking table test.

Introduction

The Federal Highway Administration (FHWA) and many state departments of transportation (DOTs) are actively promoting accelerated bridge construction (ABC) to minimize construction-related impacts to the traveling public and to enhance work-zone safety. The ABC columns offer the potential benefits of reduced construction time, minimum traffic disruptions, reduced life-cycle cost, and improved construction quality and safety. Current seismic design provisions are intended to prevent bridges collapse under maximum considered earthquake (FEMA 2006) while allowing some damage during a design earthquake (DE) in the form of rebar yielding and concrete spalling (Caltrans 2010). Larger damage would accumulate in a reinforced concrete (RC) column under near-fault pulse-like ground motions compared to that of equal magnitude near-fault motions without pulse (Gibson et al. 2002; Phan et al. 2007; Sehhati et al. 2011). This damage results in excessive residual drift which may inhibit bridge repair (Jeong et al. 2008). For example, the Japanese seismic design specifications are limiting the residual drifts of columns to 1% (Japan Road Association 2002).

Unbonded post-tensioned rocking columns (PTRC) have been investigated to reduce excessive residual drift. PTRCs can consist of a single-segment (Palermo et al. 2007; Shim et al. 2008; Marriott et al. 2009; Trono et al. 2014) or multi-segments (Chang et al. 2002; Chou and Chen 2006; ElGawady et al. 2010; Ichikawa et al. 2016). PTRCs are typically designed so the PT tendons remain elastic under earthquake ground motions;

hence, PTRCs dissipate energy through viscous and radiation damping. Therefore, multi-segment columns generally displayed relatively higher energy dissipation than single-segment due to the increase in the number of interface joints where rocking can take place (Hewes 2000).

The majority of PTRCs were investigated under static cyclic loading (Mander and Cheng 1997; Hewes and Priestley 2002; Chou and Chen 2006; Palermo et al. 2007; Shim et al. 2008; Wong et al. 2008; Marriott et al. 2009; Solberg et al. 2009; Ou et al. 2009; ElGawady et al. 2010; ElGawady and Sha'lan 2010; Kim et al. 2010; Ou et al. 2010; Ichikawa et al. 2016). During these static cyclic tests, peak drifts ranging from 3.5% to 11% and residual drifts of less than 1% were reported. Limited number of studies investigated the dynamic characteristics of PTRC having 1/5 to 1/3 scales under shaking table tests. The tests showed the viability of using PTRC in high seismic regions. However, these tests used shear keys and wet-joints, a monolithic first segment, or heavily reinforced first segment which would increase the column construction time and compromise the accelerating construction nature of PTRC.

The nature of rocking is inherently complex and the forced rocking of the segmental columns with post-tensioning adds more layers of complexity. Housner 1963 shed the light on understanding the free rocking response of rectangular rigid blocks by developing piecewise equations of motion to predict rocking periods and energy dissipaters. However, Lipscombe 1990 disproved the model experimentally for aspect ratios of less than four. Peña et al. 2007 used complex coupled rocking rotations and discrete element methods to predict the rocking response of four specimens. They found that repeatability of the rocking tests under random vibration did not exist. ElGawady et

al. 2011 investigated the effect of interface material on the rocking behavior of free rocking blocks. The tests were repeatable for higher for high amplitudes and had high scatter at lower amplitudes. In this article, the complex rocking behavior of hollow-core segmental columns was investigated using the energy of the system.

Both analytical and finite element models PTRC were also developed for segmental columns (Pampanin et al. 2001; Palermo et al. 2007; Dawood et al. 2011; ElGawady and Dawood 2012; Chou et al. 2013; Zhang and Alam 2015; Leitner and Hao 2016). The models were able to predict the capacity of the investigated columns under static cyclic loading. The models were employed in some design guidelines (ACI 2003; fib 2004; NZS 2006). However, all these models deal with static loading and the effect of dynamic loading on the analytical model needs to be investigated.

Research Significance

The apparently simple nature of free rocking motion reveals complex dynamic behavior along with chaotic and butterfly effect. That is, a minute perturbation can cause significant effects on the rocking response. This behavior is attributed to the sensitive dependence of the solution on the initial conditions. Hence, the behavior of PTRC needs to be investigated under dynamic load. Currently, the literature includes very limited number of dynamic tests on segmental columns. This manuscript investigates the behavior of segmental columns subjected to near-fault ground motion. The energy of the system is utilized to better understand the behavior and provide an insight on rocking under ground motion excitations.

An analytical model is provided in this manuscript to predict the capacity of the hollow-core segmental columns under dynamic loading.

Experimental Program

Overview of the Test Specimens

Two columns were experimentally investigated including a segmental double-skin column, hereinafter denoted as SEG, and a segmental double-skin column with external energy dissipaters, hereinafter denoted as SEG-ED. The SEG column had no reinforcement other than the internal unbonded post-tension (PT) strands. The SEG-ED was designed to sustain the maximum considered earthquake (MCE) without rupture of the external energy dissipaters.

The columns' elevations and cross sections along with the test setup are illustrated in Figures 1 and 2 for the SEG and SEG-ED columns, respectively. The columns' height measured from the top of the footing to the center of the mass was 1800 mm, resulting in an aspect ratio of approximately 6. The aspect ratio is defined as the height of the column divided by its diameter. The columns consisted of four segments of 300 mm high each. The columns had identical outside diameter of 300 mm and identical inside diameter of 175 mm. Each segmental column had four 12.7 mm diameter seven wire strands PT, each with a cross sectional area of 99 mm^2 as the main reinforcement of the column. Column SEG-ED had two external A36 steel bars with a diameter of 8 mm and unbonded length of 150 mm at the north and south directions of the column. These bars were fixed to the foundation using a stiff angle bolted in the foundation using three epoxy glued anchor wedges with a diameter of 16 mm each. The tension only bars were connected from one end to the segments through a rigid thick plate attached to the second segment with the bars passing through the plate. The bars were threaded at the ends and thick washers and double nuts were used to tighten the bars and to allow tension only. The rigid plates with

oval shaped holes were able to slide without friction in compression. The bars were lathed from a diameter of 15.6 mm to the desired diameter at the specified unbonded lengths. The energy dissipaters were connected to the second segment providing controlled rocking for the bottom two segments, where most of the rocking is expected.

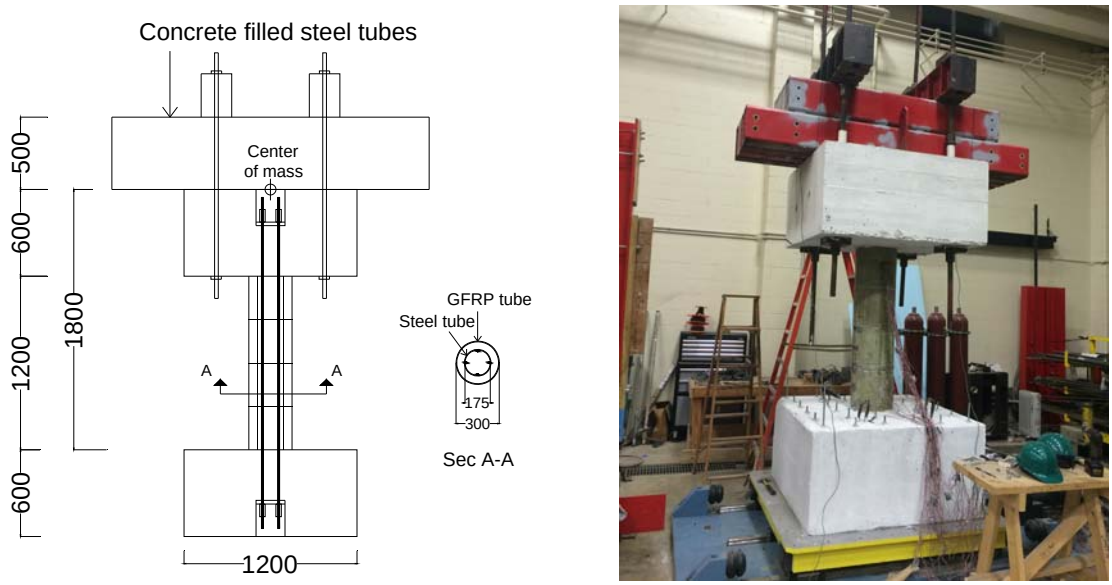

Figure 1. Configuration and dimensions of the SEG column (unit: mm)

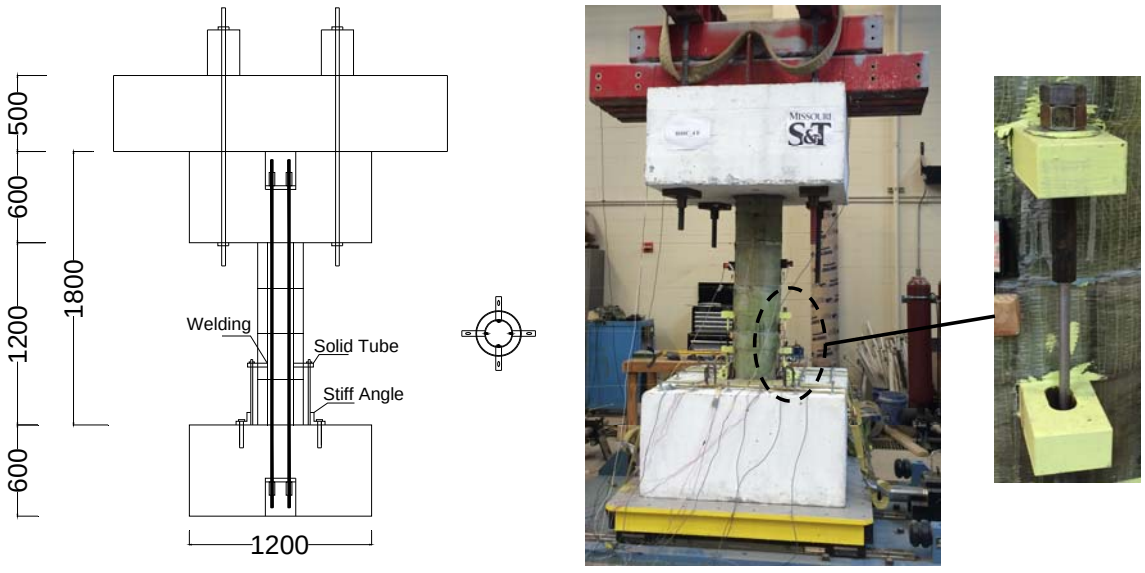

Figure 2. Configuration and dimensions of the SEG-ED column (units: mm)

Material Characteristics

The concrete compressive strength was 35 MPa. The inner steel tube thickness was 4.7 mm. The outer tube consisted of four layers of unidirectional glass fiber reinforced polymers and Tyfo S epoxy by FYFE© with a total thickness of 5 mm. Three specimens of GFRP hoops were tested according to ASTM D2290 2012. The average ultimate tensile strength in the fiber direction was 352 MPa. The elongation at break was 2.31%. The strands were distributed along the edge of the hollow part of the cross section to maximize the distance of the strands to the neutral axis. The PT strands had a diameter of 12.7 mm, a yield stress of 1675 MPa, and an ultimate strength of 1861 MPa. The external energy dissipaters were low carbon A36 steel bars. The stress-strain curves for three specimens of the A36 steel are illustrated in Figure 3.

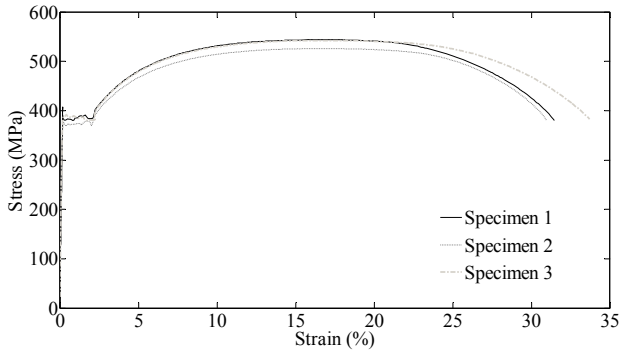

Figure 3. Stress-strain curves for the external energy dissipaters

Construction of the Columns

The system was intended for ABC with precast segments stacked on top of each other on site and post-tensioned together. This process was done at the Highbay laboratory at Missouri University of Science and Technology and took less than 8 hours for the ¼ scale

columns. However, because it was not practical to precast four segments only, the columns were constructed using match-casting technique as follows:

1- The foundation of the column was precast with a groove to accommodate the post tension anchorage.

2- The segments were match-cast one by one with the foundation being the bottom form for the bottommost segment and each segment being the bottom surface of the one on top of it (Figure 4). The segments were separated using strong paper towels to provide the necessary match casting with a rough surface without direct contact between the segments.

3- The column head was installed on top of the column.

4- The PT strands were passed through the segments and anchored to the foundation and the column head.

5- The PT force was applied in steps of 25% of the jacking force in each strand to maintain the column's balance.

6- The concrete filled steel tubes mass was then installed on top of the column head and post-tensioned to it using Dywidag bars.

7- The external energy dissipaters were attached to the stiff angle at the foundation and the solid plate at the segments for the column SEG-ED.

Figure 4. Match-casting of the columns

Test Setup and Loading Sequence

The columns were fixed to a uni-axial shaking table using 36 all-threaded bars, each with a capacity of 45 kN. The shaking table is running using a closed loop controller that can use either displacement or acceleration control. Six accelerometers were used to measure the horizontal accelerations on the shaking table, the center of the column head, and the center of mass. Eight string potentiometers were used to measure the horizontal displacements along the heights of the columns. Twelve linear potentiometers were mounted on the column to measure the vertical openings and horizontal sliding between the segments. Load cells were placed at the north and south strands to measure the forces in the strands. Strain gages were attached to the external energy dissipaters at the unbonded length.

The mass atop the column was provided by a 1200 mm x 1200 mm x 800 mm column reinforced concrete stub and eight concrete filled steel tubes (CFTs) each having

a cross section of 600 mm x 500 mm. Four of these CFTs each had a length of 2200 mm and the other four each had a length of 1925 mm. The tubes were post-tensioned to the column head with a total weight of 54 kN.

Each column was subjected to a sequence of a scaled Northridge-01 1994 earthquake at "Rinaldi Receiving Station" which is a near-fault pulse-like ground motion. The selected ground motion was scaled to the design spectrum (Figure 5), by matching the spectral acceleration at the column's first mode (Sa(T1)) to the design response spectrum. Hereinafter, the DE will refer to the design earthquake spectrum used in the current study. The columns were assumed to be in a high seismic zone in San Francisco, California, soil class D; where the prototype column is assumed. The design response spectrum (DE) with a probability of excess of 10% in 50 years and the maximum considered earthquake (MCE) response spectrum with a probability of excess of 2% in 50 years are illustrated in Figure 5.

The time coordinate of the input accelerations was compressed by a factor of $\sqrt{0.25} = 0.5$ for similitude according to the scale factor of 4. The columns were subjected to a sequence of the scaled ground motion starting at 10% of the DE to 250% of the DE with steps of 10% increments giving a total of 25 ground motions. A white noise test with duration of 75 s and 0.02g amplitude of acceleration was run after each ground motion excitation to determine the updated fundamental period of the column.

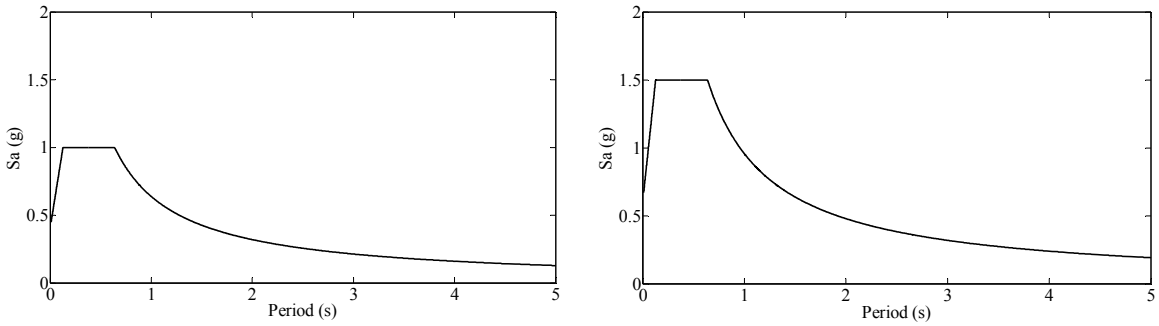

(a) (b)

Figure 5. a) Design earthquake spectrum and b) maximum considered earthquake spectrum

Experimental Results and Discussion

General Behavior

The column SEG displayed a rocking behavior at the interface between the first segment and the foundation being the most observed behavior during the tests. No apparent residual drifts were observed at all during the tests. No damage in the GFRP was noticed and the damage of the core concrete was examined after the test and was found to be minor. The column was able to resist the full sequence of the scaled earthquakes up to the 250% of the DE, where the test was terminated because the maximum velocity of the shaking table was reached. However, the analysis of the results showed yielding of the PT strands occurred at 160% of the DE, as will be shown in a later section. It should be noted that this exceeded the MCE, which corresponds to 150% of the DE.

The column SEG-ED outperformed the SEG column. It was able to sustain the full sequence of the scaled earthquakes up to the maximum of 250% of the DE without any noticeable damage or residual drift. As designed, the external energy dissipaters yielded to improve the energy dissipation. These dissipaters can be easily replaced after a

major earthquake of an intensity of the MCE or higher. The PT yielding was avoided in this column by reducing the initial PT force and relying on the energy dissipaters to supply the difference in capacity. The initial PT force was reduced from 54% to 44% of the ultimate strength. This initial PT is still in the economic range.

Hysteretic Behavior

Samples of the lateral force versus lateral drifts for the SEG and SEG-ED columns are illustrated in Figures 6 and 7, respectively, for different intensities of the simulated earthquakes as percentages of the DE. The lateral displacements were obtained by subtracting the table displacement from the displacement at the center of mass; both recorded by the string pots. The drift was then obtained by dividing the lateral displacement by the height of the column from the top of the footing to the center of mass. The lateral force was obtained by multiplying the mass on top of the column times the acceleration at the center of mass. The columns maintained the nearly symmetric response throughout the tests despite the yielding of the PT strands in the SEG column. The yielding of the PT strands led to losses in the PT force due to the inelastic response (Priestley and Tao 1993). However, the column still responded in the normal rocking mode but with lower PT force. The columns had no measurable residual drifts. The drift at zero force for the maximum force and large amplitude cycles was higher in the SEG-ED column compared to the SEG column due to yielding of the energy dissipaters. This drift at zero force was recovered in both columns by the PT force.

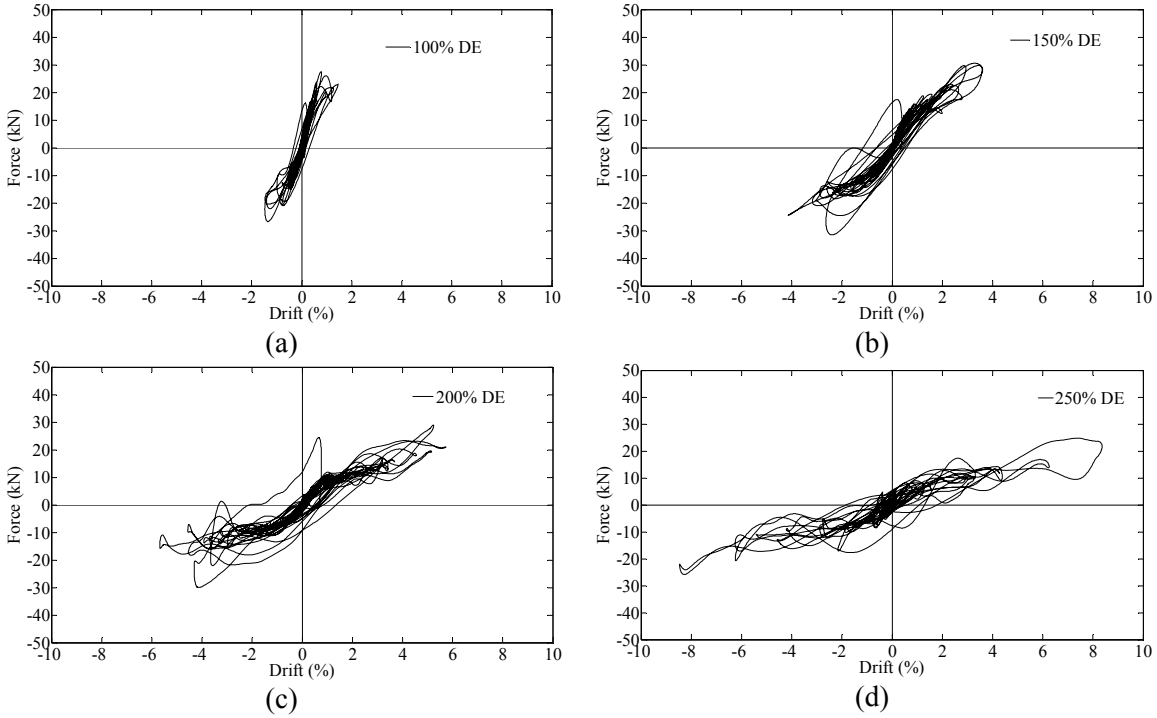

Figure 6. Measured forces versus drift ratios for the SEG column at different stages of the test at: a) DE, b) MCE, c) 200% DE, and d) SEG column test end

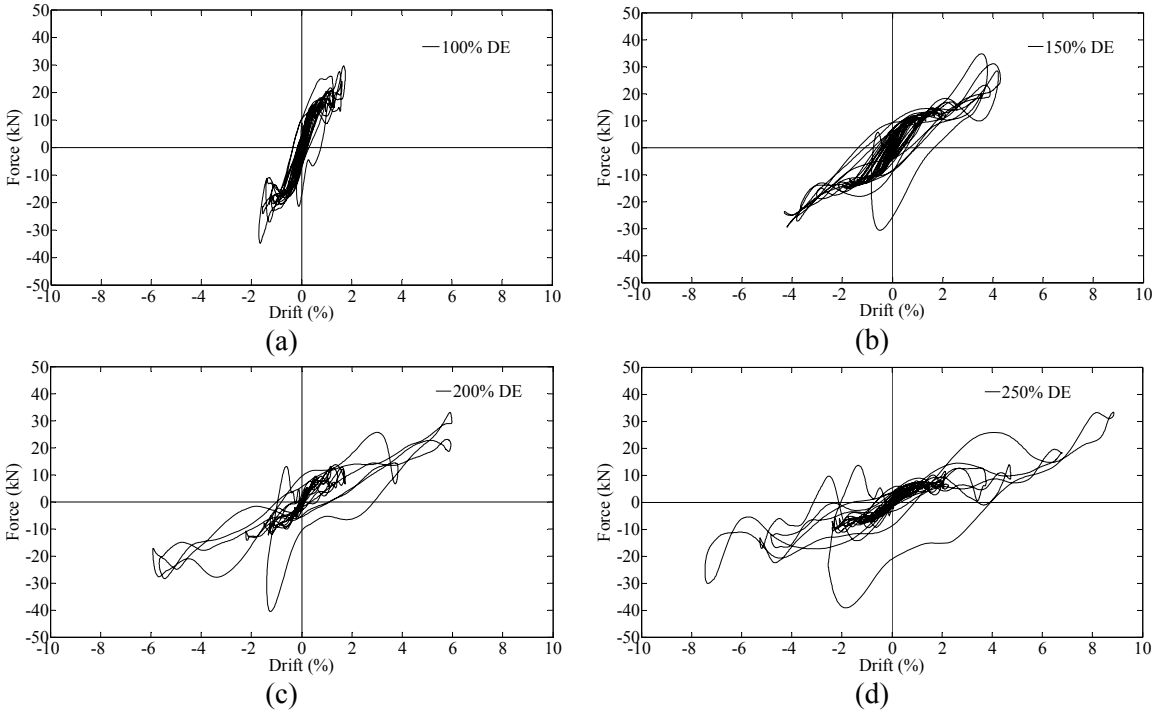

Figure 7. Measured forces versus drift ratios for the SEG-ED column at different stages of the test at: a) DE, b) MCE, c) 200% DE, and d) SEG-ED column test end

The envelopes of the lateral force versus lateral drift, known as dynamic push over curve, for the columns are illustrated in Figure 8 for comparison. Each point on the curve represents the maximum force and the corresponding drift for one of the tests from the sequence of 10% to 250% of the DE. The capacities of the two columns were the same (34.4 kN and 34.7 kN for the SEG and SEG-ED columns, respectively). The SEG column was able to sustain the imposed ground motions up to 4.55% drift followed by a reduction of strength of 22% at 160% of the DE due to yielding of the PT strands. It should be noted that the SEG column was still able to sustain the ground motions up to 250% of the DE with the modified strength due to PT losses. The maximum drift for the SEG column was 8.25%. The SEG-ED column, on the other hand, had a small reduction in capacity of only 6% at 180% of the DE due to stress softening of the energy dissipaters. The use of external energy dissipaters in this study enabled their replacement which would result in restoring the capacity of the column. The ultimate drift of the SEG-ED column was 8.85%. The initial stiffness of the two columns was also the same.

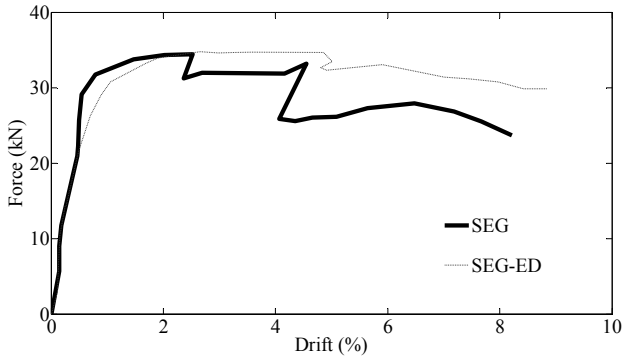

Figure 8. Envelopes of forces versus drift ratios

Post-Tension Forces

Two load cells; one with a capacity of 220 kN and the other with a capacity of 440 kN were installed in the direction of loading on the southern and the northern PT strands, respectively, to monitor the progress of the PT force during the tests. The strands had a

yield force of 165.3 kN and an ultimate strength of 183.7 kN. The maximum PT load progress during the tests is illustrated in Figure 9. The figure shows yielding at 160% of the DE for the SEG column followed by a drop in the maximum PT force and then an increase of the force in the inelastic region up to 179.2 kN at 250% of the DE at the test end. For the SEG-ED2 column, the external energy dissipaters provided an extra support with the controlled rocking reducing the maximum PT force to 155.7 kN at 250% of the DE. This reduction in the maximum PT force was achieved by reducing the initial PT force from 54% to 44% of the ultimate strength along with the external energy dissipaters.

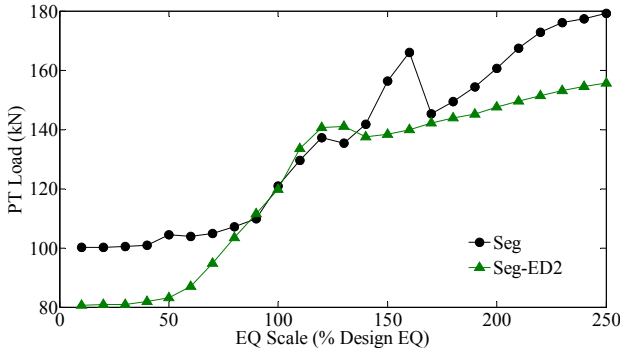

Figure 9. Maximum PT force for columns SEG and SEG-ED at different stages of the test

Dissipated Energy and Hysteresis Damping

The hysteresis is the property of systems to follow different loading and unloading paths. The hysteresis damping for the cyclic testing is calculated from the specific damping capacity (Y), which is the ratio between the energy dissipated per unit volume of the material, E_D, and the strain energy per unit volume stored in a linear elastic system, E_{S0}, as shown in eq. 1.

$$Y = \frac{E_D}{E_{S0}} \tag{1}$$

A graphical representation of ED and ES0 is shown in Figure 10 (Chopra 2007).

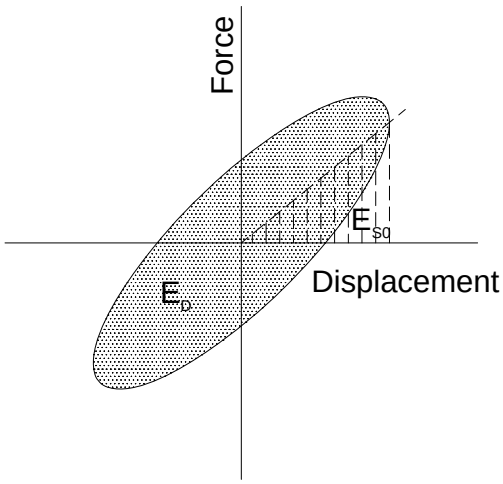

Figure 10. Dissipated energy per unit volume of the material, E_D and elastic strain energy, E_{S0}

The energy dissipated per cycle per unit volume, E_D, is measured as the area enclosed by a hysteresis loop drawn on axes of stress and strain. It can be calculated mathematically using eq. 2.

$$E_D = \sum_{i=1}^{n-1} \left(\frac{F_{i+1} + F_i}{2} \right) \left(\Delta_{i+1} - \Delta_i \right) \tag{2}$$

where, E_D is the dissipated energy (Joules), n is the total number of stress or strain points, F_i is the force at point i (N), and Δ_i is the displacement at point i (m).

The hysteresis damping can be expressed as the equivalent viscous damping and is calculated from the specific damping capacity using eq. 3.

$$\zeta_{eq} = \frac{E_D}{4\pi E_{S0}} \quad (3)$$

The cumulative dissipated energy for the test specimens is illustrated in Figure 11. The use of external energy dissipaters highly increased the energy dissipation in the SEG-ED column throughout the test runs, while the energy dissipation of the SEG column was much lower until yielding of the PT strands occurred resulting in higher energy dissipation. The cumulative dissipated energy of the SEG-ED column was 23% higher than the SEG column.

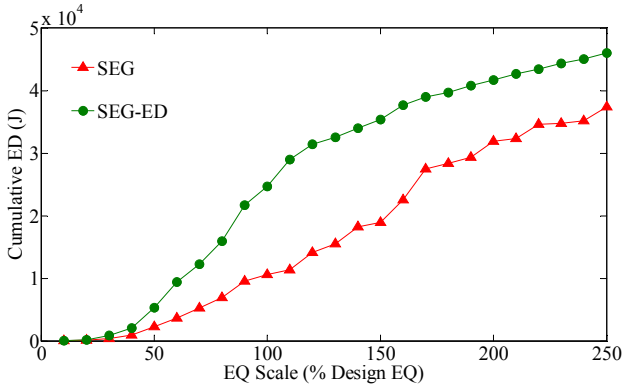

Figure 11. Cumulative dissipated energy for the test specimens at different stages

The hysteresis damping for the columns (as calculated by Eq. 3) is illustrated in Figure 12. The average hysteresis damping of the SEG-ED column was higher than that of the SEG column due to the larger energy dissipation.

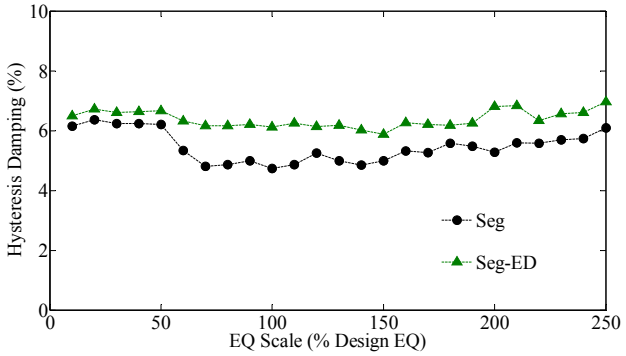

Figure 12. Hysteresis damping for the test specimens at different stages

Viscous Damping

The viscous damping ratio can be calculated using the logarithmic decrement method for the measured accelerations. The value of the damping ratio can be calculated using Eq. 4.

$$\zeta = \frac{1}{2n\pi} \ln\left(\frac{A_0}{A_n}\right) \tag{4}$$

where, A_0 is the initial acceleration amplitude and A_n is the acceleration amplitude after n cycles.

A sample acceleration output for damping calculations for each of the specimens is illustrated in Figure 13.

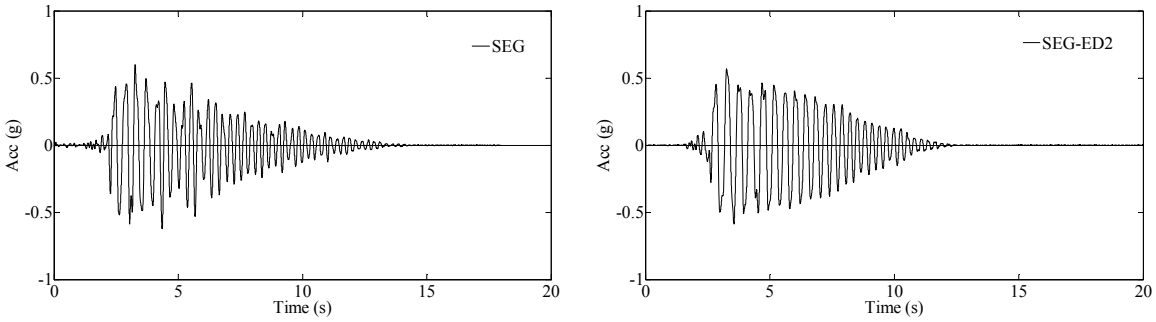

Figure 13. Sample acceleration curve in time domain for the test specimens

The change in the viscous damping is illustrated in Figure 14. The figure shows an increasing trend of the damping ratio of the RC column with the increase in the ground motion amplitude. This increase was due to the increase of the driving force along with the damage. The rebar fracture in the RC column at 140% of the DE caused the damping to increase significantly due to the reduction in column stiffness and the increased damage. After that, the damping ratio started to decrease due to the reduction of the driving force, which agrees with the force-drift curve shape. The viscous damping in the segmental columns differs in concept than the RC column. The sources of damping in

these columns consist of elastic behavior, rocking, and energy dissipaters. A constant damping occurred in the column SEG up to 160% DE, where the PT yielding resulted in an increase in damping. Constant damping was governing in the SEG-ED column up to yielding of the energy dissipaters that resulted in a slightly increasing trend. The viscous damping of the SEG-ED column was larger than the SEG column due to the energy dissipaters' effect.

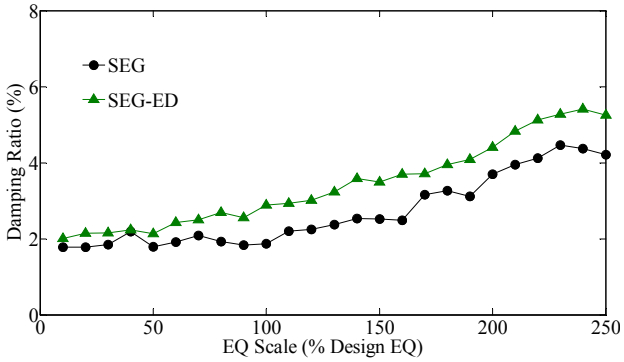

Figure 14. Viscous damping for the test specimens at different stages

Radiation Damping

The radiation damping is the damping resulting normal to the contact between the segments and between the first segment and the foundation due to rocking (ElGawady et al. 2011). The nature of the radiation damping is discussed later. The radiation damping can be estimated by the logarithmic decrement method similar to the viscous damping but for the vertical rocking displacement values. The value of the radiation damping can be calculated using Eq. 5.

$$\zeta_R = \frac{1}{2n\pi} \ln\left(\frac{d_{R0}}{d_{Rn}}\right) \tag{5}$$

where, d_{R0} is the initial rocking displacement amplitude and d_{Rn} is the rocking displacement amplitude after n cycles.

A sample column rocking displacement response for damping calculations for the specimens is illustrated in Figure 15.

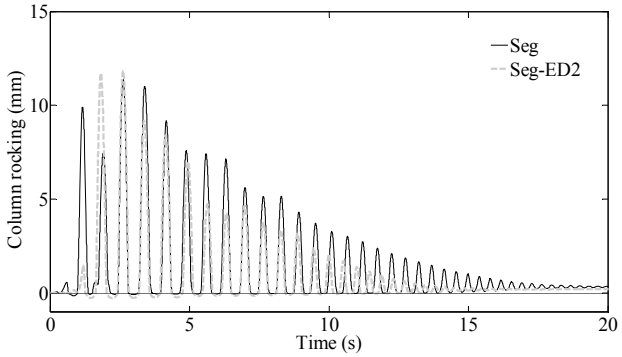

Figure 15. Sample column rocking displacement curve in time domain for the test specimens

The change in the radiation damping is illustrated in Figure 16. No rocking occurred at the beginning of the test and the elastic response was dominant and no radiation damping existed. A constant radiation damping occurred in the column SEG throughout the tests. An increasing trend in the radiation damping was observed in the SEG-ED column due to yielding of the energy dissipaters. The radiation damping of the SEG-ED column was larger than the SEG column due to the energy dissipaters' effect.

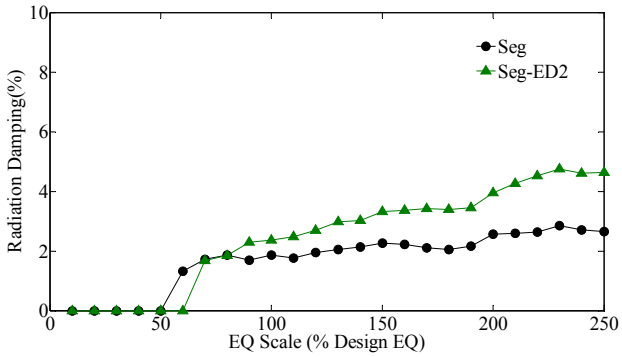

Figure 16. Radiation damping for the SEG and SEG-ED specimens at different stages

The rocking behavior is the dominant behavior in the segmental columns; hence the radiation damping is the main source for the viscous damping. This can be illustrated in Figure 17, where a comparison between the radiation damping and viscous damping for the SEG and SEG-ED specimens is presented. The figure shows a transition between the elastic viscous damping to the radiation damping for both columns. The effect of the elastic damping becomes very small as shown in the difference between the total viscous damping and the radiation damping curves. For the SEG column, the viscous damping increased at 160% of the DE due to yielding of the PT bars causing inelastic damping, while the radiation damping was constant. For the column SEG-ED, the radiation damping was dominant and the energy dissipaters imposed controlled rocking which affected its radiation damping, unlike the free rocking of the SEG column.

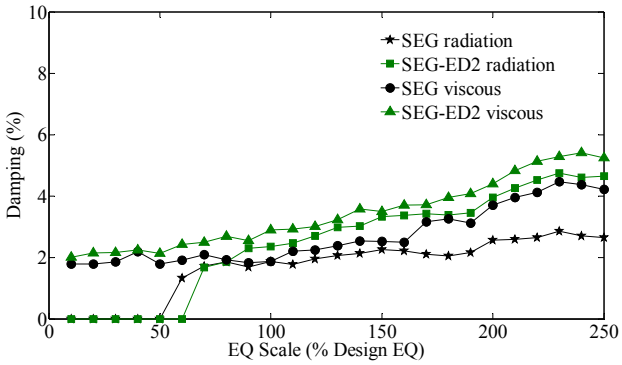

Figure 17. Comparison between radiation and viscous damping for the SEG and SEG-ED specimens at different stages

Energy of the System

The energy of a system is calculated by integrating the forces of the equation of motion with respect to displacements (Chopra 2007). The energy of the rocking system consists of different terms. During the excitation, the total input energy (E_{tot}) is the summation of

the hysteretic energy (E_{hys}), the kinetic energy (E_k), the potential energy (E_p), the elastic energy (E_e), the viscous damping energy (E_V), and the radiation energy from rocking (E_R), which is mainly concentrated at the bottommost two segments (E_{R1} and E_{R2} for the first and second segments, respectively). This is shown in eq. 6.

$$E_{tot} = E_{hys} + E_k + E_p + E_e + E_v + E_R \tag{6}$$

At the end of each test after the free vibration ($t = \infty$), the total energy is equal to the entire amount of energy dissipated during the test, because at that time the kinetic and potential energies are both equal to zero, as shown in eq. 7.

$$E_{tot}\left(t = \infty\right) = E_{hys}\left(t = \infty\right) + E_V\left(t = \infty\right) + E_R\left(t = \infty\right) \tag{7}$$

The nature of each energy part and the calculations of their values are described in the following subsections. The main objective of this section is to determine the radiation damping energy and understanding its nature for segmental columns under shaking table testing.

Input Energy (E_{tot})

The input energy is the integral of the input force with respect to the shaking table displacement. The integral is numerically calculated by the summation of the energy increment, which is the product of the input force with the measured table displacement. The input force was calculated from the measured acceleration on the shaking table by multiplying it by the total mass on top of the table as follows:

$$E_{tot} = \sum F_{g,i} * \Delta u_{g,i} = \sum F_{g,i} * \frac{u_{g,i+1} - u_{g,i-1}}{2} \quad (8)$$

$$F_{g,i} = m_{tot} * a_{g,i} \quad (9)$$

where, F_g is the input force, u_g is the table displacement, m_{tot} is the total mass on top of the table including the table, the footing, the column, and the top mass, and a_g is the measured acceleration at the table.

The input energies for the columns SEG and SEG-ED are illustrated in Figure 18. The input energy depends on the column behavior. The input energy of column SEG-ED is 13% higher than that of the column SEG. This was also noticed by Lestuzzi and Bachmann 2007 who reported a change in input energy of up to 25% depending on the wall behavior. The impulsive nature of the input ground motion is evident in the figure with most of the energy induced at a very small time.

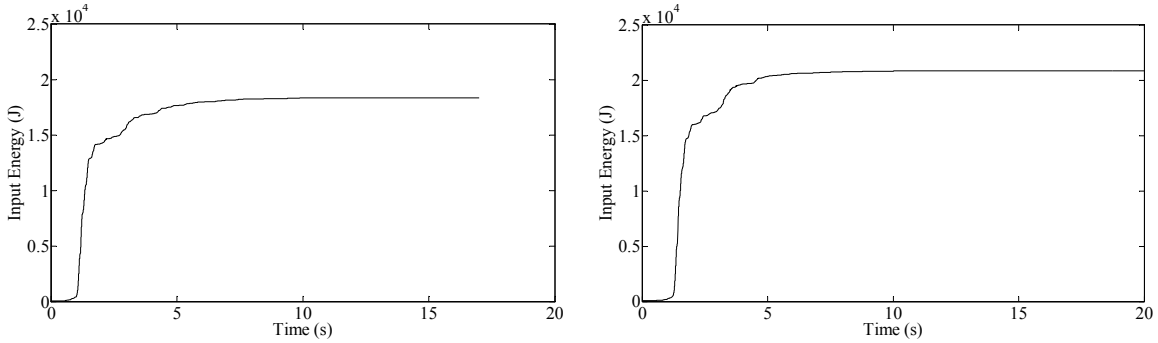

(a) (b)

Figure 18. Input energy for: (a) SEG, and (b) SEG-ED columns at DE

Hysteretic Energy (E_{hys})

The hysteretic energy is calculated as the area enclosed by a hysteresis loop drawn on axes of force and displacement. The area is also an integral and it can be calculated mathematically using eq. 10.

$$E_{hys} = \sum_{i=1}^{n} \left(\frac{F_{i+1} + F_i}{2} \right) \left(\Delta_{i+1} - \Delta_i \right) \tag{10}$$

where, E_{hys} is the hysteretic dissipated energy (Joules), n is the total number of force or displacement points, F_i is the force at point i (N), and Δ_i is the displacement at point i (m).

The hysteretic energies for columns SEG and SEG-ED are illustrated in Figure 19. The hysteretic energy of column SEG-ED is 25% higher than that of the column SEG. This can be attributed to two factors: the increase in the input energy and the addition of the energy dissipaters; the latter being more dominant, as shown before with wider loops in the force-displacement relationship of the column SEG-ED.

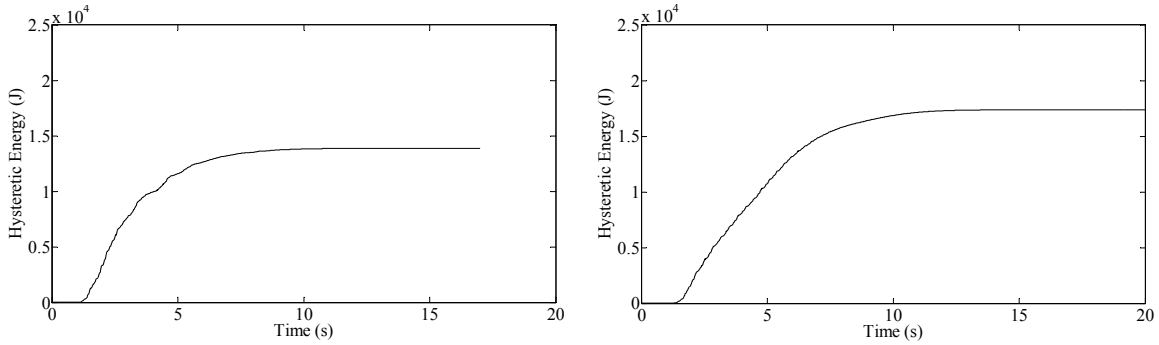

(a) (b)

Figure 19. Hysteretic energy for: (a) SEG, and (b) SEG-ED columns at DE

Kinetic Energy (E_k)

The kinetic energy is calculated from the relative velocity at the center of mass as follows:

$$E_k = \frac{1}{2} m \dot{u}^2 \tag{11}$$

where, m is the mass at the top of the column and $\dot{u}$ is the velocity at the center of mass calculated as the derivative of the measured relative displacement.

The kinetic energies for columns SEG and SEG-ED are illustrated in Figure 20. The kinetic energy is always positive, since it is calculated from the square of the velocity. It does not consist of increments that need to be summed, but rather it describes the energy stored in the mass.

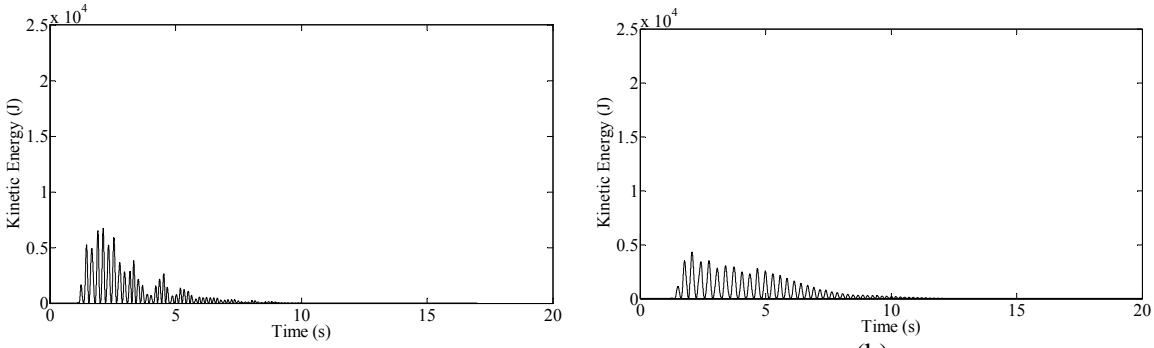

(a) (b)

Figure 20. Kinetic energy for: (a) SEG, and (b) SEG-ED columns at DE

Potential Energy (E_p)

The potential energy is calculated from the change of height of the mass as follows:

$$E_p = mg|h| \tag{12}$$

The modulus of the change of height is used to account for a full cycle of movement from rest position up and down then back to rest. The potential energies for columns SEG and SEG-ED are illustrated in Figure 21.

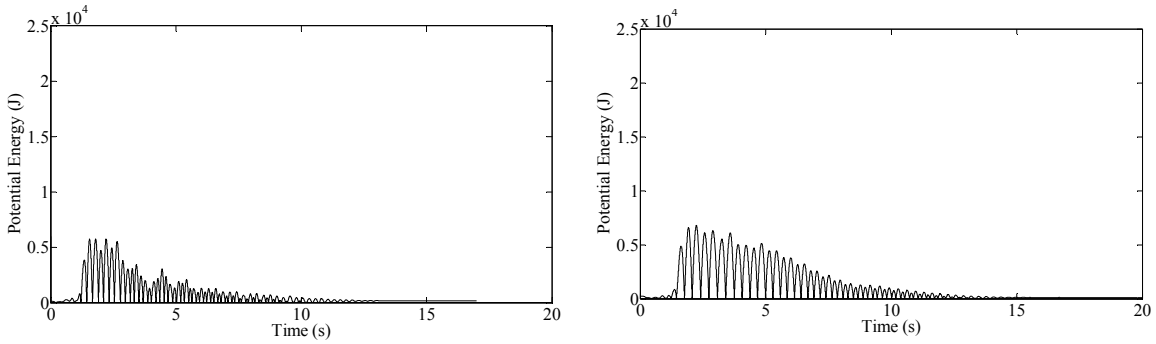

(a) (b)

Figure 21. Potential energy for: (a) SEG, and (b) SEG-ED columns at DE

Kinetic Energy (E_e)

The elastic energy is mainly resulting in the PT strands. It can be calculated as follows:

$$E_e = \frac{1}{2}kx^2 \tag{13}$$

where, k is the stiffness of the strand and x is the extension of the strand.

The elastic energies for columns SEG and SEG-ED are illustrated in Figure 22. The kinetic energy is always positive, since it is calculated from the square of the stretching. It does not consist of increments that need to be summed, but rather it describes the energy stored in the strand and returned after the end of the test.

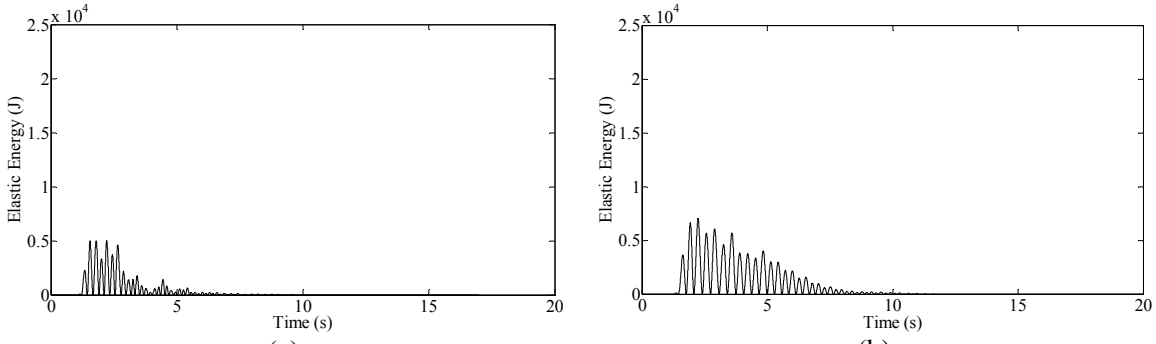

(a) (b)

Figure 22. Elastic energy for: (a) SEG, and (b) SEG-ED columns at DE

Viscous Damping Energy (E_V)

The viscous damping energy here is to account for material damping only and is calculated as follows:

$$E_V = c\sum \dot{u}_i^2 * \Delta t \tag{14}$$

$$c = 2m\omega_n\zeta \tag{15}$$

where, c is the damping constant (Ns/m), ω_n is the natural frequency of the column calculated from the white noise tests, and ζ is the viscous damping ratio of the material estimated from the free vibration of the acceleration at the end of the test with the logarithmic decrement method to account for material damping only.

The viscous damping energies for columns SEG and SEG-ED are illustrated in Figure 23. The value of the viscous damping energy is seen to be small compared to hysteretic energy.

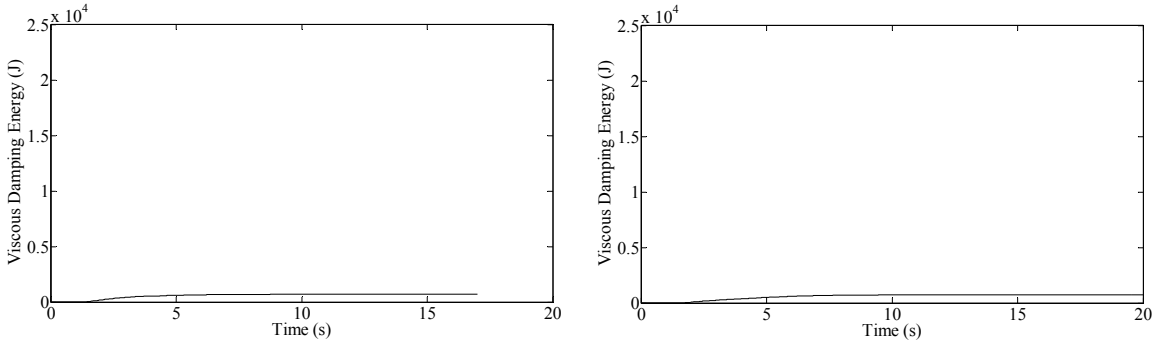

(a) (b)

Figure 23. Viscous damping energy for: (a) SEG, and (b) SEG-ED columns at DE

Radiation Damping Energy (E_R)

To better understand the nature of the radiation damping energy in the post-tensioned segmental system, phase portraits for columns SEG and SEG-ED are plotted in Figure

24. The phase portraits had a focus point representing a static attractor at the origin and the trajectory winded around it over time, before approaching it asymptotically. The experimental and numerical investigations by ElGawady et al. 2011 on a rocking block on concrete showed stepwise energy dissipation. However, Figure 24 shows continuous viscous energy dissipation by radiation which can be observed in the continuous behavior at the maximum velocity. Hence, it is evident from the phase portraits that the radiation damping is viscous rather than stepwise impact nature. This can be attributed to the following factors: 1) the rocking; hence the radiation damping, was executed on the surface of the shell of the hollow section rather than the assumed theoretical point contact, 2) the PT force was the cause of the rocking behavior forcing the column to go back after reaching the maximum drift, rather than the theoretical free vibration.

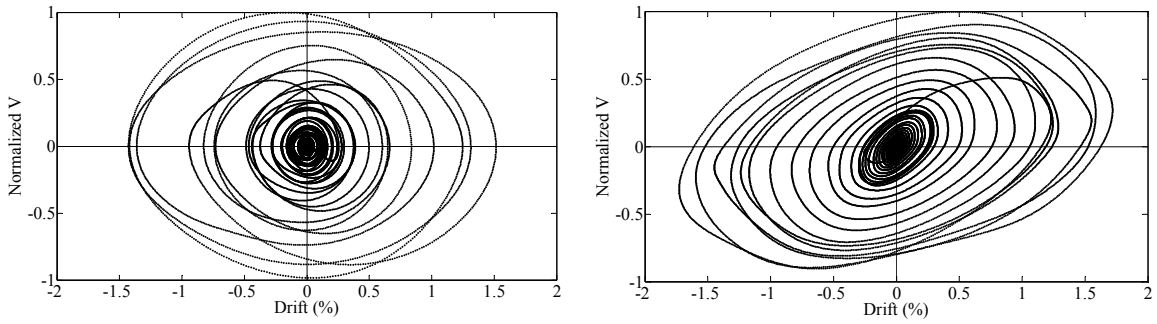

(a) (b)

Figure 24. Phase portraits for: (a) SEG, and (b) SEG-ED columns at DE

To calculate the radiation damping energy, logarithmic decrement method was used to calculate the damping ratio for the output rocking vertical displacement. The energy was then calculated using eqs. 14 and 15 above. The output vertical displacement of rocking at the first segment is illustrated in Figure 25.

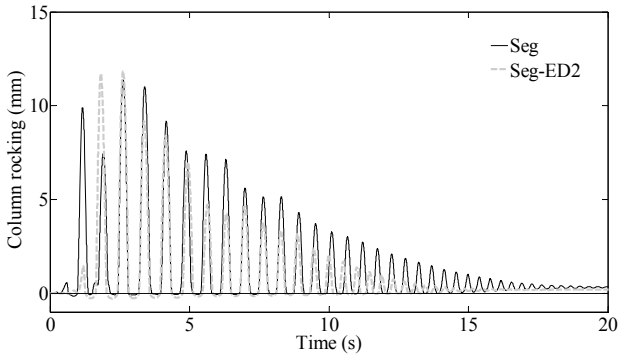

Figure 25. Columns rocking displacement curve in time domain for the test specimens at DE

The radiation damping energies of the first segment for columns SEG and SEG-ED are illustrated in Figure 26.

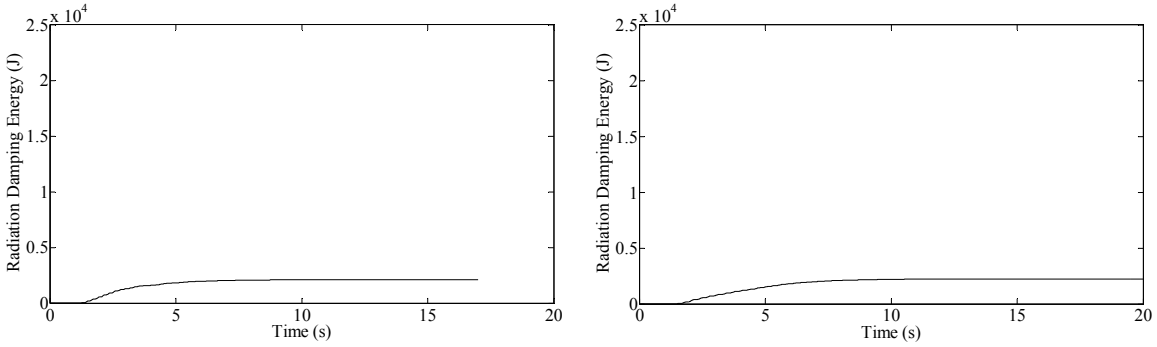

Figure 26. Radiation damping energy of the first segment for: (a) SEG, and (b) SEG-ED columns at DE

Total System Energy

The total system energies for columns SEG and SEG-ED are illustrated in Figure 27. The figure shows good correspondence between the input energy and the summation of its components, as per equations 6 and 7. Most of the energy was dissipated through hysteretic energy. The radiation damping energy was viscous and dissipated the energy continuously. The viscous damping energy from materials dissipated the lowest amount of energy, which should be expected from the system because rocking is the dominant

behavior. The radiation damping energy for the second segment was significant in the column SEG, while it was very small in column SEG-ED, where the rocking is controlled by the external energy dissipaters.

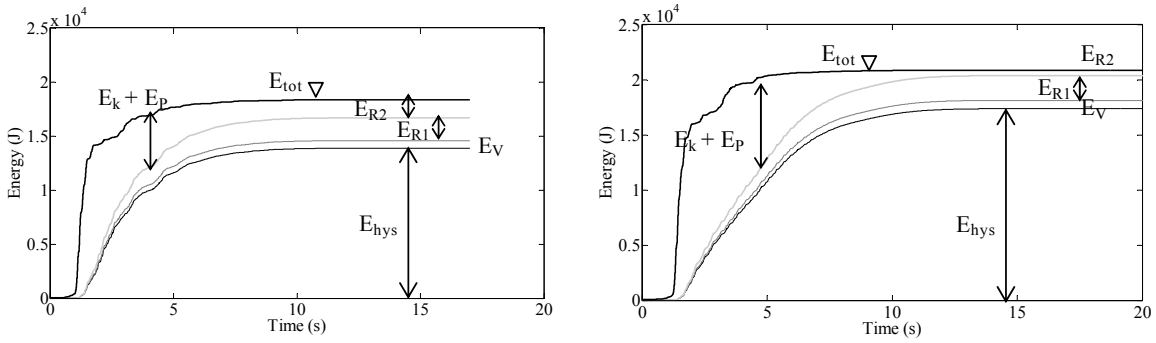

Figure 27. System energy for: (a) SEG, and (b) SEG-ED columns at DE

The contributions of the different energy dissipation mechanisms at the end of the free vibration are illustrated in Figures 28 and 29 for the SEG and SEG-ED columns, respectively. The ratio between the hysteretic energy and the total energy at the end of the free vibration generally has a small variation (Fajfar and Vidic 1994; Lestuzzi and Bachmann 2007). This ratio had an average of 0.75 and 0.82 for the SEG and SEG-ED columns respectively. The difference between the ratios in the two columns can be attributed to the enhanced energy dissipation by using the external energy dissipaters. The column SEG suffered yielding of the PT strands at 160% of the DE so the behavior changed to higher hysteretic energy and more radiation damping from the first segment compared to the second segment. The figures show that the ratio of the radiation energy to the total energy is generally constant.

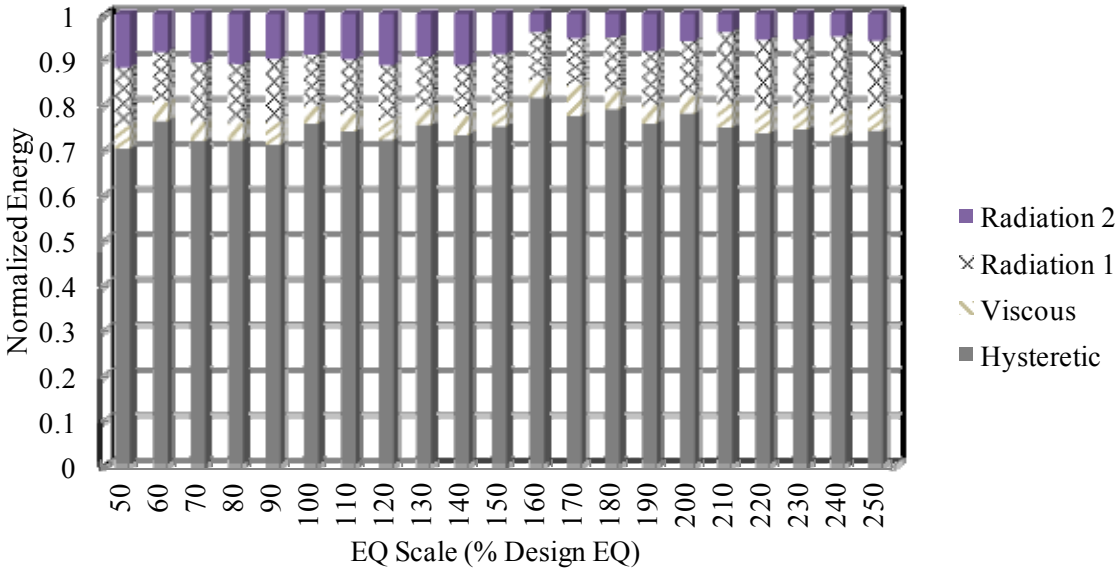

Figure 28. Energy contribution for the SEG column

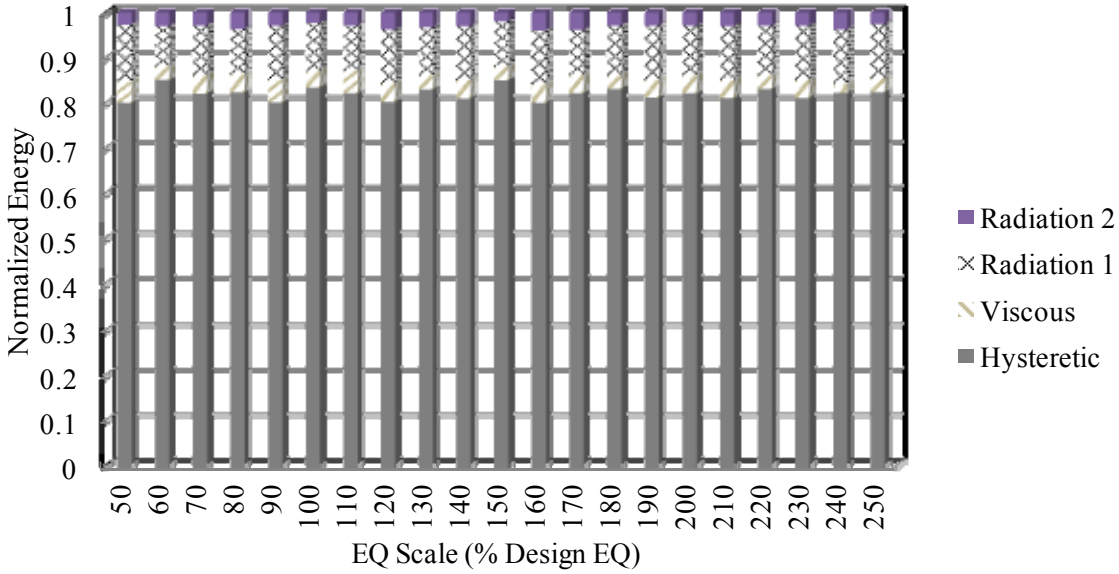

Figure 29. Energy contribution for the SEG-ED column

Analytical model

An analytical model was developed to calculate the capacity of the columns. The model was based on the monolithic beam analogy procedure by Pampanin et al. 2001. This procedure is briefly explained as follows:

1. Impose a rotation at the base of the column (θ_{imp}).
2. Assume the neutral axis position (c).
3. Evaluate the strain in the unbonded post-tensioned tendons:

$$\varepsilon_{pt} = \frac{n\Delta_{pt}}{l_{ub}} \tag{16}$$

where, n is the number of total openings along the segment, l_{ub} is the unbonded length of the tendon, and Δ_{pt} is the elongation at the level of the tendons.

4. Estimate the strains in the mild steel and concrete:

$$\varepsilon_s = \frac{(\Delta - 2\Delta_{sp})}{l'_{ub}} \tag{17}$$

where, Δ is the elongation at the level of the mild steel due to the opening of the segment, Δ_{sp} is the displacement due to strain penetration, and l'_{ub} is the unbonded length of the mild steel.

5. Use the monolithic beam analogy to apply member compatibility:

$$\Delta_{tot(precast)} = \Delta_{tot(monolithic)} \tag{18}$$

6. Apply section equilibrium:

$$C + T_s + C'_s = T_{pt} \tag{19}$$

7. Iterate for the location of the neutral axis until convergence occurs.
8. Evaluate the moment capacity.

The results of the analytical procedure versus the experimental values are presented in Figure 30. The model was able to accurately predict the capacity and behavior of the SEG column.

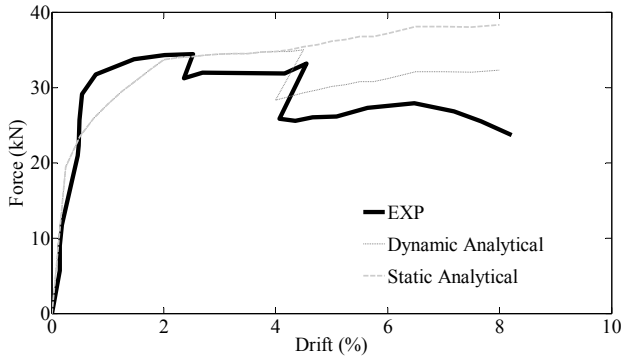

Figure 30. Analytical versus experimental results

Conclusion

This paper investigated the seismic behavior of proposed damage-resistant segmental hollow-core bridge columns with and without external energy dissipaters. The hollow-core segmental post-tensioned column inherited the combined advantages of all its components as follows: the column benefited from the confinement of the FRP from the double skin section. The columns also utilized the re-centering capability of the unbonded post-tensioned system. In addition, the columns accelerate the bridge construction due to the segmental nature and light weight because of the hollow cross section. Energy dissipation was provided by external replaceable bars for column SEG-ED.

The columns were subjected to a sequence of scaled ground motions of the Northridge-01 1994 earthquake at Rinaldi receiving station. The ground motion scales

started from 10% of the DE up to 250% of the DE with increments of 10%. The column SEG was able to sustain up to 250% of the DE. However, yielding of the PT strands occurred at 160% of the DE. This yielding was avoided in the column SEG-ED by reducing the initial PT force from 54% to 44% of the ultimate strength. The addition of the external energy dissipaters was able to make up for the difference in capacity. It is recommended to maintain the initial PT force under 40% of the ultimate strength to avoid yielding of the PT strands at large drifts.

The energy of the system was investigated to comprehend the behavior of the columns. The total energy consisted of the well known hysteretic energy (E_{hys}), kinetic energy (E_k), potential energy (E_p), elastic energy (E_e), and viscous damping energy (E_V). In addition to these, the radiation energy (E_R) played a key part in the system. Unlike the common practice that the radiation damping is step-wise, the radiation damping was found to be continuous and viscous.

The radiation damping was the main source of the overall viscous damping of the columns. The yielding of the PT strands increased the viscous damping but not the radiation damping. The addition of external energy dissipaters at the column SEG-ED increased the radiation damping.

The addition of external energy dissipaters resulted in a favorable behavior with the possibility of replacement after a major earthquake, the possibility to tailor them according to the seismic zone and the required performance, and the control of the unbonded length along with the tension only detail which prevent low cyclic fatigue.

Acknowledgments

The authors acknowledge AMSYSCO Post Tensioning corporate for their generous donations of materials used in the tests.

References

ACI (2003). "T1. 2R-03." American Concrete Institute, Farmington Hills, MI.

ASTM D2290 (2012). "Standard Test Method for Apparent Hoop Tensile Strength of Plastic or Reinforced Plastic Pipe."

Caltrans, S. (2010). Caltrans Seismic Design Criteria, Version.

Chang, K., Loh, C., Chiu, H., Hwang, J., Cheng, C. and Wang, J. (2002). "Seismic behavior of precast segmental bridge columns and design methodology for applications in Taiwan." Taiwan Area National Expressway Engineering Bureau, Taipei, Taiwan in Chinese.

Chopra, A. K. (2007). Dynamics Of Structures, 3/E, Pearson Education India.

Chou, C.-C., Chang, H.-J. and Hewes, J. T. (2013). "Two-plastic-hinge and two dimensional finite element models for post-tensioned precast concrete segmental bridge columns." Engineering Structures **46**: 205-217.

Chou, C. C. and Chen, Y. C. (2006). "Cyclic tests of post-tensioned precast CFT segmental bridge columns with unbonded strands." Earthquake engineering & structural dynamics **35**(2): 159-175.

Dawood, H., ElGawady, M. and Hewes, J. (2011). "Behavior of Segmental Precast Posttensioned Bridge Piers under Lateral Loads." Journal of Bridge Engineering **17**(5): 735-746.

ElGawady, M., Booker, A. J. and Dawood, H. M. (2010). "Seismic behavior of posttensioned concrete-filled fiber tubes." Journal of Composites for Construction **14**(5): 616-628.

ElGawady, M. A. and Dawood, H. M. (2012). "Analysis of segmental piers consisted of concrete filled FRP tubes." Engineering Structures **38**: 142-152.

ElGawady, M. A., Ma, Q., Butterworth, J. W. and Ingham, J. (2011). "Effects of interface material on the performance of free rocking blocks." Earthquake Engineering & Structural Dynamics **40**(4): 375-392.

ElGawady, M. A. and Sha'lan, A. (2010). "Seismic behavior of self-centering precast segmental bridge bents." Journal of Bridge Engineering **16**(3): 328-339.

Fajfar, P. and Vidic, T. (1994). "Consistent inelastic design spectra: hysteretic and input energy." Earthquake Engineering & Structural Dynamics **23**(5): 523-537.

FEMA, A. (2006). 445, Next-generation performance-based seismic design guidelines-program plan for new and existing buildings, Redwood City.

Gibson, N., Filiatrault, A. and Ashford, S. A. (2002). "Impulsive seismic response of bridge column-cap beam joints." ACI Structural Journal **99**(4): 470-479.

Hewes, J. T. (2000). Seismic response of unbonded post-tensioned precast concrete segmental bridge columns, University of California, San Diego.

Hewes, J. T. and Priestley, M. N. (2002). Seismic design and performance of precast concrete segmental bridge columns.

Housner, G. W. (1963). "The behavior of inverted pendulum structures during earthquakes." Bulletin of the seismological society of America **53**(2): 403-417.

Ichikawa, S., Matsuzaki, H., Moustafa, A., ElGawady, M. A. and Kawashima, K. (2016). "Seismic-Resistant Bridge Columns with Ultrahigh-Performance Concrete Segments." Journal of Bridge Engineering: 04016049.

Japan Road Association (2002). "Design specifications of highway bridges, Part V seismic design." Maruzen, Tokyo, Japan.

Jeong, H., Sakai, J. and Mahin, S. A. (2008). "Shaking table tests and numerical investigation of self-centering reinforced concrete bridge columns." Pacific Earthquake Engineering Research Center. University of California, Berkeley. Public Works Research Institute, Tsukuba, Japan.

Kim, T.-H., Lee, H.-M., Kim, Y.-J. and Shin, H. (2010). "Performance assessment of precast concrete segmental bridge columns with a shear resistant connecting structure." Engineering Structures **32**(5): 1292-1303.

Leitner, E. J. and Hao, H. (2016). "Three-dimensional finite element modelling of rocking bridge piers under cyclic loading and exploration of options for increased energy dissipation." Engineering Structures **118**: 74-88.

Lestuzzi, P. and Bachmann, H. (2007). "Displacement ductility and energy assessment from shaking table tests on RC structural walls." Engineering Structures **29**(8): 1708-1721.

Lipscombe, P. R. (1990). Dynamics of rigid block structures, University of Cambridge.

Mander, J. B. and Cheng, C.-T. (1997). Seismic design of bridge piers based on damage avoidance design, National Center for Earthquake Engineering Research, State Univ. of New York at Buffalo, Buffalo, NY.

Marriott, D., Pampanin, S. and Palermo, A. (2009). "Quasi-static and pseudo-dynamic testing of unbonded post-tensioned rocking bridge piers with external replaceable dissipaters." Earthquake Engineering & Structural Dynamics **38**(3): 331-354.

Ou, Y.-C., Wang, P.-H., Tsai, M.-S., Chang, K.-C. and Lee, G. C. (2009). "Large-scale experimental study of precast segmental unbonded posttensioned concrete bridge columns for seismic regions." Journal of structural engineering **136**(3): 255-264.

Ou, Y. C., Tsai, M. S., Chang, K. C. and Lee, G. C. (2010). "Cyclic behavior of precast segmental concrete bridge columns with high performance or conventional steel reinforcing bars as energy dissipation bars." Earthquake Engineering & Structural Dynamics **39**(11): 1181-1198.

Palermo, A., Pampanin, S. and Marriott, D. (2007). "Design, modeling, and experimental response of seismic resistant bridge piers with posttensioned dissipating connections." Journal of Structural Engineering **133**(11): 1648-1661.

Pampanin, S., Nigel Priestley, M. and Sritharan, S. (2001). "Analytical modelling of the seismic behaviour of precast concrete frames designed with ductile connections." Journal of Earthquake Engineering **5**(3): 329-367.

Peña, F., Prieto, F., Lourenço, P. B., Campos Costa, A. and Lemos, J. V. (2007). "On the dynamics of rocking motion of single rigid-block structures." Earthquake Engineering & Structural Dynamics **36**(15): 2383-2399.

Phan, V., Saiidi, M. S., Anderson, J. and Ghasemi, H. (2007). "Near-fault ground motion effects on reinforced concrete bridge columns." Journal of structural engineering **133**(7): 982-989.

Priestley, M. N. and Tao, J. R. (1993). "Seismic response of precast prestressed concrete frames with partially debonded tendons." PCI Journal **38**(1): 58-69.

Sehhati, R., Rodriguez-Marek, A., ElGawady, M. and Cofer, W. F. (2011). "Effects of near-fault ground motions and equivalent pulses on multi-story structures." Engineering Structures **33**(3): 767-779.

Shim, C. S., Chung, C.-H. and Kim, H. H. (2008). "Experimental evaluation of seismic performance of precast segmental bridge piers with a circular solid section." Engineering Structures **30**(12): 3782-3792.

Solberg, K., Mashiko, N., Mander, J. and Dhakal, R. (2009). "Performance of a damage-protected highway bridge pier subjected to bidirectional earthquake attack." Journal of structural engineering **135**(5): 469-478.

Trono, W., Jen, G., Panagiotou, M., Schoettler, M. and Ostertag, C. P. (2014). "Seismic response of a damage-resistant recentering posttensioned-HYFRC bridge column." Journal of Bridge Engineering **20**(7): 04014096.

Wong, Y., Yu, T., Teng, J. and Dong, S. (2008). "Behavior of FRP-confined concrete in annular section columns." Composites Part B: Engineering **39**(3): 451-466.

Zhang, Q. and Alam, M. S. (2015). "Evaluating the Seismic Behavior of Segmental Unbounded Posttensioned Concrete Bridge Piers Using Factorial Analysis." Journal of Bridge Engineering **21**(4): 04015073.

VII. EFFECTS OF GROUND MOTION TYPE ON THE BEHAVIOR OF SEGMENTAL POST-TENSIONED BRIDGE COLUMNS

Ayman Moustafa[1], Haitham Dawood[2], and Mohamed ElGawady[3]

Abstract

This paper investigates the effects of different ground motion types on the behavior of full scale hollow-core segmental bridge columns. This was accomplished by developing the first three-dimensional finite element (FE) analysis of segmental hollow-core bridge columns with post-tensioned unbonded strands under ground motion excitations. The FE software LS-DYNA was used to develop the seismic response under a series of different ground motions. The motion types considered were far-field motions, near-fault motions without forward directivity, near-fault motions with forward directivity, and near-fault motions with fling-step. A brief description and discussion of the shaking table tests on ¼ scale columns is also presented. The FE model was able to predict the rocking behavior of the columns using contact elements. The maximum errors of prediction of the drift and force were less than 11.5% and 15.1%, respectively. The column was able to withstand 9 consecutive runs of each ground motion, representing main-shock aftershocks without major damages and exhibited self-centering. The overall response to near-fault motions without forward directivity was similar to that of the far-field motions. The hysteretic response of the fling-step motions exhibited a unique double hysteretic behavior. The

[1] Graduate research assistant, Department of Civil, Architectural, and Environmental Engineering, Missouri University of Science and Technology, USA E-mail: ampyf@mst.edu
[2] Staff Engineer, Fugro Marine GeoServices, Inc., Norfolk, VA, 23510, email: hdawood@vt.edu

[3]Benavides Associate professor, Department of Civil, Architectural, and Environmental Engineering, Missouri University of Science and Technology, USA E-mail: elgawadym@mst.edu

effect of ground motion type was dominant in the ultimate drift of the columns and minimal in the capacity.

Keywords: Bridge columns, finite element, seismic design, segmental columns, self centering.

Introduction

Ground motions close to a ruptured fault (near-fault) can be significantly different than those observed further away from the seismic source (far-field). The near-fault zone is typically assumed to be restricted to within a distance of about 20 km from the ruptured fault. In the near-fault zone, ground motions at a particular site are significantly influenced by the rupture mechanism and slip direction relative to the site that can lead to the dynamic consequences of 'forward-directivity'. They are also influenced by the permanent ground displacement at the site resulting from tectonic movement, which is termed 'fling-step'. Thus, different types of ground motions have different characteristics, which would result in different responses in the structure subjected to them (Somerville et al. 1997; Alavi and Krawinkler 2001; Baker 2007; Amiri et al. 2011).

Incremental dynamic analysis (IDA) is a parametric analysis method that can be used to estimate the structural performance of a building or a bridge column under seismic loads. It involves subjecting a structural model to successive scaled ground motion records, with different levels of intensity, producing curves of response parameterized versus intensity level (Vamvatsikos and Cornell 2002). The motivation behind this IDA is the fact that several earthquakes were preceded and succeeded by

strong foreshocks and aftershocks, respectively. The 2011 Tohoko, Japan earthquake [moment magnitude (Mw) = 9.0] was succeeded by at least five aftershocks that had magnitudes larger than 6.5 (USGS 2012). Similarly, the 2008 Wenchuan earthquake (Mw = 7.9) was followed by an aftershock of magnitude larger than 6, that caused collapse of many structures that sustained damage from the mainshock.

Development of damage-resistant bridge columns to minimize the required repairs after an earthquake has always been emerging in the last decades. While the current conventional reinforced concrete (RC) columns are intended to prevent bridges collapse and loss of lives, these columns incur damage even at the design earthquake (DE) level. The damage can be costly and time consuming. It also may lead to long term closure of the bridges and/or full demolition in case of large residual drifts. Severe damage in RC columns in Japan after the 1995 Kobe earthquake was observed and more than 100 RC bridges had to be demolished [Jeong et al. 2008]. Residual drifts up to 2% were the main reason for demolishing the bridges and they were defined as non-functional as it was difficult to retrieve those residual drifts. Therefore, the Japanese seismic design specifications are limiting the residual drifts of columns to 1% (Japan Road Association 2002).

To reduce the excessive residual drift, the use of post-tensioning to allow controlled rocking of columns at the interface with the foundation and the superstructure can be implemented. The concept can be extended to segmental precast post-tensioned column system consisting of precast segments stacked over each other and connected by unbonded post-tensioning bars to increase the number of interfaces available for rocking

(Chang et al. 2002; Chou and Chen 2006; Marriott et al. 2009; ElGawady et al. 2010; Ichikawa et al. 2016).

Experimental investigations indicated that large peak drifts and low residual drifts were achieved using the unbonded post-tensioned bridge columns (Mander and Cheng 1997; Hewes and Priestley 2002; Billington and Yoon 2004; Chou and Chen 2006; Palermo et al. 2007; Shim et al. 2008; Wong et al. 2008; Marriott et al. 2009; Solberg et al. 2009; Ou et al. 2009; ElGawady et al. 2010; ElGawady and Sha'lan 2010; Kim et al. 2010; Ou et al. 2010; Trono et al. 2014; Ichikawa et al. 2016). The posttensioned RC columns with conventional rebar and transverse reinforcement still experienced heavy concrete spalling, rebar buckling, and in some cases loss of strand anchorage. Confinement in forms of steel or FRP tubes was adapted to overcome this issue. However, unconfined concrete above or below these tubes were often damaged. In this article, the cross-section is confined all over the column height to avoid such damage.

A new double-skin cross-section is investigated for the segmental post-tensioned columns in this article. The double-skin columns are columns consisting of outer FRP tube, inner steel tube, and concrete in between the two. This system combined and optimized the benefits of all three materials (FRP, concrete, and steel). Several experimental and finite element studies were conducted on the conventional double-skin columns under different static and cyclic loading conditions (Teng et al. 2007; Wong et al. 2008; Han et al. 2010; Ozbakkaloglu and Idris 2014; Abdelkarim and ElGawady 2014). However, the use of such cross-section in segmental construction, to the knowledge of the authors, has not been implied yet.

Finite element (FE) models for segmental columns were also developed (Ou et al. 2007; Dawood et al. 2011; ElGawady and Dawood 2012; Zhang and Alam 2015; Leitner and Hao 2016). Ou et al. 2007 developed a three-dimensional FE model of rectangular hollow columns under static cyclic loading using the software ABAQUS (ABAQUS 2011). Some discrepancy could be seen in the material degradation under cyclic loading, with larger stiffness and lateral loads at higher drifts and less residual damage. Dawood et al. 2011 used the same software for segmental circular columns under monotonic loading. The average error in the prediction of the backbone curve ranged from 7% to 15%. In another study by the authors (ElGawady and Dawood 2012), a parametric study was carried out to help understand the behavior of the segmental columns. Leitner and Hao 2016 extended the previous study for cyclic loading. Zhang and Alam 2015 used a FE model of a circular segmental column to investigate the potential interactions between the factors studied by ElGawady and Dawood 2012 and found no interaction in determining the yield force and that interaction exist between the post-tension level and post-tension ratio in determining post-elastic stiffness.

Research Significance

This study investigates the effects of different ground motions types; namely far-filed motions, near-fault motions without forward directivity, near-fault motions with forward directivity, and near-fault motions with fling-step on the behavior of full scale segmental hollow-core columns using three-dimensional FE model. The effects of different types of motions on segmental hollow sections, to the knowledge of the authors, have not been investigated. To obtain the full dynamic response of the columns, IDA was performed by

applying scaled ground motions with increments relative to the design earthquake (DE) spectrum.

Despite the efforts in developing three-dimensional FE models to predict the behavior of segmental columns, all these models, were developed under monotonic or static cyclic loading. No three-dimensional models were developed, to the knowledge of the authors, under input ground motions to predict the actual response of these columns under seismic loads. In this article, a three-dimensional model was developed using LS-DYNA 971 R3 software for segmental double-skin columns with input ground motions.

Selection and Scaling of Ground Motions

Time history analysis is routinely adopted in seismic design of structures to capture its non-linear seismic behavior. The objective is to run time history analyses using ground motions (GMs) that match the characteristics of future GMs at the project site. GMs used in time history analyses can either be artificially generated or modified from previously recorded motions (seed motions). In the current study, GMs were generated from seed motions. The generation of motions is a two step process that consists of: selection of seed motions; and scaling/altering ground motions to match a target response.

The ultimate objective was to select GMs that match the characteristics of the motions expected at the project site. This objective is strictly theoretical because the actual characteristics of future GMs are not deterministic. Even if these characteristics are considered deterministic, finding seed motions that match the target characteristics is not practically possible.

Due to the aforementioned limitations, seed motions were chosen such that they match as much parameters / characteristics of the target motions as practically viable. Matching between the seed motions and the target motions is typically conducted for the following parameters: magnitude, distance, site condition and faulting type. Seed GMs are typically obtained seismic catalogues that provide these different parameters for each motion as metadata (e.g., Dawood et al. 2016). If probabilistic seismic hazard analysis is conducted, the target parameters can be obtained from the deaggregation matrix. If deterministic seismic hazard analysis is adopted, then the characteristics of the critical scenario would be the target parameters.

For the current study, the target parameters adopted for selecting seed motions were: moment magnitude preferably between 7 and 8, source to site distance preferably between 5 and 30 km, motions recorded at sites Class D, and no target faulting type was set. The magnitude and distance ranges were selected based on the deaggergation matrix at a spectral period of 1.0 seconds for a site located in San Francisco, CA. The matrix showed that motions characterized by that magnitude-distance combination have the major contribution to the seismic hazard for 1.0 second structure at that site.

In addition to the aforementioned parameters, the seed motions were selected such that they fall within one of the following categories:

- Far-Field Motions: These are motions recorded far enough from the fault that neither a fling-step nor forward directivity effects were observed in the motion even if such effects were observed. These motions served as baseline for comparison with the other types.

- Near-Fault Motions without Forward-Directivity and Fling-Steps: Depending on the relative location between the fault and the site as well as the faulting mechanism, fling-step and forward directivity might not be observed at some near-field sites. These motions were included to isolate the effects of forward-directivity and fling-steps in near-fault motions.
- Near-Fault motions with Forward-directivity: Depending on the rupture mechanism and slip direction, GMs recorded at sites close by active faults (near-fault) can be influenced by forward-directivity effects. These GMs typically consists of one or more pulses, which are shorter in duration, and can result in higher dynamic response for structures at near-fault sites. Additional information about GMs with forward-directivity and their effects on structures can be found elsewhere (Somerville et al. 1997; Alavi and Krawinkler 2001; Bray and Rodriguez-Marek 2004; Baker 2007).
- Near-Fault Motions with Fling-Step: Ground motions recorded at near-field sites may contain a significant permanent static displacement. Such motions are known as GMs with "fling-step". These GMs are not typically processed using the conventional processing approaches because such procedure would remove or alter the permanent displacement characteristics associated with these motions (Kalkan and Kunnath 2006). For additional information about GMs with fling-step and its effects on structures, the reader is referenced to Kalkan and Kunnath 2006 and Amiri et al. 2011.

The objective of this study was to investigate the effects of the aforementioned GM types on the response of hollow segmental bridge pier systems including their effects on period elongation due to geometric non-linearity and observed damage.

Response spectrum is not strictly a characteristic of GMs, but it rather measures the response of multiple structures with different periods of vibrations when subjected to a specific GM. Nevertheless, seed motions are typically scaled to match the response spectrum predicted at the site of interest rather than matching a GM characteristic independent from structural response (e.g., Fourier spectra). The target response spectrum to which seed motions are scaled can be obtained from probabilistic seismic hazard analysis, deterministic seismic hazard analysis, or code-based response spectra. GMs can be modified in various ways to match the target response spectra; namely, scaling GMs in time domain; spectral matching in frequency domain; and spectral matching in time domain. For additional information about the different approaches, the reader is referred to Fahjan and Ozdemir 2008.

For the current study, the 2012/2015 International Building Code design spectra for a project site located in San Francisco, CA with site Class D (S_{DS}=1.0g and S_{D1}=0.638g) was used. The seed motions were modified using the linear scaling in the time domain technique. The GMs were scaled up or down in such a way that its response spectra matched a pseudo-spectral acceleration of 0.686 g at a spectral period of 0.93 seconds (first period of vibration of the studied bridge piers). The design response spectrum (DE) with a probability of excess of 10% in 50 years and the maximum considered earthquake (MCE) response spectrum with a probability of excess of 2% in 50 years are illustrated in Figure 1.

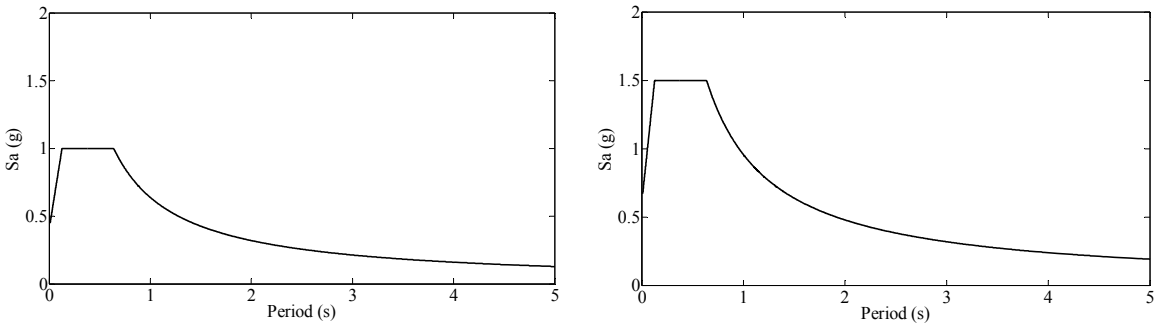

(a) (b)

Figure 1. a) Design earthquake spectrum and b) maximum considered earthquake spectrum

Experimental Investigation

Overview of the Test Specimens

To validate the FE model, the results of a segmental double-skin column tested on shaking table under successive earthquake excitations were used (Moustafa and ElGawady 2017). The column's elevation and cross section along with the test setup are illustrated in Figure 2. The specimen's length scale factor was 4, considering a hypothetical prototype column with a diameter of 1200 mm. The column's height measured from the top of the footing to the center of the mass was 1800 mm, resulting in an aspect ratio of approximately 6. The aspect ratio is defined as the height of the column divided by its diameter. The column had an outside diameter of 300 mm, an inside diameter of 175 mm, and consisted of four segments of 300 mm high each. The column had four 12.7 mm diameter PT seven wire strands, each with a cross sectional area of 99 mm^2 as the main reinforcement of the column to connect the four segments together with the foundation and the column head.

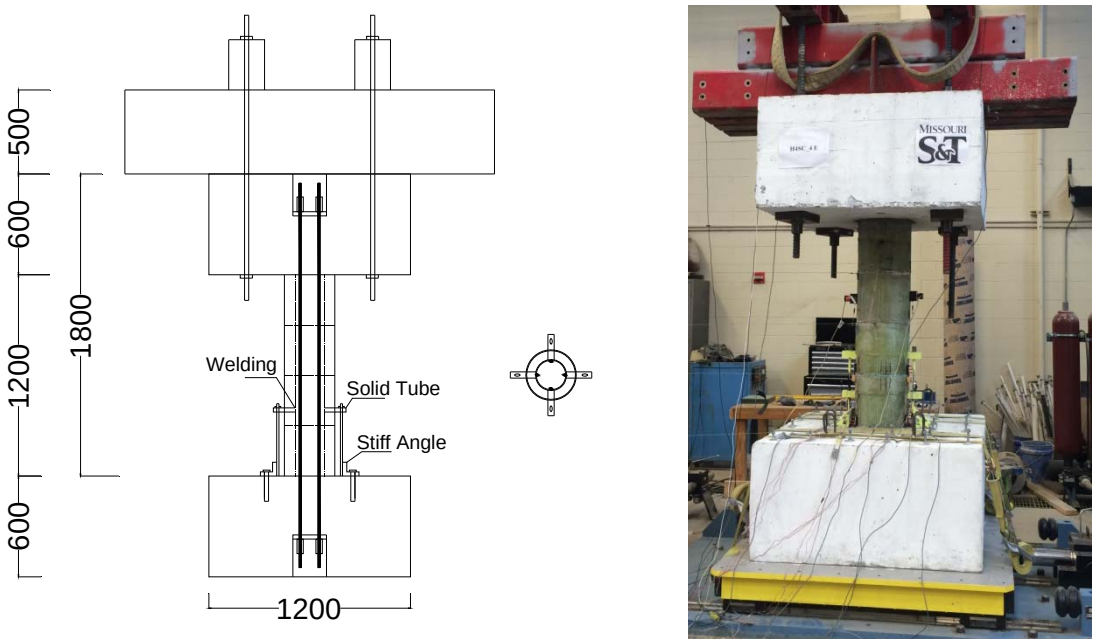

Figure 2. Configuration and dimensions of the segmental columns (units: mm)

Material Characteristics

The concrete compressive strength was 35 MPa. The inner steel tube thickness was 4.7 mm. The outer tube consisted of four layers of unidirectional glass fiber reinforced polymers and Tyfo S epoxy by FYFE© with a total thickness of 5 mm. Three specimens of GFRP hoops were tested according to ASTM D2290 2012. The average ultimate tensile strength in the fiber direction was 352 MPa. The elongation at break was 2.31%. The strands were distributed along the edge of the hollow part of the cross section to maximize the distance of the strands to the neutral axis. The PT strands had a diameter of 12.7 mm, a yield stress of 1675 MPa, and an ultimate strength of 1861 MPa.

Test Setup and Loading Sequence

The columns were fixed to a uni-axial shaking table using 36 all-threaded bars, each with a capacity of 45 kN. The shaking table is running using a closed loop controller that can

use either displacement or acceleration control. The column was subjected to a sequence of a scaled Northridge-01 1994 earthquake at "Rinaldi Receiving Station" which is a near-fault pulse-like ground motion. The selected ground motion was scaled to the design spectrum (Figure 1(a)), by matching the spectral acceleration at the column's first mode (Sa(T1)) to the design response spectrum. The columns were subjected to a sequence of the scaled ground motion starting at 10% of the DE to 250% of the DE with steps of 10% increments giving a total of 25 ground motions. A white noise test with duration of 75 s and 0.02g amplitude of acceleration was run after each ground motion excitation to determine the updated fundamental period of the column.

Finite Element Modeling

Geometry

The column dimensions and configuration were identical to the experimental setup (Figure 2). The column was modeled as four separate segments; each consisting of an outside GFRP tube, an inside steel tube, and a core concrete. Isometric views of the column and its components are pictured in Figure 3. The FE model had 35,753 elements and 41,485 nodes. A sensitivity analysis was conducted to determine the optimum element size that would achieve an acceptable accuracy and solution time.

The column's concrete core was modeled by solid elements. These elements had a height of 25.00 mm. Both the outer FRP tube and the inner steel tube were simulated by shell elements. A typical element height for both the FRP and steel tubes was 25 mm. The concrete footing and head were also modeled by solid elements. A physical mass with the same dimensions as in the experiment was modeled by solid elements with

adjusted density to give the correct weight of the concrete filled steel tubes used in the mass. Both the footing and column head were meshed into two different regions; the inside area in contact with the column was finely meshed, while for the outside area a coarse mesh was utilized (Figure 3(a)). This was compared to a model with fine mesh all over the footing and head and no differences at all were observed. All solid elements were modeled with constant-stress one-point quadrature integration to reduce the computational time and increase the model stability. This model may suffer from the hourglass effect. This effect was controlled by selecting sufficiently fine mesh and by applying Type 1 hourglass algorithm, having an hourglass coefficient of 0.1, which inhibits hourglass mode. Moreover, the deformed shapes of all the elements were inspected carefully during each run for any potential hourglass-type deformations. The hourglass energy for each model was also found to be less than 10% of the peak internal energy, indicating no hourglass modes. A preliminary investigation of the solid element type effect was performed by applying the DE only twice; one was using the fully integrated solid elements and the other using constant-stress elements. No significant differences between the results of the two approaches were found but the run time was vastly reduced. The PT strands were modeled as beam elements using “ELFORM 1” with the diameter as the input.

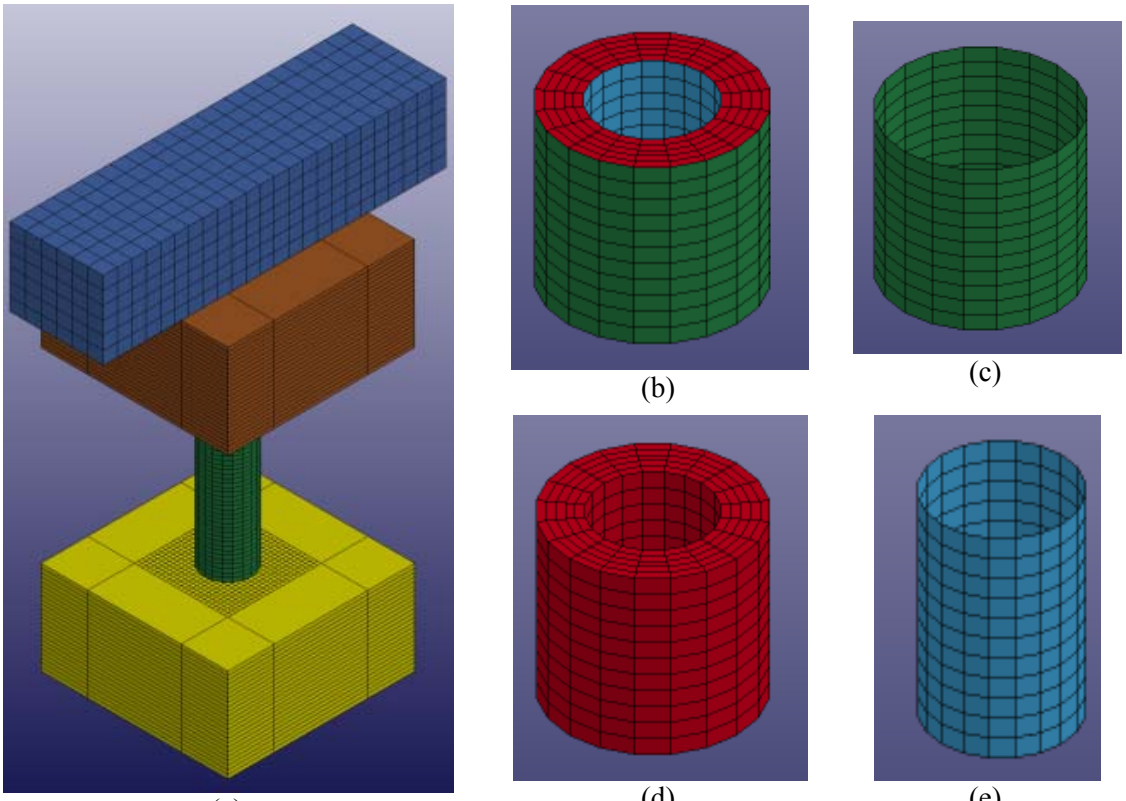

Figure 3. Isometric views for: a) column, b) segment, c) GFRP tube, d) concrete core, and e) steel tube

Material Models

- *Concrete*

The choice of concrete model is crucial for determination of the behavior of the column. Several models of concrete are available in LS-DYNA. The "CONCRETE_DAMAGE_REL3" model (Karagozian & Case, Glendale, California) was chosen in the current study. This model provided good agreement with experimental results in previous studies (Youssf et al. 2014; Abdelkarim and ElGawady 2014). The model was developed based on the theory of plasticity and it has three yield surfaces: 1) yield, 2) maximum, and 3) residual (Malvar et al. 1997). Automatic generation for the

failure surface was utilized, where the concrete compressive strength ($f_c^{'}$) and the fractional dilation parameter (ω) were the inputs. The fractional dilation parameter considers the volumetric change in concrete and the default value of 0.5 was used. The output of the automatic generation gives the equation of state, which controls the compressive behavior of concrete under triaxial stresses.

- *GFRP tube*

The GFRP was modeled as an orthotropic material using "002-ORTHOTROPIC_ELASTIC" material model. This model uses a total Lagrangian basis to model the elastic-orthotropic behavior of solids, shells, and thick shells. The inputs for this material are the engineering constants [elastic modulus (*E*), shear modulus (*G*), and Poisson's ratio (*PR*)]. The elastic modulus was assigned as 15.2 GPa based on the experimental results. Poisson's ratio was assumed to be 0.25, which is a typical value for FRP (Abdelkarim and ElGawady 2014; Ozbakkaloglu and Idris 2014). The shear modulus was calculated to be 6.08 GPa. The ultimate strain of GFRP from the experiments was assigned as the failure criterion, defined as "000-ADD_EROSION", in the EFFEPS card.

- *Steel tube*

Material model "003-PLASTIC_KINAMATIC" was used to define the steel tube's elastoplastic stress-strain curve. The inputs for this material are the material properties [elastic modulus (*E*), yield stress (*SIGY*), and Poisson's ratio (*PR*)]. The elastic modulus and the yield stress were 205.0 GPa and 350.0 MPa, respectively, according to the manufacturer's data sheet. *PR* was set to the common value of 0.30.

- *Post-tension strands*

The PT strands were modeled using material model "003-PLASTIC_KINAMATIC". The elastic modulus and the yield stress were 200.0 GPa and 1675.0 MPa, respectively, according to the manufacturer's data sheet. *PR* was set to the common value of 0.30.

- *Mass*

The mass on top of the column was modeled as "001-ELASTIC" material to speed up the analysis since the stresses in the mass itself were not of interest.

Interface Models

The interface modeling is considered the most important part in the segmental models since the behavior is mainly governed by rocking that occurs at the interfaces. A layer of complexity was added in the current model since there are interfaces between the GFRP tube and concrete and between the steel tube and concrete in addition to the interfaces between the segments.

Surface-to-surface contact elements were used to simulate the interactions between the GFRP tube and concrete and between the steel tube and concrete. This type of contact was appropriate because the interaction between these elements occurred at the entire surface rather than at some points. This type of contact could capture slip and separation that might occur between master and slave contact pairs.

The interfaces between the segments and between the segments and footing/head were modeled using two types of contact elements. In the first method, node-to-surface contact elements were used between the nodes of one segment and the surface of the other. In the second method, surface-to-surface contact elements were utilized between the segments in addition to node-to-surface contact elements between the shell elements

of GFRP and steel tubes and the surface of the other segment. This was done since the shell elements did not have surfaces and without the addition of the node-to-surface contact they would not be interfaced. The first method was easier in application and shortened the running time since less contact element existed. However, when the concrete wall thickness was reduced (as in the case of the full scale model as explained later) the second method proved to be more stable since the contact was distributed over the entire surface rather than the nodes. The coefficient of friction was taken as 0.3. This value was conservative and was less than the 0.6 used by other studies (Abdelkarim and ElGawady 2014).

Damping

Another very important parameter to consider while doing the analysis using LS-DYNA is the damping. Damping is completely optional in LS-DYNA, so the user has to include it manually. While several damping models exist in LS-DYNA, the current study implemented "DAMPING FREQUENCY_RANGE_DEFORM". This is a frequency-independent damping option which targets a range of frequencies. Damping_frequency_range was developed by Richard Sturt of Arup and its theoretical details are owned by Arup and are confidential. It was developed with the intent of helping LS-DYNA to handle damping in vibration prediction problems properly including time-history analysis as well as certain classes of seismic problems and civil/structural vibration problems. The "DEFORM" option applies damping to deformable elements and excludes rigid elements. This damping is used for low amounts of damping only, e.g. up to 1% or 2%. The frequency range specified by the user should

ideally be no more than a factor of 30 between highest and lowest. Damping is still achieved outside the frequency range but the amount of damping reduces.

Boundary Conditions and Loading

The footing was constrained in all directions except the translation in x-direction to simulate the experimental conditions of fixed base on a uni-directional shaking table. The PT load was applied as "INITIAL STRESS_BEAM" option and the "DYNAMIC_RELAXATION" was monitored to assure the entire load was applied before the earthquake load was. The earthquake load was applied as accelerations input in the x-direction with the same levels of intensities as the experiments starting from 10% of the DE up to 250% of the DE with steps of 10%.

Validation of the Model

The FE model was able to capture the rocking behavior of the segmental hollow column under ground motion, as illustrated in Figure 4. The rocking occurred at the bottommost two segments with the first segment producing higher rocking. The rocking occurred in both directions and the model was able to capture the behavior exhibited in the experiments.

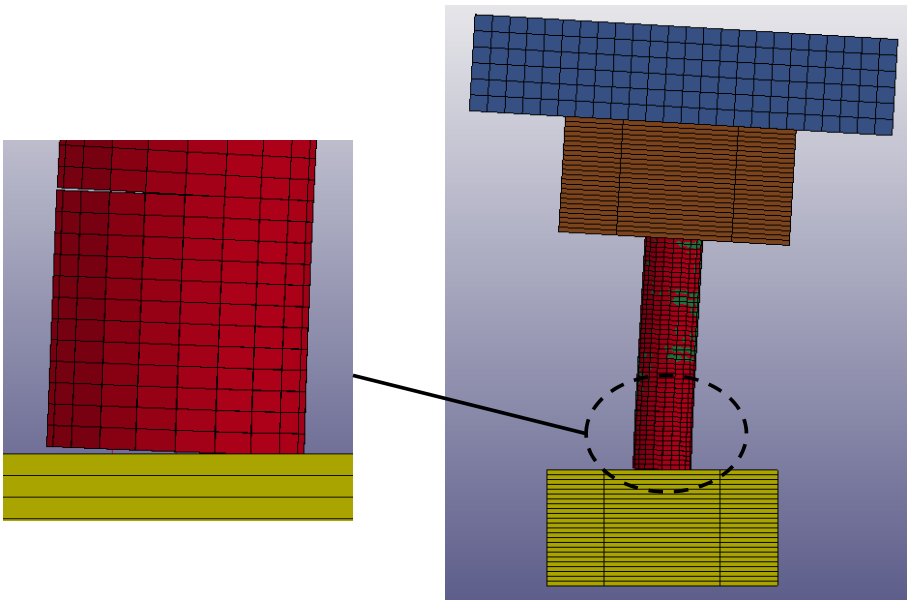

Figure 4. FE modeling for the behavior of the column

The experimental versus FE lateral drift and lateral force time histories for key levels of excitations (DE, MCE, 200% DE, and test end) are illustrated in Figures 5 and 6, respectively. The drift was obtained by dividing the relative displacement (the difference between the displacement at the center of mass and the displacement at the footing) by the height of the column from the footing to the center of mass. The experimental force was calculated by multiplying the acceleration at the center of mass times the mass on top of the column. The FE force was obtained by "SECFORCE" option which obtained the force at a section at the bottom of the column.

Overall, the FE model was able to capture the behavior of the column under 25 consecutive ground motion excitations with a very high level of accuracy. The errors of prediction of the maximum drift ranged between 3.3% and 11.5%, while the error of prediction of the maximum force ranged between 6.6% and 15.1%. The larger error in force prediction can be attributed to neglecting the weights of the column and the additional beams used to post-tension the mass to the column head.

Samples of the lateral force versus lateral drifts for key levels of excitations (DE, MCE, 200% DE, and test end) are illustrated in Figures 7. The FE model was able to capture the hysteresis behavior under 25 consecutive ground motion excitations accurately. The stiffness of the FE model after 160% of the DE was higher than that of the experiment due to yielding of the PT strands in the experiments. The yielding of the PT strands caused them to exhibit inelastic response, where permanent plastic strain occurred leading to the strand to follow a different stress-strain relationship (Priestley and Tao 1993). The "003-PLASTIC_KINAMATIC" material model provided an approximation of the behavior, which led to higher stiffness.

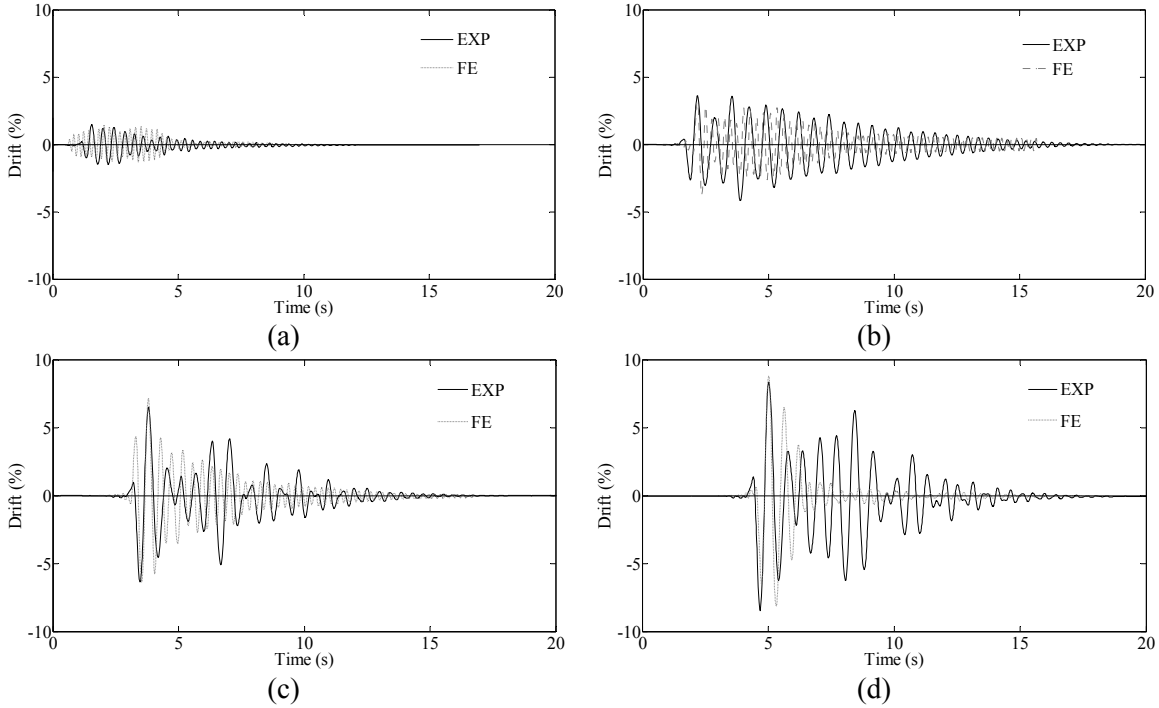

Figure 5. Experimental versus FE drift time histories for: a) DE, b) MCE, c) 200% DE, and d) test end (250% DE)

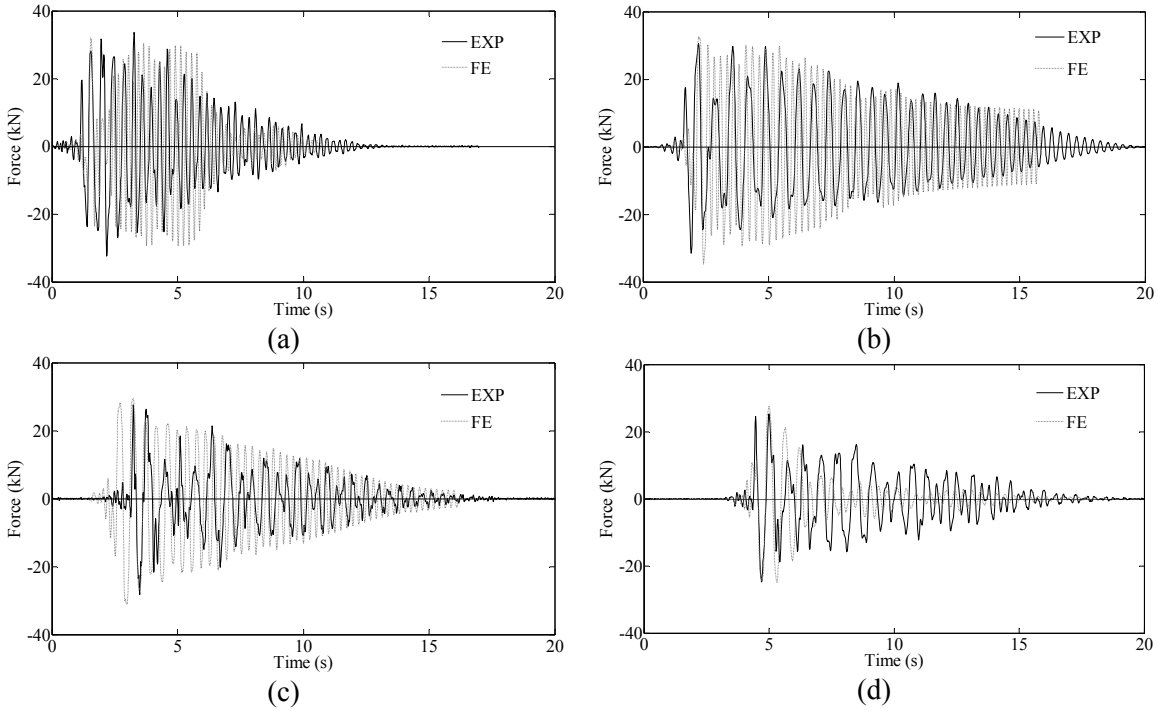

Figure 6. Experimental versus FE force time histories for: a) DE, b) MCE, c) 200% DE, and d) test end (250% DE)

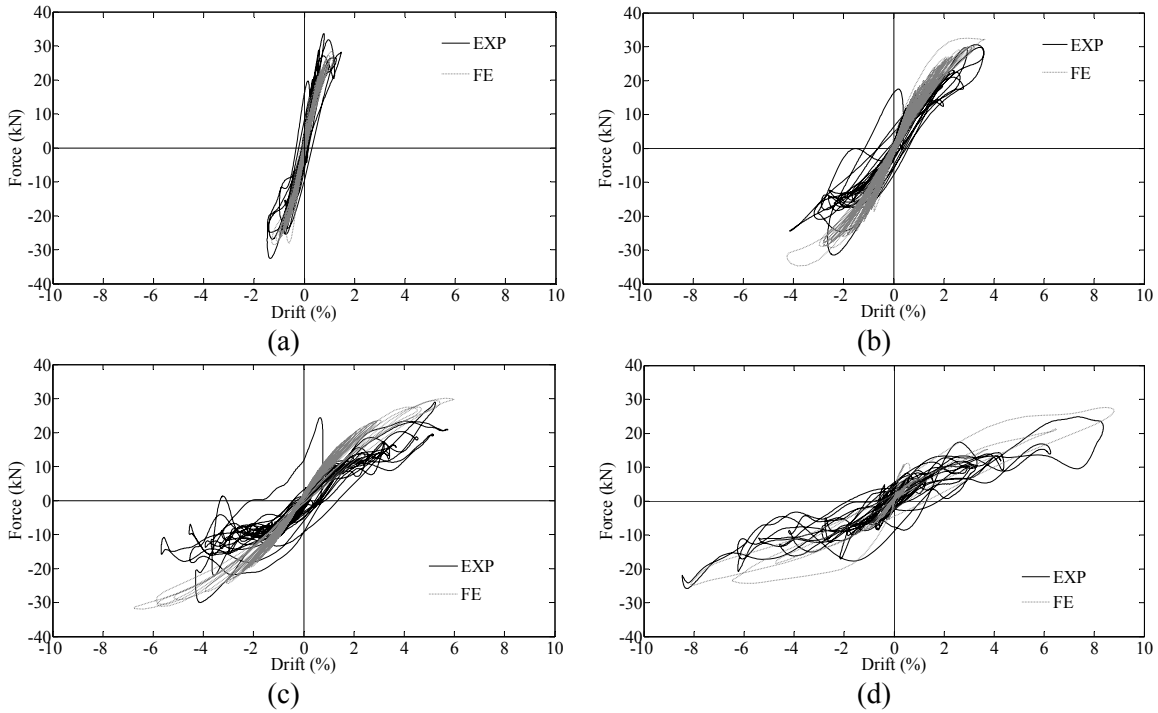

Figure 7. Experimental versus FE force-drift hysteresis for: a) DE, b) MCE, c) 200% DE, and d) test end (250% DE)

The envelopes of the lateral force versus lateral drift, known as dynamic push over curve, for the experimental versus FE model are illustrated in Figure 8. Each point on the curve represents the maximum force and the corresponding drift for one of the tests from the sequence of 10% to 250% of the DE. The FE results were in good agreement with the experimental results.

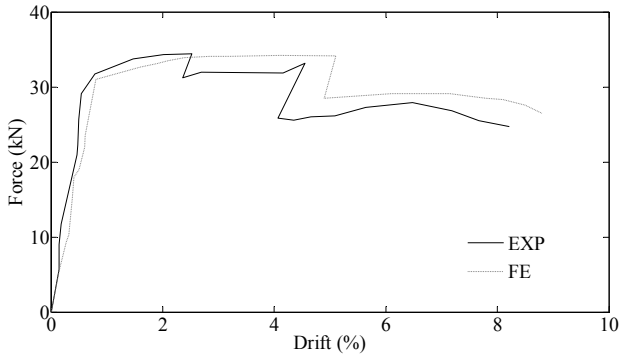

Figure 8. Experimental versus FE force-drift envelope

Full Scale Model

The verified model was adopted to construct a full scale model for parametric study. The similarities and differences between the full scale and the ¼ scale models are discussed in this section.

Geometry

The model was scaled up by a scale of length scale of 4. The diameter of the column was 1200 mm. The concrete core wall thickness was reduced to 100 mm instead of 250 mm that would result from the length scale factor. This was achieved by changing the steel tube diameter to 1000 mm. The small wall thickness was adopted to reduce the weight of the segments and save money on the amount of concrete and transportation. Nine PT ducts; each consisting of two PT strands of diameter 15.2 mm or three PT strands of

diameter 12.7 mm could be used depending on the availability and ease of construction. One duct was placed at the center of the column and the other eight were distributed on a circle with a diameter of 400 mm. This can be easily achieved by arranging them on a temporary PVC tube that can be used for construction purpose only. The reason behind this arrangement, rather than arranging them inside the steel tube like the small scale, was to avoid early yielding of the PT strands that might result in loss of capacity. The thicknesses of the GFRP and steel tubes were 100 mm and 50 mm, respectively. The overall geometries of the footing, column head, and mass were kept the same as the small scale configuration (Figure 3(a)).

Loading

The weight on top of the column was increase to an axial load ratio (ALR) of 7% of the nominal capacity of a solid column to represent the value of the weight of a superstructure of a typical RC bridge column as follows:

$$ALR = \frac{W}{f_c^{'} A_g} \tag{1}$$

where, W is the weight on top of the column, and A_g is the area of a solid column.

The initial PT level at each tendon was 40% of the ultimate strength of the tendons to provide an economic level without early yielding. The total axial load from PT corresponded to 19% of the nominal capacity of the hollow section. This value was in the range recommended by Dawood et al. 2011.

The earthquake loading was limited by the computational capabilities and running time for 20 different ground motions, each with different levels of scaling. These limitations led to running the motions up to 200% of the DE with steps of 20%. The 200% of the DE level was already high enough as it was far beyond the MCE. The final runs went as 60%, 80%, 100%, 120%, 140%, 150%, 160%, 180%, and 200% of the DE with rest period after each motion to allow the free vibration to end. This procedure was repeated for all the 20 ground motions from different categories. This loading pattern was adopted to capture any possible damage accumulation that might occur at the bridge column under a main-shock, foreshocks, and aftershocks.

Effect of Ground Motion Type

The effects of different ground motion types on the behavior of the segmental hollow columns are investigated, rather than the effects of the geometric parameters like dimensions and PT level. For the effects of the geometric parameters on segmental columns, the reader is referred to ElGawady and Dawood 2012 and Leitner and Hao 2016. As mentioned before, the ground motion categories considered in this study are far-field motions (hereinafter denoted as FAR), near-fault motions without forward-directivity (hereinafter denoted as NO FD), near-fault motions with forward-directivity (hereinafter denoted as FD), and near-fault motions with fling-step (hereinafter denoted as FLING). A list of the selected ground motions is provided in Table 1.

Cumulative damage

The columns were subjected to nine consecutive runs, as explained earlier. A sample output drift time history is illustrated in Figure 9. The columns exhibited a rocking behavior during each motion, and at the end of each motion the column was brought back to its original position by the PT cables. The columns showed excellent self-centering capability allowing them to withstand the aftershocks even when they were higher in intensity. The cross-section used also aided to achieve that behavior with confinement of concrete using GFRP to prevent its damage and containment of the inside using the steel tube. The behavior of the columns was much favorable than the expected behavior of a RC column, where rebar yielding and concrete spalling would be inevitable causing permanent damages that weaken the column and make the effect of aftershocks more damaging.

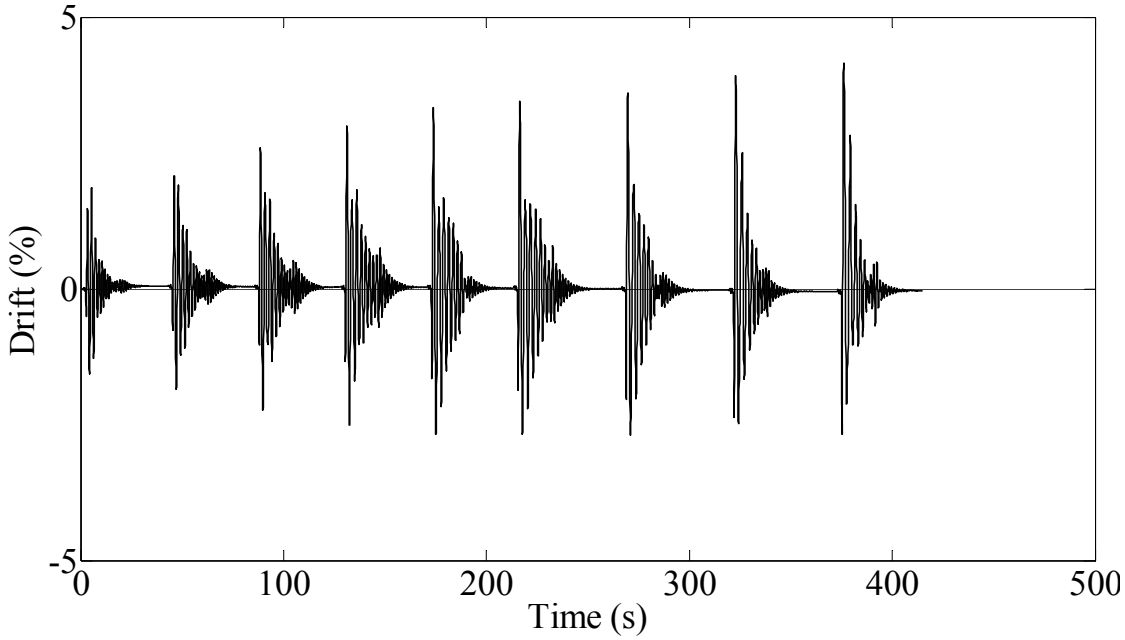

Figure 9. Drift time history for consecutive runs

Table 1. List of the selected ground motions

Category	Year	Earthquake	M_W	Mechanism	Station	Rjb (km)	Site Class	Component	PGA (g)
FAR	1989	Loma Prieta	6.93	Reverse Oblique	SF Intern. Airport	58.52	D	0	
	1986	Taiwan SMART1(45)	7.3	Reverse	SMART1 I12	56.2	D	EW	
	1989	Loma Prieta	6.93	Reverse Oblique	Bear Valley #12_ Williams Ranch	50.71	D	220	
	2007	Chuetsu-oki_ Japan	6.8	Reverse	NGN001	51.48	D	EW	
	1999	Kocaeli_ Turkey	7.51	strike slip	Atakoy	56.49	D	0	
NO FD	1999	Chi-Chi_ Taiwan	7.62	Reverse Oblique	HWA014	51.49	D	EW	
	1989	Loma Prieta	6.93	Reverse Oblique	Hayward - BART Sta	54.01	D	220	
	1989	Loma Prieta	6.93	Reverse Oblique	Bear Valley #12_ Williams Ranch	50.71	D	310	
	1940	Imperial Valley-02	6.95	strike slip	El Centro Array #9	-	D	270	
	1979	Imperial Valley-06	6.53	strike slip	Chihuahua	7.29	D	12	
FD	1994	Northridge	6.7		Rinaldi				
	2004	Parkfield	6.4	strike slip	Cholame 1E	6.5	D	FN	0.47
	1992	Cape Mendocino	7.1	Thrust	Petrolia, General Store	15.9	C	090	0.66
	1999	Kocaeli	7.4	strike slip	Duzce	11.0	D	180	0.31
	1994	Northridge	6.7	Thrust	Sylmar Olive View Hospital	6.4	D	360	0.84
FLING	1999	Chi-Chi	7.6	Thrust	TCU074	13.8	D	EW	0.59
	1999	Chi-Chi	7.6	Thrust	TCU129	2.2	D	EW	0.98
	1999	Kocaeli	7.4	strike slip	Sakarya	3.2	C	EW	0.41
	1999	Chi-Chi	7.6	Thrust	TCU084	11.4	C	EW	0.98
	1999	Chi-Chi	7.6	Thrust	TCU067	1.1	D	EW	0.48

Hysteretic Behavior

The hysteretic behavior of the columns under different types of motions is illustrated in Figure 10 using the force-drift relationship at 200% of the DE. The FAR motions produced a symmetric curve with high self-centering capability. The NO FD motions were also symmetric with higher irregularities. However, the effects of both motions could be considered similar with the main difference being the NO FD motions were closer to the source producing more energy. The FD on the other hand had a different behavior with asymmetric behavior due to the pulse acting in one direction. The behavior of the column after the pulse got back to symmetry with lower amplitudes. The FLING motions resulted in a strange behavior of the column. The behavior appeared as if the column was hit by two separate motions, and was resisting using two different stiffnesses. This can be attributed to the nature of the fling-step motions hitting the column causing response and then producing permanent residual displacement, which transferred the column with displacement rather than acceleration. This behavior is interesting and has not been reported before because of the lack of studies of the effect of fling-step motions on post-tensioned columns.

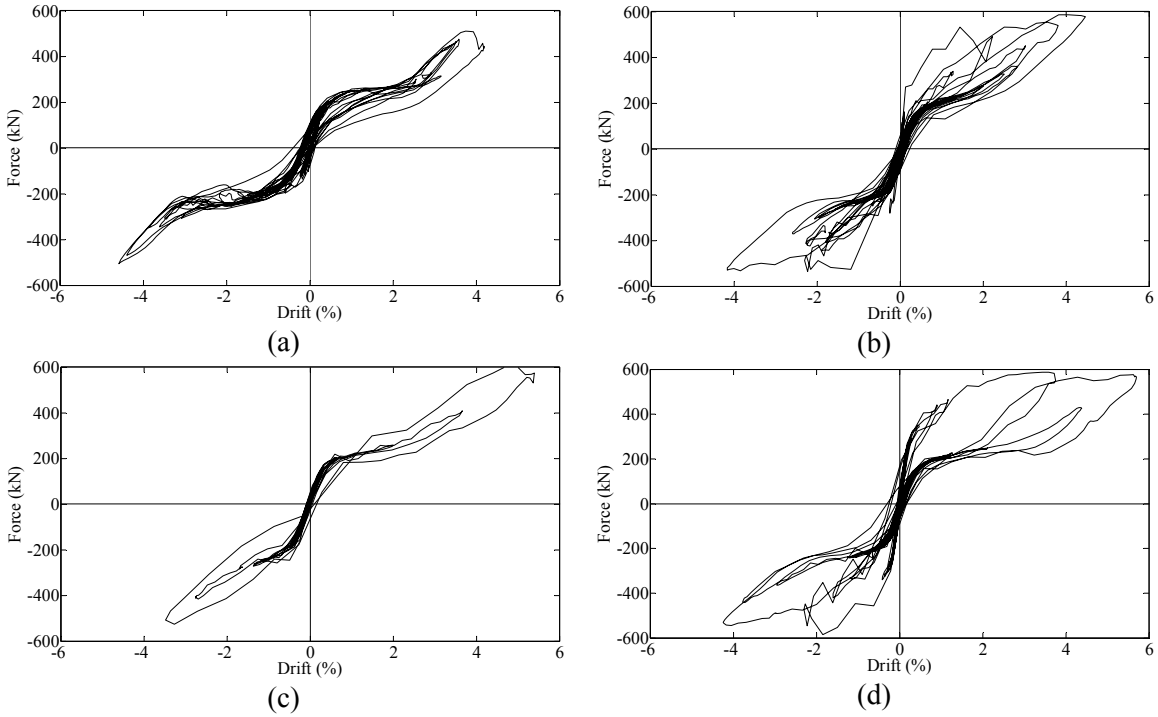

Figure 10. Force versus drift curves at 200% of the DE for: a) FAR, b) NO FD, c) FD, and d) FLING

Columns' Capacity

The effect of ground motion type on columns' capacity is illustrated in Figure 11. The ground motion type, in general, had little effect on the capacity with the maximum average difference in capacity of 6% only.

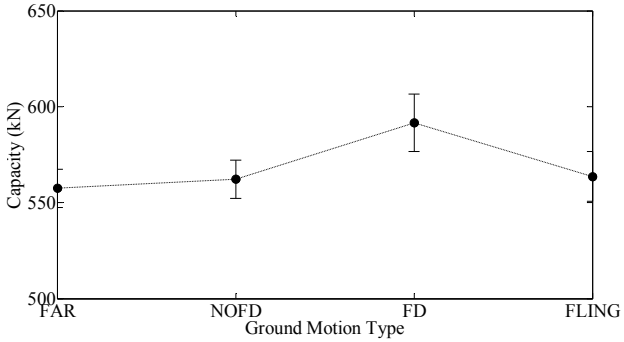

Figure 11. Effect of the ground motion type on columns' capacity

Ultimate Drift

The effect of ground motion type on columns' ultimate drift is illustrated in Figure 12. Unlike the capacity, the ground motion type had a very large effect on the ultimate drift. The average of the ultimate drift for the NO FD was 7.7% higher than that of the FAR motion. This again shows the similarity of response between the two types of motions. On the other hand, the averages of the ultimate drifts for the motions FD and FLING were 58.2% and 46.1% higher than that of the FAR motion. The pulse of the FD increased the drift demand, and so did the hysteretic response of the columns to the FLING motions. It should be mentioned that the standard deviation for the FLING motions was the highest, which can be attributed to the strange hysteretic response.

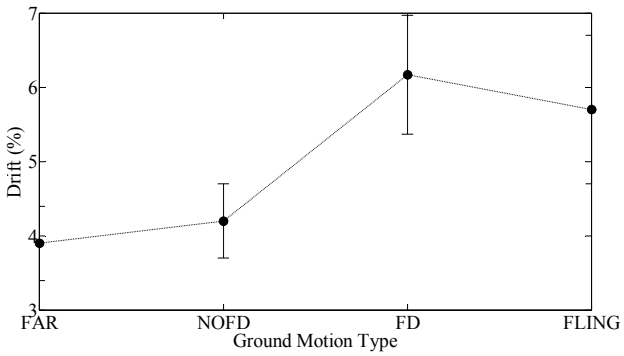

Figure 12. Effect of the ground motion type on columns' ultimate drift

Conclusions

This article investigated the effects of ground motion type on the behavior of segmental hollow-core columns. The motion types considered were far-field motions, near-fault motions without forward directivity, near-fault motions with forward directivity, and near-fault motions with fling-step. A three-dimensional finite element (FE) model using

software LS-DYNA was developed to predict the behavior. This model was the first three-dimensional model under input ground motions. The earthquake load was applied as accelerations input in the x-direction with the same levels of intensities as the experiments starting from 10% of the DE up to 250% of the DE with steps of 10%. The model was validated against experimental results under the same loading conditions. The model was able to capture the rocking behavior using contact elements. The model was able to accurately predict the drift and force time histories. The errors of prediction of the maximum drift ranged between 3.3% and 11.5%, while the error of prediction of the maximum force ranged between 6.6% and 15.1%. The larger error in force prediction can be attributed to neglecting the weights of the column and the additional beams used to post-tension the mass to the column head.

The full scale columns were able to withstand 9 consecutive runs of each ground motion, representing main-shock aftershocks without major damages and exhibited self-centering. The hysteretic response to the FLING motions was characterized by two separate loops with two different stiffnesses as if the column was hit by two different ground motions. This can be attributed to the nature of the fling-step motions hitting the column causing response and then producing permanent residual displacement, which transferred the column with displacement rather than acceleration. The overall behavior of the NO FD motions was closer to the FAR motions than it was to the FD ones; despite these were near-fault motions. The effect of the ground motion type on the capacities of the columns was negligible. The ultimate drift was highly affected by the type of motion with increases of 58.2% and 46.1 for the FD and FLING motions, respectively, compared to the FAR motions. Higher standard deviation was observed in the FLING response.

References

ABAQUS (2011). 6.11 Documentation, ABAQUS, Inc.

Abdelkarim, O. I. and ElGawady, M. A. (2014). "Analytical and Finite-Element Modeling of FRP-Concrete-Steel Double-Skin Tubular Columns." Journal of Bridge Engineering.

Alavi, B. and Krawinkler, H. (2001). Effects of near-fault ground motions on frame structures, John A. Blume Earthquake Engineering Center.

Amiri, G., Razeghi, H. R. and Davoudi, A. R. T. (2011). "The effect of fling step and forward directivity on the seismic response of MSSS bridges." Transportation Research Journal **1**(1): 9.

ASTM D2290 (2012). "Standard Test Method for Apparent Hoop Tensile Strength of Plastic or Reinforced Plastic Pipe."

Baker, J. W. (2007). "Quantitative classification of near-fault ground motions using wavelet analysis." Bulletin of the Seismological Society of America **97**(5): 1486-1501.

Billington, S. L. and Yoon, J. (2004). "Cyclic response of unbonded posttensioned precast columns with ductile fiber-reinforced concrete." Journal of Bridge Engineering **9**(4): 353-363.

Bray, J. D. and Rodriguez-Marek, A. (2004). "Characterization of forward-directivity ground motions in the near-fault region." Soil dynamics and earthquake engineering **24**(11): 815-828.

Chang, K., Loh, C., Chiu, H., Hwang, J., Cheng, C. and Wang, J. (2002). "Seismic behavior of precast segmental bridge columns and design methodology for applications in Taiwan." Taiwan Area National Expressway Engineering Bureau, Taipei, Taiwan in Chinese.

Chou, C. C. and Chen, Y. C. (2006). "Cyclic tests of post-tensioned precast CFT segmental bridge columns with unbonded strands." Earthquake engineering & structural dynamics **35**(2): 159-175.

Dawood, H., ElGawady, M. and Hewes, J. (2011). "Behavior of Segmental Precast Posttensioned Bridge Piers under Lateral Loads." Journal of Bridge Engineering **17**(5): 735-746.

Dawood, H. M., Rodriguez-Marek, A., Bayless, J., Goulet, C. and Thompson, E. (2016). "A Flatfile for the KiK-net Database Processed Using an Automated Protocol." Earthquake Spectra **32**(2): 1281-1302.

ElGawady, M., Booker, A. J. and Dawood, H. M. (2010). "Seismic behavior of posttensioned concrete-filled fiber tubes." Journal of Composites for Construction **14**(5): 616-628.

ElGawady, M. A. and Dawood, H. M. (2012). "Analysis of segmental piers consisted of concrete filled FRP tubes." Engineering Structures **38**: 142-152.

ElGawady, M. A. and Sha'lan, A. (2010). "Seismic behavior of self-centering precast segmental bridge bents." Journal of Bridge Engineering **16**(3): 328-339.

Fahjan, Y. and Ozdemir, Z. (2008). Scaling of earthquake accelerograms for non-linear dynamic analysis to match the earthquake design spectra. The 14th World Conference on Earthquake Engineering, Chinese Society for Earthquake Engineering Beijing, China.

Han, L.-H., Tao, Z., Liao, F.-Y. and Xu, Y. (2010). "Tests on cyclic performance of FRP–concrete–steel double-skin tubular columns." Thin-Walled Structures **48**(6): 430-439.

Hewes, J. T. and Priestley, M. N. (2002). Seismic design and performance of precast concrete segmental bridge columns.

Ichikawa, S., Matsuzaki, H., Moustafa, A., ElGawady, M. A. and Kawashima, K. (2016). "Seismic-Resistant Bridge Columns with Ultrahigh-Performance Concrete Segments." Journal of Bridge Engineering: 04016049.

Japan Road Association (2002). "Design specifications of highway bridges, Part V seismic design." Maruzen, Tokyo, Japan.

Jeong, H., Sakai, J. and Mahin, S. A. (2008). "Shaking table tests and numerical investigation of self-centering reinforced concrete bridge columns." Pacific Earthquake Engineering Research Center. University of California, Berkeley. Public Works Research Institute, Tsukuba, Japan.

Kalkan, E. and Kunnath, S. K. (2006). "Effects of fling step and forward directivity on seismic response of buildings." Earthquake spectra **22**(2): 367-390.

Kim, T.-H., Lee, H.-M., Kim, Y.-J. and Shin, H. (2010). "Performance assessment of precast concrete segmental bridge columns with a shear resistant connecting structure." Engineering Structures **32**(5): 1292-1303.

Leitner, E. J. and Hao, H. (2016). "Three-dimensional finite element modelling of rocking bridge piers under cyclic loading and exploration of options for increased energy dissipation." Engineering Structures **118**: 74-88.

Malvar, L. J., Crawford, J. E., Wesevich, J. W. and Simons, D. (1997). "A plasticity concrete material model for DYNA3D." International Journal of Impact Engineering **19**(9): 847-873.

Mander, J. B. and Cheng, C.-T. (1997). Seismic design of bridge piers based on damage avoidance design, National Center for Earthquake Engineering Research, State Univ. of New York at Buffalo, Buffalo, NY.

Marriott, D., Pampanin, S. and Palermo, A. (2009). "Quasi-static and pseudo-dynamic testing of unbonded post-tensioned rocking bridge piers with external replaceable dissipaters." Earthquake Engineering & Structural Dynamics **38**(3): 331-354.

Ou, Y.-C., Chiewanichakorn, M., Aref, A. J. and Lee, G. C. (2007). "Seismic performance of segmental precast unbonded posttensioned concrete bridge columns." Journal of Structural Engineering **133**(11): 1636-1647.

Ou, Y.-C., Wang, P.-H., Tsai, M.-S., Chang, K.-C. and Lee, G. C. (2009). "Large-scale experimental study of precast segmental unbonded posttensioned concrete bridge columns for seismic regions." Journal of structural engineering **136**(3): 255-264.

Ou, Y. C., Tsai, M. S., Chang, K. C. and Lee, G. C. (2010). "Cyclic behavior of precast segmental concrete bridge columns with high performance or conventional steel reinforcing bars as energy dissipation bars." Earthquake Engineering & Structural Dynamics **39**(11): 1181-1198.

Ozbakkaloglu, T. and Idris, Y. (2014). "Seismic behavior of FRP-high-strength concrete–steel double-skin tubular columns." Journal of Structural Engineering **140**(6).

Palermo, A., Pampanin, S. and Marriott, D. (2007). "Design, modeling, and experimental response of seismic resistant bridge piers with posttensioned dissipating connections." Journal of Structural Engineering **133**(11): 1648-1661.

Priestley, M. N. and Tao, J. R. (1993). "Seismic response of precast prestressed concrete frames with partially debonded tendons." PCI Journal **38**(1): 58-69.

Shim, C. S., Chung, C.-H. and Kim, H. H. (2008). "Experimental evaluation of seismic performance of precast segmental bridge piers with a circular solid section." Engineering Structures **30**(12): 3782-3792.

Solberg, K., Mashiko, N., Mander, J. and Dhakal, R. (2009). "Performance of a damage-protected highway bridge pier subjected to bidirectional earthquake attack." Journal of structural engineering **135**(5): 469-478.

Somerville, P. G., Smith, N. F., Graves, R. W. and Abrahamson, N. A. (1997). "Modification of empirical strong ground motion attenuation relations to include the amplitude and duration effects of rupture directivity." Seismological Research Letters **68**(1): 199-222.

Teng, J., Yu, T., Wong, Y. and Dong, S. (2007). "Hybrid FRP–concrete–steel tubular columns: concept and behavior." Construction and Building Materials **21**(4): 846-854.

Trono, W., Jen, G., Panagiotou, M., Schoettler, M. and Ostertag, C. P. (2014). "Seismic response of a damage-resistant recentering posttensioned-HYFRC bridge column." Journal of Bridge Engineering **20**(7): 04014096.

Vamvatsikos, D. and Cornell, C. A. (2002). "Incremental dynamic analysis." Earthquake Engineering & Structural Dynamics **31**(3): 491-514.

Wong, Y., Yu, T., Teng, J. and Dong, S. (2008). "Behavior of FRP-confined concrete in annular section columns." Composites Part B: Engineering **39**(3): 451-466.

Youssf, O., ElGawady, M. A., Mills, J. E. and Ma, X. (2014). "Finite element modelling and dilation of FRP-confined concrete columns." Engineering Structures **79**: 70-85.

Zhang, Q. and Alam, M. S. (2015). "Evaluating the Seismic Behavior of Segmental Unbounded Posttensioned Concrete Bridge Piers Using Factorial Analysis." Journal of Bridge Engineering **21**(4): 04015073.

SECTION

3. SUMMARY, CONCLUSIONS AND RECOMMENDATIONS

3.1. SUMMARY OF RESEARCH WORK

The purpose of this research was to develop, test, and evaluate innovative techniques for seismic-resistant bridge columns that could outperform conventional reinforced concrete (RC) bridge columns. Two techniques were proposed for this project. The first technique was based on changing the material damping by using recycled scrap crumb tire rubber as a replacement of fine aggregate in concrete to create rubberized concrete. The second technique was based on increasing external damping combined with a self-centering system and new column cross section. The proposed new cross section, called a hollow-core fiber reinforced polymer-concrete-steel (HC-FRPCS) segmental cross-section, consists of an outer fiber reinforced polymer (FRP) tube, an inner steel tube, and concrete in between the two. The proposed research plan included a description of nine tasks necessary to accomplish these goals. These tasks were:

Task 1: Review the Literature

Task 2: Experimentally Characterize the Mechanical Properties of Rubberized Concrete

Task 3: Experimentally Investigate the Dynamic Properties of Rubberized Concrete using Three Different Techniques

Task 4: Conduct Fidelity Testing of the New Shaking Table

Task 5: Experimentally Investigate Large-scale RC, Rubberized Concrete, and Segmental Double-skin Columns under Simulated Earthquakes

Task 6: Develop Energy Dissipating Mechanisms for the Segmental Double-skin Columns

Task 7: Develop a Three-dimensional Finite Element Model for Post-tensioned Segmental Columns under Simulated Earthquakes

Task 8: Numerically Investigate Full-scale Segmental Double-skin Columns under Simulated Earthquakes

Task 9: Develop Design Tools for Segmental Columns

Conclusion and recommendations based on the results are presented in the following sections.

3.2. CONCLUSIONS

The following section summarizes the conclusions from the experimental, modeling, and analytical studies of the seismic-resistant columns.

3.2.1. Rubberized Concrete. The first part of this phase had shown that the mix design for CS has lower variation in the damping results and higher damping properties compared to either the conventional concrete or VS mixes. It showed the importance of maintaining the workability of concrete for better dispersion of rubber particles in the concrete rather than being a fresh property. It is recommended to replace up to 20% of fine aggregate with scrap tire rubber to achieve both lower reduction of compressive strength and enhanced dynamic properties compared to 30% replacement. Hence, the CS mix can be used for structural elements subjected to dynamic loads. However, before this can be achieved, testing of structural elements constructed out of rubberized concrete

needs to be carried out. The rubberized concrete's confinement provided a good solution to reducing of the compressive strength loss to 25% compared to 41.9% for the unconfined concrete. It should be noted that in papers I and II, the behavior of high strength rubberized concrete was investigated, while in paper III, the behavior of normal strength rubberized concrete were investigated. The conclusions from papers I and II were for guidance on paper IV, while the conclusions for paper III of using the CS mix with 20% replacement ration were applied in paper IV.

This research presented the first shake-table test of a large-scale rubberized column and compared its behavior to that of a conventional column with identical dimensions. Both columns were subjected to a sequence of scaled ground motions of the Northridge-01 1994 earthquake at Rinaldi receiving station. The ground motion scales started from 10% of the DE up to 200% of the DE with increments of 10%. The rebar fracture in the RC column occurred at 140% of the DE. The use of rubberized concrete delayed the rebar fracture to 190% of the DE. The RC column started losing its capacity at 3.4% drift and it lost 20.6% of its capacity at 4.8% drift. This can be attributed to the earlier rebar fracture. The rubberized column, on the other hand, was able to maintain its integrity up to 5.4% drift due to the delayed rebar fracture caused by the higher energy dissipation. The rubberized column reached a peak drift of 5.4% as compared to 4.8% in the RC column with an increase of 12.5%. The cumulative dissipated energy was increased by 16.5% in the rubberized column compared to the RC column. The rubberized column showed a higher average hysteresis damping before the rebar fracture in the RC column. The viscous damping of the rubberized column was higher than that of the RC column due to the visco-elastic nature of the rubber. The rebar fracture in the RC

column at 140% of the DE caused the damping to increase significantly due to the reduction in column stiffness and the increased damage. The improved performance of the rubberized column along with the ease of use because of maintaining the construction technique makes the rubberized columns a superior candidate for bridge columns in high seismic regions.

3.2.2. Double-Skin Segmental Columns. The double-skin segmental post-tensioned column inherited the combined advantages of all its components as follows: the column benefited from the confinement of the FRP from the double skin section. The columns also utilized the re-centering capability of the unbonded post-tensioned system. In addition, the columns accelerate the bridge construction due to the segmental nature and light weight because of the hollow cross section. Energy dissipation was provided by external replaceable bars for two columns SEG-ED1 and SEG-ED2. The columns were subjected to a sequence of scaled ground motions of the Northridge-01 1994 earthquake at Rinaldi receiving station. The ground motion scales started from 10% of the DE up to 250% of the DE with increments of 10%. The rebar fracture in the RC column occurred at 140% of the DE and the column started losing its capacity at 3.4% drift and it lost 20.6% of its capacity at 4.8% drift. The column SEG was able to sustain up to 250% of the DE. However, yielding of the PT strands occurred at 160% of the DE. This yielding was avoided in the column SEG-ED2 by reducing the initial PT force from 54% to 44% of the ultimate strength. The addition of the external energy dissipaters was able to make up for the difference in capacity. It is recommended to maintain the initial PT force under 40% of the ultimate strength to avoid yielding of the PT strands at large drifts.

All the segmental columns exhibited an excellent re-centering capability with only 0.08% maximum residual drift after being subjected to the sequence of ground motions while the RC column suffered 1.5% residual drift. The SEG-ED2 column was able to achieve energy dissipations and damping close to the reference RC column.

The energy of the system was investigated to comprehend the behavior of the columns. The total energy consisted of the well known hysteretic energy (E_{hys}), kinetic energy (E_k), potential energy (E_p), elastic energy (E_e), and viscous damping energy (E_V). In addition to these, the radiation energy (E_R) played a key part in the system. Unlike the common practice that the radiation damping is step-wise, the radiation damping was found to be continuous and viscous.

The radiation damping was the main source of the overall viscous damping of the columns. The yielding of the PT strands increased the viscous damping but not the radiation damping. The addition of external energy dissipaters at the column SEG-ED2 increased the radiation damping.

The addition of external energy dissipaters resulted in a favorable behavior with the possibility of replacement after a major earthquake, the possibility to tailor them according to the seismic zone and the required performance, and the control of the unbonded length along with the tension only detail which prevent low cyclic fatigue.

The SEG-ED2 column outperformed the rest of the columns providing a superior candidate for damage-resistant columns in high seismic zones.

3.2.3. Finite Element Study. This research presented the first three-dimensional finite element (FE) analysis of segmental hollow-core bridge columns with post-tensioned unbonded strands under ground motion excitations. The FE software LS-

DYNA was used to develop the seismic response under a series of different ground motions. The earthquake load was applied as accelerations input in the x-direction with the same levels of intensities as the experiments starting from 10% of the DE up to 250% of the DE with steps of 10%. The model was validated against experimental results under the same loading conditions. The model was able to capture the rocking behavior using contact elements. The model was able to accurately predict the drift and force time histories. The errors of prediction of the maximum drift ranged between 3.3% and 11.5%, while the error of prediction of the maximum force ranged between 6.6% and 15.1%. The larger error in force prediction can be attributed to neglecting the weights of the column and the additional beams used to post-tension the mass to the column head.

A parametric study was conducted on full scale models to investigate the effects of ground motion type on the behavior of the columns. The motion types considered were far-field motions, near-fault motions without forward directivity, near-fault motions with forward directivity, and near-fault motions with fling-step. The column was able to withstand 9 consecutive runs of each ground motion, representing main-shock aftershocks without major damages and exhibited self-centering. The hysteretic response to the FLING motions was characterized by two separate loops with two different stiffnesses as if the column was hit by two different ground motions. This can be attributed to the nature of the fling-step motions hitting the column causing response and then producing permanent residual displacement, which transferred the column with displacement rather than acceleration. The overall behavior of the NO FD motions was closer to the FAR motions than it was to the FD ones; despite these were near-fault motions. The effect of the ground motion type on the capacities of the columns was

negligible. The ultimate drift was highly affected by the type of motion with increases of 58.2% and 46.1 for the FD and FLING motions, respectively, compared to the FAR motions. Higher standard deviation was observed in the FLING response.

3.3. RECOMMENDATIONS

Based on the results of this study, the CS mix is recommended for use in rubberized concrete. Replacement of 20% of fine aggregate with rubber is recommended. The use of external energy dissipaters with tension only details, similar to column SEG-ED2, is recommended for energy dissipation. The initial post-tension force should be limited to 40% of the ultimate load to avoid PT yielding

Based on the conclusions stated in the previous section, future research could be considering the following:

- Full-scale shaking table testing for the proposed columns under different ground motions.
- The use of large particles of rubber as a replacement for coarse aggregate and testing it on the shaking table.
- Durability studies of rubberized concrete.
- Shear strength of short segmental columns.
- Integration of non-destructive techniques for monitoring the long term losses of PT force.
- Investigation of construction techniques that give similar contact as match casting and being fully precast.

- Investigation of connection details for tension-only bars to be applicable in the field.
- Durability studies of the segments; especially the steel tube.

APPENDIX A

PHOTOGRAPHS OF MATERIALS TESTING SPECIMENS AND TESTS

Figure A.1. Sulfur capping preparation for the cylinders

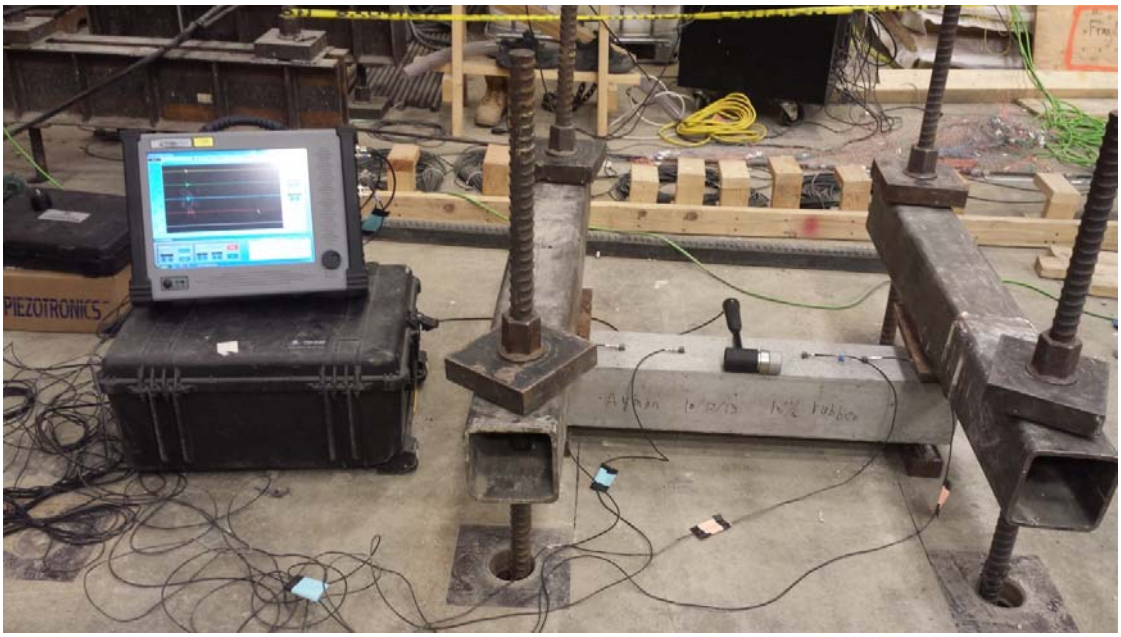

Figure A.2. Initial test setup for impact hammer testing (the modified setup can be found in Paper II)

Figure A.3. Slump test for the SCC

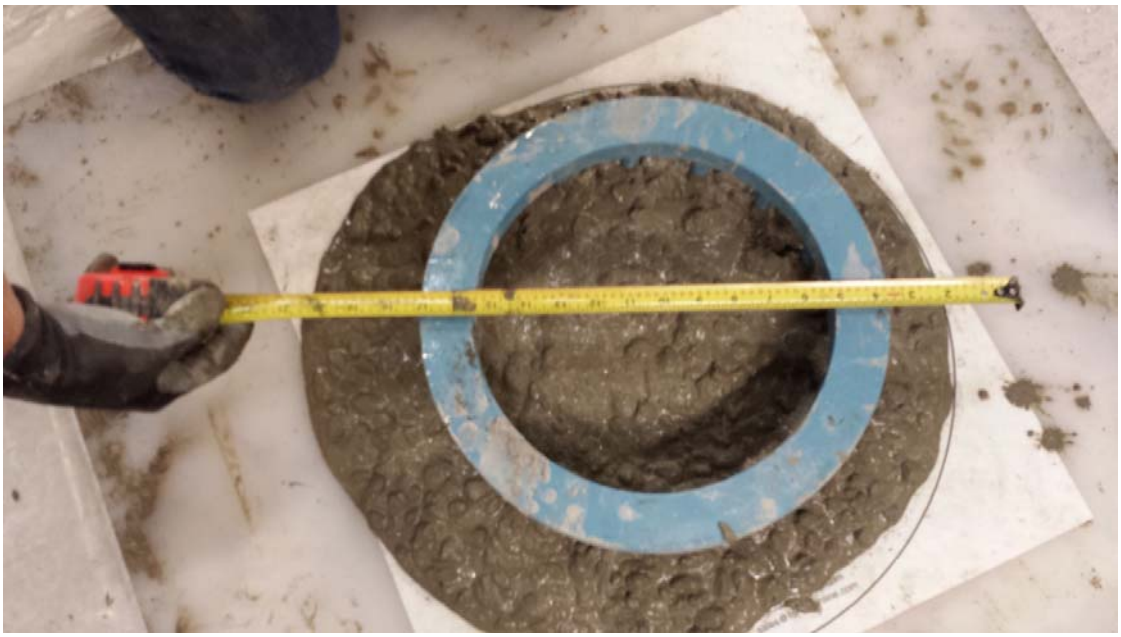

Figure A.4. Ring test for the SCC

Figure A.5. GFRP ring tests

Figure A.6. Scaffold construction for drop weight testing

APPENDIX B

LARGE-SCALE TESTING PICTURES

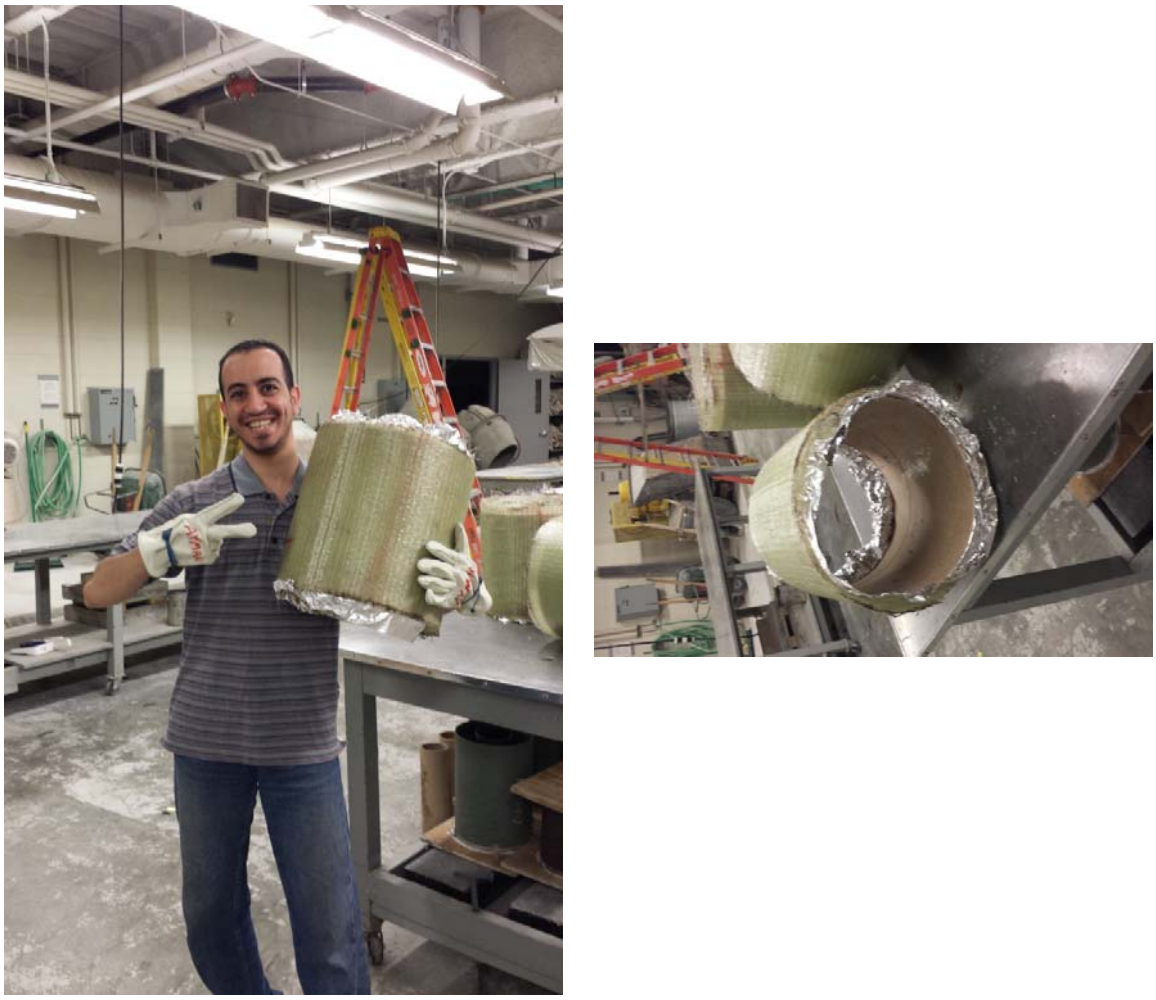

Figure B.1. GFRP tube preparation

Figure B.2. Mass preparation

Figure B.3. Foundation steel cage preparation

Figure B.4. Foundation and head steel cages ready

Figure B.5. Foundation and head concrete pouring

Figure B.6. Construction of the segmental column

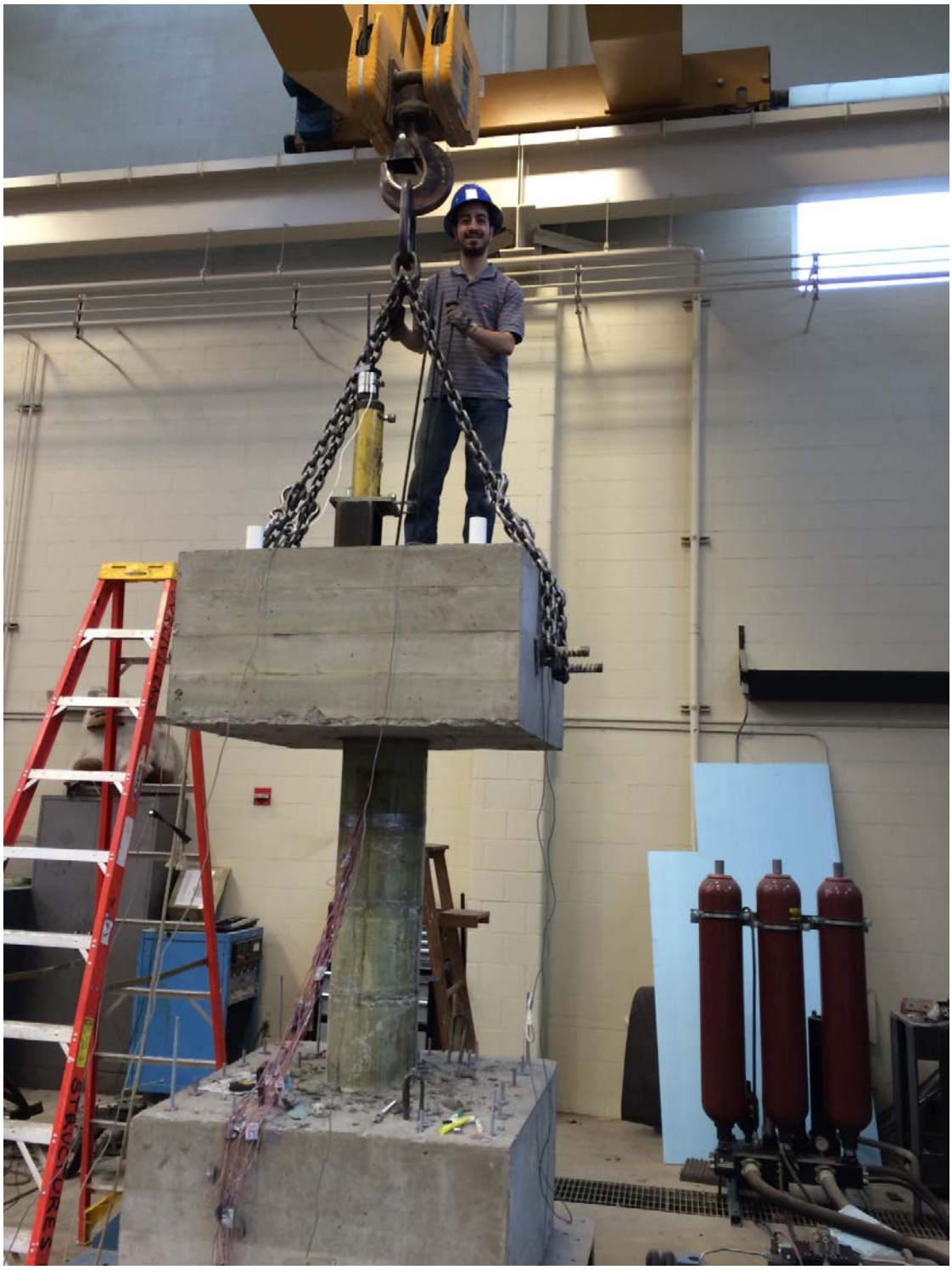

Figure B.7. Post-tensioning of the segmental column

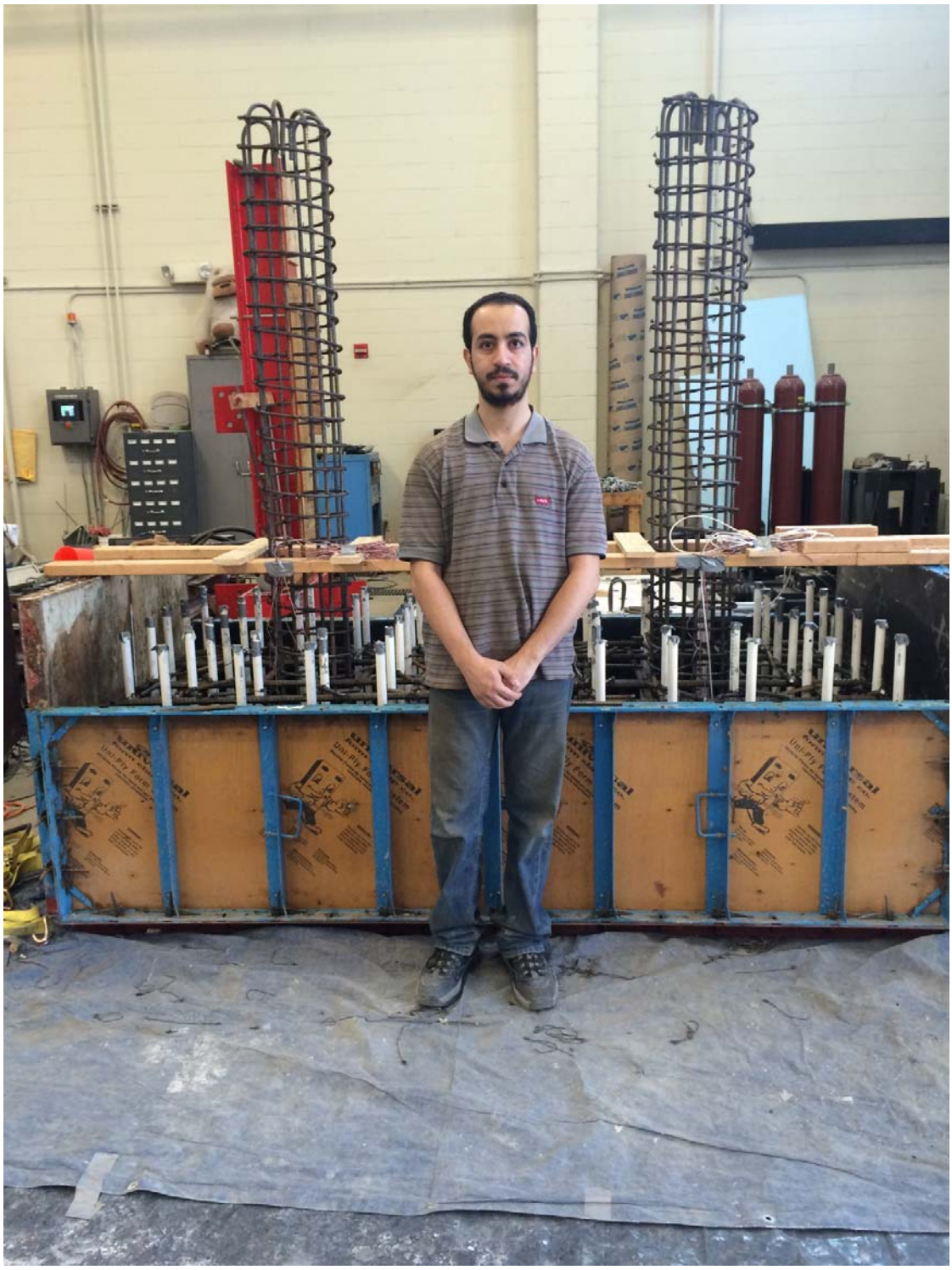

Figure B.8. Steel cages for the RC and rubberized columns

Figure B.9. Concrete pouring for the RC and rubberized columns

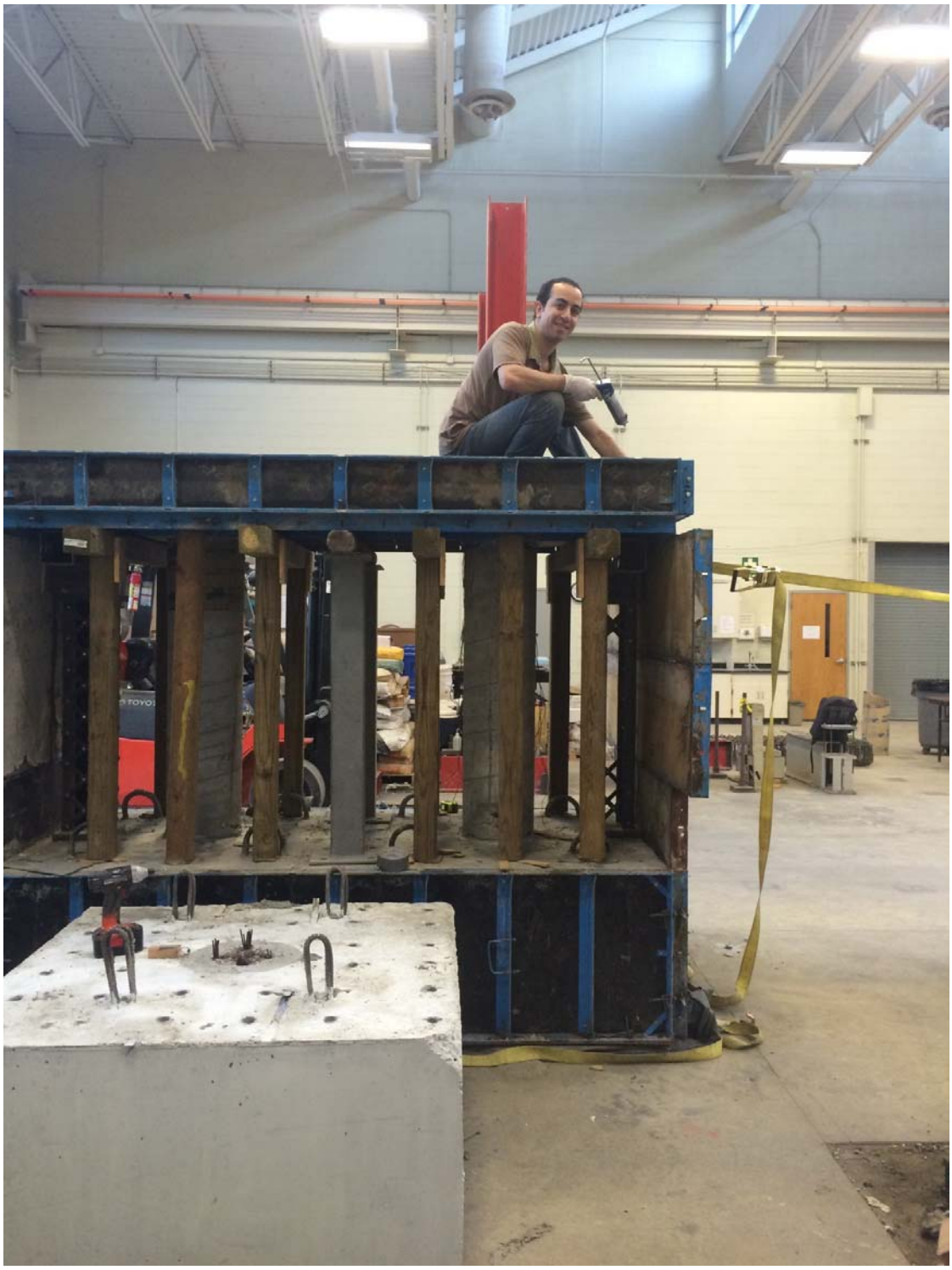

Figure B.10. Supports for the top slabs of the RC and rubberized columns

Figure B.11. RC and rubberized columns

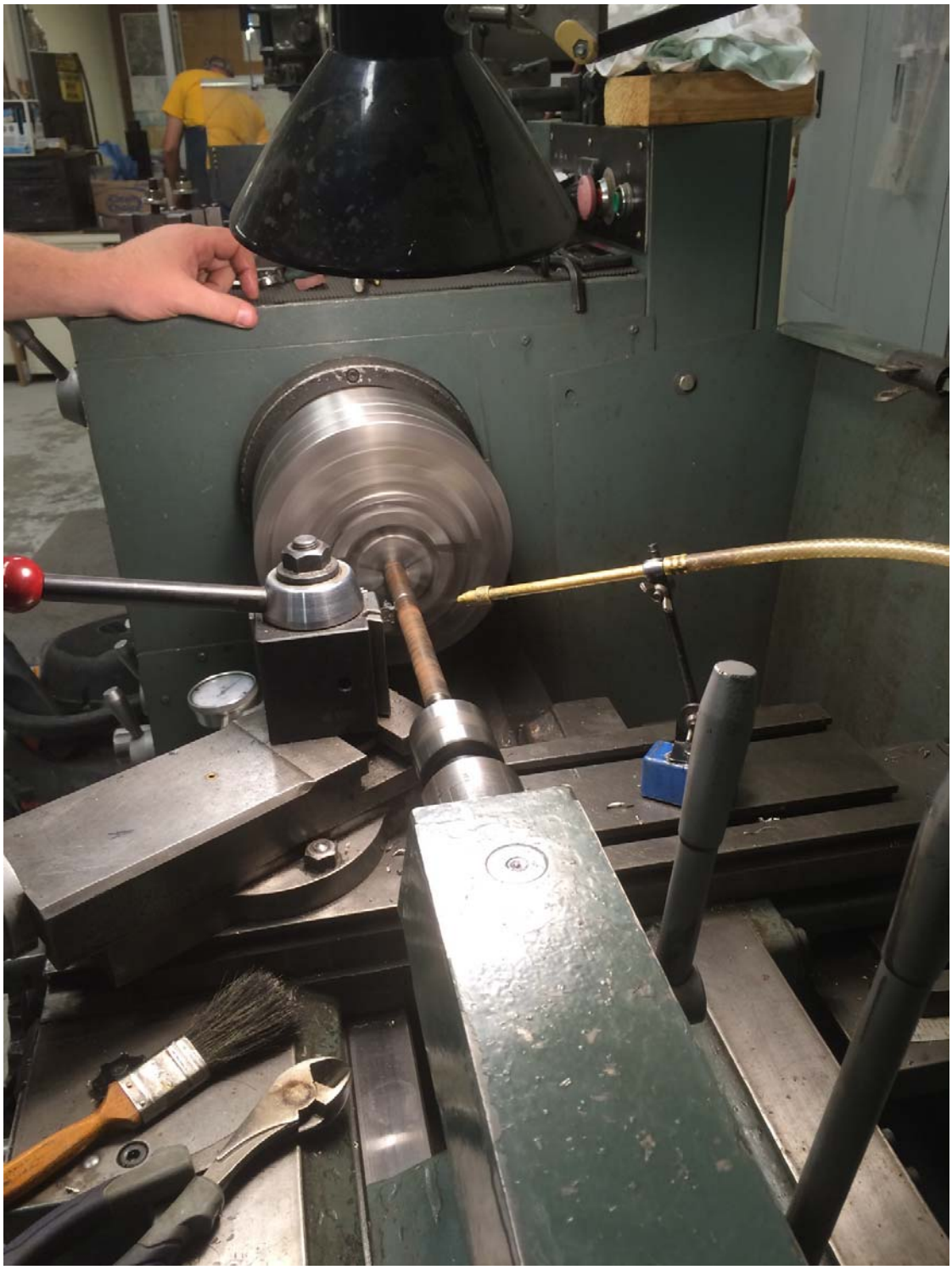

Figure B.12. Lathing of the energy dissipaters

APPENDIX C

FINITE ELEMENT RESULTS

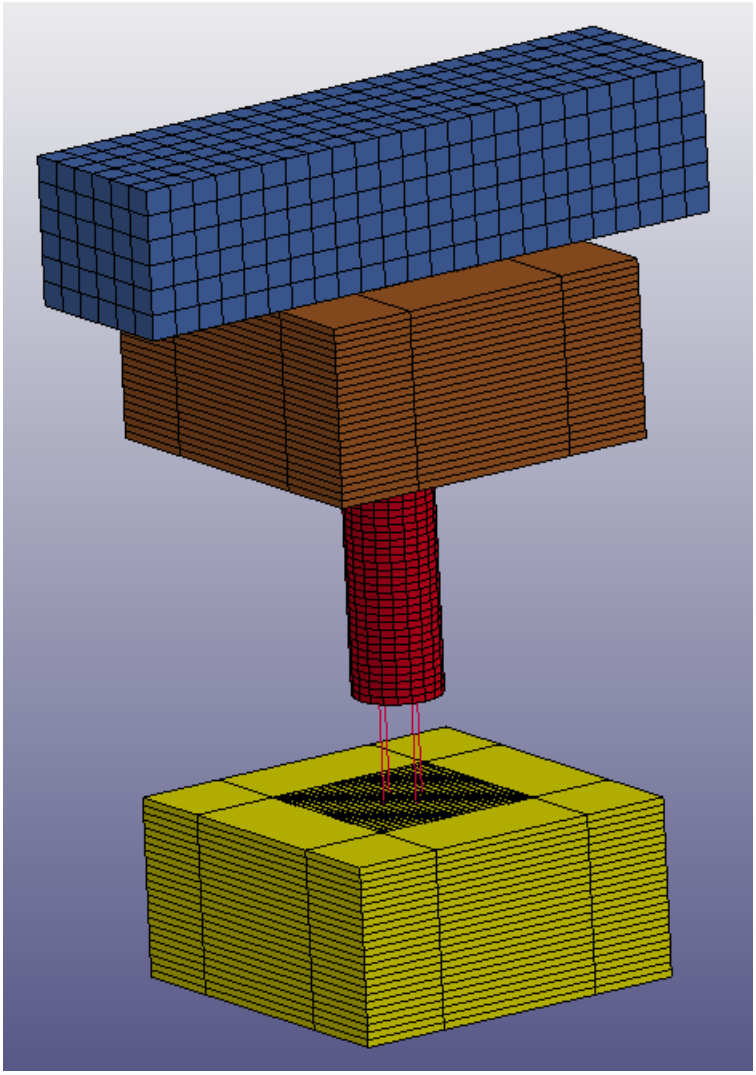

Figure C.1. 3D-View with PT cables

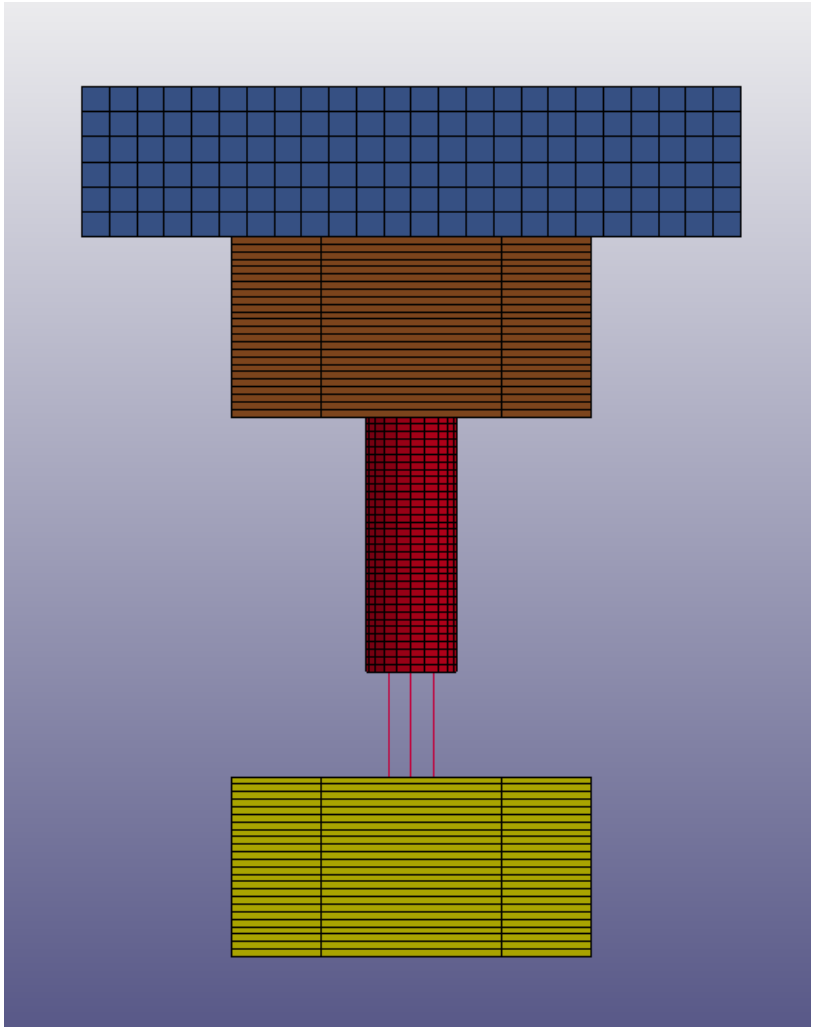

Figure C.2. Elevation with PT cables

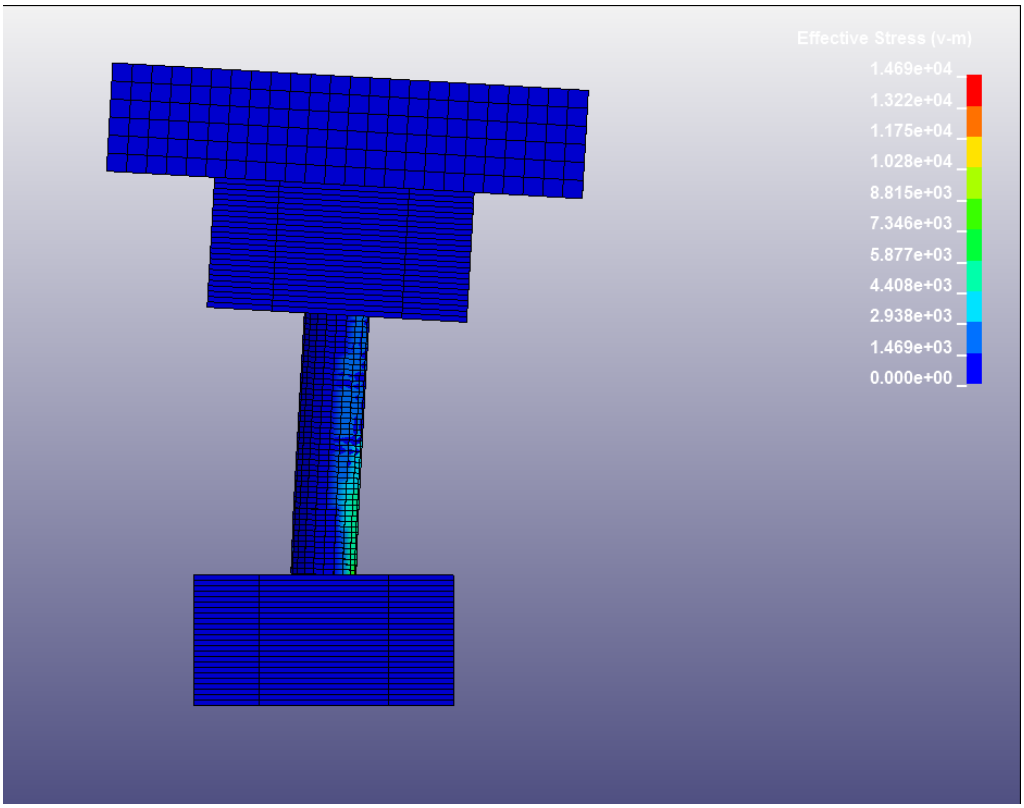

Figure C.3. Effective stresses (Von-Mises)

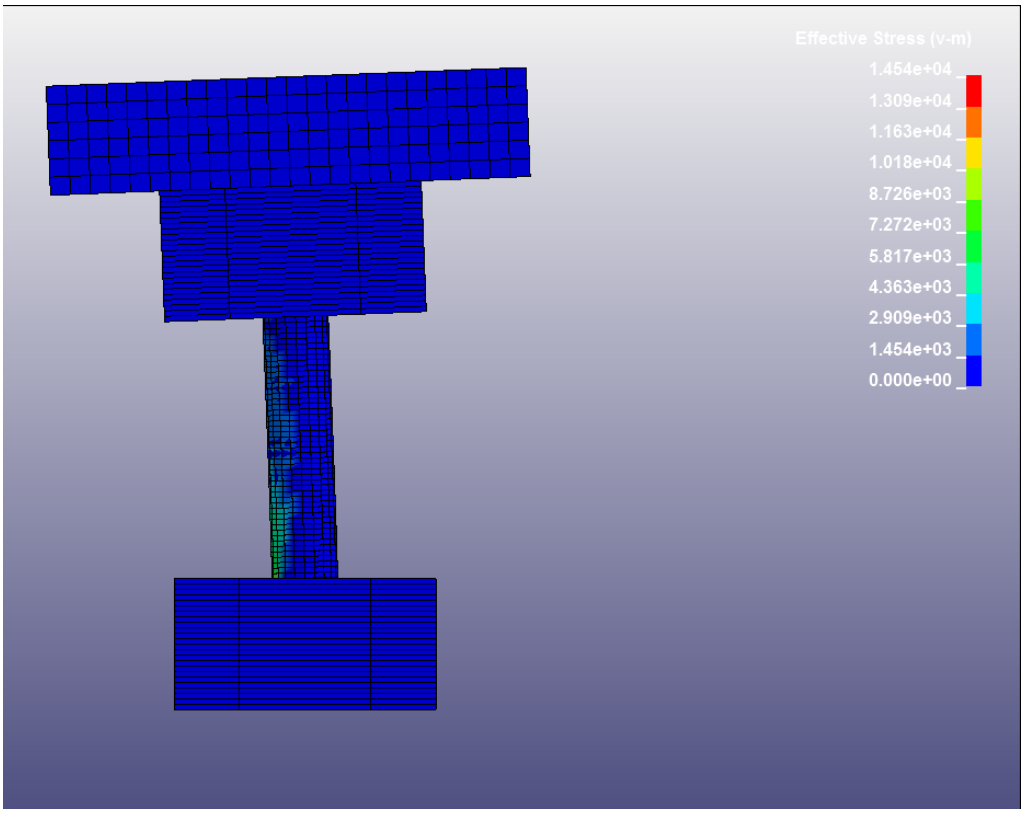

Figure C.4. Effective stresses (Von-Mises)

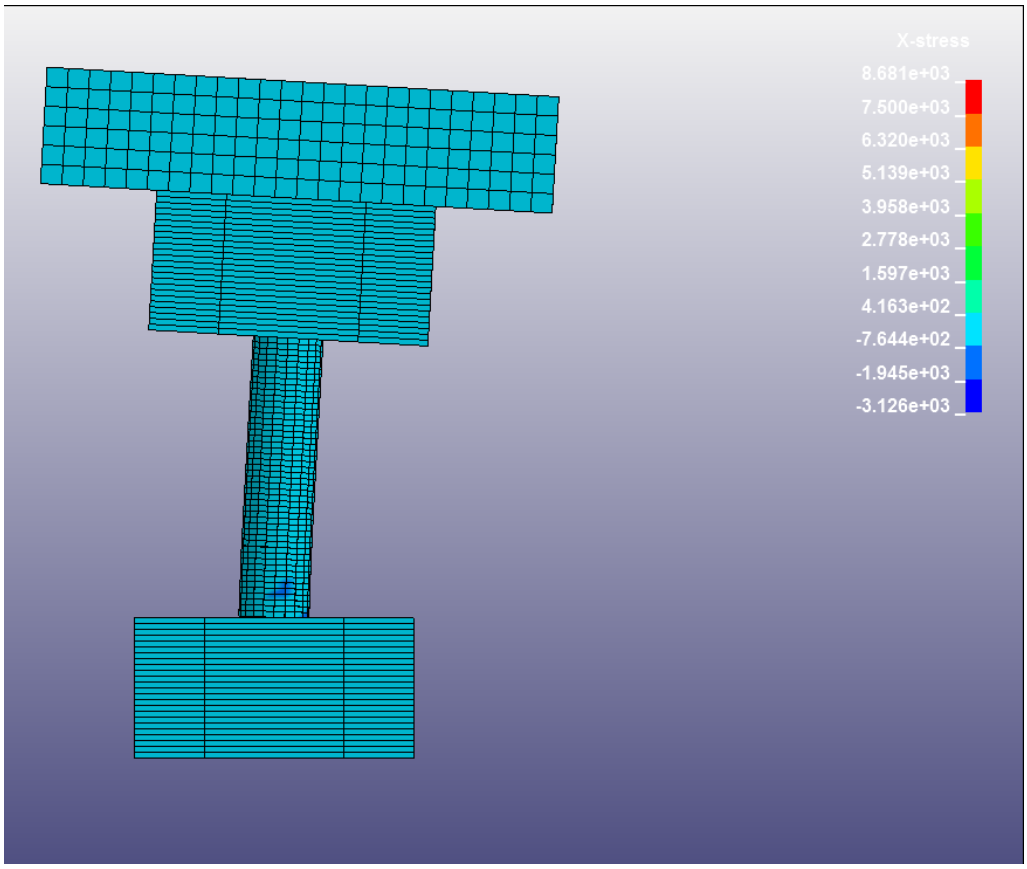

Figure C.5. X-Stresses

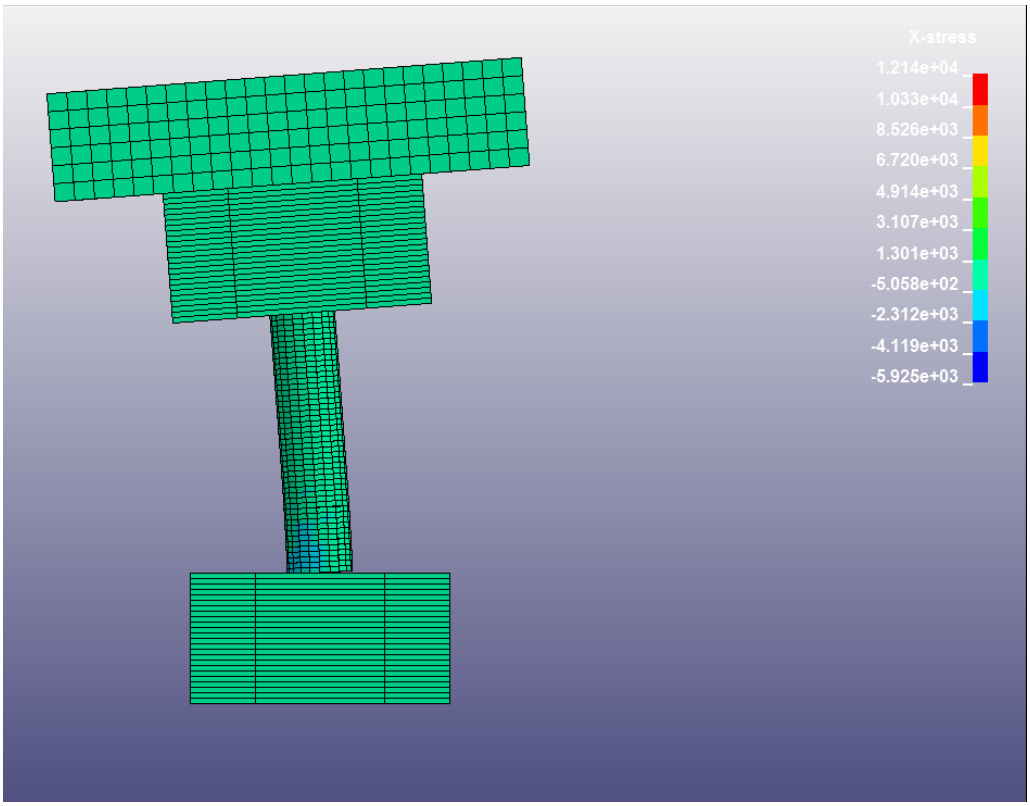

Figure C.6. X-Stresses

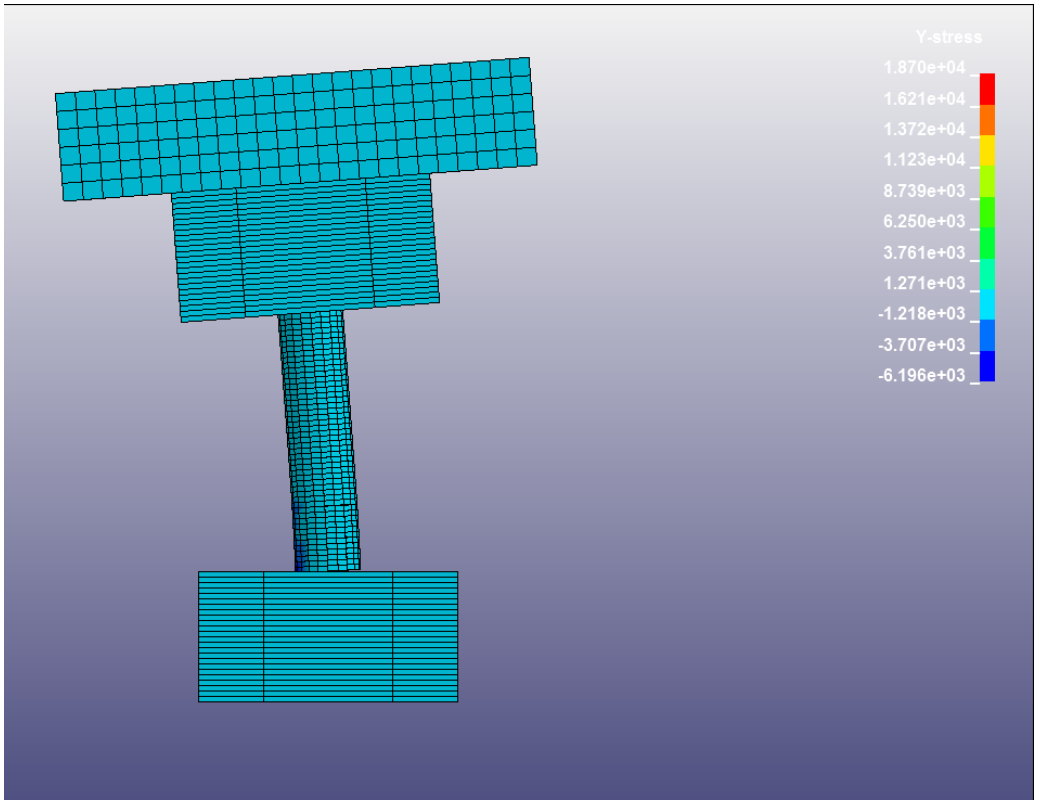

Figure C.7. Y-Stresses

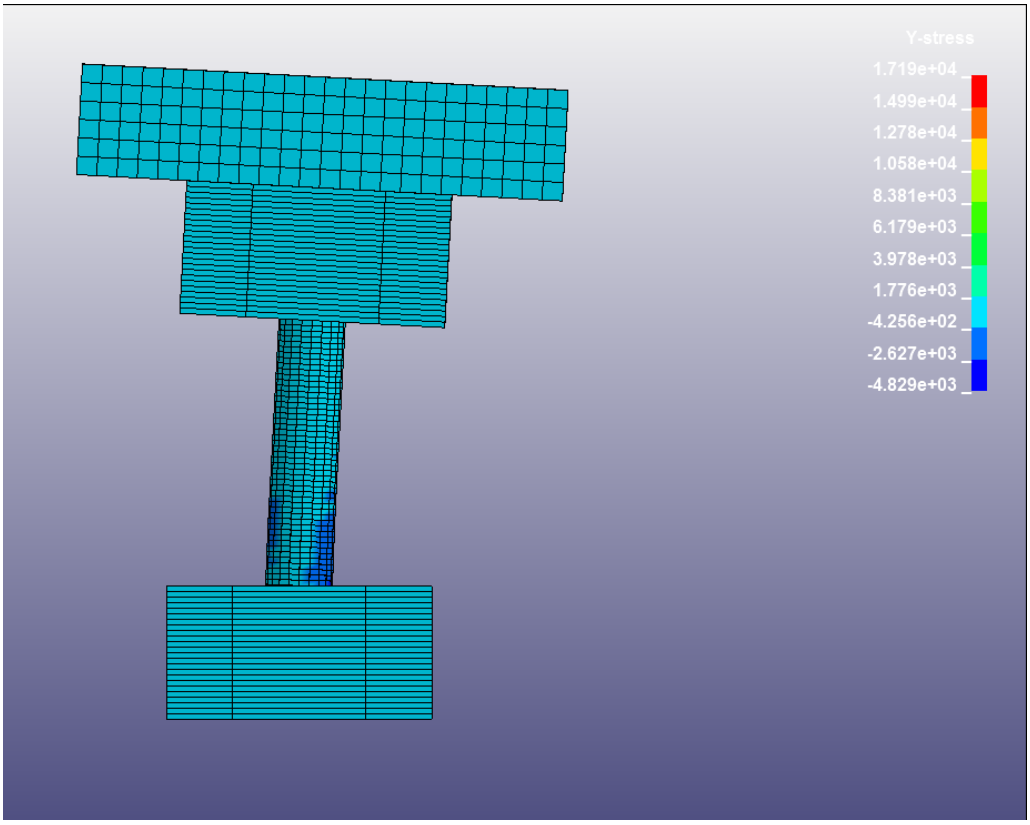

Figure C.8. Y-Stresses

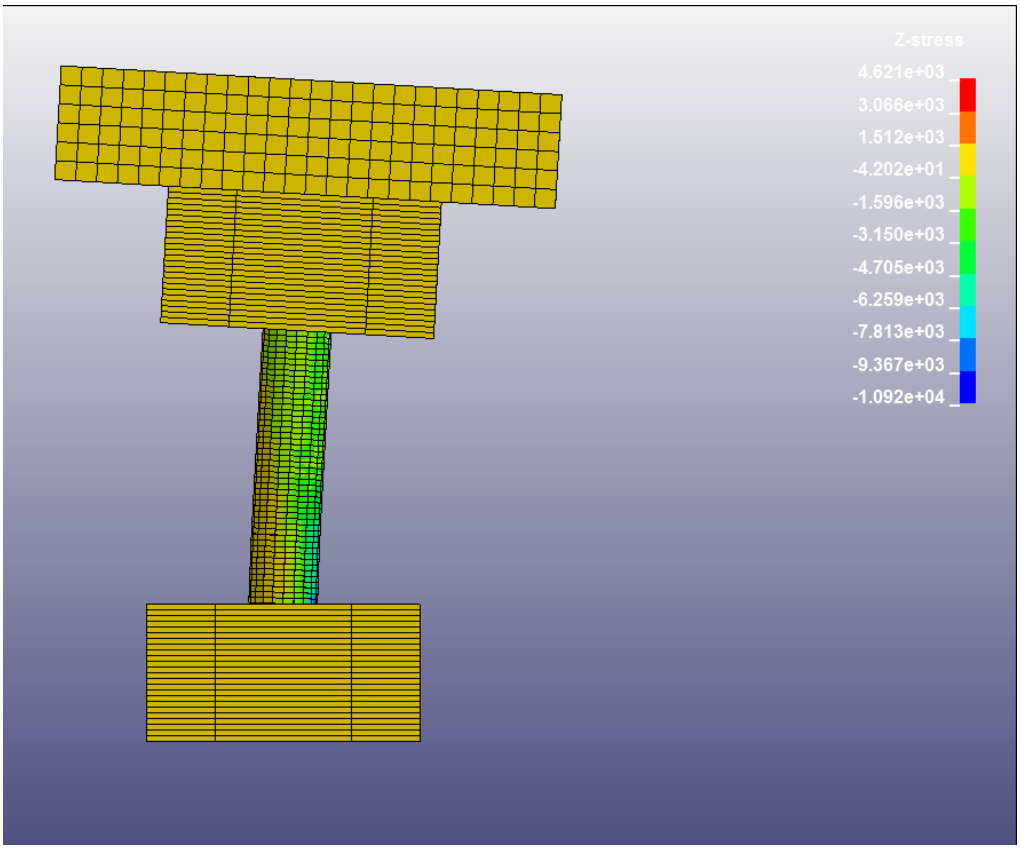

Figure C.9. Z-Stresses

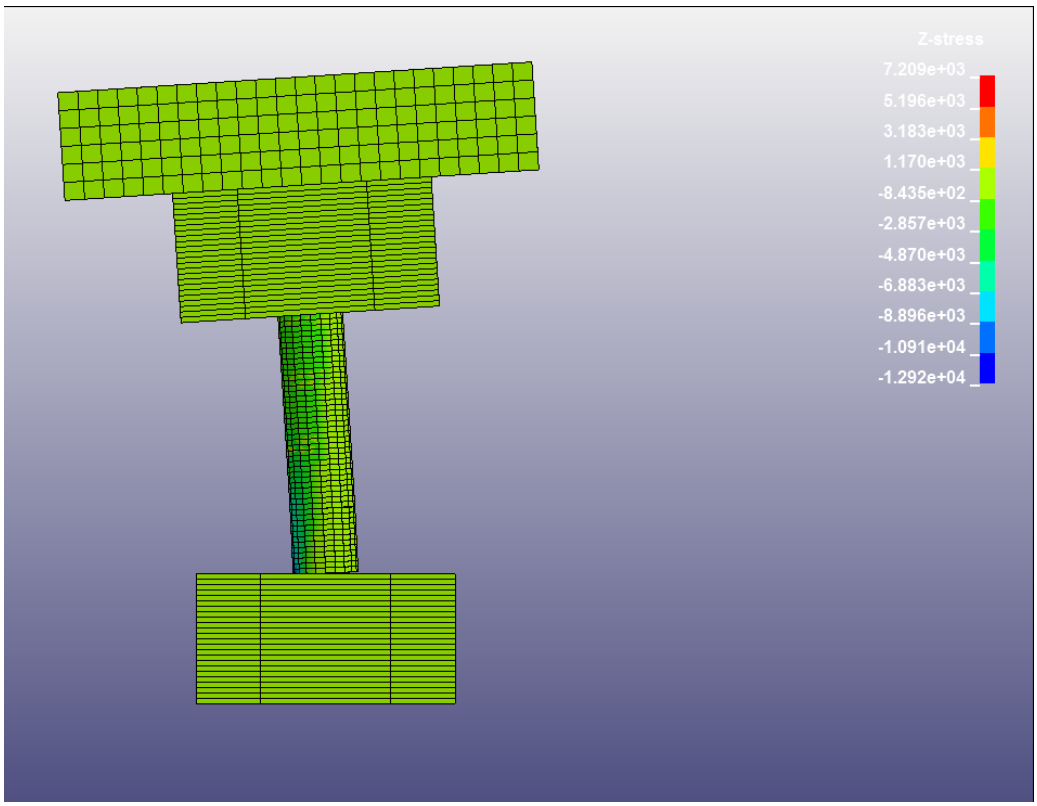

Figure C.10. Z-Stresses

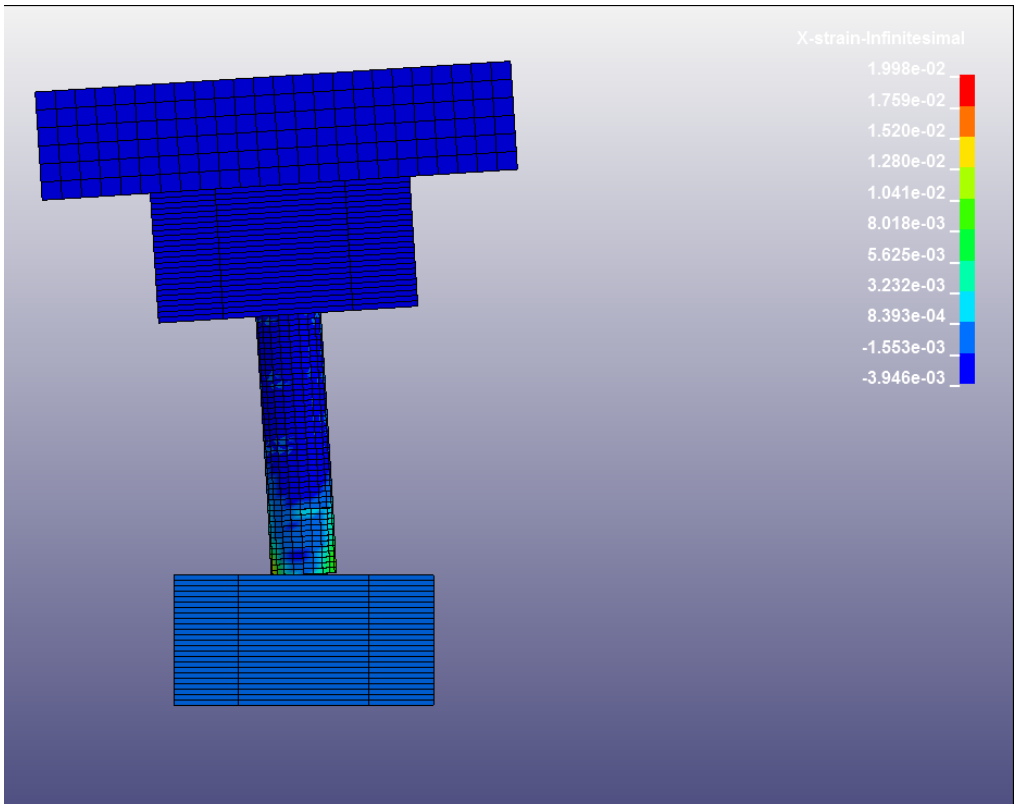

Figure C.11. X-Strains

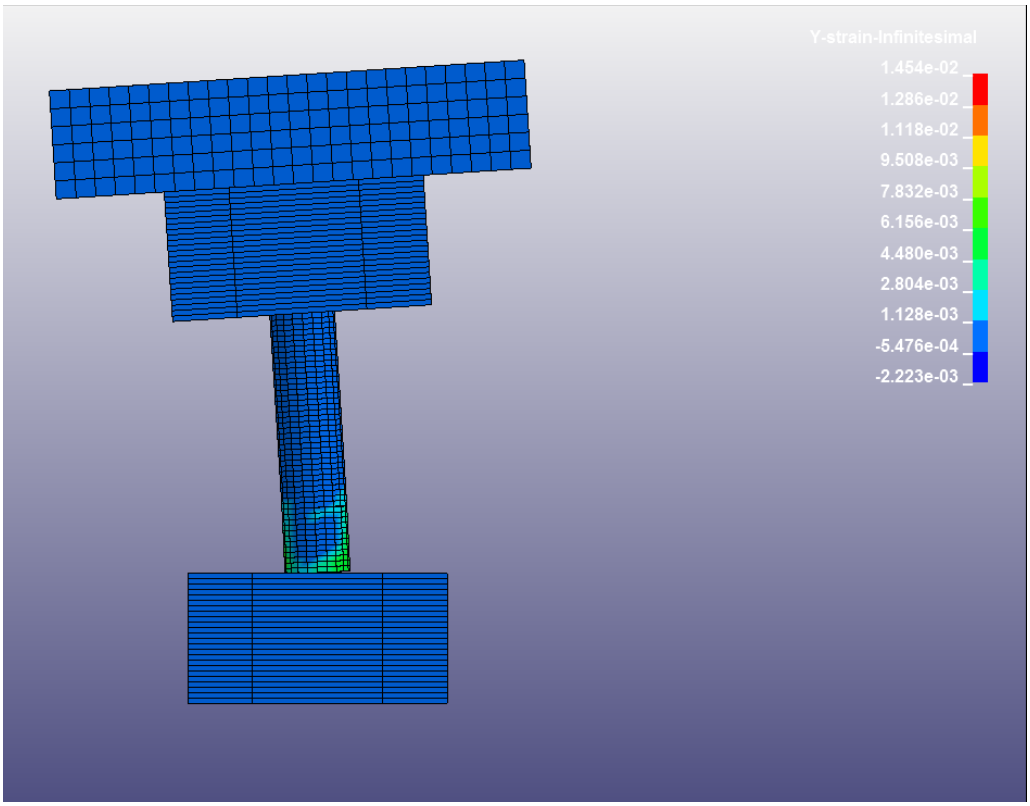

Figure C.12. Y-Strains

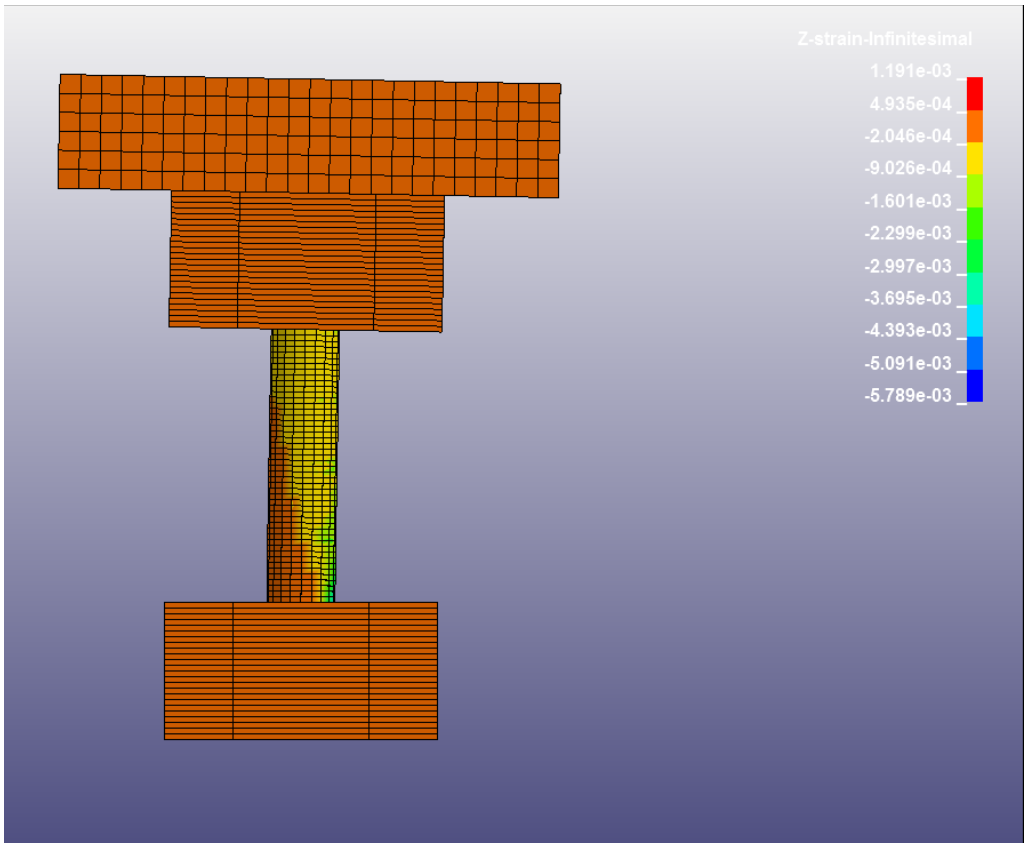

Figure C.13. Z-Strains

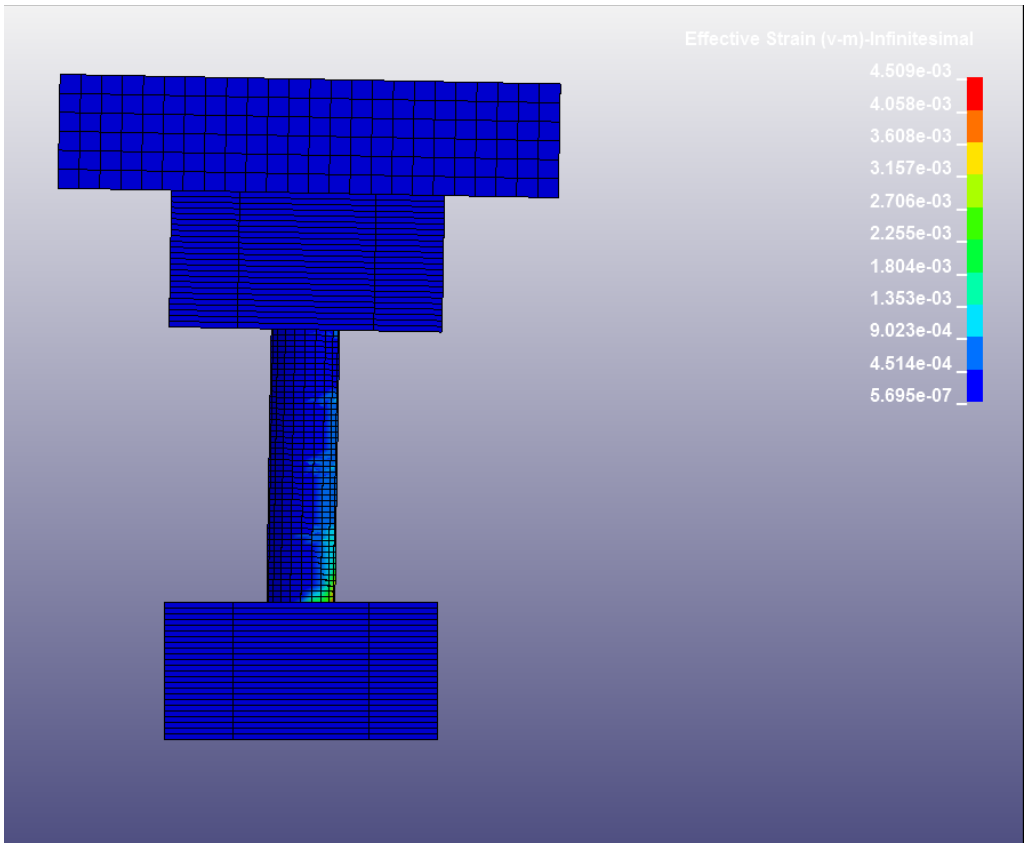

Figure C.14. Effective strains (Von-Mises)

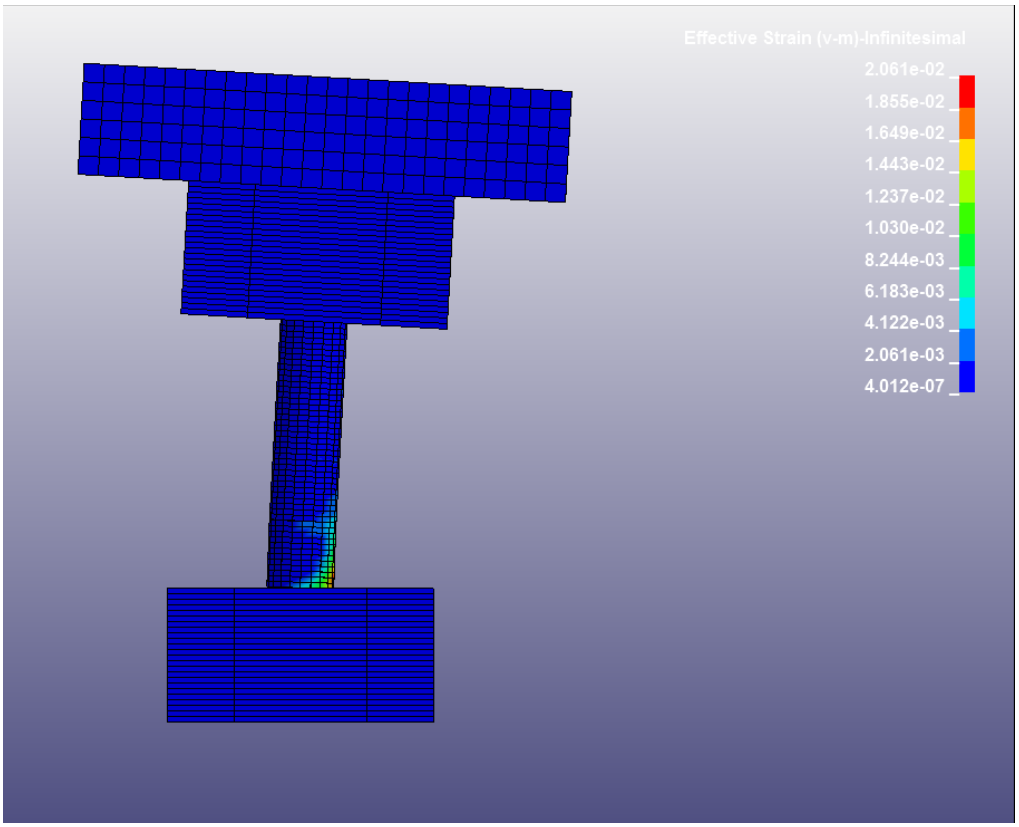

Figure C.15. Effective strains (Von-Mises)

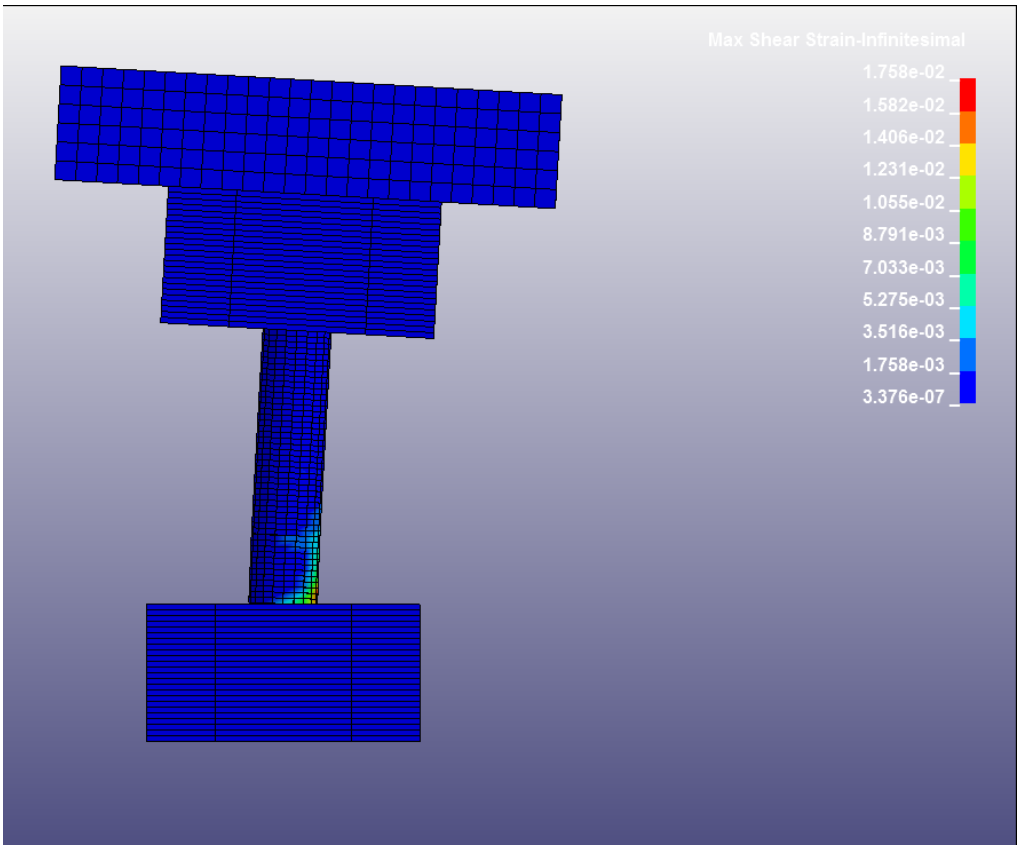

Figure C.16. Maximum shear strains

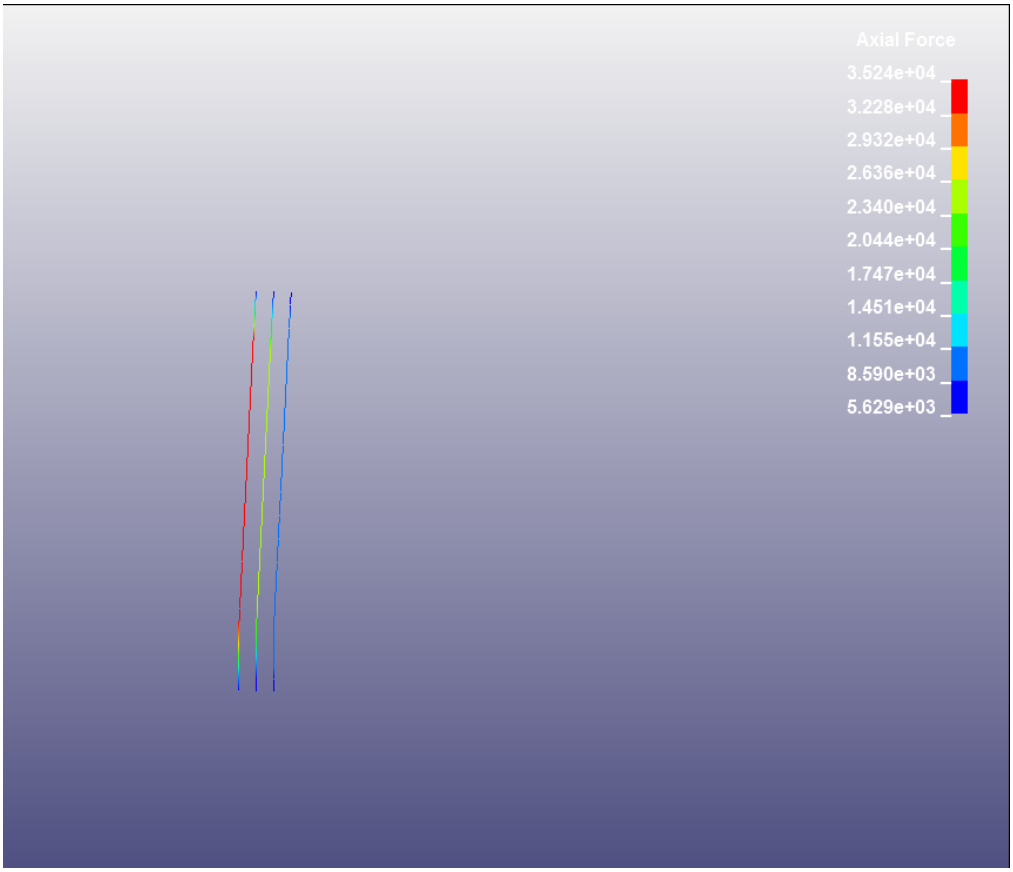

Figure C.17. Axial Force in PT cables

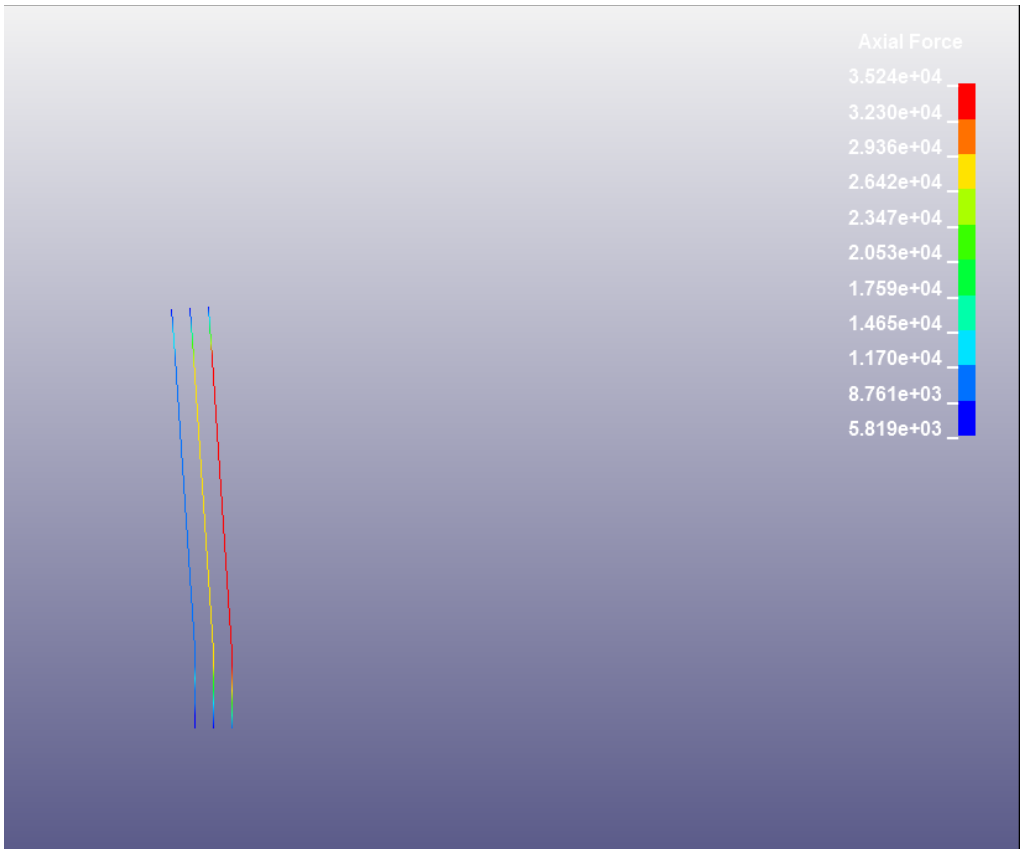

Figure C.18. Axial Force in PT cables

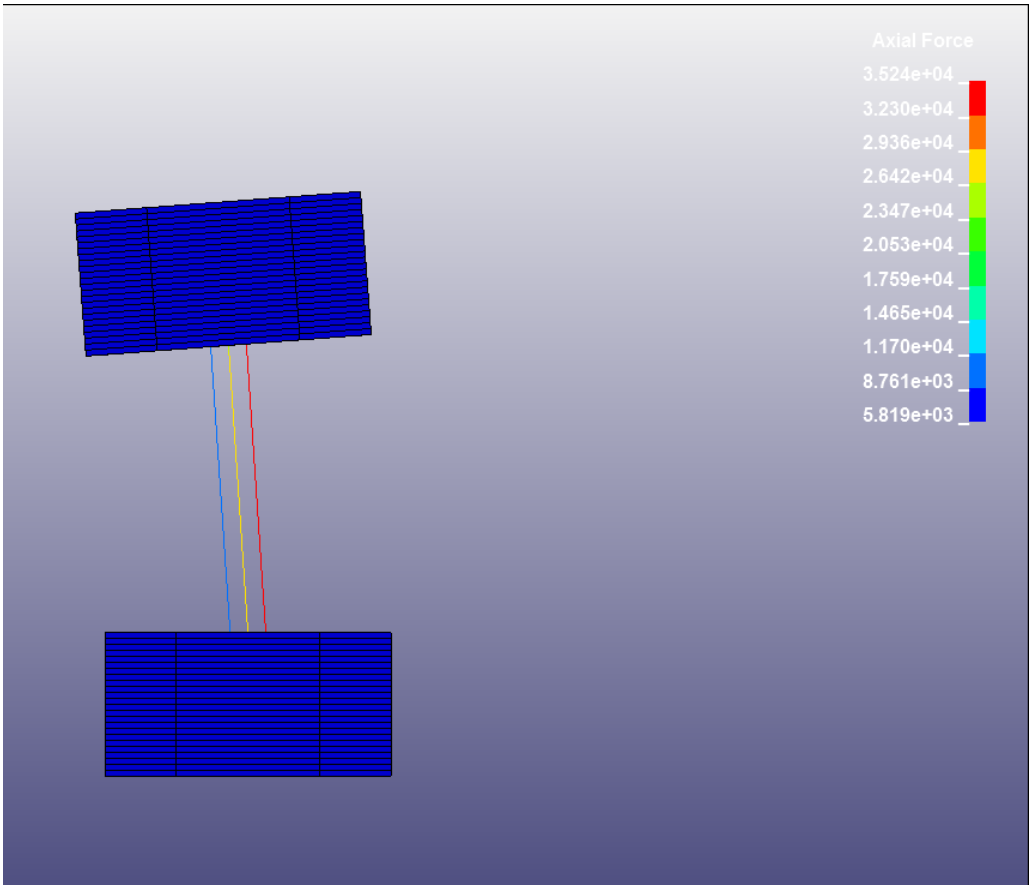

Figure C.19. Axial Force in PT cables

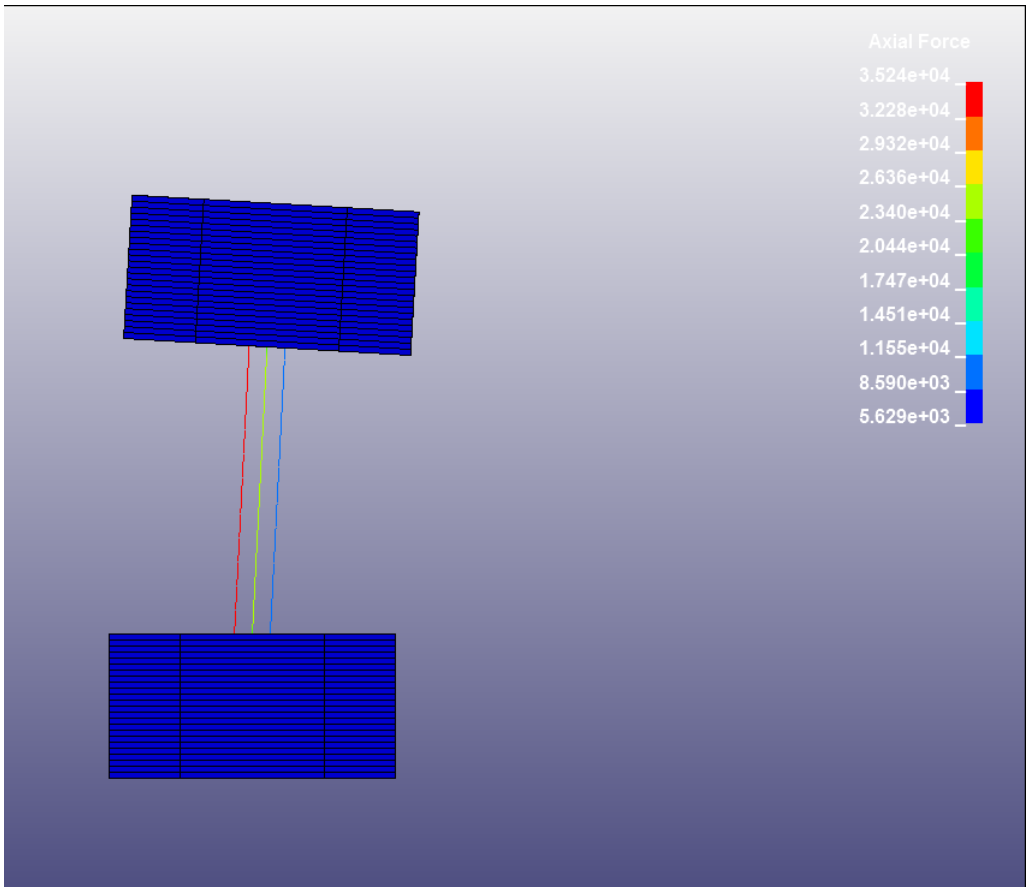

Figure C.20. Axial Force in PT cables

REFERENCES

Abdelkarim, O. I. and ElGawady, M. A. (2014). "Analytical and Finite-Element Modeling of FRP-Concrete-Steel Double-Skin Tubular Columns." Journal of Bridge Engineering.

ASTM C1723. (2010). "Standard Guide for Examination of Hardened Concrete Using Scanning Electron Microscopy."

Billington, S. and Yoon, J. (2004). "Cyclic response of unbonded posttensioned precast columns with ductile fiber-reinforced concrete." Journal of Bridge Engineering **9**(4): 353-363.

Bowland, A. G. (2011). Comparison and Analysis of the Strength, Stiffness, and Damping Characteristics of Concrete with Rubber, Latex, and Carbonate Additives, Virginia Polytechnic Institute and State University.

Chang, K., Loh, C., Chiu, H., Hwang, J., Cheng, C. and Wang, J. (2002). "Seismic behavior of precast segmental bridge columns and design methodology for applications in Taiwan." Taiwan Area National Expressway Engineering Bureau, Taipei, Taiwan in Chinese.

Chou, C.-C., Chang, H.-J. and Hewes, J. T. (2013). "Two-plastic-hinge and two dimensional finite element models for post-tensioned precast concrete segmental bridge columns." Engineering Structures **46**: 205-217.

Chou, C. C. and Chen, Y. C. (2006). "Cyclic tests of post-tensioned precast CFT segmental bridge columns with unbonded strands." Earthquake engineering & structural dynamics **35**(2): 159-175.

Dawood, H., ElGawady, M. and Hewes, J. (2011). "Behavior of Segmental Precast Posttensioned Bridge Piers under Lateral Loads." Journal of Bridge Engineering **17**(5): 735-746.

Eldin, N. N. and Senouci, A. B. (1993). "Rubber-tire particles as concrete aggregate." Journal of Materials in Civil Engineering **5**(4): 478-496.

ElGawady, M., Booker, A. J. and Dawood, H. M. (2010). "Seismic behavior of posttensioned concrete-filled fiber tubes." Journal of Composites for Construction **14**(5): 616-628.

ElGawady, M. A. and Dawood, H. M. (2012). "Analysis of segmental piers consisted of concrete filled FRP tubes." Engineering Structures **38**: 142-152.

ElGawady, M. A. and Sha'lan, A. (2010). "Seismic behavior of self-centering precast segmental bridge bents." Journal of Bridge Engineering **16**(3): 328-339.

Guerrini, G. and Restrepo, J. (2013). Seismic response of composite concrete-dual steel shell columns for accelerated bridge construction. Proc., 7th National Seismic Conf. on Bridges and Highways, MCEER.

Han, L.-H., Tao, Z., Liao, F.-Y. and Xu, Y. (2010). "Tests on cyclic performance of FRP–concrete–steel double-skin tubular columns." Thin-Walled Structures **48**(6): 430-439.

Hewes, J. T. and Priestley, M. N. (2002). Seismic design and performance of precast concrete segmental bridge columns.

Ichikawa, S., Matsuzaki, H., Moustafa, A., ElGawady, M. A. and Kawashima, K. (2016). "Seismic-Resistant Bridge Columns with Ultrahigh-Performance Concrete Segments." Journal of Bridge Engineering: 04016049.

Jeong, H., Sakai, J. and Mahin, S. A. (2008). "Shaking table tests and numerical investigation of self-centering reinforced concrete bridge columns." Pacific Earthquake Engineering Research Center. University of California, Berkeley. Public Works Research Institute, Tsukuba, Japan.

Khatib, Z. K. and Bayomy, F. M. (1999). "Rubberized Portland cement concrete." Journal of materials in civil engineering **11**(3): 206-213.

Kim, T.-H., Lee, H.-M., Kim, Y.-J. and Shin, H. (2010). "Performance assessment of precast concrete segmental bridge columns with a shear resistant connecting structure." Engineering Structures **32**(5): 1292-1303.

Kirk, R. S. and Mallett, W. J. (2013). "Highway bridge conditions: Issues for Congress." Rep. No. R43103.

Leitner, E. J. and Hao, H. (2016). "Three-dimensional finite element modelling of rocking bridge piers under cyclic loading and exploration of options for increased energy dissipation." Engineering Structures **118**: 74-88.

Mander, J. B. and Cheng, C.-T. (1997). Seismic design of bridge piers based on damage avoidance design, National Center for Earthquake Engineering Research, State Univ. of New York at Buffalo, Buffalo, NY.

Marriott, D., Pampanin, S. and Palermo, A. (2009). "Quasi-static and pseudo-dynamic testing of unbonded post-tensioned rocking bridge piers with external replaceable dissipaters." Earthquake Engineering & Structural Dynamics **38**(3): 331-354.

Motaref, S., Saiidi, M. S. and Sanders, D. (2013). "Shake table studies of energy-dissipating segmental bridge columns." Journal of Bridge Engineering **19**(2): 186-199.

Moustafa, A. and ElGawady, M. A. (2015). "Mechanical properties of high strength concrete with scrap tire rubber." Construction and Building Materials **93**: 249-256.

Ou, Y.-C., Wang, P.-H., Tsai, M.-S., Chang, K.-C. and Lee, G. C. (2009). "Large-scale experimental study of precast segmental unbonded posttensioned concrete bridge columns for seismic regions." Journal of structural engineering **136**(3): 255-264.

Ou, Y. C., Tsai, M. S., Chang, K. C. and Lee, G. C. (2010). "Cyclic behavior of precast segmental concrete bridge columns with high performance or conventional steel reinforcing bars as energy dissipation bars." Earthquake Engineering & Structural Dynamics **39**(11): 1181-1198.

Ozbakkaloglu, T. and Idris, Y. (2014). "Seismic behavior of FRP-high-strength concrete–steel double-skin tubular columns." Journal of Structural Engineering **140**(6).

Palermo, A., Pampanin, S. and Marriott, D. (2007). "Design, modeling, and experimental response of seismic resistant bridge piers with posttensioned dissipating connections." Journal of Structural Engineering **133**(11): 1648-1661.

Pampanin, S., Nigel Priestley, M. and Sritharan, S. (2001). "Analytical modelling of the seismic behaviour of precast concrete frames designed with ductile connections." Journal of Earthquake Engineering **5**(3): 329-367.

Reda Taha, M. M., El-Dieb, A., Abd El-Wahab, M. and Abdel-Hameed, M. (2008). "Mechanical, fracture, and microstructural investigations of rubber concrete." Journal of materials in civil engineering **20**(10): 640-649.

Resende, F., Roitman, N., Magluta, C. and Toledo Filho, R. (2003). "Influence of Scrap Rubber Tires and Steel Fibers on the Damping Characteristics of Normal Concrete." Civil Engineering Department, COPPE/Federal University of Rio de Janeiro, Rio de Janeiro, Brazil.

Rubber Manufacturers Association (2014). Tire industry facts, Rubber Manufacturers Association.

Shim, C. S., Chung, C.-H. and Kim, H. H. (2008). "Experimental evaluation of seismic performance of precast segmental bridge piers with a circular solid section." Engineering Structures **30**(12): 3782-3792.

Solberg, K., Mashiko, N., Mander, J. and Dhakal, R. (2009). "Performance of a damage-protected highway bridge pier subjected to bidirectional earthquake attack." Journal of structural engineering **135**(5): 469-478.

Teng, J., Yu, T., Wong, Y. and Dong, S. (2007). "Hybrid FRP–concrete–steel tubular columns: concept and behavior." Construction and Building Materials **21**(4): 846-854.

Topcu, I. B. (1995). "The properties of rubberized concretes." Cement and Concrete Research **25**(2): 304-310.

Toutanji, H. (1996). "The use of rubber tire particles in concrete to replace mineral aggregates." Cement and Concrete Composites **18**(2): 135-139.

Trono, W., Jen, G., Panagiotou, M., Schoettler, M. and Ostertag, C. P. (2014). "Seismic response of a damage-resistant recentering posttensioned-HYFRC bridge column." Journal of Bridge Engineering **20**(7): 04014096.

Wang, J. C., Ou, Y. C., Chang, K. C. and Lee, G. C. (2008). "Large-scale seismic tests of tall concrete bridge columns with precast segmental construction." Earthquake Engineering & Structural Dynamics **37**(12): 1449-1465.

Wong, Y., Yu, T., Teng, J. and Dong, S. (2008). "Behavior of FRP-confined concrete in annular section columns." Composites Part B: Engineering **39**(3): 451-466.

Xue, J. and Shinozuka, M. (2013). "Rubberized concrete: A green structural material with enhanced energy-dissipation capability." Construction and Building Materials **42**: 196-204.

Yamashita, R. and Sanders, D. H. (2009). "Seismic performance of precast unbonded prestressed concrete columns." ACI structural journal **106**(06).

Youssf, O., ElGawady, M. A. and Mills, J. E. (2015). "Experimental Investigation of Crumb Rubber Concrete Columns under Seismic Loading." Structures **3**: 13-27.

Youssf, O., ElGawady, M. A. and Mills, J. E. (2016). "Static Cyclic Behaviour of FRP-confined Crumb Rubber Concrete Columns." Engineering Structures.

Youssf, O., ElGawady, M. A., Mills, J. E. and Ma, X. (2014). "An experimental investigation of crumb rubber concrete confined by fibre reinforced polymer tubes." Construction and Building Materials **53**(0): 522-532.

Zhang, Q. and Alam, M. S. (2015). "Evaluating the Seismic Behavior of Segmental Unbounded Posttensioned Concrete Bridge Piers Using Factorial Analysis." Journal of Bridge Engineering **21**(4): 04015073.

Zheng, L., Sharon Huo, X. and Yuan, Y. (2008). "Experimental investigation on dynamic properties of rubberized concrete." Construction and Building Materials **22**(5): 939-947.

VITA

Ayman Moustafa was born in Kuwait, Kuwait in 1985. He received his Bachelor of Science in Civil Engineering degree in 2006 from Ain Shams University; one of the top universities of Egypt. He was ranked 1st out of 193 students in his class. He received his Master of Science in Civil Engineering degree from Ain Shams University in 2009. He acquired another Master of Science in Structural Engineering degree in 2012 from State University of New York at Buffalo. He began his Ph.D. at Missouri University of Science and Technology in January 2013.

After graduation with a Bachelor's degree, he worked as a part timer in two consultant engineering companies (AACE for one year and Dar Al-Handasah for two years), while doing his Masters. He was involved in design structural buildings at AACE and bridges at Dar Al-Handasah. He also participated in technical meetings with clients and contractors to resolve technical debates and individual site problems. Mr. Moustafa also worked as a teaching assistant at Ain Shams University for three years; a position that is highly praised back home and is only granted for the top 4 of the class. In December 2016, he received his Ph.D. in Civil Engineering from Missouri University of Science and Technology.